MODELLING LONG TERM CONDITIONS IN CANADIAN DEEP GEOLOGICAL REPOSITORY

MD ABDULLAH ASAD

A DISSERTATION SUBMITTED TO THE FACULTY OF GRADUATE STUDIES
IN PARTIAL FULFILLMENT OF THE REQUIREMENTS FOR THE DEGREE OF
DOCTOR OF PHILOSOPHY

GRADUATE PROGRAMME IN CIVIL ENGINEERING
YORK UNIVERSITY
TORONTO, ONTARIO

NOVEMBER 2024

ABSTRACT

Canada's plan for long term (1 million years) management of high-level nuclear waste includes a deep geological repository (DGR). The DGR design involves an engineered barrier system (EBS) within a low permeability host rock (crystalline or sedimentary) that serves as a natural barrier. The EBS includes copper coated used fuel containers (UFCs) within highly compacted bentonite. Over the DGR lifetime, different hydrogeological and geochemical conditions can evolve in the repository. These transient conditions include bentonite saturation, UFC heating, evaporation and condensation, geochemical reaction, adsorption, and microbial activity. Depending on site-specific conditions, bisulfide (HS^-) produced by sulfate reducing bacteria in the host rock could slowly transport (diffuse) through the bentonite to the UFC surface and corrode the copper coating and produce hydrogen (H_2). Therefore, HS^- corrosion assessment is complex and requires a robust numerical model. This thesis describes the development of a HS^- transport and reaction model and explores how DGR transient hydrogeological and geochemical conditions affect HS^- transport and UFC corrosion. The model predicted slower saturation evolution in the sedimentary DGR due to the rock's low permeability compared to the crystalline DGR. The slower saturation evolution in the sedimentary DGR delayed HS^- transport and therefore HS^- corrosion. The model also assessed the relative importance of different processes (e.g. heating, saturation, reaction, adsorption), and system behaviour over time due to the inclusion of these processes, was understood. For example, heating accelerated bisulfide transport while partially saturated bentonite and bisulfide reaction, or adsorption, limited it. In addition, the combined effects of heating, saturation, and bisulfide reaction or adsorption with bentonite were not pronounced over the long DGR life span. Bisulfide transport was simulated for the entire DGR lifespan and was found to be delayed (~50-800 years) due to HS^- and iron (Fe^{2+}) reaction or HS^- adsorption. However, the HS^- diffusion delays are relatively short in a DGR lifespan (1 million years) and does not impact long term HS^- corrosion, which stays below Canada's HS^- corrosion depth tolerance. Lastly, amongst various modelling scenarios, the H_2 solubility limit was never surpassed, indicating the unlikelihood of H_2 gas pressure build-up in a DGR under explored modelling conditions.

CO-AUTHORSHIP STATEMENT

Chapter 2: Modelling Hydrogeological and Geochemical Processes Occurring in a Deep Geological Repository for Nuclear Waste Management – State of Science Review (**Unpublished**)

Authorship Contribution Statement

Md Abdullah Asad: Conceptualization, Data curation, Investigation, Formal analysis, Roles/Writing - original draft. **Tarek L. Rashwan:** Conceptualization, Writing - review & editing. **Ian L. Molnar:** Conceptualization, Project administration, Supervision, Writing - review & editing. **Mehran Behazin**: Project administration, Resources, Supervision, Writing - review & editing. **Peter G. Keech**: Project administration, Resources, Supervision, Writing - review & editing. **Magdalena M. Krol:** Conceptualization, Funding acquisition, Project administration, Supervision, Writing – Writing, review & editing.

Chapter 3: Modelling Corrosive Species Transport through the Engineered Barrier System under Repository Conditions **(Published)**

1. Asad, A., T. Rashwan, I. Molnar and M. Krol. 2022. Modelling Bisulfide Transport through the Engineered Barrier System under Repository Conditions: Coupling Unsaturated Flow and Refining Boundary Conditions. Nuclear Waste Management Organization Report NWMO-TR-2022-06. Toronto, Canada.

Authorship Contribution Statement

Md Abdullah Asad: Conceptualization, Data curation, Formal analysis, Investigation, Methodology, Software, Validation, Visualization, Roles/Writing - original draft. **Tarek L. Rashwan:** Conceptualization, Formal analysis, Methodology, Writing - review & editing. **Ian L. Molnar:** Conceptualization, Formal analysis, Methodology, Project administration, Software, Supervision, Writing - review & editing. **Magdalena M. Krol:** Conceptualization, Funding acquisition, Formal analysis, Methodology, Project administration, Resources, Supervision, Writing – review & editing.

2. Rashwan, T.L., M.A. Asad, I.L. Molnar, M. Behazin, P.G. Keech and M.M. Krol. 2022. Exploring the governing transport mechanisms of corrosive agents in a Canadian deep geological repository. Science of The Total Environment, 1–43.

Authorship Contribution Statement

Tarek L. Rashwan: Formal analysis, Investigation, Methodology, Software, Validation, Visualization, Roles/Writing - original draft. **Md Abdullah Asad:** Conceptualization, Data curation, Formal analysis, Investigation, Methodology, Software, Validation, Visualization, Writing - review & editing. **Ian L. Molnar:** Conceptualization, Formal analysis, Methodology, Project administration, Resources, Software, Supervision, Writing - review & editing. **Mehran Behazin**: Project administration, Resources, Supervision, Writing - review & editing. **Peter G. Keech**: Project administration, Resources, Supervision,

Writing - review & editing. **Magdalena M. Krol:** Conceptualization, Funding acquisition, Methodology, Project administration, Resources, Supervision, Writing - review & editing.

Chapter 4: Assessment of Hydrogen Gas Formation Using Numerical Modelling Under Deep Geological Repository Environments **(Submitted to Engineering Geology)**

Authorship Contribution Statement

Md Abdullah Asad: Conceptualization, Data curation, Formal analysis, Investigation, Methodology, Software, Validation, Visualization, Roles/Writing - original draft. **Tarek L. Rashwan:** Conceptualization, Formal analysis, Methodology, Writing - review & editing. **Ian L. Molnar:** Conceptualization, Formal analysis, Methodology, Project administration, Software, Supervision, Writing - review & editing. **Mehran Behazin**: Project administration, Resources, Supervision, Writing - review & editing. **Peter G. Keech**: Project administration, Resources, Supervision, Writing - review & editing. **Magdalena M. Krol:** Conceptualization, Funding acquisition, Methodology, Project administration, Resources, Supervision, Writing – Writing, review & editing.

Chapter 5: Modelling Key Reactive Processes Relevant to Bisulfide Transport through Highly Compacted Bentonite **(Published)**

1. M. A. Asad, T. L. Rashwan, I. L. Molnar., M. Behazin, P.G. Keech, and M.M. Krol. 2024. Modelling key reactive processes relevant to bisulfide transport through highly compacted bentonite. Results in Engineering, 24:103486.

Authorship Contribution Statement

Md Abdullah Asad: Conceptualization, Data curation, Formal analysis, Investigation, Methodology, Software, Validation, Visualization, Roles/Writing - original draft. **Tarek L. Rashwan:** Conceptualization, Formal analysis, Methodology, Writing - review & editing. **Ian L. Molnar:** Conceptualization, Formal analysis, Methodology, Project administration, Software, Supervision, Writing - review & editing. **Mehran Behazin**: Project administration, Resources, Writing - review & editing. **Peter G. Keech**: Project administration, Resources, Writing - review & editing. **Magdalena M. Krol:** Conceptualization, Funding acquisition, Formal analysis, Methodology, Project administration, Resources, Supervision, Writing – review & editing.

DEDICATION

To my beloved parents, parents in law, my lovely wife, my dearest son, and siblings.

ACKNOWLEDGEMENTS

I have been fortunate enough to be supervised by Dr. Magdalena Krol and Dr. Ian Molnar, who are great researchers and very kind-hearted persons. I really appreciate their continual support, feedback, and encouragement throughout my PhD. Their guidance and suggestion were a great help for the implementation of this work.

I am thankful to Dr. Tarek Rashwan, Dr. Peter Keech, Dr. Mehran Behazin, Dr. Matthew Perras, Dr. Shooka Karimpour and my PhD examination Committee for their support. I am thankful to York University, all faculty members and non-faculty members of department of Civil Engineering. During my journey as a PhD student, I have met many wonderful colleagues and friends. I am thankful to them.

I am forever indebted to my father who always encourages me to believe in myself which has a great role in building my confidence to complete this dissertation and to my mother who struggled throughout her life to raise me to this position. I am also very grateful to my parents-in-law for their encouragement and support. I want to thank my wife for being patient and understanding during this journey; I am very lucky to have her company and huge support during my studies. I am thankful to my beloved son whose adorable presence inspired me to complete this work. I am also thankful to my siblings, and family members for their encouragement.

TABLE OF CONTENTS

ABSTRACT ii

CO-AUTHORSHIP STATEMENT iii

DEDICATION vii

ACKNOWLEDGEMENTS viii

TABLE OF CONTENTS ix

LIST OF TABLES xv

LIST OF FIGURES xvi

CHAPTER 1 Introduction 1

1.1 Motivation 1

1.2 Research Objectives 3

CHAPTER 2 Modelling Hydrogeological and Geochemical Processes Occurring in a Deep Geological Repository for Nuclear Waste Management – State of Science Review 5

2.1 Introduction 5

2.2 DGR Conceptual Model 12

2.2.1 Temperature 13

2.2.2 Saturation and Swelling 13

2.2.3 Species Diffusion 14

2.2.4 Corrosion 14

2.2.5 Gases 15
2.2.6 Other Processes 15
2.3 Modelling Platforms 17
2.4 Modelling Hydrogeological Processes 19
2.4.1 Buffer Saturation 20
2.4.2 Heat Transport 29
2.4.3 Aqueous Species Transport 32
2.5 Modelling Geochemical Processes 40
2.5.1 Species Sorption 41
2.5.2 Species Reaction 43
2.6 Challenges of Modelling a Large Domain 50
2.7 Key Lessons Learned 53
2.8 Conclusions 55
CHAPTER 3 Modelling Corrosive Species Transport through the Engineered Barrier System under Repository Conditions 57
3.1 Introduction 57
3.2 Background 59
3.2.1 Temperature Evolution 60
3.2.2 Evolution of Bentonite Saturation and Oxic Conditions 61
3.2.3 Microbiologically Influenced Corrosion 63

3.2.4 Conceptual Model of Coupled Processes in Canadian DGR 64
3.3 Model Approach and Methodology 67
3.3.1 Model Development 70
3.3.2 Parameters 73
3.3.3 Convergence and Repeatability 75
3.3.4 Model Validation 76
3.4 Model Results 77
3.4.1 Model Implementation and Sensitivity Study 77
3.4.2 Saturation Time 82
3.4.3 Bisulfide Flux and MIC Depth 84
3.4.4 THC versus Other Models 86
3.4.5 Predicted DGR Environmental Conditions 91
3.5 3-D THC Model 92
3.6 Theoretical and Numerical Bisulfide Flux 96
3.7 Conclusions 97
CHAPTER 4 Assessment of Hydrogen Gas Formation Using Numerical Modelling Under Deep Geological Repository Environments 102
4.1 Introduction 102
4.2 Model Approach and Methodology 106
4.2.1 Model Development 106

4.2.2 Parameters 111
4.3 Model Results 112
4.3.1 Model Confirmation 112
4.3.2 Sensitivity Study 113
4.3.3 DGR H_2 Concentration from Sensitivity Cases 127
4.3.4 Effects of Temperature and Saturation 128
4.4 Conclusions 130
CHAPTER 5 Modelling Key Reactive Processes Relevant to Bisulfide Transport through Highly Compacted Bentonite 133
5.1 Introduction 133
5.2 Methodology 138
5.2.1 Model Development 138
5.2.2 Parameters 144
5.3 Results and Discussion 145
5.3.1 Influence of Anion Exclusion on Species Diffusion 145
5.3.2 HS^- Adsorption Models' Results 149
5.3.3 HS^- Reaction Model's Results 151
5.3.4 Modelled HS^- Transport Dynamics 155
5.3.5 3-D HS^- Transport and Reaction Models 156
5.4 Conclusions 161

CHAPTER 6 Discussion and Conclusions 164
6.1 Discussion 164
6.2 Key Results from THC, THC-S, THC-R, and THC-H_2 Models (Chapters 3, 4, and 5) 166
6.2.1 3-D THC Model 167
6.2.2 3-D THC-S and THC-R Models 172
6.2.3 2-D THC-H_2 Model 178
6.3 Conclusions 183
6.4 Implications and Research Novelty 185
6.5 Recommendations for Future Work 187
References 189
Appendix A: Supplementary Materials for “Assessment of Hydrogen Gas Formation Using Numerical Modelling Under Deep Geological Repository Environments” 210
A.S.1 Boundary and Initial Conditions of the THC Model 210
A.S.2 THC-H_2 Model Implementation 212
A.S.3 Species Conversion Rate Comparison 213
A.S.4 Species Concentration in the THC-H_2 Model 215
A.S.5 Species Concentration in the THC-H_2 Model 217
A.S.6 DGR Level H_2 Solubility 218
A.S.7 Diffusion Time Scale Analysis 219

A.S.8 Average Species Conversion Rate at Rock-Bentonite Interface 221

A.S.9 References 222

Appendix B: Supplementary Materials for “Modelling Key Reactive Processes Relevant to Bisulfide Transport Through the Highly Compacted Bentonite” 224

B.S.1 Proposed Design of Canadian DGR 224

B.S.2 Diffusivity and Accessible Porosity in the Cl^- Diffusion Model 225

B.S.3 HS^- Adsorption Confirmation 226

B.S.4 Fitting HS^- Adsorption Parameters through Varying Data 227

B.S.5 Kinetically Irreversible HS^- Reaction (C-R_I) Model Confirmation 229

B.S.6 Sensitivity of Reaction Rate to Arrhenius Frequency Factor 230

B.S.7 References 231

Appendix C: Reproduction Licenses 232

LIST OF TABLES

Table 2.1 : Applications of modelling platforms 18

Table 3. 1: Evolution of dgr conditions with time (adapted from (king 2005)) 63

Table 3. 2: Model parameters 74

Table 3. 3: Total maximum MIC depths calculated by the various models..... 90

Table 4. 1: Conservative assumptions made in modelling h_2 dynamics 107

Table 4. 2: Key parameters for H_2 dynamics..... 112

Table 4. 3: Sensitivity analysis simulations 115

Table 5. 1: Reactive 1-D models 139

Table 5. 2: Model parameters 144

Table 6. 1: Sensitivity analysis simulations 181

LIST OF FIGURES

Figure 2.1: DGR designs in different countries: (a) KBS-3V (Sweden, Finland) (SKB 2010a) (b) NWMO's design (Canada) (Hall and Keech 2017) (c) NAGRA's design (Switzerland) (Patel et al. 2012) (d) Placement tunnel in Yucca mountain repository, Nevada, USA (U.S. DOE 2002) and (e) Barrier design examples for ILW and HLW (RWM 2017) (Adapted from Hall et al. (2021) with permission of Elsevier)..... 9

Figure 2.2: A conceptual model of various processes impacting the DGR's EBS (Adapted from Asad et al. (2022) 16

Figure 2.3: Key DGR transport processes relevant to bentonite saturation (adapted from Sena et al. (2010))..... 20

Figure 2.4: Validation of the China-Mock-Up test for HLW disposal: a) Model of the China-Mock-Up test, b) Comparison of temperature profiles from experiment and model, c) Comparison of relative humidity profiles from experiment (r=0.3 m, z= 0.123 m) and model, and d) Comparison of swelling pressure profiles from experiment (r= 0.15 m, z= 0.123 m) and model. (Adapted from Liu et al. (2014)). Note that r represents radial distance from the centre of the heater (representing waste heating) and z represents vertical distance. 26

Figure 2.5: Key geochemical processes in bentonite porewater (adapted from Itälä (2009) and Itälä and Olin (2017) with permission from Elsevier). 41

Figure 2.6: a) A regional scale model (several km width), where very small black boxes represent the location of a repository site scale model from SKB, Sweden, b) Repository site scale model domains (hundred m scale). (Adapted from Abarca et al. (2013)). 51

Figure 3. 1: Multiple barrier system in Canadian DGR (adapted from Hall et al. (2021) with permission of Elsevier)..... 58

Figure 3. 2: Approximated DGR environmental conditions (adapted from (King et al. 2008) with permission of Elsevier) 60

Figure 3. 3: Estimated copper corrosion depth (modified from (Scully et al. 2016))64

Figure 3.4: Key DGR transport processes (adapted from Sena et al. (2010)).... 65

Figure 3.5: Coupled DGR processes governing MIC and saturation of DGR; red font indicates processes modelled in this study 66

Figure 3.6: COMSOL modelling domain (10,000 m deep) with 10 m segment of a single placement room in (a) 2-D and (b) 3-D. The placement room contains one used fuel container (UFC) in 2-D and two UFCs in 3-D, gap fill (GF), high compacted bentonite (HCB), and host rock..... 70

Figure 3.7: Initial and boundary conditions of the THC model for: (a) hydraulic (Richard's equation), (b) thermal (heat transfer), (c) chemical (Fick's 2nd law), and (d) 2-D triangular mesh (12850 elements), and 3-D tetrahedral mesh (551500 elements). Note that the geothermal gradient and boundary temperatures in the thermal module are shown for the crystalline domain..... 72

Figure 3.8: Mesh convergence study showing the change in maximum MIC with various minimum element sizes 76
Figure 3.9: Comparison of experimental data from the unsaturated soil hydraulic database and a 1-D saturation model developed using the Richards' Equation in COMSOL 77
Figure 3.10: Domain depth sensitivity, (a) boundary effect: placing bottom boundary 10 m below the EBS underpredicted the UFC temperature, (b & c) UFC temperature rose to the expected value (i.e., maximum temperature above 80 ˚C) when bottom boundary was moved away from the EBS. Note that the figures are not to scale. 79
Figure 3.11: Temperature profiles in different depth models 79
Figure 3.12: Flow boundary conditions sensitivity for: (a) Type 2: No flow boundary conditions (b) Type 1: Pressure head boundary conditions. Results are shown at 630 years. 80
Figure 3.13: Heat source sensitivity using a: (a) boundary heat source, and (b) domain heat source for a 2-D model. Total domain depth of 10,000 m was used in both cases 81
Figure 3.14: Water saturation in the crystalline DGR after a) 2 years, b) 5 years, and c) 15 years. Average permeability of rock and bentonite are 4.08×10^{-17} m^2 and 6×10^{-21} m^2, respectively. 83

Figure 3.15: Water saturation in the sedimentary DGR after a) 15 years, b) 50 years, and c) 100 years. Horizontal and vertical permeabilities of rock are 2×10^{-21} m^2 and 2×10^{-22} m^2, respectively. Average bentonite permeability is 1×10^{-19} m^2. 83
Figure 3.16: Average water saturation over the estimated life span of the DGR for varying a) average permeabilities of the crystalline rock (bentonite k= 6×10^{-21} m^2), b) horizontal permeabilities of the sedimentary rock while keeping the vertical permeability unchanged (bentonite k= 1×10^{-19} m^2). 84
Figure 3.17: Bisulfide flux in the crystalline DGR after a) 2 years, b) 5 years, and c) 15 years 85
Figure 3.18: Bisulfide flux in the sedimentary DGR after a) 15 years, b) 50 years, and c) 100 years 86
Figure 3.19: MIC rates (max, min, average) in the crystalline DGR under different conditions a) C model simulates bisulfide diffusion under fully saturated-isothermal conditions, b) HC model simulates bisulfide diffusion under variably saturated-isothermal conditions, c) TC model simulates bisulfide diffusion under fully saturated-non-isothermal conditions, d) THC model simulates bisulfide diffusion under variably saturated-non-isothermal conditions, and e) maximum MIC rates in all the different models..... 88
Figure 3.20: MIC rates (max, min, average) in the sedimentary DGR models under different conditions a) C model simulates bisulfide diffusion under fully saturated-

isothermal conditions, b) HC model simulates bisulfide diffusion under variably saturated-isothermal conditions, c) TC model simulates bisulfide diffusion under fully saturated-non-isothermal conditions, d) THC model simulates bisulfide diffusion under variably saturated-non-isothermal conditions, and e) maximum MIC rates in all the different models..... 89
Figure 3.21: Maximum MIC rates in different models, plotted against a linear time scale, a) crystalline DGR, and b) sedimentary DGR..... 91
Figure 3.22: Predicted environmental conditions from the THC models in the a) crystalline DGR, and b) sedimentary DGR. Note that the average bentonite air content and bisulfide flux values are normalized..... 92
Figure 3.23: 2-D THC versus 3-D THC models of the crystalline DGR, a) maximum MIC rates, b) temperature, and c) average DGR saturation 93
Figure 3.24: (a, b) average DGR effective saturation and (c, d) average UFC surface temperature from varying the initial saturation, isotropic rock permeabilities (in the crystalline model in frames a and c), and horizontal rock permeabilities (in the sedimentary model in frames b and d). The base case scenarios are bolded (Rashwan et al. 2022). 94
Figure 3.25: Relative bisulfide fluxes estimated at UFC surface (upper end-caps) in (a) crystalline and (b) sedimentary DGR models under different modelling conditions. C model simulates bisulfide diffusion under fully saturated-isothermal conditions, HC

model simulates bisulfide diffusion under variably saturated-isothermal conditions, TC model simulates bisulfide diffusion under fully saturated-non-isothermal conditions, THC model simulates bisulfide diffusion under variably saturated-non-isothermal conditions. (c and d) Prediction hydrogeological conditions in the crystalline and sedimentary domains. Note that the average bentonite air content and bisulfide flux values are normalized (Rashwan et al. 2022)..... 95

Figure 3.26: HS^- corrosion depths under different modelling conditions (i.e., C, HC, TC, and THC) in the crystalline or sedimentary domains. The slopes are calculated from 200,000 to 1,000,000 years in each model using linear regression analyses. Note that the horizontal axis represents a linear timescale (Rashwan et al. 2022). The HS^- corrosion depth tolerance is reported in Hall et a. (2021)..... 96

Figure 3.27: Comparison of bisulfide fluxes from an analytical model and numerical C models of the crystalline DGR..... 97

Figure 4.1: a) Proposed multiple barrier system in Canadian DGR (adapted from Hall et al. 2021) and b) Conceptual model of key processes relevant to H_2 production and consumption in Canada's proposed DGR. 104

Figure 4.2: a) Key initial and boundary conditions for HS^- and H_2 in the THC-H_2 model and b) Transport directions of HS^- and H_2 108

Figure 4.3: Key initial and boundary conditions for HS^- and H_2 in the THC-H_2 feedback model and b) Transport directions of HS^- and H_2 109

Figure 4.4: HS^- concentration over time in the a) THC-H_2 model and b) THC model 113
Figure 4.5: Effect of HS^- initial background concentration on a) maximum H_2 concentration at the UFC and b) average species conversion rate at the UFC. Note that the positive and negative species conversion rates indicate species production and consumption, respectively. 116
Figure 4.6: Effect of constant HS^- concentration at the RBI on a) maximum H_2 concentration at the UFC and b) average species conversion rate at the UFC. Note that the positive and negative species conversion rates indicate species production and consumption, respectively. Also note that tL1 represents time lag due to HS^- transport from the RBI to the UFC and x_1 is the minimum horizontal distance between RBI and UFC cap, 0.343 m. 118
Figure 4.7: Effect of H_2 initial concentration on a) maximum H_2 concentration at the UFC and b) average species conversion rate at the UFC. Note that the positive and negative species conversion rates indicate species production and consumption, respectively. Also note that tL1 represents time lag due to HS^- transport from the RBI to the UFC and x_1 is the minimum horizontal distance between RBI and UFC cap, 0.343 m. tL2 represents time lag due to H_2 transport from the far-field rock boundary to the RBI where x_2 is the minimum horizontal distance between far-field rock boundary and RBI, 8.4 m. 120

Figure 4.8: Effect of constant H_2 concentration at the far-field rock boundary on a) maximum H_2 concentration at the UFC and b) average species conversion rate at the UFC. Note that the positive and negative species conversion rates indicate species production and consumption, respectively. Also note that tL2 represents time lag due to H_2 transport from the far-field rock boundary to the RBI where x_2 is the minimum horizontal distance between far-field rock boundary and RBI, 8.4 m. 122
Figure 4.9: Effect of effective H_2 rock diffusivity (THC-H_2 model) on a) maximum H_2 concentration at the UFC and b) average species conversion rate at the UFC. Note that the positive and negative species conversion rates indicate species production and consumption, respectively. Also note that tL1 represents time lag due to HS^- transport from the RBI to the UFC and x_1 is the minimum horizontal distance between RBI and UFC cap of 0.343 m. 124
Figure 4.10: H_2 concentration in the DGR after 10^6 years due to different rock H_2 diffusivities a) case 1, effective H_2 rock diffusivity, H_2 $D_{e\ rock}$ = 8.4×10-13 m2s-1 and b) case 5, H_2 $D_{e\ rock}$ = 8.4×10-12 m2s-1. Note that the figures are not drawn to correct aspect ratio (DGR is represented by a line), to help to visualize the H_2 accumulation and dissipation. Also note that the effective H_2 bentonite diffusivity was kept the same. 125
Figure 4.11: Effect of effective H_2 rock diffusivity (THC-H_2 feedback model) on a) maximum H_2 concentration at the UFC and b) average species conversion rate at the

UFC. Note that the positive and negative species conversion rates indicate species production and consumption, respectively. Also note that tL1 represents time lag due to HS^- transport from the RBI to the UFC where x_1 is the minimum horizontal distance between RBI and UFC cap, 0.343 m. tL2 represents time lag due to H_2 transport from the far-field rock boundary to the RBI where x_2 is the minimum horizontal distance between far-field rock boundary and RBI, 8.4 m. 126

Figure 4.12: H_2 concentration in the DGR after 10^6 years due to different rock H_2 diffusivities a) C6, H_2 $D_{e\ rock}$ = 8.4×10-13 m2s-1 and b) C10, H_2 $D_{e\ rock}$ = 7.5×10-10 m2s-1. Note that the effective H_2 diffusivity in bentonite was kept the same. 127

Figure 4.13: Maximum DGR H_2 concentrations obtained from sensitivity cases (C1 to C10) 128

Figure 4.14: Maximum H_2 concentrations in the bentonite under different conditions a) C-H_2 model simulates H_2 dynamics under fully saturated-isothermal conditions, b) HC-H_2 model simulates H_2 dynamics under variably saturated-isothermal conditions, c) TC-H_2 model simulates H_2 dynamics under fully saturated-non-isothermal conditions, d) THC-H_2 model simulates H_2 dynamics under variably saturated-non-isothermal conditions 129

Figure 5.1: A conceptual model of various geochemical (purple) and surface mediated processes (blue) in saturated bentonite clay. Adapted from (Bradbury and Baeyens 2003) with permission of Elsevier..... 137

Figure 5.2: a) Experimental setup of HS^- diffusion through 7.4 mm, medium density compacted bentonite (ρM=1330 kg m-3) from (Chowdhury et al. 2021b, 2024). b) to d) schematics representing the initial and boundary conditions in the 1-D models: b) Linear HS^- adsorption (C-S_L) model, c) Non-linear HS^- adsorption (C-S_{NL}) model, and d) Kinetically irreversible HS^- reaction (C-R_I) model. 141

Figure 5.3: The cumulative Cl^- mass from Chowdhury et al. (2021) was compared to the two numerical models. The red bars represented the error bars in the experimental data, which are not visible on most data points because of the small errors. ... 146

Figure 5.4: a) Cumulative HS^- mass at the compacted bentonite outlet in the C-R_I model for time and space dependent D_e (i.e., Eq. 5) and constant D_e and b) time and space dependent D_e (i.e., Eq. 5.5) in the C-R_I model. Note that the initial Fe^{2+} concentration was kept at 700 mol m^{-3} and x represented the bentonite length. 147

Figure 5.5: Cumulative HS^- mass at the compacted bentonite outlet in the C-S_L and C-S_{NL} models from varying the sorption parameters K_d and KL,HS- and CP,max,HS-, respectively. The models were compared to the cumulative HS^- mass breakthrough curve from Chowdhury et al. 2024. Note that the K_d= 0.34 m^3kg^{-1} (L:S=200) and K_d= 0.90 m^3kg^{-1} (L:S=1000); KL,HS-= 41.35 m^3 mol^{-1} and CP,max,HS- =0.03 mol kg^{-1}

(L:S=200) and K_{L,HS^-}= 5.85 $m^3\ mol^{-1}$ and C_{P,max,HS^-} =0.24 mol kg^{-1} (L:S=1000) values were obtained from batch experiments of powdered bentonite (Papry et al. 2023). 151

Figure 5.6: Cumulative HS^- mass at the compacted bentonite outlet in the C-R_I model from varying the initial Fe^{2+} concentration compared to the cumulative HS^- mass from Chowdhury et al. 2024. 153

Figure 5.7: Cumulative HS^- mass at the HCB outlet in the C-R_I model from varying the A_h and comparison to the cumulative HS^- mass from Chowdhury et al. 2024. Note that initial Fe^{2+} concentration and E_h were kept at 700 mol m^{-3} and 35 kJ mol^{-1}, respectively. 155

Figure 5.8: Cumulative HS^- mass at the compacted bentonite outlet in the C-S_L, C-S_{NL}, and C-R_I models compared to experimental data from Chowdhury et al. 2024.156

Figure 5.9: Bisulfide flux estimated at upper UFC end cap in the THC, THC-S_L, and THC-S_{NL}, and THC-R_I models. 159

Figure 5.10: The simulated spatial distribution of relative HS^- flux (i.e., HS^- flux (NHS'') compared to maximum HS^- flux (NHS''max) or $NHS''NHS''max$) over time in the 3-D a) THC model, b) THC-S_L model, c) THC-S_{NL} model, and d) THC-R_I model 160

Figure 5.11: HS^- corrosion depths in the THC, THC-S_L, THC-S_{NL}, and THC-R_I models. Note that the horizontal axis represents a linear timescale. 161

Figure 6.1: Coupled hydrogeological and geochemical processes governing HS^- corrosion; red font indicates modelled processes in the THC model..... 167
Figure 6.2: (a, b) average DGR effective saturation and (c, d) average UFC surface temperature from varying the initial saturation, isotropic rock permeabilities (in the crystalline model in frames a and c), and horizontal rock permeabilities (in the sedimentary model in frames b and d). The base case scenarios are bolded (Rashwan et al. 2022). 169
Figure 6.3: Relative bisulfide fluxes estimated at UFC surface (upper end-caps) in (a) crystalline and (b) sedimentary DGR models under different modelling conditions. C model simulates bisulfide diffusion under fully saturated-isothermal conditions, HC model simulates bisulfide diffusion under variably saturated-isothermal conditions, TC model simulates bisulfide diffusion under fully saturated-non-isothermal conditions, THC model simulates bisulfide diffusion under variably saturated-non-isothermal conditions. (c and d) Prediction hydrogeological conditions in the crystalline and sedimentary domains. Note that the average bentonite air content and bisulfide flux values are normalized (Rashwan et al. 2022)..... 170
Figure 6.4: HS^- corrosion depths under different modelling conditions (i.e., C, HC, TC, and THC) in the crystalline or sedimentary domains. The slopes are calculated from 200,000 to 1,000,000 years in each model using linear regression analyses. Note that

the horizontal axis represents a linear timescale (Rashwan et al. 2022). The HS^- corrosion depth tolerance is reported in Hall et a. (2021). 172
Figure 6.5: Coupled hydrogeological and geochemical processes governing HS^- corrosion; red font indicates modelled processes in the THC-S_L and THC-S_{NL} models (i.e., adsorption as a part of sorption), and THC-R_I (i.e., a reaction between Fe^{2+} and HS^-) 174
Figure 6.6: Cumulative HS^- mass at the compacted bentonite outlet in the C-S_L, C-S_{NL}, and C-R_I models compared to experimental data from Chowdhury et al. 2024.175
Figure 6.7: Bisulfide flux estimated at upper UFC end cap in the THC, THC-S_L, and THC-S_{NL}, and THC-R_I models. 176
Figure 6.8: The simulated spatial distribution of relative HS^- flux (i.e., HS^- flux (NHS'') compared to maximum HS^- flux (NHS''max) or NHS''NHS''max) over time in the 3-D a) THC model, b) THC-S_L model, c) THC-S_{NL} model, and d) THC-R_I model 177
Figure 6.9: HS^- corrosion depths in the THC, THC-S_L, THC-S_{NL}, and THC-R_I models. Note that the horizontal axis represents a linear timescale. 178
Figure 6.10: Coupled hydrogeological and geochemical processes governing HS^- corrosion; red font indicates modelled processes in the THC-H_2 model..... 179
Figure 6.11: Boundary conditions in the a) THC-H_2 model and b) THC-H_2 feedback model. Note that arrows indicate transport directions of HS^- and H_2 180

Figure 6.12: Maximum H_2 concentration at the UFC using hydrogen and hydrogen feedback models, at different rock diffusivity values. 182
Figure 6.13: Maximum DGR H_2 concentrations obtained from sensitivity cases (C1 to C10) 182
Figure 6.14: Coupled hydrogeological and geochemical processes governing HS^- corrosion; red font indicates modelled processes in this research 184

Chapter 1 Introduction

1.1 Motivation

About 15% of Canada's electricity is produced from nuclear energy (WNA 2019). To produce nuclear energy, reactors use radioactive fuel (i.e., Uranium). The Uranium becomes nuclear waste after producing energy (Feiveson et al. 2011). Nuclear waste is different from other types of waste (e.g., wastes from fossil fuel combustion) as the nuclear waste can remain radioactive for million years (WNA 2022). The radioactivity of nuclear waste poses risks to human health and environment if it is not managed properly. As of 2023, Canada has 3.3 million used nuclear fuel bundles or nuclear waste reported by nuclear waste management organization of Canada (NWMO) (NWMO 2023). The expected spent fuel volume is 12,718 cubic meters (Natural Resources Canada 2019) .In Canada, nuclear fuel bundles are cooled for 10 years in water-filled pools to reduce the radioactivity. Then, they are stored in dry storage container made of thick concrete that can prevent radiation to escape up to 50 years (NWMO 2019). This is a very short time solution compared to the long radioactive lifetime of used nuclear fuel and long-term management is necessary.

Over 50 countries around the world have nuclear waste (WNA 2024). Many countries including Canada are considering deep geological repositories (DGRs) as a long-term solution for safe management of used nuclear fuel (Bodansky 2004, European Commission 2004, Walke et al. 2015, Faybishenko et al. 2016). The current design of DGR by the Canadian Nuclear Waste Management Organization (NWMO) proposes an engineered barrier system (EBS) which includes a 3 mm copper-coated steel used fuel

container (UFC) surrounded by highly compacted bentonite (HCB) clay (NWMO 2019). EBS will be emplaced ~500-800 m deep in a low permeability, stable host rock (either crystalline or sedimentary). Although the copper coating is thermodynamically stable in oxygen-free environments, it is susceptible to microbiologically influenced corrosion (MIC) (i.e., HS^- corrosion). Depending on site-specific conditions (e.g., host rock type, groundwater chemistry, microbial growth conditions), bisulfide (HS^-) produced by sulfate reducing bacteria in the host rock could transport (diffuse) slowly through the HCB to the UFC surface and corrode the copper coating (Cloet et al. 2017). In addition, hydrogen (H_2), produced from HS^- corrosion may also affect DGR integrity. HS^- corrosion assessment is important since if HS^- corrosion exceeds the 3 mm copper coating and carbon steel is exposed, it can corrode much faster, produce gas, and increase the risk of UFC failure and radionuclide release. However, HS^- corrosion assessment is complex as bisulfide transport is affected by the transient hydrogeological conditions in the DGR, such as saturation (from the host rock), temperature (from the used fuel), and microbial and geochemical reactions (e.g., HS^- sorption in bentonite, HS^- reaction with iron (Fe^{2+}) in bentonite) which are all interconnected and, therefore, requires a robust numerical model to understand possible transport mechanisms (King 2008, Sena et al. 2010, Guo 2016). Such a model would increase the understanding of bisulfide transport and limit HS^- corrosion. However, to date, no studies have investigated bisulfide transport through the HCB under various conditions including saturation, temperature, reactions (e.g., HS^- retardation in bentonite clay due to iron sulfide formation or HS^- adsorption), and HS^- corrosion generated H_2 dynamics. Therefore, addressing this knowledge gap can aid in assessing NWMO's current DGR design.

1.2 Research Objectives

As HS^- transport through bentonite may occur over a long period, long term hydrogeological and geochemical conditions may affect HS^- transport. Therefore, it is vital to understand HS^- transport behaviour through the bentonite to accurately understand HS^- transport mechanisms and assess the extent of corrosion to ensure safe and long-term performance of copper as a corrosion barrier. The objective of this research was to estimate HS^- corrosion over the DGR lifespan (1 million years), and to better understand how DGR hydrogeological and geochemical processes influence HS^- corrosion. Towards these goals, numerical models in COMSOL were developed to answer these key research questions (RQs):

1. *How long will it take to fully saturate the bentonite (Chapter 3)?*
2. *How do various hydrogeological properties affect key processes in the DGR (Chapter 3)?*
3. *What is the overall influence of saturation and temperature (heating from used fuel) on HS^- transport and corrosion (Chapter 3)?*
4. *How does H_2 from HS^- corrosion* evolve *in the DGR (Chapter 4)?*
5. *Does produced H_2 from HS^- corrosion form gas (Chapter 4)?*
6. *How do geochemical reactions (HS^- adsorption, HS^- and Fe^{2+} reaction) affect HS^- transport and corrosion (Chapter 5)?*

These research questions are answered using numerical models that have been developed and are presented in chapters of this dissertation (see Chapter 3, Chapter 4, and Chapter 5). A literature review was also conducted to understand hydrogeological and geochemical processes in a DGR (see Chapter 2). The literature review incudes DGR

concepts, conceptual model of coupled hydrogeological and geochemical processes in a DGR, and numerical modelling approaches and assumptions.

Chapter 3 includes a model of bisulfide transport under thermal (T), hydraulic (H), and chemical (C) species transport (diffusion) conditions. This model is referred to as the thermal- hydraulic-chemical (THC) model and used to answer RQs 1-3. The THC model is developed coupling unsaturated flow (i.e., Richards' equation), heat transfer, and solute (HS^-) transport (i.e., Fick's 2nd law). The THC model is used to understand how saturation and heating influence HS^- transport and corrosion.

Chapter 4 includes a model of hydrogen transport, which is based on the THC model and referred to as the THC-H_2 model. The THC-H_2 model is used to answer RQs 4-5. A surface equilibrium reaction approach is used to simulate H_2 generation from HS^- corrosion and understand if produced H_2 from HS^- corrosion forms gas.

Chapter 5 includes models of bisulfide transport and adsorption or geochemical reaction (i.e., HS^- and Fe^{2+} reaction), which are termed as the THC-S or THC-R models, respectively. Therefore, these models are also based on the THC model. The THC-S or THC-R models are used to answer RQ 6. Fitted adsorption and reaction parameters from laboratory and model comparison are included in these models to understand how HS^- adsorption or HS^- and Fe^{2+} reaction affect HS^- transport and corrosion.

Chapter 2 Modelling Hydrogeological and Geochemical Processes Occurring in a Deep Geological Repository for Nuclear Waste Management – State of Science Review

2.1 Introduction

Long term (10^5-10^6 years) management of nuclear waste is an important issue for current and future generations. The deep geological repository (DGR) concept has become the go-to design in many countries (Faybishenko et al. 2016) considering technical feasibility, safety, cost, and environmental impact (Bodansky 2004, European Commission 2004, Walke et al. 2015). Nuclear agencies around the world have designed distinct DGR barrier systems based on their specific waste types and inventories (e.g., low level waste (LLW), intermediate level waste (ILW), and high level waste (HLW)), potential site characteristics (geology and presence of natural resources), along with socio-political and technical constraints. These agencies are at various stages in the process of selecting sites, assessing proposed designs, and constructing the repositories (e.g., Posiva Oy, Finnish nuclear agency) (Faybishenko et al. 2016, Posiva 2020). Typically, an implementation program consists of design and safety analysis using numerical models, site characterization and in situ geological testing (e.g., drilling, sampling, testing, and monitoring of deep boreholes), and experimental programs for developing repository science. Early scientific research on geological disposal of radioactive waste in shallow and deep land (NAS 1957) touched off widespread international cooperative studies in this field (IAEA 1993, 2003, 2006, 2011, 2017, 2018, 2020, NEA 1999, Alexander and McKinley 2011). Decades of research have assessed the DGR concept and barrier

system design by employing various numerical models which have large variability in terms of data processing, assumptions, interpretations, and implications. While it is not feasible to construct a fully holistic DGR model, the current approach of building in discrete processes of interest (e.g., Thermal-Hydraulic-Mechanical (THM)) limits our ability to understand how the full suite of processes and environmental conditions interact and impact DGR performance. A much larger research gap is a lack of site-specific data. Many current DGR models employ a generic site condition which, while useful for understanding how coupled processes impact system performance, leaves the ultimate fate of real DGR environments as variable and uncertain.

The typical DGR concept refers to a multi-barrier approach for containment and isolation of waste in a suitable rock formation (e.g., salt deposits, crystalline rock, sedimentary rock) at a depth of hundreds of metres (e.g., 500 m) (Bianchi et al. 2015) (Figure 2.1). While a suitable rock formation serves as a natural barrier, an engineered barrier system (EBS) is placed within that rock to further minimize transport of energy and compounds into and out of the repository. Generally, the EBS includes: the wasteform itself packaged within a waste container, surrounded by low-permeability or geochemical barrier layers and then placed within a rock formation (Figure 2.1). Wasteforms can range from grouted organic sludge (ILW) to vitrified spent nuclear fuel (HLW) (Patel et al. 2012, RWM 2017) while their containers are typically constructed from copper, carbon steel, or cast iron; steel and iron containers may also have a corrosion resistant coating applied (e.g., copper) (Hall and Keech 2017).

A low permeability barrier (10^{-19} to 10^{-21} m^2) (Pusch 1980, Dixon et al. 2018, Dixon 2019) surrounding the container will minimize transport of radionuclides in the event of a container breach and, if using materials like HCB, will provide both high swelling ability to seal cracks and adsorption capacity that can retard radionuclide migration (Ichikawa and Selvadurai 2012, Apted and Ahn 2017). Some DGR designs, typically LLW or ILW, utilise an alkaline cement barrier instead of HCB as it contributes to high sorption and low solubility of radionuclides (RWM 2017, Abarca et al. 2019). Finally, the backfill material, consisting of bentonite and crushed rock, is used to seal the placement rooms, further limiting groundwater flow (Keto et al. 2009).

Reducing container corrosion is the one of the major objectives of the EBS design and a key component in DGR performance. For instance, Alkaline cements and shotcrete will reduce steel container corrosion via the formation of a thin oxide film (Kursten et al. 2011). Additionally, bentonite – which is often used in EBS – swells upon contact with water, limiting transport and decreasing the water activity. However, despite the low water activity of bentonite, sulfate reducing bacteria present at the EBS/host rock interface may still produce corrosive species and compromise DGR safety, which is called microbiologically influenced corrosion (MIC) (Cloet et al. 2017, King et al. 2017).

Bentonite based EBS designs have been adopted by: Sweden (SKB), Canada (NWMO), Finland (Posiva Oy), Switzerland (NAGRA), Japan (NUMO), and Czech Republic (SURAO). Unlike others, France's nuclear agency (Andra) considers placing carbon steel HLW containers in argillite (predominantly clay) rock formation relying on its retention

properties, thus avoiding engineered clay barriers such as bentonite (Andra 2015). Germany's nuclear agency, DBE-Technology, considered placing HLW containers in a salt dome host rock and depend on the salt's self-sealing mechanism (halted due to safety concerns) (NDA 2010, CEW 2017). USA (US-DOE) has currently an operational Waste Isolation Pilot Plant (WIPP) repository where ILW containers are enclosed by magnesium oxide salt buffer (NDA 2010, WIPP 2019). USA considered managing their HLW in Yucca mountain where the waste was supposed to be placed above the groundwater table but this was halted due to a political decision, which was fueled by safety concerns (e.g., rainwater infiltration into the repository, volcanic eruptions in the vicinity of the Yucca mountain) (Feiveson et al. 2011). Although minimizing waste-groundwater interaction through storing waste above groundwater table in the Yucca Mountain seems advantageous, increased surface water flow rate through fractures can breach the EBS and move contaminants towards groundwater (Schwartz 2019). UK's nuclear agency, Nuclear Waste Services (NWS) (formerly Radioactive Waste Management Limited (RWM)), is examining suitable DGR options for both HLW and ILW for a range of host rocks (e.g., low strength sedimentary and evaporates) and barrier materials (e.g., cementitious); considered options such as the Swedish concept (KBS-3V), Swiss concept and Germany's DBE technology (RWM 2018). Many other countries including Brazil, Belgium, Bulgaria, China (CNNC), Hungary, India (AEC), Italy, Korea (KORAD), Latvia, Lithuania, Mexico, Netherlands (COVRA), Russia (NORAO), Slovak Republic, Slovenia, South Africa, Spain, and Ukraine are also active in DGR research (Faybishenko et al. 2016).

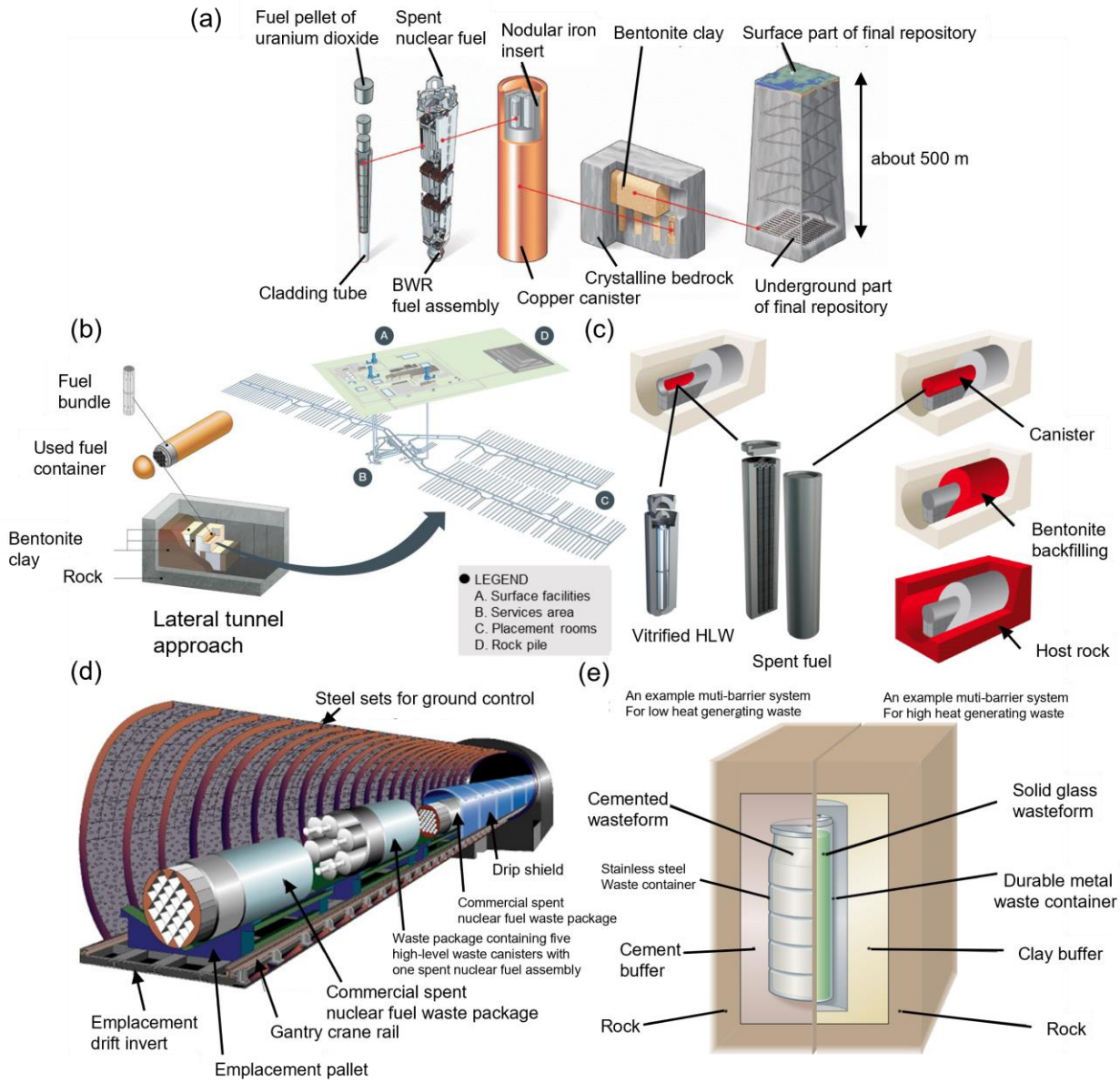

Figure 2.1: DGR designs in different countries: (a) KBS-3V (Sweden, Finland) (SKB 2010a) (b) NWMO's design (Canada) (Hall and Keech 2017) (c) NAGRA's design (Switzerland) (Patel et al. 2012) (d) Placement tunnel in Yucca mountain repository, Nevada, USA (U.S. DOE 2002) and (e) Barrier design examples for ILW and HLW (RWM 2017) (Adapted from Hall et al. (2021) with permission of Elsevier).

Hydrogeological and geochemical processes exert key controls on the long-term corrosion of the waste container, and its ability to mitigate radionuclide release. While many of these processes are well understood in isolation, the interactions between them especially over a million-year DGR lifespan may be unexpected. Relevant

hydrogeological DGR processes include: energy transport (due to the thermal field produced by the container) (Bejan and Kraus 2003, Guo 2016, 2017, 2018), groundwater movement through rock and rock fractures (Singhal and Gupta 2010, Baxter et al. 2017), saturation of low permeability sealing materials (e.g., bentonite clay) (Baxter et al. 2017, Geier et al. 2018, Dodd et al. 2019), and diffusion of corrosive species through sealing materials to the containers from sources such as microbiological activities (Cloet et al. 2017, Maanoja et al. 2020, Hall et al. 2021, Rashwan et al. 2022), contaminant transport through saturated sealing materials to the host rock (e.g., radionuclide transport) (Albinsson et al. 1996, Tachi et al. 2014, Kouhail et al. 2021, Liang et al. 2021). Geochemical processes include hydrolysis, complexation, and redox reaction (Jofré et al. 2011, Pekala et al. 2019, Kiczka et al. 2021), cation exchange (Wersin 2003, Montes-H et al. 2005, Marsal 2007, Pekala et al. 2019, Kiczka et al. 2021), sorption (Freundlich 1907, Langmuir 1917, Wersin 2003, Tachi et al. 2014), mineral dissolution-precipitation (Pekala et al. 2019, Kiczka et al. 2021), organic matter dissolution (Pekala et al. 2019, Kiczka et al. 2021), and microbiologically influenced geochemical reactions (King and Kolar 2006, Wersin et al. 2017, Pekala et al. 2019, Kiczka et al. 2021) that can change the composition of groundwater and bentonite porewater chemistry.

Long term DGR performance (e.g., container and barrier integrity, container corrosion resistance) is governed by highly coupled processes, such as those discussed above, and predicting DGR performance over their million-year lifespan amid interconnected evolution of temperature, saturation, various chemical species (i.e., corrosive, and non-corrosive species), geochemical, and microbiological conditions require appropriate

numerical models and careful consideration of which relevant processes to couple and implement.

Nuclear agencies and associated companies and researchers around the world have developed numerical models to study the wide range of complex**,** coupled subsurface processes that can occur in a DGR (Steefel et al. 2015) and to examine their impact on its performance. However, these models typically only couple a small number of processes at a time. For example, Pekala et al. (2019, 2020) coupled mass transfer with geochemical reactions to estimate copper corrosion but did not include processes like bentonite saturation, heat transfer, and hydro-mechanical bentonite behavior among others. Zheng and Fernández (2023) coupled mass transfer, heat transfer, bentonite saturation, and hydro-mechanical bentonite behavior but did not include long term evolution of heating and saturation, microbial growth dynamics, and container corrosion. In contrast, many studies explored models of a single process to understand its long term evolution and estimate its impact on large datasets (e.g., permeability data of a regional sale domain) (Abarca et al. 2013, 2016, 2019, Vidstrand et al. 2017, Baxter et al. 2017). Given the huge array of coupled processes occurring over a DGR's lifespan, with each of those processes having a range of mathematical models, specific parameters, and coupling approaches, it is simply not feasible for researchers to identify every relevant process and build fully integrated models that capture the complex behavior of these systems.

This chapter reviews numerical models used by nuclear agencies and nuclear waste storage researchers, which simulate and examine the effect of various hydrogeological and geochemical processes occurring in a DGR on the performance of the containers and barriers. This review chapter focuses on modelling the hydrogeological and geochemical processes relevant to DGRs, but processes such as gas and radionuclide transport, bentonite erosion, concrete degradation, glacial stress, and earthquakes, are also highlighted in the conceptual model of relevant DGR processes (Figure 2.2). The chapter first presents a conceptual DGR model and discusses the interconnected processes. Following that, section 2.3 presents capabilities and broad applications of numerical modelling tools. Sections 2.4 and 2.5 review DGR specific applications of numerical modelling tools in the context of hydrogeological and geochemical processes, respectively. Section 2.6 discusses challenges of modelling a large regional domain where a DGR is situated and section 2.7 discusses the key lessons learned from this review.

2.2 DGR Conceptual Model

Conceptual models help identify governing processes, select governing equations, and develop numerical models. As discussed in section 2.1, there is a vast array of relevant processes that can be included in a DGR's hydrogeochemical conceptual model and Figure 2.2 presents one possible example that could be used to, among other things, explore EBS integrity and container corrosion rates.

2.2.1 Temperature

High level nuclear waste generates heat as it undergoes radioactive decay (Faybishenko et al. 2016). Heat from the waste container establishes a thermal gradient as it moves outwards across the EBS (high temperature near the UFC and low temperature near the host rock) (Sena et al. 2010). A hydraulic head and saturation gradient establishes in the opposite direction to the thermal – as water flows inwards from the high head/fully saturated host rock to the partially saturated buffer material surrounding the UFC (Sena et al. 2010).

2.2.2 Saturation and Swelling

DGR host rocks are expected to have low permeability so capillary dominated water flow will govern the buffer saturation. However, advective water flow may govern the buffer saturation if the buffer receives water from natural or repository excavation induced rock fracture (Yu et al. 2021). Moreover, expansive buffer materials planned in numerous HLW repositories (e.g., bentonite clay) will swell (i.e., volume expansion) as they saturate, and their permeability and water activity will be reduced (Kröhn 2003, Stroes-Gascoyne et al. 2010). The swelling process is important as the swelling induced permeability reduction will seal the container tightly from the host rock. During swelling, porewater hydrates interlayers and electric double layers in clay particles, and therefore, clay expands in volume (Bradbury and Baeyens 2002, 2003, Itälä 2009). Due to the heat produced from the container, some groundwater will evaporate, cooling the local area via latent heat of evaporation, and become water vapour. This water vapour will either transport through the pores or condense back to the liquid phase, converting the latent to sensible heat and heating the local area. Therefore, the interlinkage of saturation and heating could

complicate the transport of dissolved species (e.g., iron (Fe), chloride (Cl^-), HS^-; and radionuclides in the event of a container breach) through the buffer materials.

2.2.3 Species Diffusion

The transport of dissolved species through the EBS is governed by diffusion due to low permeability of buffer materials (Idiart and Pekala 2016, Tanaka 2022). More specifically, species diffusion through the buffer materials will depend upon the buffer properties (e.g., density, porosity, tortuosity, sorption, saturation), water properties (e.g., temperature, salinity), and geochemical reactions (Pedersen 2010, Dixon et al. 2018, Pekala et al. 2019, Kiczka et al. 2021). Diffusion of ionic species (e.g., Cl^-) through the bentonite buffer will reduce the swelling rate due to increase in ionic strength, and therefore, bentonite permeability in saline groundwater will be relatively high (Dixon et al. 2018, Dixon 2019). In addition, various geochemical reactions – e.g., hydrolysis, complexation, oxidation-reduction, cation exchange, mineral dissolution-precipitation, organic matter dissolution – within the saturated buffer (e.g., bentonite) can control species transport through changing porewater composition and pore structure (Villar et al. 2012, Wersin et al. 2014, Pekala et al. 2019).

2.2.4 Corrosion

Various types of container corrosion can occur during the DGR lifespan. For example, uniform copper corrosion (UC) and stress corrosion cracking (SCC) can occur during the initial oxic period (a few months to a few years) (King et al. 2017, Giroud et al. 2018, Johansson et al. 2020). UC and SCC will be governed by the amount of trapped oxygen and length of oxic period, both of which will depend on buffer properties (porosity,

saturation), oxygen solubility, ideal gas law (relating oxygen volume to temperature and pressure of the system), oxidation of minerals in the host rock and bentonite, and aerobic microbial activity (Hall et al. 2021). After the oxic period, corrosion will still occur during the much longer anoxic period (hundreds of thousands or millions of years) for steel (Crusset et al. 2017) and copper (i.e., MIC) (Hall et al. 2021).

2.2.5 Gases

Gases (e.g., hydrogen) may be generated due to anoxic container corrosion and repository construction material (e.g., steel) corrosion (Silva et al. 2019a, 2019b). The generated gas may be trapped or transported through the buffer, which can be governed by rock and barrier diffusive properties or fractures. Gas entrapment in the DGR may damage the integrity of the container (e.g., cracking) (Wu et al. 2019). Hydrogen can embrittle metals as it gets absorbed (Dwivedi and Vishwakarma 2018, Sobola and Dallaev 2024, Chen et al. 2024) , further weakening the container. And preferential pathways created by gas may compromise the buffer, which is designed to protect the container (Harrington and Horseman 2003, Olivella and Alonso 2008, King 2012, Guo and Fall 2019, Radeisen et al. 2024).

2.2.6 Other Processes

Other processes impacting EBS integrity include bentonite erosion, concrete degradation, glacial stress, and earthquakes. Bentonite particles can be eroded and transported with the flowing water (i.e. piping) if the swelling pressure is not high enough to prevent water influx from water bearing fractures (Börgesson et al. 2020, Xu et al. 2023). Concrete degrades due to various mineral dissolution-precipitation reactions which change

porosity, permeability, and diffusive properties of concrete (Trotignon et al. 2007, Idiart et al. 2019, Marquie et al. 2019, Pernicova et al. 2023). Glacially induced stress and earthquake are the processes which can impact the structural stability of repository (Guzina et al. 2015, McEvoy et al. 2016, Craig et al. 2023). Many of these processes can occur throughout an unknown period of the much longer anoxic period and therefore uncertainty exists in evaluating impact on EBS integrity. In addition, many of these processes include assessing various dataset (e.g., regional scale permeability data) and combination of datasets can produce a big data if coupled processes are evaluated. Altogether, there is a vast array of possible processes in a DGR with variety of mechanisms and large data variability.

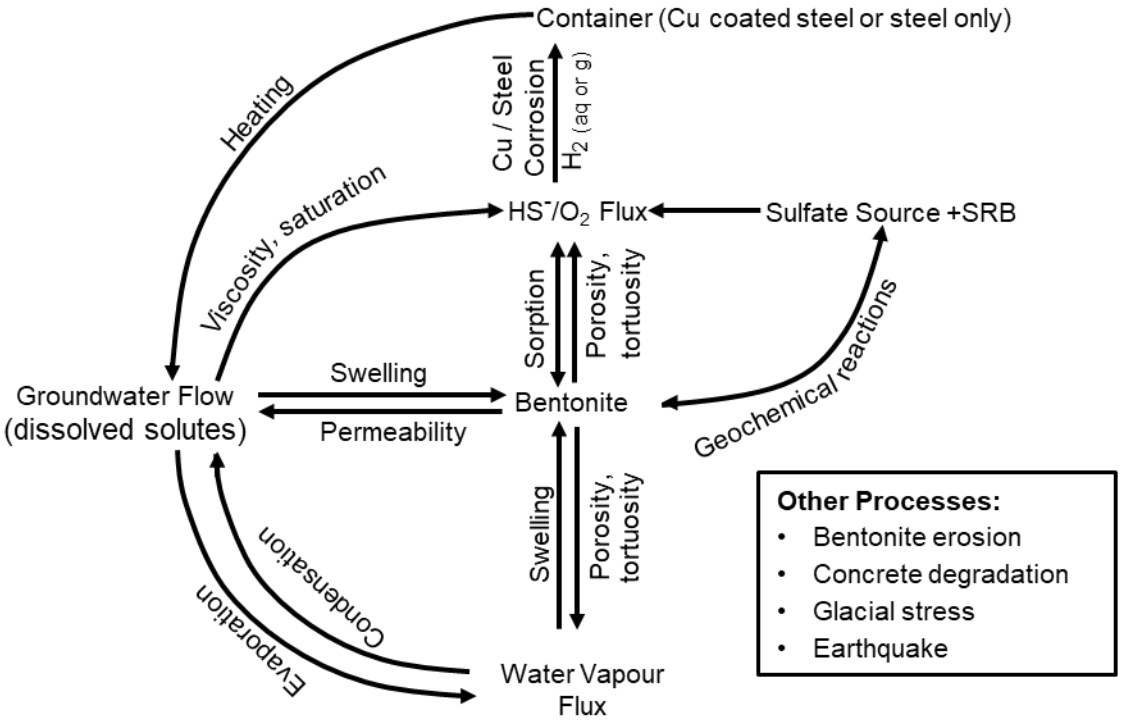

Figure 2.2: A conceptual model of various processes impacting the DGR's EBS (Adapted from Asad et al. (2022)

2.3 Modelling Platforms

When discussing DGR models it is useful to differentiate between modelling platforms and the numerical models implemented within them. Hereafter, modelling platforms are used to refer to the software package in which numerical models are implemented and run, these include packages such as COMSOL Multiphysics, OpenGeoSys, and TOUGH2 and are highlighted in Table 2.1 with the references directing readers to their respective user guides or methodologies. Whereas the term “model”, “numerical model”, or variation thereof refers to the suite of governing equations, process couplings, and numerical approaches for a set of simulations. This distinction between model and platform is not always black and white as terms are often used interchangeably within the literature and modelling community.

While this review does not focus on modelling platforms, it is useful to be aware of the range of suitable software packages employed for DGR hydrogeological modelling and their applications to highlight lesser known, or regional packages, that may be useful to readers. For instance, OpenGeoSys (Kolditz et al. 2012) is often referred to as a TOUGH2 (Pruess et al. 2012) European competitor as they are both large, customizable, open-source platforms which couple thermo-hydro-mechanical-chemical (THMC) processes; both are also generalist platforms that can couple to more specialised platforms such as PHREEQC (Parkhurst and Appelo 2013) for geochemical reactivity. The choice of modelling platform also depends on whether characteristics such as open-source, cost, research-oriented or commercial capabilities are desired. For instance, BGE (Germany) is utilizing OpenGeoSys in their site selection process for transparency and public participation.

Table 2.1 : Applications of modelling platforms

Computational Models	Applications	References	Availability
FRAC3DVS-OPG	Groundwater flow	(Sykes et al. 2011)	Commercial
FEFTRA	Groundwater flow	(Löfman and Keto 2007)	Commercial
DarcyTools	Groundwater flow	(Svensson and Ferry 2010)	Proprietary
ConnectFlow	Groundwater flow	(AMEC 2012)	Commercial
OpenGeoSys	Thermo-hydro-mechanical-chemical analysis	(Kolditz et al. 2012)	Open source
TOUHG2	Multiphase flow, solute transport, heat transport	(Pruess et al. 2012)	Commercial
COMSOL	Groundwater flow, solute transport, heat transport	(COMSOL 2021a)	Commercial
CodeBright	Thermo-hydro-mechanical analysis	(Vaunat and Olivella 2009)	Open source
KAPSEL	Heat conduction analysis	(Ikonen and Raiko 2015)	Proprietary
PASULA	Heat conduction analysis	(Ikonen and Raiko 2015)	Proprietary
MIN3P	Groundwater flow, solute transport, complexation, oxidation-reduction	(Mayer et al. 2012)	Proprietary
PHREEQC	Hydrolysis, complexation, oxidation-reduction, cation exchange, dissolution-precipitation, organic matter dissolution	(Parkhurst and Appelo 2013)	Open source
PFLOTRAN	Hydrolysis, complexation, oxidation-reduction, cation exchange, sorption, dissolution-precipitation, organic matter dissolution, microbially influenced reaction	(Lichtner et al. 2015)	Open source
KIRMAT	cation exchange, dissolution-precipitation	(Gérard et al. 1998)	Proprietary
HYTEC	cation exchange, dissolution-precipitation	(van der Lee et al. 2003)	Proprietary
PHAST	Groundwater flow, solute transport, hydrolysis, complexation, oxidation-reduction, cation exchange, dissolution-precipitation, organic matter dissolution	(Parkhurst et al. 2016)	Open source
TOUGHREACT	Heat transport, solute transport, gas transport, hydrolysis, complexation, oxidation-reduction, cation exchange, dissolution-precipitation	(Xu et al. 2005)	Commercial
CCM-MIC	Microbially influenced reaction	(King and Kolar 2006)	Proprietary

2.4 Modelling Hydrogeological Processes

As discussed above, the presence and behaviour of groundwater impacts on almost every aspect of the DGR and EBS (e.g., container corrosion, radionuclide transport, mechanical stability) and is a central consideration in most DGR models. As a result, there is a huge range of hydrogeological DGR models that encompass numerous processes, couplings, and mathematical descriptions. This section discusses the various types of hydrogeologic/flow models that are used as well as closely associated processes, before moving onto species transport and geochemical reactions. Bentonite saturation will occur due to groundwater flow (Figure 2.3). The swelling process will be governed by the rate of bentonite saturation. DGR host rocks are expected to have low permeability so capillary dominated water flow will govern the buffer saturation. However, advective water flow may govern the buffer saturation if the buffer receives water from natural or repository excavation induced rock fracture (Yu et al. 2021). Due to the heat produced from the container, some groundwater will evaporate, cooling the local area via latent heat of evaporation, and become water vapour. This water vapour will either transport through the pores or condense back to the liquid phase, converting the latent to sensible heat and heating the local area. Once the bentonite is fully saturated, the flow occurs due to natural hydraulic gradients.

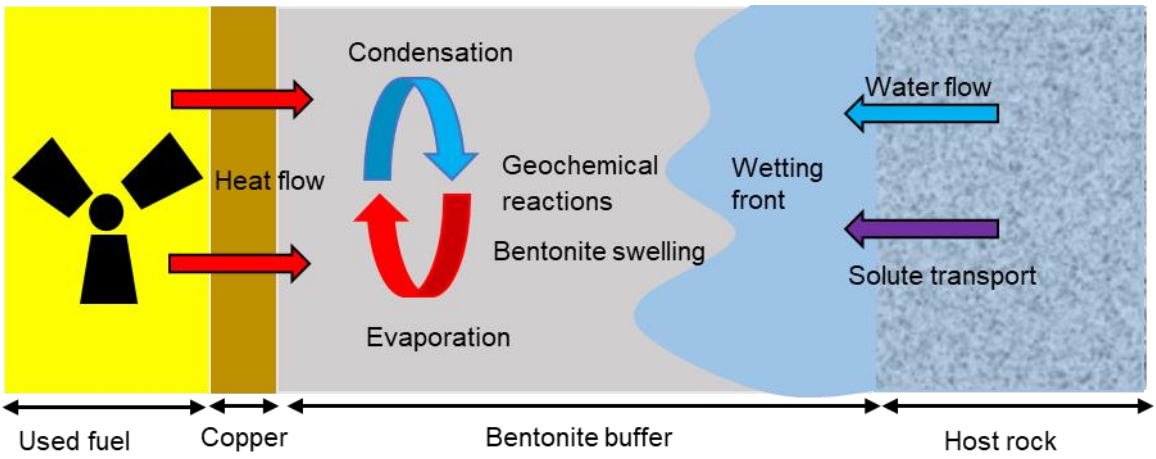

Figure 2.3: Key DGR transport processes relevant to bentonite saturation (adapted from Sena et al. (2010))

2.4.1 Buffer Saturation

Buffer materials in the EBS (e.g., highly compacted bentonite) are planned to be partially saturated during emplacement; NWMO is planning an initial saturation of 89% (Brachman et al. 2021), SKB will use an adapted buffer (Kronberg et al. 2020) and explored a saturation of 36-41% in their studies (Baxter et al. 2017, 2018), while NAGRA explored 45-75% (Garitte et al. 2015, Müller et al. 2017), and POSIVA used 6% in a buffer test (Pintado et al. 2012, Li et al. 2020). As a result, the initial heat and species transport is occurring within variably saturated pore space in all the designs, impacting parameters such as aqueous and gas diffusivity, specific heat capacity and thermal conductivity, as well as the swelling pressure of bentonite (if used). There is a great deal of interest in modelling the saturation rate of the EBS to better track the evolution of the aforementioned parameters. Modelling buffer saturation includes implementation of groundwater flow through the porous buffer (e.g., bentonite), where the pore space may be partly occupied by gases (e.g., entrapped air leftover from the DGR construction, hydrogen gas generated from the corrosion of containers and DGR materials (e.g., steel)). In other words, a multiphase flow modelling approach is required if buffer

saturation effects are of interest. Generally speaking, two main approaches are used to describe buffer saturation, the first is the full multiphase flow formulation (e.g., two phase flow) while the second is Richards' equation.

2.4.1.1 Multiphase Flow

Flow of a fluid through a porous medium is described using Darcy's law (Wiest 1966):

$$\vec{q}=-\frac{k}{\mu}\nabla P \tag{2.1}$$

where q is the Darcy velocity, k is the permeability of the porous medium, μ is the dynamic viscosity of fluid, and P is the pressure head. Darcy's law with the continuity equation is expressed as:

$$\frac{\partial(\varphi\rho)}{\partial t}+\nabla\,(\rho\vec{q})=Q \tag{2.2}$$

where ρ is the density of fluid, φ is the porosity, and Q is the mass source. Eq. 2.2 can be used to describe multiphase flow of fluids (e.g., liquid (l), gas (g)) through a porous medium:

$$\frac{\partial(\varphi\rho_i S_i)}{\partial t}+\nabla\,(\rho_i\vec{q}_i)=Q_i \tag{2.3}$$

where i represents fluid phases and S is the fluid saturation. The capillary pressure P_c, which is the pressure differences between fluid phases, governs the flow (Van Genuchten 1980):

$$P_c=-\frac{1}{\alpha}[S_{ec}^{-\frac{1}{m}}-1]^{\frac{1}{n}} \tag{2.4}$$

$$S_{ec}=\frac{S_l-S_{lr}}{1-S_{lr}} \tag{2.5}$$

where α, n, and m are the shape parameters of the capillary pressure curve, S_{ec} is the effective saturation from the capillary pressure curve, S_l is the liquid saturation, and S_{lr} is the residual liquid saturation. Relative permeability of liquid and gas phases can be estimated as follows (Van Genuchten 1980):

$$k_{rl}=S_{ek}^{0.5}\left(1-\left[1-S_{ek}^{\frac{1}{m}}\right]^{m}\right)^{2} \tag{2.6}$$

$$k_{rg}=(1-S_{ek})^{\frac{1}{3}}\left[1-S_{ek}^{\frac{1}{m}}\right]^{2m} \tag{2.7}$$

$$S_{ek}=\frac{S_l-S_{lr}}{1-S_{lr}-S_{gr}} \tag{2.8}$$

where S_{ek} is the effective saturation from the relative permeability curve and S_{gr} is the residual gas saturation.

2.4.1.2 Richards' Equation

While the full multiphase flow formulation is rigorous, simplifications can be made to improve model convergence and solver speed. The most common is to assume liquid (e.g., water) flows due to a pressure head gradient through unsaturated pores, while gas acts a passive bystander and exists at a constant, uniform pressure. These assumptions are reflected in Richards' equation (Richards 1931):

$$\frac{\partial}{\partial t}\phi S_l=\nabla\left[K\nabla P\right] \tag{2.9}$$

$$K=\frac{k_a k_{rl}\rho_l g}{\mu_l} \text{ and } h=z+\frac{P_l}{\rho_l g} \tag{2.10}$$

where K is the hydraulic conductivity of liquid through the unsaturated pores, k_a is the absolute permeability, g is the gravitational constant, μ_l is the liquid viscosity, h is the pressure head, and z is the elevation head.

2.4.1.3 Richards' Equation Versus Multiphase Models

Richards' equation has been used in some buffer saturation models (Abarca et al. 2019, Dodd et al. 2019). Whereas the multiphase flow formulation has been simulated in some other buffer saturation models (Lanyon et al. 2009, Lanyon and Senger 2011, Senger et al. 2014, Baxter et al. 2017, Geier et al. 2018, Abarca et al. 2019, Dodd et al. 2019, Eriksson 2019) and for simulating the famous bentonite rock interaction experiment at Aspo Hard Rock Laboratory in Sweden (Dessirier et al. 2014, 2017). Richards' buffer saturation model underpredicted saturation time compared to the full two phase flow model (Dessirier et al. 2014, 2017, Baxter et al. 2017). For example, in Dessirier's et al.'s work, it took 362 days to reach 98% saturation in the Richard's model while the full two phase flow model reached the same saturation after 488 days. In addition, 99% saturation was reached in 373 days using the Richard's equation while the two phase flow model did not reach 99% saturation in 1000 days (simulation time). Richards' equation would be appropriate for modelling buffer saturation if the DGR is vented (as is planned for Canada (Noronha 2016), Sweden (SKB 2011), Finland (Palomäki and Ristimäki 2013), and UK (NEA 2021)) so that liquid phase does not cause changes in gas pressure gradient.

Typically, buffer saturation is modelled using multiphase formulations in the buffer (described above, Eq. 2.3) and single-phase Darcy flow in the rock (Eq. 2.3 with a single phase only), which is assumed to be saturated given planned DGR depths (Kosakowski

2004, Löfman et al. 2009, Abarca et al. 2016, 2019, Baxter et al. 2017). However, the interface between this coupled saturated/unsaturated model can also impact saturation time predictions; incorporating a saturated pressure head at the rock-buffer interface can create large pressure gradients and unrealistically large water inflow into the buffer during initial time steps of the simulation (Abarca et al. 2019). This discrepancy can be resolved by defining a mass flow at the rock-buffer interface which is proportional to the difference of saturated pressure (i.e., buffer is saturated) and unsaturated pressure (i.e., buffer is unsaturated) (Abarca et al. 2019). Overall, capturing DGR saturation evolution seems to be challenging due to above mentioned reasons. Complicating the simulation of EBS hydraulics is vapour flow and bentonite swelling.

2.4.1.4 Water Vapour Transport

Heat and water transport are linked not only by changes in density, but also by phase changes between liquid and gaseous states. Water evaporation near the hot used fuel canisters will cool the system via the removal of latent heat and vapour will travel from the area of hotter to cooler regions and condense, converting latent back into sensible heat. In theory, bentonite saturation through vapour diffusion may become the dominant mechanism in the absence of liquid water in the pore space (Kröhn 2003, 2004). A number of studies have focused on modelling this behaviour (Kröhn 2003, 2004, 2011, 2019, Eriksson 2019) with a number of different formulations. One method for simulating vapour flow is a balance equation for vapour in the pore space (Eq. 2.11) and hydrated water in the interlayer space (Eq. 2.12) (Kröhn 2011):

$$\frac{\partial(\phi\rho_{vp})}{\partial t} - \nabla(\phi\tau D_{vpm}\nabla\rho_{vp}) = r_{vp} \qquad (2.11)$$

$$\rho_d \frac{\partial w}{\partial t} - \rho_d \nabla(\tau_i D_i \nabla w) = r_w \quad (2.12)$$

where τ is the tortuosity of the pore space, D_{vpm} is the binary vapour diffusion coefficient in air, ρ_{vp} is the vapour density, r_{vp} source of vapour, ρ_d is the dry density of bentonite, w is the water content, τ_i is the tortuosity of the interlayer space, D_i is the diffusion coefficient of interlayer water, and r_w is the source of interlayer water. Vapour generation is also described by taking Richards' equation, or the full multiphase formulation, and adding a source term defining phase change (i.e., evaporation and condensation) (Eriksson 2019):

$$Q_H = -R_e M_l \left(\frac{P_{svp}^{e^{\ln(r_h)}}}{RT} - C_{vp} \right) \quad (2.13)$$

where R_e is the evaporation-condensation rate constant, M_l is the molar mass of liquid, P_{svp} is the saturation pressure of water vapour in the air, r_h is the relative humidity, R is the universal gas constant, and C_{vp} is the vapour concentration of water. This vapour generation approach needs to be linked to heat transport via latent heat ((Nield and Bejan 2013, Al-abidi et al. 2013)):

$$\rho \frac{\partial H}{\partial t} + \rho_l U \nabla H = (\lambda_{eff} \nabla T) + q + h(T_s - T_l) \quad (2.14)$$

$$H = H_S + Q_H \quad (2.15)$$

where H is the total heat energy, H_S is the sensible heat, and Q_H is the latent heat. Although concepts of various buffer saturation models (e.g., two phase flow, vapour flow and hydration, Richards' equation) are different, they can be applied to simulate the same buffer saturation experiment as very similar diffusion coefficients have been obtained by various authors (Kröhn 2017, 2019). This similarity is because of the basic similarity in the mathematical descriptions of the models (i.e., Richard's equation is a simplified

version of two-phase flow model). Poor prediction of relative humidity compared to experiment was observed due to incorrect prediction of pressure head (Eriksson, 2019). In general, it is difficult to reproduce experimental relative humidity profiles as two phase flow model struggles to accurately capture saturation processes such as preferential paths and heat's drying effect (Figure 2.4) (Zheng and Samper 2008, Liu et al. 2014).

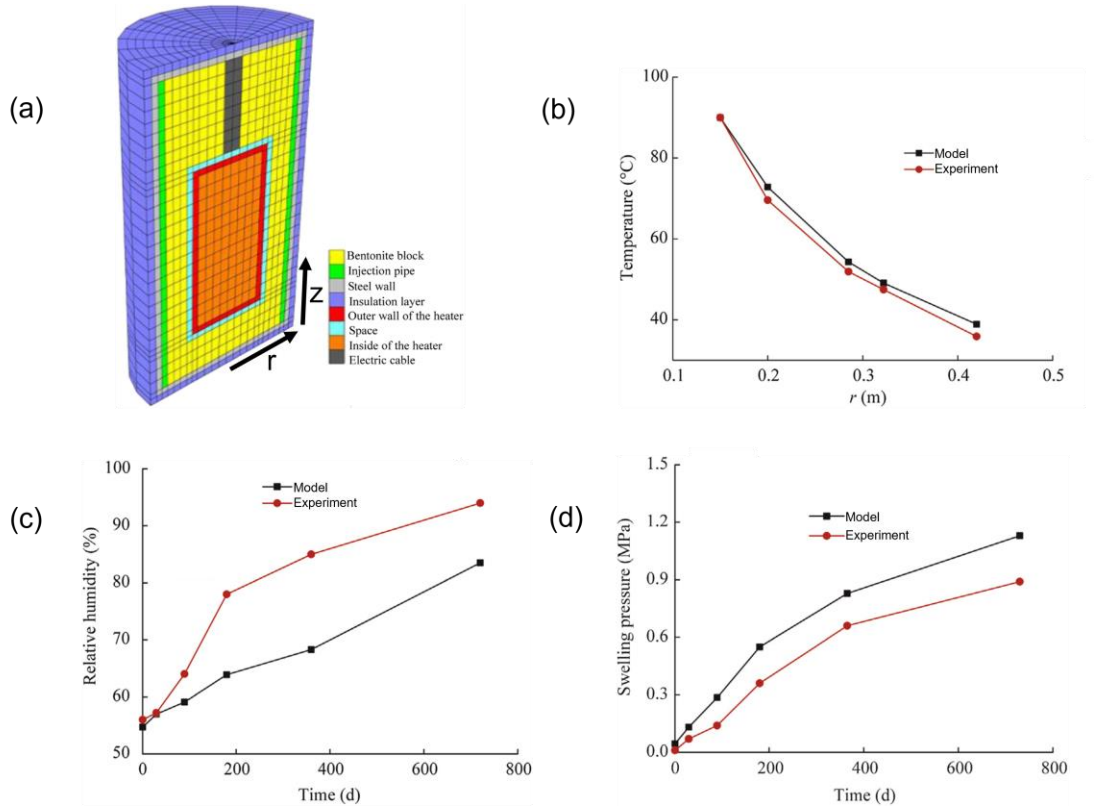

Figure 2.4: Validation of the China-Mock-Up test for HLW disposal: a) Model of the China-Mock-Up test, b) Comparison of temperature profiles from experiment and model, c) Comparison of relative humidity profiles from experiment (r=0.3 m, z= 0.123 m) and model, and d) Comparison of swelling pressure profiles from experiment (r= 0.15 m, z= 0.123 m) and model. (Adapted from Liu et al. (2014)). Note that r represents radial distance from the centre of the heater (representing waste heating) and z represents vertical distance.

Therefore, vapour flow through preferential paths needs to be explored. Altogether, capturing vapour flow is complicated due to the application of governing equations to

capture different physical processes like latent heat energy, relative humidity evolution, heat's drying effect, and preferential vapour flux. Bentonite swelling is another complicated process because swelling process may be governed by liquid water uptake or vapour flow (Villar et al. 2023).

2.4.1.5 Bentonite Swelling

Bentonite swells as water is taken up during saturation resulting in volume increase. This volume increase (i.e., swelling) is due to porewater entering the internal layers of bentonite (interlayer and double layer) which causes the bentonite to expand in volume (Bradbury and Baeyens 2002, Villar et al. 2023). This swelling makes bentonite both an ideal candidate for a low permeability EBS material, but also difficult to simulate.

Modelling bentonite swelling includes temporal reduction in permeability due to water uptake in the pore space, interlayer space, and double layer space (Bradbury and Baeyens 2002). The temporal reduction in permeability can be approximated using temporal changes in the swelling pressure (Dueck and Börgesson 2007, Åkesson et al. 2010, Liu et al. 2014, Dessirier et al. 2014, Kröhn 2017, 2019):

$$P_S = \frac{P_c^{free}(w) - P_c^{conf}(w)}{\omega} \tag{2.16}$$

where P_S is the swelling pressure, w is the volumetric water content, P_c^{free} and P_c^{conf} are the capillary pressure under free and confined swelling conditions, respectively, and ω is an empirical parameter. Another method of estimating swelling pressure is using total suction pressures of saturated bentonite (Ψ_t) and hydrating fluids under confined condition (Ψ_f) (Lang et al. 2019):

$$P_S = \Psi_t - \Psi_f \tag{2.17}$$

Therefore, this method considers the effect of external fluids (e.g., chloride) on swelling behaviour (Ψ_f=0 if the aqueous solution is deionized water). It is worth noting that, a greater decrease (70%) in swelling pressure occurs in bentonite hydrated with brine than bentonite hydrated with de-ionised water (Li et al. 2020, Sun et al. 2022). This decrease is because of the decrease in double layer length due to increased anion (i.e., Cl^-) concentration (Van Loon et al. 2007). A steady state swelling pressure was obtained in few years in bentonite hydrated with brine suggesting that a constant bentonite swelling pressure (i.e., constant permeability) may be used in buffer saturation models as groundwater of many DGRs are saline (Vieno 2000, Bath 2012, King et al. 2017).

While some studies considered swelling in the pore space (Dueck and Börgesson 2007, Åkesson et al. 2010, Dessirier et al. 2014), others considered swelling in both pore space and interlayer space (Kröhn 2017, 2019). However, all these studies neglected swelling in double layer space. Changes in saturation complicate swelling process as typical relationships like capillary pressure-saturation, relative permeability, diffusivity, thermophysical properties all depend on swelling – which can potentially change depending on site groundwater composition and geochemical evolution of the EBS system – and saturation. As a result of this complexity, many modelling studies neglected bentonite swelling (i.e., used constant bentonite permeability assuming instantaneous swelling) (Lanyon et al. 2009, Lanyon and Senger 2011, Senger et al. 2014, Baxter et al. 2017, Abarca et al. 2019) but these studies may have not perfectly captured species diffusion through bentonite (as swelling induced temporal reduction of permeability would reduce species diffusion rate), saturation (as saturation rate depends on permeability),

and thermophysical evolution (as effective thermophysical properties depend on saturation). Effect of bentonite swelling on these variables has not been extensively studied. Other effects not currently modelled greatly complicate incorporating bentonite swelling into saturation models; for instance, non-uniform swelling behaviour will make bentonite in the outer region (i.e. near the host rock) denser and less permeable compared to inner region (Kim 2017). Reproducing experimental bentonite swelling evolution in models has proven difficult, Liu et al (2014) noted that their model could not accurately capture low saturation near the heater where water evaporation/drying and temperatures are the highest. Altogether, bentonite swelling appears to be one of the most challenging factors in modelling buffer saturation due to complicated saturation process (i.e., water or vapour uptake in different bentonite pore spaces), non-uniform swelling behaviour, and determining a suitable method for modelling bentonite swelling (confined, free or both conditions, swelling in double layer).

2.4.2 Heat Transport

High level nuclear waste generates heat as it undergoes radioactive decay over time, but waste such as intermediate and low-levels are considered Low Heat Generating Wastes (LHGW) and typically ignore heat generation and transport (Bergstroem et al. 2011). Modelling heat generation includes incorporating heat sources with heat output from nuclear waste in the model (Guo 2017) which can use, for e.g., an exponential decay function to model heat generation (Ikonen 2003). This heat is produced within the UFC and has been estimated to reach maximum UFC temperatures such as 84°C and 93°C in Canada's conceptual DGR in crystalline and sedimentary rock, respectively (Guo 2016, 2018) and 90° in Swedish KBS-3 conceptual DGR in crystalline rock (Karnland et al. 2009,

Salas et al. 2014). This heat is then conducted outwards through the engineered and natural barriers. The heat energy balance in a DGR can be expressed using local thermal non-equilibrium (LTNE) which accounts for heat transfer between solid (s) and fluid (f) phases (Nield and Bejan 2013):

$$(1-\varphi)(\rho c)_s \frac{\partial T_s}{\partial t} = (1-\varphi)\nabla\cdot(\lambda_s \nabla T_s) + (1-\varphi)q_s''' + h(T_f - T_s) \quad (2.18)$$

$$\varphi(\rho c_P)_f \frac{\partial T_f}{\partial t} + (\rho c_P)U\cdot\nabla T_f = \varphi\nabla(\lambda_f \nabla T_f) + \varphi q_f''' + h(T_s - T_f) \quad (2.19)$$

where c is the specific heat of the solid, c_P is the specific heat at constant pressure of the fluid, λ is the thermal conductivity, ρ is the density, U is the Darcy velocity, T is the temperature, q''' is the heat production per unit volume, and h is the heat transfer coefficient. Another approach of expressing heat energy balance is the use of local thermal equilibrium (LTE) which does not account for heat transfer between solid and fluid phases (i.e., h=0).

2.4.2.1 Applicability of LTE and LTNE Approaches

The LTE approach (Eqs. 2.18-2.19) is commonly used for DGR temperature evolution simulations (Hartley et al. 2006, Johannesson et al. 2014, Guo 2016, 2017, 2018, Schenck 2018). LTNE approach is more accurate than the simplified local thermal equilibrium (LTE) as it considers heat transfer between phases (Pati et al. 2022) . LTNE is the more rigorous modelling approach, but due to its additional complexity is typically only used in fast flow scenarios such as through fracture rock (Gelet et al. 2012, 2013, Li et al. 2018, Heinze and Pastore 2023). In slow fluid flow scenarios, such as in an EBS, as the rate of transport is much slower than the rate of heat transfer between fluids and solids, the simplified LTE may be employed.

2.4.2.2 DGR Temperature Evolution

Accurate prediction of DGR temperature evolution is important as interlinkage of saturation and heating could complicate the transport of dissolved species (e.g., iron (Fe), chloride (Cl^-), HS^-; and radionuclides in the event of a container breach) through the buffer materials (Figures 2.2 and 2.3). DGR heat generation and transport models by others predicted the key trends in the DGR temperature evolution well; this involved a gradual rise in temperature due to heat production, gradual fall in temperature due to heat dissipation through the DGR and rock (Hartley et al. 2006, Johannesson et al. 2014, Guo 2016, 2017, 2018, Schenck 2018). In addition, Liu et al. (2014) reproduced heater temperature from their experiment (see Figure 2.4). However, the model boundary conditions in Guo's work (Guo 2016, 2017, 2018) were found to influence the temperature evolution. For example, an adiabatic symmetry boundary, which was applied around the domain perimeter to represent heat sources (i.e., UFCs) from many placement rooms, overpredicted DGR temperature as the adiabatic condition and added some non-existent heat loads (see Guo 2016, 2017, 2018).

2.4.2.3 Heat Convection

Heat convection (Eqs. 2.18-2.19) was neglected in many numerical models due to low flow velocity (Liu et al. 2014, Guo 2016, 2017, 2018, Schenck 2018); however, it may be worthwhile to explore heat convection when flow velocity is high due to rock fracture. Heat convection through rock fractures may influence bentonite desiccation as observed through comparison of modelling and experimental results (Johannesson et al. 2014). The desiccation (i.e., extreme dryness) depends on the temperature and temperature

difference between the bentonite and fractured rock (Johannesson et al. 2014). The desiccation of bentonite is crucial for DGR integrity as it may lead to cracks due to loss of moisture. Such interconnected cracks may form preferential flow paths (Luo et al. 2023, Taheri and El-Zein 2023).

2.4.2.4 Thermophysical Properties

Thermophysical Properties are used in the DGR models to define heat transport properties of the DGR barriers. Thermophysical properties of rock, engineered barriers, and nuclear waste were assumed to be constant in modelling studies (Hartley et al. 2006, Johannesson et al. 2014, Liu et al. 2014, Guo 2016, 2017, 2018, Schenck 2018). Implementing temperature dependent thermophysical properties of rock, engineered barriers, and nuclear waste in the DGR models would be ideal; however, thermophysical properties of the barriers do not vary significantly with temperature and would not affect DGR temperature evolution greatly . For example, Yoon et al. (2022) reported that thermal conductivity of dry bentonite (1700 kg m^{-3}) varied only by ~2% due to a change in temperature from 20°C to 80°C.

2.4.3 Aqueous Species Transport

The aqueous species of most interest in a DGR are chloride (Cl^-), sulfate (SO_4^{2-}), bicarbonate (HCO_3^-), and bisulfide (HS^-) (King et al. 2017). Transport of Cl^-, SO_4^{2-}, and HCO_3^- through EBS to the containers is important as the concentration of these species control localized corrosion of copper (pitting) (Cong et al. 2008). The Cl^- increases bentonite permeability through decreasing swelling pressure (see section 2.4.2.5) which would accelerate aqueous species transport through the DGR. The HS^- could transport

through bentonite to the UFC surface and corrode the copper coating and compromise the long term performance of UFCs (Hall et al. 2021).

2.4.3.1 Aqueous Species Transport Mechanism

Aqueous species transport is primarily via advection or diffusion depending on the Peclet number (ratio of advective to diffusive transport) (Huysmans and Dassargues 2005, Erfani et al. 2021). Diffusion is an expected species transport process in intact rock and EBS whereas advection is expected to occur in rock fractures (natural or repository excavation induced fractures) (Idiart et al. 2019, Soler et al. 2019). The transport of species in porous media is generally modelled using advection-dispersion equation (Tufenkji 2007):

$$\varphi \frac{\partial C}{\partial t} = D_{disp} \nabla^2 C - \nabla(\vec{q} C) \tag{2.22}$$

where C is the aqueous species concentration, D_{disp} is the hydrodynamic dispersion coefficient, and $\vec{q}=\varphi v$, where v is the porewater velocity. The term $D_{disp} \nabla^2 C$ in Eq. 2.23 represents effective dispersive transport, which is described using the effective species diffusion coefficient (D_e), longitudinal dispersity (α_L), and v (Fetter et al. 1993):

$$D_{disp} = D_e + \alpha_L v \tag{2.23}$$

2.4.3.2 Species Advection

Modelling species advection is important to understand various species transport through fractured geology in the vicinity of a proposed DGR. Advective transport was simulated in some numerical models to represent species transport through rock fractures (Abarca et al. 2016, 2019). Advective and diffusive mass transport was simulated using Eq. 2.23 in these models. However, these studies neglected natural heterogeneity of rock fractures assuming a constant Peclet number. Many studies simulated only diffusive transport in

bentonite (i.e., liquid species transport) considering the self-sealing nature of intact bentonite and its low permeability (i.e., advection was ignored as fractures were not present) expect some studies (Graham et al. 2002, Cui et al. 2023, Tamayo-Mas et al. 2024), which explored advection of repository gases (generated through radioactive decay of waste, metal corrosion, radiolysis of water) in bentonite.

2.4.3.3 Species Diffusion

Modelling species diffusion is important to understand if corrosive species would transport through the EBS and contact the nuclear waste containers. Diffusive transport of species was simulated in many studies using Fick's 2nd law (Fick 1855):

$$\frac{\partial C}{\partial t} = D_e \nabla^2 C \tag{2.24}$$

The D_e depends on species specific diffusion coefficient in porewater (D_0), saturation S, temperature (T), dynamic viscosity of water (μ_w), diffusion accessible porosity (φ_e), and tortuosity (τ) (Shackelford and Moore 2013):

$$D_e = S \frac{\varphi_e}{\tau} D_0 \tag{2.25}$$

$$\frac{D_{0,T_1}}{D_{0,T_2}} = \frac{T_1}{T_2} \frac{\mu_{w,T_2}}{\mu_{w,T_1}} \tag{2.26}$$

The τ depends on effective length between pores. The φ_e depends on pore structure (narrow or wide pores) and anion exclusion effect (which reduces the diffusion accessible porosity of anionic species) (Shackelford and Moore 2013). In addition, many geochemical reactions influence transport of species through the EBS by altering structure of the transport paths and speed of transport (see section 2.5).

Modelling studies have often incorporated experimentally determined porosity and diffusivity values instead of considering many of above mentioned properties including saturation, temperature, and diffusion accessible porosity (Eqs. 2.25-2.26). For example, many studies used a single total porosity value instead of modelling anion exclusion effect to account for diffusion accessible porosity (Johannesson et al. 2014, Nasir et al. 2014, Abarca et al. 2016, 2019, Cloet et al. 2017, Eriksson 2019, Pekala et al. 2019, 2020). In fact, there are few studies on anion exclusion in compacted bentonite (Van Loon et al. 2007). Van Loon et al. (2007) explored Cl^- diffusion through bentonite and proposed an empirical relation between Cl^- effective diffusion coefficient (D_{e,Cl^-}) and diffusion accessible porosity (φ_{e,Cl^-}) where φ_{e,Cl^-} varies with local Cl^-concentration. However, such empirical relations are not available for other anions (e.g., HS^-). Some studies ignored effects of saturation and temperature on diffusion (Cloet et al. 2017, Pekala et al. 2019, 2020). In addition, the same diffusion coefficient was used for various aqueous species in these models (Cloet et al. 2017, Pekala et al. 2019, 2020). Incorporating the same diffusion coefficient for different species will move both cationic and anionic species with the same speed through pore space which would result in incorrect effective diffusivity and mass balance in the system. In contrast, effects of saturation and temperature on diffusion were modelled in some studies Altogether, modelling species diffusion through EBS is challenging because species effective diffusivity depends on many parameters and assuming the same diffusivities for various species will result in incorrect predictions.

2.4.3.4 Species Diffusion in A Variably Saturated DGR

As discussed in Section 2.4.1, different nuclear agencies plan to saturate buffer materials with different degrees of saturation (6%-89%) before emplacement (Pintado et al. 2012, Garitte et al. 2015, Müller et al. 2017, Baxter et al. 2017, 2018, Kronberg et al. 2020). As a result, a variably saturated DGR will control species diffusion. Theoretically, a larger saturation delay will reduce species diffusion rate as $D_e \propto S$ (Eq. 2.25). Some studies simulated species diffusion in a variably saturated DGR (Abarca et al. 2019, Dodd et al. 2019). The saturation time greatly varies due to assumption of the active or passive gas phase (see section 2.4.2.3) (Dessirier et al. 2014, 2017, Baxter et al. 2017). The saturation time also varies with temperature as $D_e \propto T$ (Eqs. 2.25-2.26), other complicating factors like evaporation and condensation (i.e., drying-cooling effects on saturation), and bentonite swelling (i.e., swelling induced permeability evolution) (see section 2.4.2.5). Altogether, it is challenging to evaluate impact of saturation on species transport due to above mentioned reasons.

2.4.3.5 Corrosive Species Transport

The corrosive species of most interest in a DGR are oxygen (O_2), chloride (Cl^-), sulfate (SO_4^{2-}), bicarbonate (HCO_3^-),and bisulfide (HS^-) (King et al. 2017). The transport of these corrosive species through EBS may control various types of container corrosion.

2.4.3.5.1 Container Corrosion

Transport of $Cl^-$and O_2 through EBS can cause uniform corrosion of copper containers during the oxic phase through formation of $CuCl^-$ and Cu_2O films (Guo et al. 2020):

$$Cu + Cl^- = CuCl^- \quad (2.27)$$

$$2CuCl^- + 2OH^- = Cu_2O + H_2O + 2Cl^- \quad (2.28)$$

Transport of O_2 through EBS can cause uniform corrosion of steel containers during the oxic phase through formation of FeOOH (Eq. 2.29) which may continue during the anoxic phase through formation of $Fe(OH)_2$(Eq. 30) (King 2007):

$$4Fe + 2H_2O + 3O_2 = 4FeOOH \quad (2.29)$$

$$2FeOOH + Fe + 2H_2O = 3Fe(OH)_2 \quad (2.30)$$

Transport of Cl^-, SO_4^{2-}, and HCO_3^- through EBS to the containers is important as the concentration of these species and pH of the system will control localized corrosion (pitting corrosion, which is more aggressive than uniform corrosion) of copper and steel (King 2007, Cong et al. 2008, Verhoeven et al. 2022). For example, pitting corrosion of copper is prevented by HCO_3^- through formation of stable copper carbonate film ($CuCO_3Cu(OH)_2$) under alkaline conditions (Adeloju and Duan 1994). Pitting corrosion of steel can be accelerated by SO_4^{2-} through the formation of $FeSO_4$ rust (i.e., breakdown of passive film) (King 2007).

In the host rock, sulfate-reducing bacteria (SRB) could use hydrogen (H_2) (Eq.(2.31) or organic compounds (e.g., lactate) (Eq. 2.32) as electron donors to reduce SO_4^{2-} and produce HS^- in the host rock (Abrahamsen-Mills and Small 2019):

$$4H_{2(g)} + SO_{4\,(aq)}^{2-} + H^+_{(aq)} \rightarrow HS^-_{(aq)} + 4H_2O \quad (2.31)$$

$$2(CH_2O)_{(aq)} + SO_{4\,(aq)}^{2-} + 2H^+_{(aq)} \rightarrow 2HCO_{3(aq)} + HS^-_{(aq)} + 3H^+_{(aq)} \quad (2.32)$$

The produced HS^- in the host rock (Eq. 2.31-2.32) could transport through bentonite to the UFC surface and corrode the copper coating under acidic (Eq. 2.33) and alkaline conditions (Eq. 2.34) (Hall et al. 2021).

$$2Cu_{(s)}+HS^-_{(aq)}+H^+ \leftrightarrow Cu_2S_{(s)}+H_{2(g)} \quad (2.33)$$

$$2Cu_{(s)}+HS^-_{(aq)}+H_2O \leftrightarrow Cu_2S_{(s)}+H_{2(g)}+OH^-_{(aq)} \quad (2.34)$$

Eqs. 2.33-2.34 describe the anoxic corrosion of copper in the presence of HS^- which is likely to be the largest contributor to long-term copper corrosion in the DGR (Hall et al, 2021). Another form of corrosion is stress corrosion cracking, SCC. SCC occurs due to the combined action of applied tensile stress and a corrosive environment dominated by Cl^-, and O_2 (through formation of FeC_2 or CuO_2) (Suzuki and Hisamatsu 1981, Karlsdóttir 2012, Lu et al. 2020).

2.4.3.5.2 Redox Conditions

Redox conditions play a strong role in governing corrosion reaction pathways and should be accounted for in model simulations. For instance, some of the trapped oxygen from repository construction will dissolve into the buffer fluid (e.g., bentonite porewater) and the remaining gaseous oxygen will stay in the unsaturated pore. This dissolved oxygen will be consumed by oxic container corrosion, oxidation of minerals in the host rock and bentonite, and aerobic microbial activity (King et al. 2017). These different reaction pathways can generate an O_2 concentration gradient, driving its flux throughout the EBS (Barnichon et al. 2018). These oxic conditions and reactions are expected to dominate for a few months to a few years of the DGR life (King et al. 2017, Giroud et al. 2018, Johansson et al. 2020). However, an oxic period of several years or longer is measured

through predictive models (King et al. 2024). Understanding the oxic period and its length are very important not only because of the corrosion mechanism in this period, but also because of choice of the metals for containment of nuclear waste. For instance, some metals that are more prone to pitting (e.g., titanium (Ti), nickel (Ni), Chromium (Cr), and manganese (Mn) can be used to make nuclear waste containers if the oxic period lasts for only a few weeks because such shorter oxic period will contribute to negligible oxic corrosion (King et al. 2024). Some modelling studies explored oxygen diffusion and consumption during oxic period (Wersin et al. 2003, De Windt et al. 2014, Barnichon et al. 2018). These studies found that the oxygen gets completely consumed in few months to years in a closed DGR, but a redox contrast occurs in a ventilated DGR involving both oxic and anoxic phases. While these studies modelled species transport during the oxic phase (ignored anoxic phase), other studies modelled species transport during anoxic phase (ignored oxic phase) (Cloet et al. 2017, Pekala et al. 2020, Kiczka et al. 2021).

2.4.3.5.3 Saturation and Heating

Corrosion via aqueous species is controlled, in part, by the water saturation; bentonite in HLW DGR's start with a varying level of water saturation (NWMO: 89%, SKB: 36-41% (explored), NAGRA: 45-75% (explored), POSIVA: 6% (used)) whereas cement buffers are expected to be approximately 80% (Wieland 2001, Thouvenot et al. 2013), and repositories situated in salt deposits (e.g., halite) will have almost 0 water saturation throughout its lifespan (Johnson et al. 2019). This initial emplaced saturation will go up when groundwater infiltrates (as discussed in section 2.4.2) which will speed up the rate at which corrosive species can migrate towards the containers as $D_e \propto S$ (Eq. 2.25 (King et al. 1996, 2017)). Like saturation, heating also speeds up the species diffusion rate as

$D_e \propto T$ Eq. 2.26, however, high thermal gradient can move moisture away from the containers through vapour diffusion (i.e., dry the buffer) and cease aqueous species transport (Hall et al. 2021). While some studies modelled corrosion due to HS^- transport (Cloet et al. 2017, Pekala et al. 2020, Kiczka et al. 2021), other studies modelled corrosion due to O_2, Cl^-, SO_4^{2-},and HCO_3^- transport (King 2007, 2008). Some studies ignored effects of saturation and heating on corrosion (Cloet et al. 2017, Pekala et al. 2019, 2020, Kiczka et al. 2021). Given the variability in modelling assumptions among these studies, predicted corrosion was found to be in the order of millimetres or below the corrosion tolerance set by nuclear agencies. . Overall, corrosive species transport modelling needs to combine effects of hydrogeological conditions (saturation, heating) and species evolution during oxic and anoxic phases to evaluate total oxic and anoxic corrosions.

2.5 Modelling Geochemical Processes

The DGR geochemical environment is remarkably dynamic and complex, undergoing a range of different reactions and processes at each stage of operating life. These geochemical reactions include sorption, hydrolysis, complexation, and oxidation-reduction reactions, cation exchange, and mineral dissolution-precipitation (Mayer et al. 2002) and may either be equilibrium or kinetic processes (King et al. 2002) (see an overview of possible interactions, Figure 2.5). Modelling geochemical reactions is important to understand changes in porewater chemistry, mobility, reactivity, retardation of species during transport through buffer materials, effective flux of species, and how these behaviours change with DGR environmental conditions in space and time. Being able to predict this geochemical evolution, and its impact on the DGRs storage security, is vital to long-term storage security.

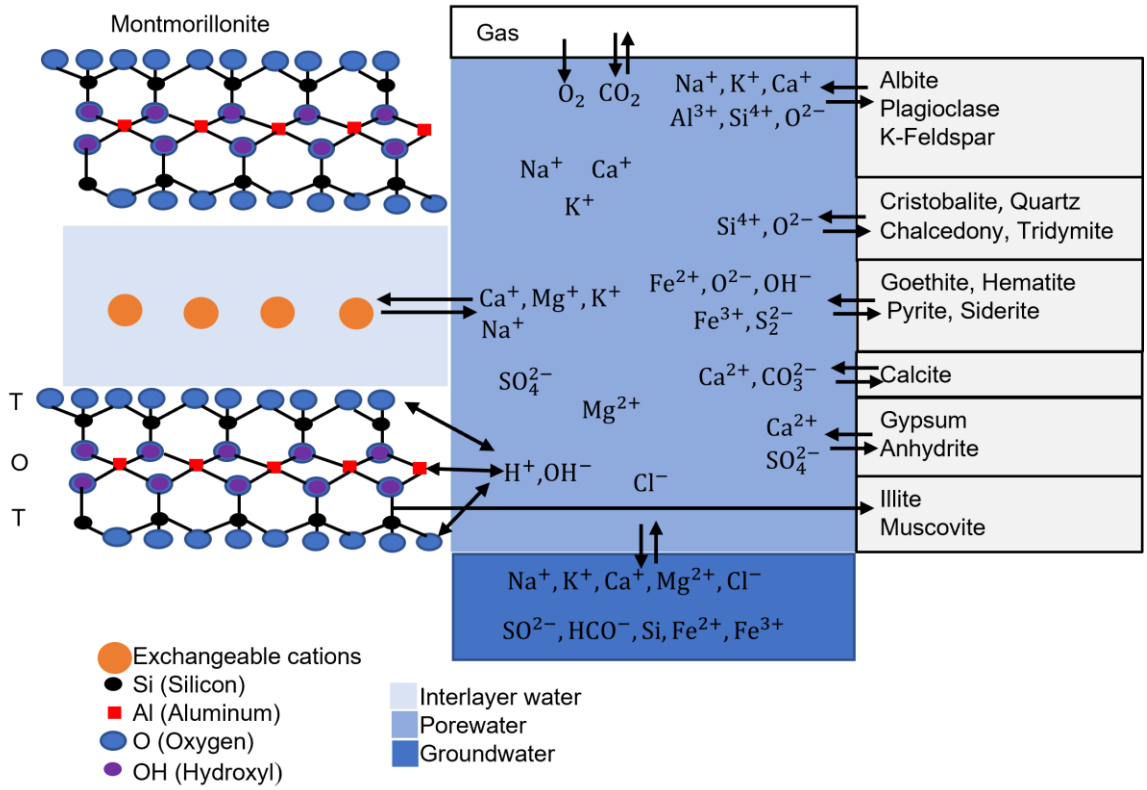

Figure 2.5: Key geochemical processes in bentonite porewater (adapted from Itälä (2009) and Itälä and Olin (2017) with permission from Elsevier).

2.5.1 Species Sorption

Species sorption refers to the attachment (i.e., adsorption), detachment (desorption), and absorption of species to the soil particles. Modelling species sorption is important as species (e.g., corrosive and radionuclide species) can be retarded in buffer materials due to adsorption or absorption (Khan et al. 1994, 1995, Wersin 2003). Although species sorption is a surface mediated process, it retards species in porous media (through adsorption or absorption) like species reaction and therefore, sorption is discussed here under geochemical reactions.

Species adsorption can be described through a linear sorption isotherm (Eq. 2.35) or nonlinear Langmuir isotherm (Eq. 2.36) or Freundlich isotherm (Eq. 2.37) (Langmuir 1917, Freundlich 1907):

$$C_P = K_d\ C \tag{2.35}$$

$$C_P = \frac{K_L\ C_{P,max}\ C}{1 + K_L\ C} \tag{2.36}$$

$$C_P = K_F\ (\frac{C}{C_{Ref}})^{N_F} \tag{2.37}$$

where C_P, represents adsorbed concentration; K_d represents partitioning coefficient due to adsorption, K_L and K_F represents the Langmuir constant and Freundlich constant, respectively; C and C_{Ref} represent concentration and reference concentration, respectively; $C_{P,max}$ represents sorption maximum. Species retardation (R_D) due to adsorption is expressed as (Shackelford and Moore 2013):

$$R_D = 1 + \frac{\rho_d}{\varphi}\frac{\partial C_P}{\partial C} \tag{2.38}$$

2.5.1.1 Coupled Diffusive and Adsorptive Transport

Species diffusion and retardation due to adsorption can be described incorporating retardation factor in Fick's 2nd law (Fick 1855, Shackelford and Moore 2013):

$$\frac{\partial C}{\partial t} = \frac{D_e}{R}\nabla^2 C \tag{2.39}$$

As bentonite exhibits sorption affinity to cations (e.g., cesium, strontium), experimental studies explored cation sorption onto bentonite to find sorption parameters for bentonite (Oscarson et al. 1994, Khan et al. 1994, 1995, Norrfors 2011, Tachi et al. 2014). Some studies tested both granular and compacted bentonite and found that there are less sorption sites in compacted bentonite compared to granular bentonite (Oscarson et al. 1994, Tachi et al. 2014). These experimental studies also provide empirical relations to

estimate K_d of compacted bentonite. Although cation transport through bentonite was simulated in some studies (Tachi et al. 2014), anion sorption was not explored using numerical models. Anion exclusion effect (anions get excluded from the pore space due to repulsion from the negatively charged clay particles) controls sorption behaviour of anions (e.g., Cl^-,HS^-) in compacted bentonite (Van Loon et al. 2007). Due to anion exclusion effect, anions may occupy a small part of the pore space in compacted bentonite (i.e., diffusion accessible part) and therefore, anion sorption onto the compacted clay particles becomes an unlikely process (Tournassat and Appelo 2011). Hence, the likely process that can lead to retention of anions in compacted bentonite is the reaction of anions with various species (e.g., Fe) in bentonite (Chowdhury et al. 2021, Papry et al. 2023).

2.5.2 Species Reaction

Many geochemical reactions impact aqueous species transport beyond just porewater velocity, permeability, and dispersion/diffusivity. Understanding species reaction in buffer materials is important as it can provide an idea of flux from various species after reactions at the nuclear waste containers. In addition, it can be important to know if geochemical reactions in buffer materials are able to retard corrosive species completely (and irreversibly) because a complete retardation could protect the DGR from corrosion. Geochemical reactions in buffer materials can be categorized into homogeneous (only one phase) and heterogeneous reactions (two or more phases).

2.5.2.1 Hydrolysis, Complexation, and Oxidation-Reduction

Homogeneous geochemical reactions are hydrolysis, complexation, and oxidation-reduction while heterogeneous reactions are precipitation-dissolution, cation exchange, organic matter dissolution, and microbiologically influenced reaction. These geochemical reactions can occur in the pore space or at the container surface (Savage et al. 2010, 2011). Therefore, they interact with various species transport through bentonite and contribute to corrosion of the containers. For example, hydrolysis reaction breaks potassium feldspar ($kAlSi_3O_8$) into kaolin ($Al_2Si_2O_5(OH)_4$), potassium (K^+), silicic acid (H_4SiO_4), and bicarbonate (HCO_3^-) (Earle 2019):

$$2kAlSi_3O_8+2CO_2+11H_2O \rightarrow Al_2Si_2O_5(OH)_4+2K^++4H_4SiO_4+2HCO_3^- \quad (2.40)$$

Like Eq. 2-40, various hydrolysis reactions occur in the buffer materials (Savage et al. 2010, 2011). In addition, hydrolysis of $CuCl^-$ produces Cu_2O (i.e., corrosion of copper container (Eq. 2.28) (Guo et al. 2020). Similarly, many aqueous complexation reactions occur in the buffer materials (e.g., formation of CaCl) (Savage et al. 2010, 2011). Like aqueous complexation, surface complexation reaction at the copper container surface can form stable cuprous-chloro complex ($CuCl_y^{x-y}$) under high Cl^- levels in the buffer and cease Cu_2O formation (Sharma and Millero 1988, King 2008).

Oxidation-reduction reactions govern the redox chemistry in the DGR. Under oxidizing condition (i.e., during the oxic phase), goethite (Fe^{3+}mineral) is formed through oxidation of pyrite or magnetite (Fe^{2+}minerals) (Mota-Heredia et al. 2024). In contrast, Fe^{3+}minerals can be reduced to Fe^{2+}minerals under reducing condition. Therefore, these reactions

control the redox state of Fe in the buffer. The Fe redox chemistry may become very important in retarding corrosive HS^- in the bentonite buffer through formation of FeS under anoxic condition. The HS^- may reduce ferric iron, Fe^{3+} to ferrous iron, Fe^{2+} (Eq. 2.41), which could react with the free HS^- (i.e., free HS^- after forming elemental sulphur, S^0) and form FeS (Eq. 2.42):

$$2Fe^{3+}_{(aq)} + HS^-_{(aq)} \rightarrow 2Fe^{2+}_{(aq)} + S^0_{(s)} + H^+_{(aq)} \quad (2.41)$$

$$Fe^{2+}_{(aq)} + HS^-_{(aq)} \rightarrow FeS_{(s)} + H^+_{(aq)} \quad (2.42)$$

$$2Fe^{3+}_{(aq)} + 2HS^-_{(aq)} \rightarrow Fe^{2+}_{(aq)} + S^0_{(s)} + FeS_{(s)} + 2H^+_{(aq)} \quad (2.43)$$

Geochemical reactions can be modelled either using chemical equilibrium at a specified temperature or a kinetic reaction rate (Pekala et al. 2019, Kiczka et al. 2021). The chemical equilibrium is expressed using an equilibrium constant which depends on stoichiometry and species concentrations (at a given temperature) and thus dependence of reaction rate on temperature is ignored. In contrast, a kinetic reaction rate is dependent on temperature and thus relevant to DGR's non-isothermal condition due to temporal waste heating. For example, a kinetic reaction rate for FeS precipitation (Eq. 2.44) can be expressed as (Rickard 1997, Cloet et al. 2017):

$$R = k\,[Fe^{2+}_{(aq)}]\,[HS^-_{(aq)}] \quad (2.44)$$

$$k = A_h\, e^{\frac{-E_h}{RT}} \quad (2.45)$$

where k is the rate constant which depends on Arrhenius frequency factor (A_h), Arrhenius activation energy (E_h), gas constant (R_g), and temperature (T). Hydrolysis, complexation, and oxidation-reduction reactions were modelled assuming chemical equilibrium (Pekala et al. 2019, 2020, Kiczka et al. 2021).

2.5.2.2 Dissolution-Precipitation

Mineral dissolution-precipitation refers to the breakdown of the mineral into aqueous species and formation of the mineral. For example, The reactions in Eqs. 2.41-2.43 show the total reaction as irreversible process through FeS precipitation. However, FeS may dissolve into Fe and HS^- (i.e., FeS dissolution), which depends on the solubility state of bentonite (Davison 1991, Rickard and Luther 2007, Lemire et al. 2020, Behazin et al. 2021). Therefore, exploring FeS dissolution-precipitation is important as dissolution produces HS^-. Gypsum ($CaSO_4.2H_2O$) in MX-80 bentonite may produce SO_4^{2-}source through dissolution which may be used to produce corrosive HS^- through microbial sulfate reduction (Eq. 2.31-2.34). Therefore, gypsum dissolution-precipitation can impact the effectiveness of MX-80 bentonite and is worth exploring. Dissolution-precipitation reactions were modelled using kinetic rate in some studies (Pekala et al. 2019, 2020, Kiczka et al. 2021) but dependence of reaction rate on temperature was ignored.

2.5.2.3 Cation Exchange

Cation exchange refers to the exchange of cations between interlayer water and porewater. Cation exchange occurs when a weakly bonded cation in the diffuse double layer water is displaced into the interlayer water and another cation from porewater moves through the interlayer to the diffuse double layer (Schaetzl and Thompson 2015). Cation exchange is important as the exchange can transform bentonite mineral and degrade the sealing capacity (Montes-H et al. 2005). For example, Ca^{2+} and K^+ from groundwater can replace Na^+ in MX-80 bentonite (reference bentonite in the design of SKB, POSIVA, and NWMO) and this exchange can reduce the swelling capacity (i.e., enhance permeability)

through reduction of interlayer space (Karnland and Birgersson 2006, Appelo 2013, Xiang et al. 2020). Since bentonite is chosen as a buffer for nuclear waste since species transport is controlled (via diffusion) due to its low permeability (driven by self swelling capacity), reduction of swelling capacity due to cation exchange reactions may question its performance as an effective barrier. Cation exchange was modelled using cation exchange capacity of cations in some studies (Pekala et al. 2019, 2020, Kiczka et al. 2021). However, swelling degradation of bentonite due to cation exchange was not explored by these authors.

2.5.2.4 Organic Matter Dissolution

Various organic compounds may be present in deep groundwater (Abrahamsen-Mills and Small 2019). These solid compounds may dissolve into groundwater through dissolution and may influence DGR performance as they act as electron donor in corrosive bisulfide production (Eq. 2. 32) (Pekala et al. 2019, Kiczka et al. 2021). It is worth noting that the organic carbon in MX-80 bentonite is low (<0.1%) and therefore bioavailability of the organic compounds in the DGR will be low (Marshall et al. 2015). Solid organic matter (SOM) dissolution can be modelled using SOM dissolution rates (Pekala et al. 2019):

$$R_{SOM} = k_{SOM}\left(1-\frac{C_{DOM}}{C_{DOM,\,max}}\right) \tag{2.46}$$

where DOM represents dissolve organic matter, R_{SOM} and k_{SOM} represents the SOM dissolution rate and SOM dissolution rate constant respectively; C_{DOM} and $C_{DOM,\,max}$ represent DOM concentration and maximum DOM concentration, respectively. Organic matter dissolution reactions were modelled using kinetic rate in some studies (Pekala et

al. 2019, 2020, Kiczka et al. 2021) but dependence of reaction rate on temperature was ignored.

2.5.2.5 Microbiologically Influenced Reaction

Microbiologically influenced corrosion reaction (e.g., MIC) refers to the species production due to microbiological mediation (Eqs. 2-31-34). MIC particularly important as it is the largest contributor to the UFC corrosion (see section 2.4.3.5). When modelling MIC reaction, it is important to know the SO_4 reduction rate and understand corrosive bisulfide evolution. Since the SRB may produce corrosive bisulfide by using sulfate (SO_4) and DOM (Eqs. 2.31-2.32) (Cloet et al. 2017), sulfate reduction rate depends on both the presence and abundance of SO_4 and DOM. MIC reaction can be modelled using Monod reaction (Pekala et al. 2019):

$$R_{SRB} = k_{SRB}\left(\frac{C_{DOM}}{C_{DOM} + K^{s}_{DOM}}\right)\left(\frac{C_{SO4}}{C_{SO4} + K^{s}_{SO4}}\right) \quad (2.47)$$

where R_{SRB}, k_{SRB}, C_{DOM}, C_{SO4}, K^{s}_{DOM}, and K^{s}_{SO4} represent SO_4 reduction rate, SRB activity rate constant, DOM concentration, SO_4 concentration, half saturation constant for DOM, and half saturation constant for SO_4, respectively. Some studies modelled microbiologically influence reaction rate (Eq. 2.47) (Pekala et al. 2019, 2020, Kiczka et al. 2021). These studies assumed instantaneous HS^- consumption at the copper container surface following stoichiometry of Eq. 2.33 (i.e., 2 mol of copper consumed 1 mol of HS^-). Therefore, these studies ignored formation of solid Cu_2S and passivity of corrosion layer (i.e., Cu_2S layer) to protect copper container from continued corrosion. In addition, these studies ignored the dependence of reaction rate on temperature.

2.5.2.6 Coupled Diffusive and Reactive Transport

Species diffusion and reaction can be described by incorporating reaction rate R in Fick's 2nd law (Fick 1855, Shackelford and Moore 2013):

$$\frac{\partial C}{\partial t} = D_e \nabla^2 C + R \tag{2.48}$$

Some studies coupled species diffusion with reactions (Pekala et al. 2019, 2020, Kiczka et al. 2021). Although these studies predict that the copper coating will not be compromised due to MIC, parametric uncertainties in geochemical calculations were acknowledged. It is challenging to predict geochemical evolution in DGR due to uncertainties in the maximum rate of SRB activity, concentrations of DOM, SOM dissolution rates, and sulfide solubility (Pekala et al. 2019). It is worth mentioning that all these parameters are site specific and long term in-situ tests are generally performed to understand them. In addition, the geochemical models (Pekala et al. 2019, 2020, Kiczka et al. 2021) ignored the anticipated DGR environment (e.g., varying thermal and hydraulic conditions), which can affect geochemical evolution.

Overall, a huge range geochemical processes may affect integrity of the DGR which are vital to long-term security. However, it is not easy to predict geochemical evolution due to uncertainties in parameters and temporal nature of various processes. There are also a limited number of studies which explored various DGR geochemical reactions, mostly either modelling geochemical reactions in bentonite or geochemical reactions over the nuclear waste containers. None of these studies included the DGR environment when modelling reactions, such as saturation or temperature evolution. Therefore, geochemical modelling under temporal DGR volition is an underexamined area of research and should be explored in-depth to ensure DGR integrity and security.

2.6 Challenges of Modelling a Large Domain

Typically, a DGR site will encompass an area of a few kilometres which is significantly smaller than the region it is situated (Figure 2.6). Local (site)-scale models which incorporate detailed DGR geometries (e.g., used fuel canisters, low permeability barriers) rely on boundary conditions which may or may not be well characterized or even known. For instance, groundwater heads or gradients along with flow directions and speed may not be known near the proposed site, and to approximate a representative boundary condition often requires a regional-scale groundwater flow model. However, it is challenging to model such a large domain. Due to the difference in estimation techniques (e.g., interpolation, discretization, control volume measurement) between the regional scale and site scale models, information transfer using an interface can lead to incorrect outputs (e.g., 15-20% difference in total flow) (Abarca et al. 2013, 2016). In addition, regional-scale models which do not have a well characterized groundwater baselines, such as lack of permeability data or head measurements, will result in limited model validation (Löfman et al. 2009) resulting in inaccurate results (e.g., over/under-estimation of heads). However, identifying the source of inaccuracy can help improve model development process and drive regional sampling campaigns. Although these regional models need detailed groundwater data for accurate predictions, they can still be used even without that for sensitivity analyses to study the implications of possible groundwater flow scenarios and safety cases. For example, sensitivity of Peclet number was performed by Abarca et al. (2016) where a constant Peclet number was chosen because of little sensitivity of groundwater flow to Peclet numbers.

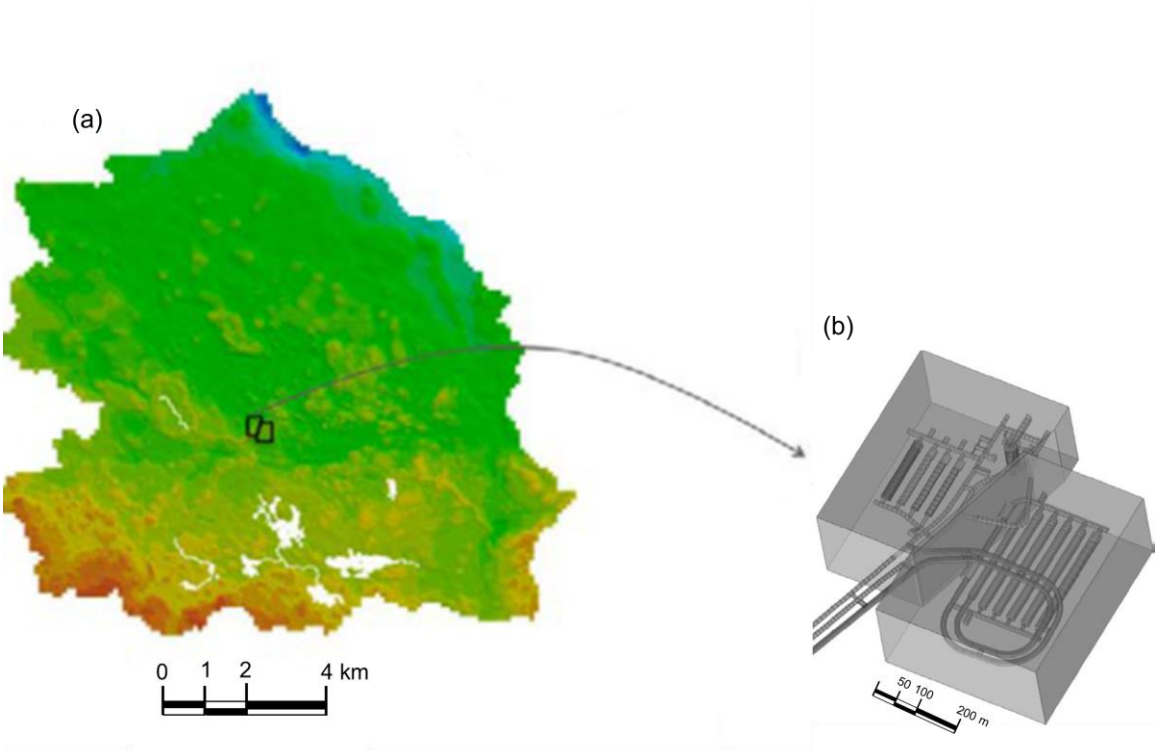

Figure 2.6: a) A regional scale model (several km width), where very small black boxes represent the location of a repository site scale model from SKB, Sweden, b) Repository site scale model domains (hundred m scale). (Adapted from Abarca et al. (2013)).

Another challenging factor is capturing fractured geology of the region surrounding a DGR. While the typical approach for regional scale modelling is to use the groundwater equation (Eqs. 2.1-2.3), fractured geology can be better represented with fracture-specific approaches such as Discrete Fracture Networks (DFN). DFN is applicable for steady state modelling with local-scale rock fractures (Smith et al. 2012). However, some formations possess larger-scale heterogeneities (e.g., discrete discontinuities in crystalline rock) and also, some numerical codes (e.g., TOUHG2) cannot use DFN; instead an Equivalent Continuous Porous Medium (ECPM) approach can also be used (Singhal and Gupta 2010, Baxter et al. 2017). For example, ConnectFlow was used by Baxter et al. (2017) to convert DFN to ECPM as it has both DFN and ECPM options.

Although DFN to ECPM conversion may result in incorrect permeability if flow fields at the corners of the rectangular grids are missed (Baxter et al. 2017), the approach seems reasonable for incorporating large scale rock heterogeneity.

Another issue is estimating permeability of the excavation damage zone (EDZ), which forms around the excavated nuclear waste placement rooms during DGR construction. The rock fractures can create a local, irreversible damage zone (a few meters in width) (Diederichs and Day 2021). Since the fracture initiation and propagation behavior of EDZ is uncertain, it is difficult to predict EDZ permeability (Lanyon 2011). EDZ fractures enhance rock permeability, and therefore create preferential flow paths for radionuclide transport (Williams 2021). Many researchers have used different factors and assumptions to model EDZ permeability evolution (Marschall et al. 2017, Hale et al. 2021, Seyedi et al. 2021). For example, EDZ permeability (k_d) can be estimated as a function of both the rock's average effective stress (σ'_{avg}) and permeability reduction due to EDZ swelling ($e^{D(t-t_0)}$) (i.e., self-healing of the EDZ) (Eqs. 2.49-2.50) (Walsh et al. 2015), and can also be estimated as a function of EDZ fracture aperture (a_h) (Eq. 2.51) (Rutqvist et al. 2008, He et al. 2021):

$$Logk_d = A + Be^{C\sigma'_{avg}} \tag{2.49}$$

$$k = k_d e^{D(t-t_0)} \tag{2.50}$$

$$k_d = \frac{a_h^2}{12} \tag{2.51}$$

where A, B, C, and D in Eq's 2.49 and 2.50 are empirical parameters. Other simpler methods also exist, like estimating a higher permeability. For example, Hartley et al

(2006) assumed that the EDZ permeability was increased by half an order of magnitude. Overall, EDZ permeability evolution is uncertain but site specific observation and data (e.g., fracture width, hydraulic gradient in the EDZ) may help better predict EDZ permeability (Poteri and Laitinen 1999).

2.7 Key Lessons Learned

In this chapter, the applicability of various hydrogeological and geochemical models in capturing DGR processes is reviewed. Some key lessons are:

1) Proper implementation of boundary conditions is important for accurately predicting DGR heat generation and transport process. Over prediction of DGR temperature occurs due to adiabatic boundary conditions around the DGR which can be avoided when a finite DGR domain is modelled (Guo 2016, 2017, 2018).
2) Richards' buffer saturation model under predicted saturation time compared to the full two-phase flow model (Dessirier et al. 2014, 2017). However, Richards' equation would be useful for modelling buffer saturation if the DGR is vented (as is planned for many countries) so that liquid phase does not cause changes in gas pressure gradient.
3) Capturing vapour flow is complicated due to the application of governing equations to capture different physical processes like latent heat energy, relative humidity evolution, heat's drying effect, and preferential vapour flux.
4) Bentonite swelling appears to be one of the most challenging factors in modelling buffer saturation due to complicated saturation process (i.e., water or vapour uptake in different bentonite pore spaces), non uniform swelling behaviour, and

determining a suitable method for modelling bentonite swelling (confined, free or both conditions, swelling in double layer).

5) Modelling species diffusion through EBS is challenging because species effective diffusivity depends on many parameters and assuming same diffusivities for various species will result in incorrect prediction.
6) Corrosive species transport modelling needs to combine effects of hydrogeological conditions (saturation, heating) and species evolution during oxic and anoxic phases to evaluate total oxic and anoxic corrosions.
7) Although cation transport through bentonite was simulated in some studies (Tachi et al. 2014), anion sorption was not explored using numerical models. Dissolution-precipitation reactions were modelled using kinetic rate in some studies (Pekala et al. 2019, 2020, Kiczka et al. 2021) but dependence of reaction rate on temperature was ignored.
8) While bentonite is chosen as the buffer for nuclear waste as species transport through bentonite is controlled (via diffusion) due to its low permeability (driven by self swelling capacity), reduction of swelling capacity due to cation exchange reactions may impact its performance as an effective barrier. Cation exchange was modelled by some using cation exchange capacity of cations (Pekala et al. 2019, 2020, Kiczka et al. 2021). However, swelling capacity degradation of bentonite was not explored.
9) Although some studies (Pekala et al. 2019, 2020, Kiczka et al. 2021) modelled MIC reaction rate, all studies (Pekala et al. 2019, 2020, Kiczka et al. 2021) assumed instantaneous HS^- consumption at the copper container surface

following stoichiometry of Eq. 2.33 (i.e., 2 mol of copper consumed 1 mol of HS^-). Therefore, these studies ignored formation of solid Cu_2S and passivity of corrosion layer (i.e., Cu_2S layer) to protect copper container from continued corrosion.

10) It is challenging to predict geochemical evolution in DGR due to uncertainties in the maximum rate of SRB activity, concentrations of DOM, SOM dissolution rates, and sulfide solubility (Pekala et al. 2019).

11) Different studies modelled either geochemical reactions in bentonite or geochemical reactions over the nuclear waste containers. In addition, DGR environmental conditions were not included in these geochemical studies and remains an unexplored area of research.

12) It is challenging to model a large regional scale domain where a DGR is situated. Due to the difference in estimation processes (e.g., interpolation, discretization, control volume measurement) between the regional scale and site scale models, information transfer using an interface can lead to incorrect outputs (e.g., 15-20% difference in total flow) (Abarca et al. 2013, 2016).

13) EDZ permeability evolution is uncertain but site specific observation and data (e.g., fracture width, hydraulic gradient in the EDZ) may help better predict EDZ permeability (Poteri and Laitinen 1999).

2.8 Conclusions

Nuclear agencies and DGR researchers have developed a wide variety of hydrogeological and geochemical models to assess long term DGR performance. The objective of this chapter was to discuss different DGR designs, establish a conceptual model, review DGR processes, and numerical models. The chapter also focused on

assumptions and research gaps, utility of models, challenges of integrating many different processes, and future research opportunities.

It is understood that assumptions and simplifications have been made in many numerical models due to computational effort, problem statement, and complex and coupled processes. The chapter has identified those assumptions, described modelling approaches, and cited corresponding research articles and reports. Some of the assumptions include neglecting heat convection, thermophysical properties, preferential vapour transport, non-uniform swelling behaviour, swelling in double layer, saturation, temperature, species-specific diffusivity, transition from oxic to anoxic periods, anion sorption, dependence of reaction rate on temperature, degradation of bentonite due to cation exchange, and evolution of corrosion byproduct (e.g., Cu_2S). Although the current models are helpful for understanding many different processes and their implications on DGR safety, their accuracy could be improved due to the abovementioned assumptions. It is worth mentioning that integrating many processes together is challenging due to lack of data, complex evolution (e.g., buffer saturation, swelling), fractured geology, EDZ permeability, numerical accuracy, and computational efficiency. The predictability of the models can be improved through incorporating detailed site-specific data into models, conducting laboratory and in-situ test, and validating models using data.

Chapter 3 Modelling Corrosive Species Transport through the Engineered Barrier System under Repository Conditions

3.1 Introduction

In response to the need for a long-term solution for disposal of Canada's used nuclear fuel, the Canadian Nuclear Waste Management Organization (NWMO) developed the "Adaptative Phase Management (APM)" for Canada's deep geological repository (DGR). This plan is a combination of both technical mechanisms and a management system, which aims to isolate used nuclear fuel in a DGR located within crystalline or sedimentary rock, about 500 m deep below the ground surface. As of 2024, the NWMO has identified two potential sites- the Ignace area and the south Bruce area, both in Ontario (NWMO 2024). The NWMO is working with Canadian universities, scientists, and other countries' nuclear safety organizations to build confidence in the DGR design by performing a robust performance assessment with state-of-the-art predictive tools.

The NWMO's DGR design includes an engineered barrier system (EBS) within placement rooms constructed in a low permeability host rock, which acts as a natural barrier. The EBS consists of used fuel containers (UFCs) made of carbon steel and coated with 3 mm of copper, which serves as a corrosion resistant barrier. The UFCs are designed to hold 48 bundles of Canada Deuterium Uranium (CANDU), and are surrounded by highly compacted bentonite (HCB) clay buffer boxes (Hall et al. 2021) (Figure 3.1). Bentonite clay spacer blocks (made of HCB) separate the buffer boxes, and bentonite clay gapfill (GF) fills any open spaces in the placement room.

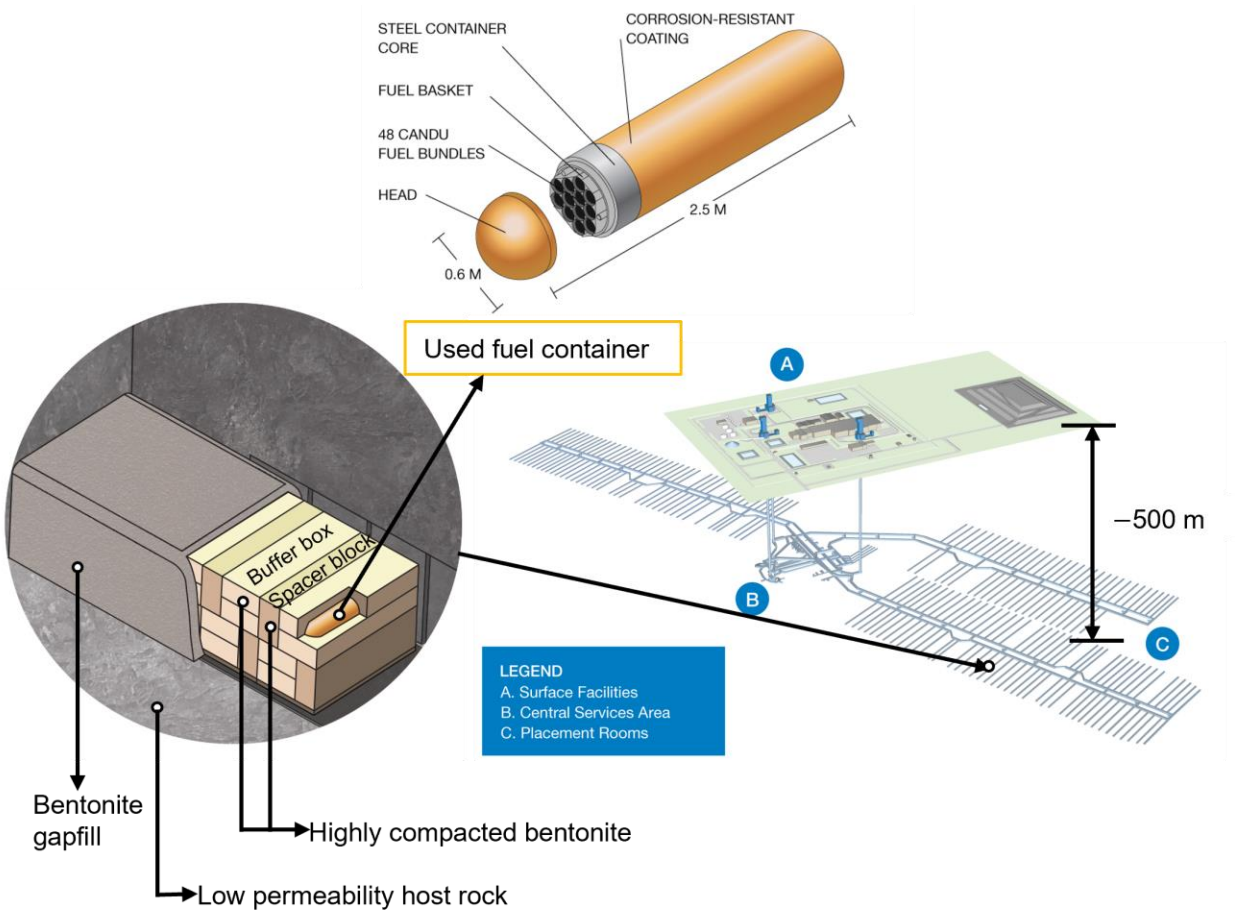

Figure 3. 1: Multiple barrier system in Canadian DGR (adapted from Hall et al. (2021) with permission of Elsevier)

The objective of this chapter is to showcase an extension of a numerical model originally developed by Briggs and Krol (2018), as well as a verification and validation study of the model to aid in the assessment of the DGR under a range of conditions. This model couples DGR temperature evolution, bentonite saturation, and bisulfide transport to simulate UFC corrosion driven by bisulfide. Bisulfide is anticipated to be generated at the rock-bentonite interface by sulfate-reducing bacteria, diffusive through the bentonite and reach the UFC where it can corrode the copper (i.e., microbiologically-influenced corrosion (MIC)). This chapter outlines long term evolution of DGR conditions and the conceptual model framework of the coupled DGR processes. Moreover, verification and

validation studies are presented including mesh convergence tests and comparisons with similar studies, respectively.

3.2 Background

As part of the EBS, HCB was chosen as it possesses good sealing properties against groundwater infiltration (i.e., low intrinsic permeability and self-sealing due to swelling), can retard transport of radionuclides in the event of a UFC breach, and suppress microorganism activity near the UFC (Stroes-Gascoyne et al. 2010). In addition, the HCB can also limit the flux of corrosive species from the surrounding subsurface. The DGR near-field environment, where the HCB is placed, will evolve from an initially warm and oxic environment to a cool and anoxic condition in a span of a million years (King et al 2017) although the depletion of oxygen is anticipated to occur within a period of a few months (Giroud et al. 2018) to a few years (Johansson et al. 2020). In addition, the bentonite will saturate as water infiltrates from the host rock. Under saturated-anoxic conditions, bisulfide may be produced through microbial processes at the rock-bentonite interface and could transport through the HCB to the UFC surface where it could corrode the UFC's copper coating. The long-term prediction of this corrosion is necessary to aid in the performance assessment of the barrier system design and ensure adequate corrosion allowance. This prediction requires conceptual understanding of the time-dependent evolution of the DGR environment (Figure 3.2), which includes changes in different physical and chemical processes (King et al 2017).

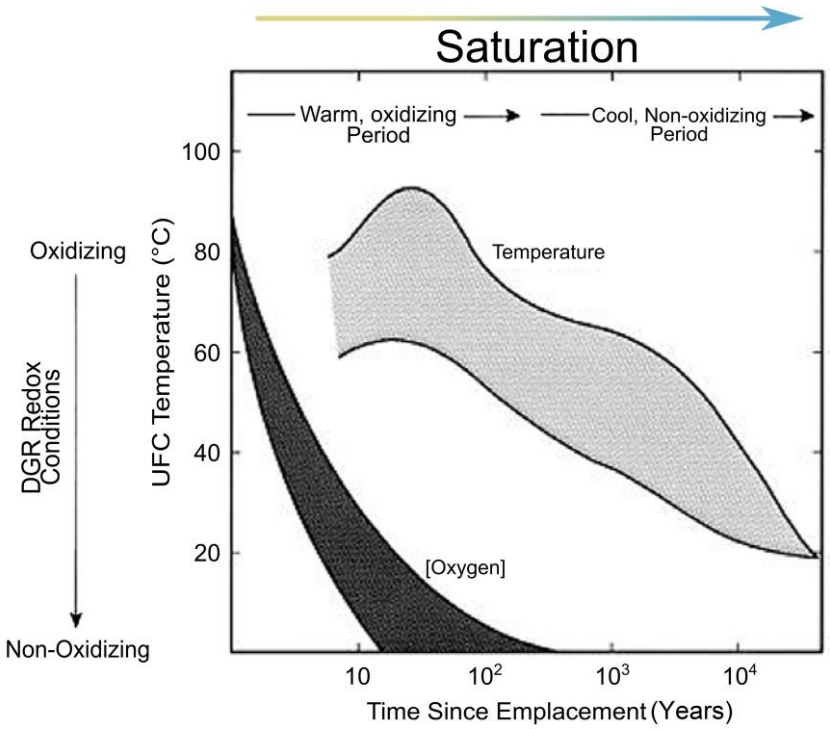

Figure 3. 2: Approximated DGR environmental conditions (adapted from (King et al. 2008) with permission of Elsevier)

3.2.1 Temperature Evolution

According to King et al. (2008) and Guo (2016), DGR temperature will gradually increase due to the heat produced from the used fuel, reaching a peak temperature of above 80 ˚C after 10 years and then decrease gradually to approximately 20 ˚C over 10,000 years (Figure 3.2). Understanding this temperature evolution is important as thermal gradients in the bentonite buffer may dry the bentonite initially and stop aqueous UFC corrosion (King et al. 2017). Moreover, it may impact the UFC corrosion behaviour as reaction rates and solubility of minerals (i.e., bentonite clay minerals) vary with temperature (King et al. 2017). Temperature may also affect bentonite saturation and bisulfide aqueous diffusion through the bentonite as solute diffusion rates also vary with temperature (Einstein 1905, King et al. 2017).

3.2.2 Evolution of Bentonite Saturation and Oxic Conditions

The bentonite is expected to gradually saturate with time, increasing from initial saturation to fully saturated conditions (Figure 3.2). The saturation time will vary with the host rock type (King et al 2017), temperature gradient (Villar et al. 2012), bentonite density and permeability, and initial saturation conditions. The current assumption is that the DGR will fully saturate within 50 years for crystalline rock and 5,000 years in sedimentary rock (King et al 2017). These estimations are based on simplified assumptions and a more detailed study is needed to robustly understand DGR conditions and their implications on UFC corrosion.

Initial saturation of the emplaced HCB in the Canadian DGR design has evolved from 65% to 89%. According to the current Canadian DGR design, the emplaced HCB will have an initial saturation of 89% and the bentonite gapfill will have an initial saturation of 9% (Gobien et al. 2016, King et al. 2017, Dixon et al. 2018, Dixon 2019). The heat evolved from the used fuel will dry the bentonite, and subsequent water infiltration from the host rock will saturate the bentonite once the temperature decreases (King et al. 2017). As the DGR host rock is expected to have low permeability, capillary dominated water flow will govern the saturation and bentonite swelling processes. The saturation rate may affect the rate of species transport through the bentonite to the UFC surface (King et al. 2017), as aqueous dissolved species will only transport through partially and fully saturated pores and no aqueous transport will occur in unsaturated soil (unsaturated being defined as no water-connected pores present). In addition, the saturation process may affect the temperature distribution in the DGR (King et al. 2017). Overall, the DGR will undergo a

range of saturation conditions (i.e., unsaturated, partially saturated, and fully saturated) throughout its lifetime (Figure 3.2).

The initial DGR redox condition will be oxic due to entrapped air leftover from DGR construction and operation. The amount of initial oxygen can be estimated using the buffer properties (porosity, degree of saturation, solubility in water), and ideal gas law (Hall et al. 2021). Typically, the oxygen content is assumed to be 1 to 10 mol per m^2 of the UFC surface for oxic copper corrosion (King et al. 2017). However, this value would be lower (Hall et al. 2018), as oxygen may be consumed by other processes, for example, oxidation of minerals in the host rock and bentonite, and aerobic microbial activity (King et al. 2017). The speed of these processes will govern the oxic period length, which is important as it will affect the oxic corrosion processes such as uniform copper corrosion (UC) and stress corrosion cracking (SCC), although copper is not susceptible to SCC (Scully et al. 2016, King et al. 2017). According to King et al (2008)'s prediction (Figure 3.2), the oxic condition in the DGR will last for about 100 years, but recent field studies suggest a shorter oxic period may occur (Müller et al. 2017). The study conducted in the Mon Terri underground laboratory, Switzerland, showed a maximum time period of 1.5 years by which all oxygen in the DGR will be used up (Müller et al. 2017). In addition, indications from more recent large-scale *in situ* experiments suggest that the O_2 is fully consumed within a period of a few months (Giroud et al 2018) to a few years (Johansson et al. 2019). Although the estimates of the oxic period vary widely, these estimates are still well below the anoxic period length (which will last until the end of the DGR design life) and therefore, the anoxic period will govern many long-term processes in the DGR

(King et al. 2017). Table 3.1 shows the evolution of the DGR conditions under three different phases in the DGR (as discussed above). These phases are distinct in terms of their bentonite saturation, temperature, bentonite swelling, and redox conditions.

Table 3. 1: Evolution of DGR conditions with time (Adapted from (King 2005))

Property	Initial Phase	Transition Phase	Final Phase
Temperature	Temperature increases	Temperature decreases	Temperature reaches background levels
Saturation	Redistribution of initial moisture content	Gradual saturation of bentonite	Complete saturation of bentonite
Thermal Conduction	Poor thermal conduction	Thermal conduction improves	Good thermal conduction
Bentonite Swelling	No swelling of bentonite	Bentonite swelling starts	Bentonite swelling complete
Redox condition	Oxic	Oxic/Anoxic	Anoxic

3.2.3 Microbiologically Influenced Corrosion

Once the DGR is saturated, anoxic conditions will govern in the subsurface. Anoxic UFC corrosion may occur through microbiologically influenced corrosion (MIC) if bisulfides (HS^-) are present or produced in the DGR. Bisulfide may be produced at the rock-bentonite interface due to sulfate reduction by sulfate-reducing bacteria (SRB). If bisulfide transports through the bentonite to the UFC, it may corrode the copper barrier as follows (Cloet et al. 2017):

$$2Cu_{(s)}+HS^-_{(aq)}+H^+_{(aq)}\leftrightarrow Cu_2S_{(s)}+H_{2(g)} \quad (3.1)$$

Equation 1 describes the anoxic corrosion of copper in the presence of aqueous bisulfide which is likely to be the largest contributor to long-term copper corrosion in the DGR (Hall et al, 2021). Although bentonite in the Canadian DGR can hinder microbial activity due to its high density which lowers the water activity Pedersen 2010), SRB may be active at the bentonite-rock interface and drive HS^- production (King et al. 2002, King 2009, Stroes-

Gascoyne et al. 2010, Standish et al. 2016, Cloet et al. 2017). Due to the uncertainty of various parameters, previous studies estimated MIC as the highest UFC corrosion contributor compared to other types of corrosion (Figure 3.3).

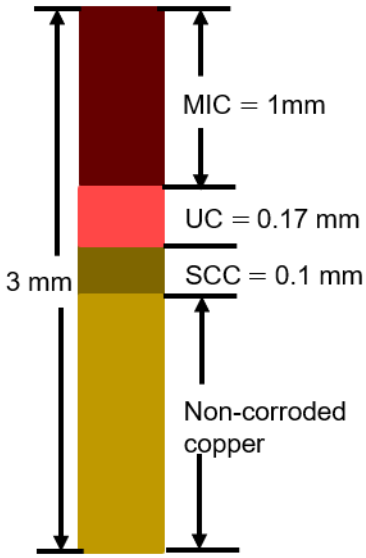

Figure 3. 3: Estimated copper corrosion depth (modified from (Scully et al. 2016))

3.2.4 Conceptual Model of Coupled Processes in Canadian DGR

Figure 3.4 represents the key phenomena expected in a DGR. Heating from the UFC establishes a thermal gradient across the EBS (high temperature near the UFC and low temperature near the host rock) with saturation occurring in the opposite direction – from host rock to UFC (Sena et al. 2010). The saturation process under this thermal gradient can affect diffusion-dominated transport through the bentonite as diffusion is assumed to only occur in the water phase therefore it is limited in partially saturated systems (Martín et al. 2000). In addition, the interlinking between saturation and heating could complicate the diffusive transport of corrosive species. Geochemical reactions (e.g., precipitation, dissolution) can also occur within the bentonite, causing changes in the bentonite

porewater chemistry and bentonite pore structure (Villar et al. 2012) with implications for bisulfide flux through the bentonite (Wersin et al. 2014).

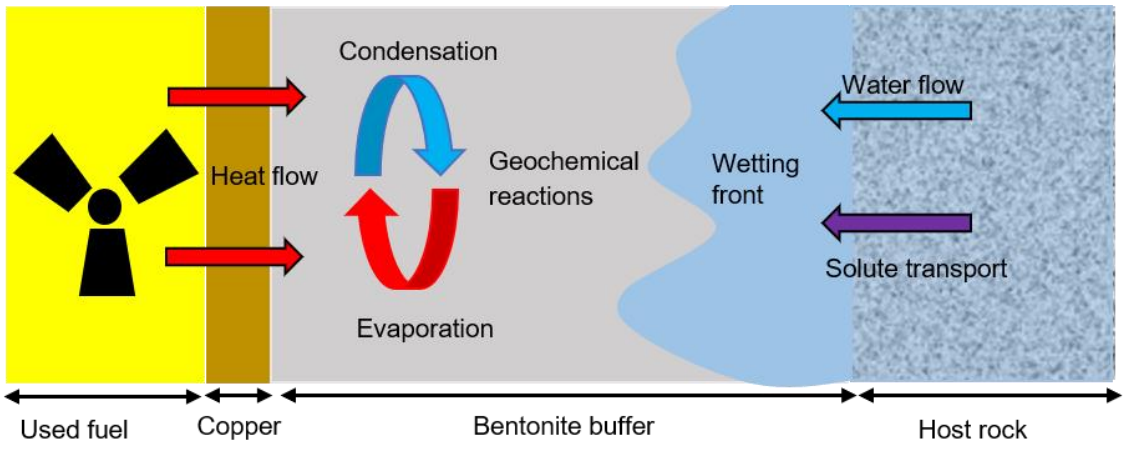

Figure 3.4: Key DGR transport processes (adapted from Sena et al. (2010))

Figure 3.5 shows how the governing processes (identified in Figure 3.4) are coupled in the Canadian DGR environment. As bentonite saturates, it will swell, and its permeability and water activity will be reduced. Due to the heat produced from UFCs, some groundwater will evaporate and become water vapour. This water vapour will either transport through the bentonite pores or condense back to the liquid phase. Sulfate present in the rock or groundwater may be reduced to bisulfide through SRB, but its flux through the EBS will depend upon the geochemical reactions within the bentonite, the bentonite and water properties, and bentonite degree of saturation. More specifically, bisulfide diffusion through the bentonite will depend upon the bentonite properties (e.g., density, porosity, tortuosity, sorption, saturation) and water properties (e.g., temperature, salinity). The bisulfide that reaches the UFC surface, despite the low permeability and high adsorptive capacity of bentonite, can corrode the copper surrounding the UFC.

While the ultimate goal of the model is to include all the processes discussed above, the current study considers the phenomena highlighted in red in Figure 3.5, including bisulfide transport, water saturation, and heat generation. This conceptual model in Figure 3.5 informs the experimental and numerical studies related to DGR safety analysis and provides valuable information about the importance of certain phenomena and interactions. At the same time, as the information through models and experiments become available, some of these interactions may be found to be insignificant, which may necessitate revisiting the conceptual model.

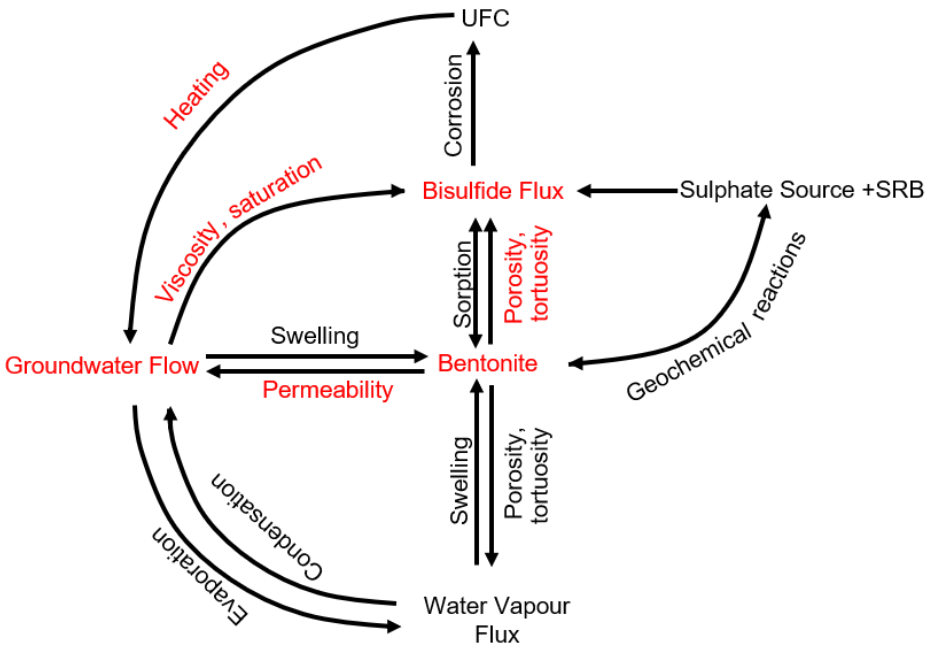

Figure 3.5: Coupled DGR processes governing MIC and saturation of DGR; red font indicates processes modelled in this study

The goal of the Thermal-Hydraulic-Chemical (Diffusion) model (referred to as the "THC model") is to explore the impact of the highly coupled processes illustrated in Figures 3.4

and 3.5 on DGR performance and answer key questions including: how long will it take to fully saturate the bentonite, how do various parameters affect bisulfide transport, what is the distribution of bisulfide flux over the UFC surface, and what is the estimated MIC depth?

3.3 Model Approach and Methodology

This section discusses the development, mesh convergence, and validation of the newly coupled 2-D and 3-D Thermal-Hydraulic-Chemical (Diffusion) model (referred to as the "THC model"). This modelling work directly builds upon the work from Briggs and Krol (2018) who developed DGR models using COMSOL Multiphysics, a commercial finite element software package. They explored the effects of saturation and temperature separately on bisulfide transport and MIC. The THC model presented herein extends their work to explore the combined effect of temperature and saturation on bisulfide transport using a non-isothermal and variably saturated model as well as extending it to three dimensions. Like Briggs and Krol (2018), no sorption and geochemical reactions, vapour transport, and bentonite swelling were considered (Figure 3.5).

The transport of aqueous dissolved compounds (bisulfide) is governed by diffusion due to the low permeability of bentonite (mass Peclet number of 2×10^{-4}) and is described by Fick's 2nd law (Fick 1855) as follows:

$$\varepsilon \frac{\partial C}{\partial t} + C C_m \frac{\partial H_p}{\partial t} = D_e \nabla^2 C \qquad (3.2)$$

where ε is the porosity, C is the bisulfide concentration, C_m is the specific moisture capacity, and D_e is the effective bisulfide diffusion coefficient. The transient heat equation was used to model energy transfer, also dominated by thermal diffusion:

$$\rho_s \, c_p \frac{\partial T}{\partial t} = \nabla \cdot (k_{eff} \nabla T) + q(t) \tag{3.3}$$

where T is the temperature, k_{eff} is the effective thermal conductivity, c_p is the specific heat, ρ_s is the density, and q is the heat source. Richards' equation (Richards 1931) was used to model water infiltration into the DGR:

$$(C_m + S_e S_s) \frac{\partial H_p}{\partial t} + \nabla \cdot \left(-K \nabla \left(H_p + z \right) \right) = 0 \tag{3.4}$$

where S_e is the effective saturation of the bentonite, S_s is the storage coefficient, H_p is the pressure head, K is the soil or rock hydraulic conductivity, and z is the depth of the system. The constitutive relationships used within Richards' equation to model unsaturated flow followed the formulations from e.g., van Genuchten [1]:

$$S = \begin{cases} S_r + S_e (S_f - S_r) & H_p < 0 \text{ m} \\ S_f & H_p \geq 0 \text{ m} \end{cases}$$

$$S_e = \begin{cases} \dfrac{1}{\left(1 + \left|\alpha H_p\right|^n\right)^m} & H_p < 0 \text{ m} \\ 1 & H_p \geq 0 \text{ m} \end{cases}$$

$$C_m = \begin{cases} \dfrac{\alpha m}{1-m} (\varepsilon S - \varepsilon S_r) S_e^{\frac{1}{m}} \left(1 - S_e^{\frac{1}{m}}\right)^m & H_p < 0 \text{ m} \\ 0 & H_p \geq 0 \text{ m} \end{cases} \tag{3.5}$$

$$k_r = \begin{cases} S_e^{0.5} \left(1 - \left[1 - S_e^{\frac{1}{m}}\right]^m\right)^2 & H_p < 0 \text{ m} \\ 1 & H_p \geq 0 \text{ m} \end{cases}$$

Where S, S_f, and S_r are the saturation, full saturation, and residual saturation, respectively, k_r is the relative permeability, α, n, and m are constant properties inherent to the soil and are given in Table 2 (note that m=1- 1/n). Equations 3.2-3.4 are the governing equations in the THC model. The interactions between the governing equations are

captured in temperature and saturation-dependent parameters. For example, k_{eff} and effective heat capacity, $\rho C_{P_{eff}}$, are functions of ε, S, while they are dependent on the heat capacity and thermal conductivity of water (k_w, C_{P_w}), bentonite (k_s, C_{P_s}), and air (k_a, C_{P_a}), as seen through equations 3.6 and 3.7.

$$\rho C_{P_{eff}} = \varepsilon \rho_w S C_{P_w} + (1-\varepsilon)\rho_s C_{P_s} + \varepsilon \rho_a (1-S) C_{P_a} \quad (3.6)$$

$$k_{eff} = \varepsilon k_w S + (1-\varepsilon) k_s + \varepsilon k_a (1-S) \quad (3.7)$$

The soil hydraulic conductivity is also a function of soil permeability, water density (ρ_w), and dynamic viscosity of water (μ) which are temperature dependent. The relationship between bisulfide diffusion coefficient in water, temperature, and viscosity of water was defined as follows (Einstein, 1905):

$$\frac{D_{T_1}}{D_{T_2}} = \frac{T_1}{T_2} \frac{\mu_{T_2}}{\mu_{T_1}} \quad (3.8)$$

Where D is the bisulfide diffusion coefficient in water, T_1 and T_2 are the respective temperatures and μ is the dynamic viscosity of water at the various temperatures.

Lastly, the effective bisulfide diffusion coefficient in bentonite is a function of bisulfide diffusion coefficient in water, saturation, diffusion accessible porosity (ε_e), and tortuosity (τ) following Shackelford and Moore (2013):

$$D_e = S \frac{\varepsilon_e}{\tau} D \quad (3.9)$$

$$\tau = \left(\frac{L_e}{L} \right)^2 \quad (3.10)$$

where L and L_e are the straight-line and actual travel distances in the porous medium.

3.3.1 Model Development

A single placement room and the surrounding host rock were approximated in 2-D and 3-D as shown in Figure 3.6. The EBS was placed 500 m below the ground surface and the model domain extended up to 9,500 m below this level (total domain of 10,000 m). The whole domain was symmetric about the two vertical axes (i.e., one half or quarter of the placement room and surrounding rock was simulated for 2-D and 3-D, respectively), which reduced the computational time.

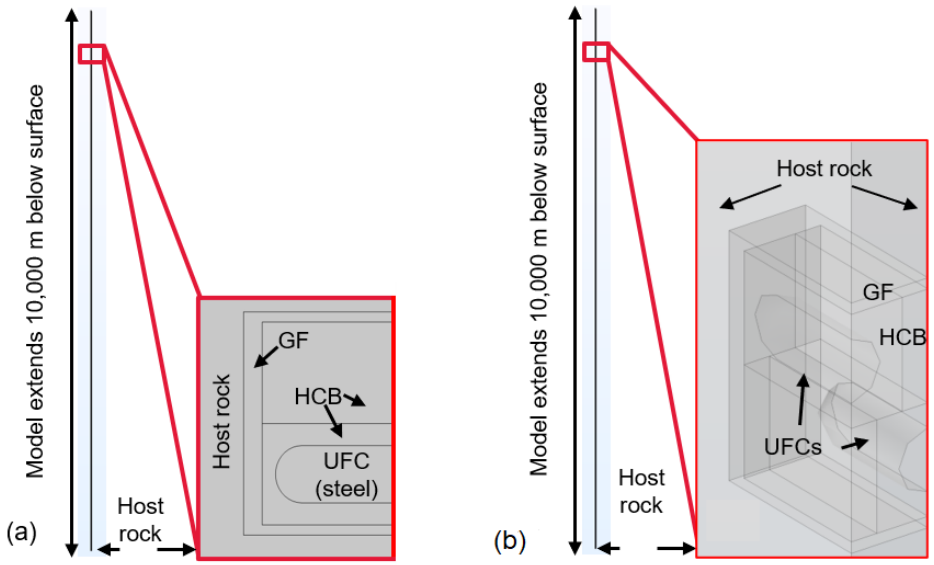

Figure 3.6: COMSOL modelling domain (10,000 m deep) with 10 m segment of a single placement room in (a) 2-D and (b) 3-D. The placement room contains one used fuel container (UFC) in 2-D and two UFCs in 3-D, gap fill (GF), high compacted bentonite (HCB), and host rock.

The parameters were obtained from NWMO case studies and other studies (Baumgartner 2006, SKB 2010b, Sykes et al. 2011, Gobien et al. 2016, 2018, Guo 2016, 2018, Dixon et al. 2018, Dixon 2019) while the UFC heating was estimated from Tait et al. (2000). The

Richards' equation (Equation 3.4) simulated water movement into a partially saturated bentonite from a fully saturated host rock, the heat transfer equation (Equation 3.3) simulated conductive heat transfer, and Fick's law (Equation 3.2) simulated bisulfide diffusion through the bentonite due to a concentration gradient.

The model boundary conditions and mesh configurations are shown in Figure 3.7. This figure shows the 2-D domain; however, the third dimension has the same boundary conditions as the vertical axis shown. The pressure head boundary conditions were set at the top, sides and bottom of the domain to represent the system at hydrostatic equilibrium (Avis et al. 2012). The initial conditions assumed the host rock was assumed fully saturated, and the bentonite (HCB) and gap fill (GF) were 67% saturated (6^{th} case study) (Figure 3.7a). An isothermal boundary was imposed on the ground surface (top boundary), at a temperature of 5 ˚C and 10 ˚C in the crystalline and sedimentary rock, respectively (Guo 2016, Guo 2018). The bottom boundary was also set as isothermal with temperatures of 125 ˚C and 113 ˚C in the crystalline and sedimentary rock, respectively, obtained from geothermal gradients of 0.012 ˚C/m and 0.0103 ˚C/m in the crystalline and sedimentary rock, respectively (Guo 2016, Guo 2018). The UFC heating was defined by a boundary heat source (i.e., along a line) and a domain heat source (i.e., over a volume) in the 2-D and 3-D models, respectively. An adiabatic symmetry boundary condition was applied on the outside vertical boundary which represents an infinite number of UFC heat sources (Figure 3.7b).

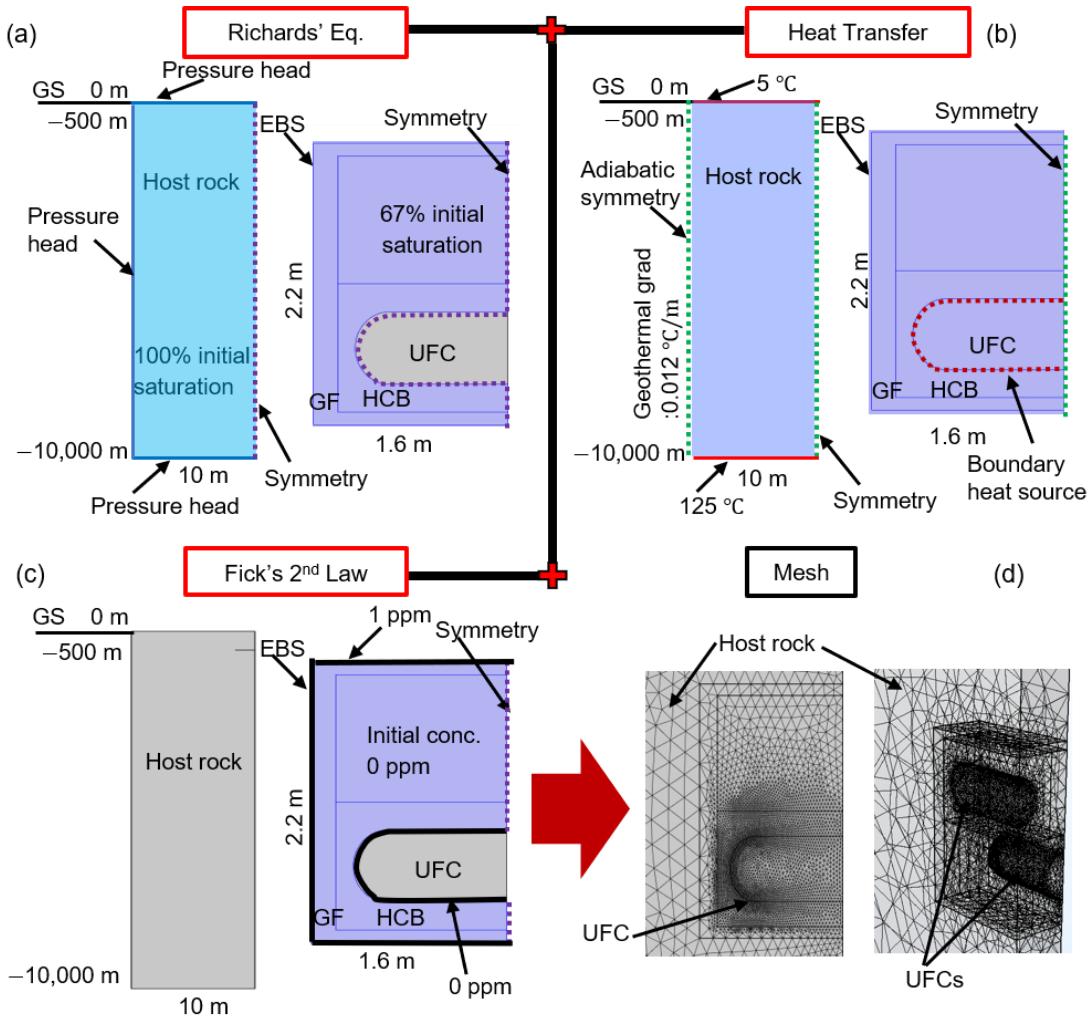

Figure 3.7: Initial and boundary conditions of the THC model for: (a) hydraulic (Richard's equation), (b) thermal (heat transfer), (c) chemical (Fick's 2nd law), and (d) 2-D triangular mesh (12850 elements), and 3-D tetrahedral mesh (551500 elements). Note that the geothermal gradient and boundary temperatures in the thermal module are shown for the crystalline domain.

The far field bisulfide concentration at the host rock-GF (bentonite) interface was assumed to be 1 ppm (0.001 kg m^{-3}) and was implemented as a constant concentration boundary condition. This value was chosen as unity to help simplify conversion when site specific bisulfide concentrations for the Canadian DGR are available (Briggs and Krol 2018). The expected bisulfide concentrations in a Canadian DGR are over an order of

magnitude lower than 1 ppm, i.e., 30-90 ppb (Gascoyne 1997, Kremer 2017). The UFC surface was also modelled as a constant concentration boundary condition with a value of 0 ppm, which assumed that MIC occurs instantaneously at the UFC surface (Briggs and Krol 2018) (Figure 3.7c). The model used a finer mesh around the UFC to effectively capture the bisulfide diffusion in the region of interest, and a progressively larger mesh was applied towards the host rock to reduce computational cost. The hemispherical UFC end cap was meshed with extremely fine mesh due to its complex geometry. Triangular meshing was used in the 2-D model and tetrahedral meshing was used in the 3-D model (Briggs et al. 2017) and a total of 12,850 and 551,500 elements were used in the 2-D and 3-D models respectively (Figure 3.7d).

3.3.2 Parameters

Table 3.2 shows the model parameters obtained from (Gobien et al. 2016, Baumgartner 2006, Guo 2016, 2018, Gobien et al. 2018, SKB 2010b, COMSOL 2021b, Sykes et al. 2011, Dixon 2019, Dixon et al. 2018). These parameters represent the properties of groundwater, bisulfide, bentonite, UFC, and host rock.

Table 3. 2: Model parameters

Parameter		Domain	Value
General parameters			
Water, Air		All	Thermophysical properties from COMSOL 5.6 Material Library[1]
Hydraulic parameters			
Saturated liquid volume fraction[1]		HCB	0.382 (porosity)
Residual liquid volume fraction			0.001
Initial pressure head[2,3,4]			-8144.58 m in the crystalline DGR (67% initial in place average saturation)
			-10536.37 m in the sedimentary DGR (67% initial in place average saturation)
Permeability[3,4,5,6]		HCB	6×10^{-21} m^2 (crystalline groundwater)
			1×10^{-19} m^2 (sedimentary groundwater)
		Rock	4.08×10^{-17} m^2 (crystalline, average)
			2×10^{-21} m^2 (sedimentary, horizontal)
			2×10^{-22} m^2 (sedimentary, vertical)
Van Genuchten properties[3,4,8]	α	HCB	0.00022 m^{-1} (crystalline DGR)
			0.0000908 m^{-1} (sedimentary DGR)
	n		1.5 (crystalline DGR)
			2.71 (sedimentary DGR)
	m = 1-1/n		0.333 (crystalline DGR)
			0.63 (sedimentary DGR)
Thermal Parameters			
Density[2,7]		HCB	1700 kg m^{-3}
		Rock	2700 kg m^{-3}
		UFC	7750 kg m^{-3}
Thermal conductivity[4,5,7,8]		HCB	1.2 W/m K
		Rock	3 W/m K (crystalline)
			2.48 W/m K (sedimentary)
		UFC	60.5 W/m K
Specific heat[2,4,5,7]		HCB	1460 J/kg K
		Rock	845 J/kg K (crystalline)
			603.7 J/kg K (sedimentary)
		UFC	434 J/kg K
Surface temperature[2,7]		Rock	5 ˚C (crystalline)
			10 ˚C (sedimentary
Thermal gradient[2,7]			0.012 ˚C/m (crystalline)
			0.0103 ˚C/m (sedimentary)
Chemical Parameters			
Bisulfide concentration		Rock-bentonite interface	1 ppm
Bisulfide diffusion coefficient in water[9]		HCB	1×10^{-9} m^2/s

[1]COMSOL (2021), [2]Gobien et al. (2016), [3]Baumgartner (2006), [4]Dixon et al. (2018), [5]Dixon (2019) [6]Sykes et al. (2011), [7]Guo (2016, 2018), [8]Gobien et al. (2018), [9]SKB (2010).

3.3.3 Convergence and Repeatability

The model domain was discretized in space using tetrahedral mesh in 3-D and triangular mesh in 2-D. Iterative convergence and mesh convergence were performed to ensure the model was properly discretized. Since the model simulates multiple coupled nonlinear processes, the iterative convergence value is important to ensure that errors do not propagate throughout the solution (An et al. 2011, Patankar 2018) . Iterative convergence is achieved by setting a relative tolerance/error criterion so that the error between current and previous iteration stays below the relative tolerance/error of the solver (i.e., $\frac{\text{Current iteration-Previous iteration}}{\text{Previous iteration}}$ < relative tolerance). This is a self-correction method where the error calculated from the previous iteration is corrected by later iterations to reach at a solution, which is close to the exact solution (Logan 2007). For this model, the COMSOL solver was set with a relative tolerance of 10^{-5} to get repeatable results (i.e., the same result in different runs of the solver). Reducing the relative tolerance increased the solution accuracy (due to increasing iterations with smaller timesteps) but also increased the computation time. A relative tolerance of 10^{-5} was heuristically found to provide good repeatability at a reasonable computational time. A mesh convergence study was also performed to ensure the model was sufficiently discretized in space. This was done by changing the minimum element size and examining the maximum MIC rate (i.e., MIC depth over time, Eq. 3.11). As seen in Figure 3.8, maximum MIC rates do not vary significantly for element sizes less than 0.05 m and therefore 0.01 m was chosen as the minimum element size.

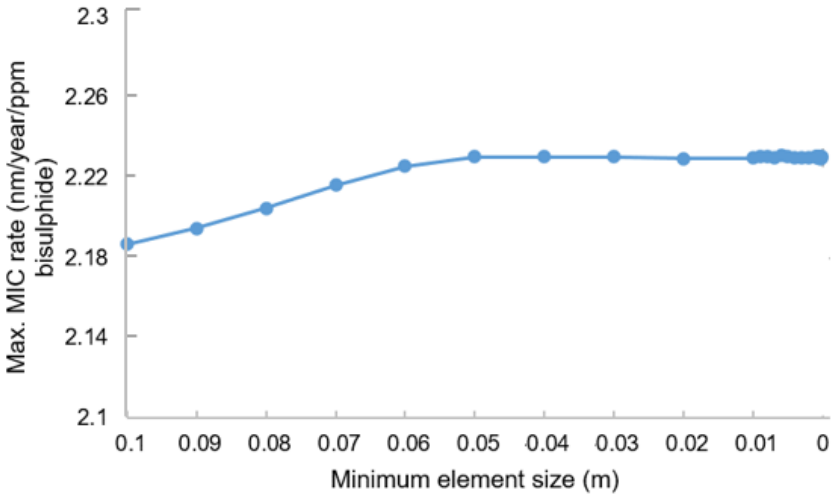

Figure 3.8: Mesh convergence study showing the change in maximum MIC with various minimum element sizes

3.3.4 Model Validation

The mass transport and thermal processes have been verified by Briggs and Krol (2018) and the hydraulic process (Richard's equation) validation is presented here. As no 2-D experiments have been completed, the saturation process was validated by developing a 1-D saturation model that reproduced a quasi-1-D water infiltration experiment into clay (Figure 3.9). The 1-D saturation model used similar initial and boundary conditions compared to the THC model. The measured experimental infiltration data were taken from the unsaturated soil hydraulic database (UNSODA) (Nemes et al. 2001) and Moore (1939). The UNSODA data were fitted in the Microsoft Excel Solver to get the van Genuchten constitutive properties for the infiltration experiment, which were used as inputs in the 1-D saturation model.

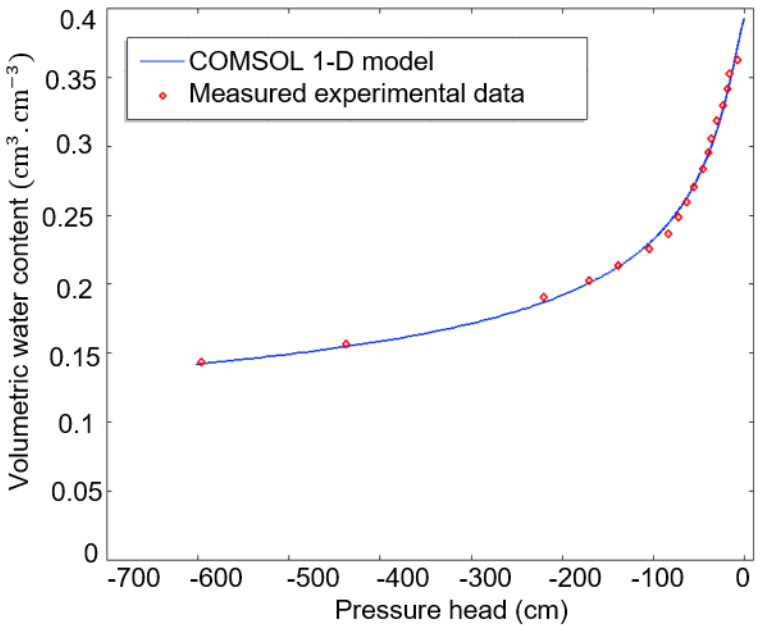

Figure 3.9: Comparison of experimental data from the unsaturated soil hydraulic database and a 1-D saturation model developed using the Richards' Equation in COMSOL

3.4 Model Results

3.4.1 Model Implementation and Sensitivity Study

This section discusses sensitivity of the THC model to different boundary conditions, such as domain depth (section 3.4.1.1), pressure boundary conditions (section 3.4.1.2), and heat source implementations (section 3.4.1.3). These sensitivity analyses were done on the crystalline domain for the 2-D model and highlight characteristic trends that could be extended to the results in a 3-D domain.

3.4.1.1 Domain Depth

Identifying an optimal model domain depth is important to minimize both boundary effects and computation time. The model's domain needs to be large enough to avoid boundary effects, specifically those relating to groundwater flow and UFC heat dissipation.

Since the THC model used a constant temperature bottom boundary condition; it was important to set this boundary far below the UFC at a depth that did not affect UFC heat dissipation. When the bottom boundary was set too close to the EBS (i.e., 10 m below the EBS in the 510 m model) the model underpredicted UFC temperatures (with a maximum temperature close to 60 ˚C) (Figure 3.10a). This is because the constant temperature boundary condition forced an unrealistically high thermal gradient (Eq. 3.3) toward the bottom boundary, which cooled down the UFC.

On the other hand, this false cooling was not observed when the bottom boundary was set far from the EBS (i.e., in 1,000 m and 9,500 m below the EBS in the 1,500 m and 10,000 m models, respectively). In these models, the UFC temperatures rose to the expected values (i.e., up to maximum temperatures above 80 ˚C, Figures 3.10b and 3.10c). Thus, this sensitivity study showed that a proper domain depth was needed to minimize boundary effects and provide accurate temperature estimates. However, the 10,000 m domain was used in the model as UFC heat dissipation was slower compared to the 1,500 m domain (Figure 3.11). In addition, the 10,000 m deep model is comparable to other developed DGR models (e.g., Guo, 2016). It is important to note that the second temperature “bump” in the 1,500 and 10,000 m models (Figure 3.11) is due to the heat symmetry boundary condition and is not representative of the true temperature in the DGR. See additional commentary on this phenomenon in Guo (2016).

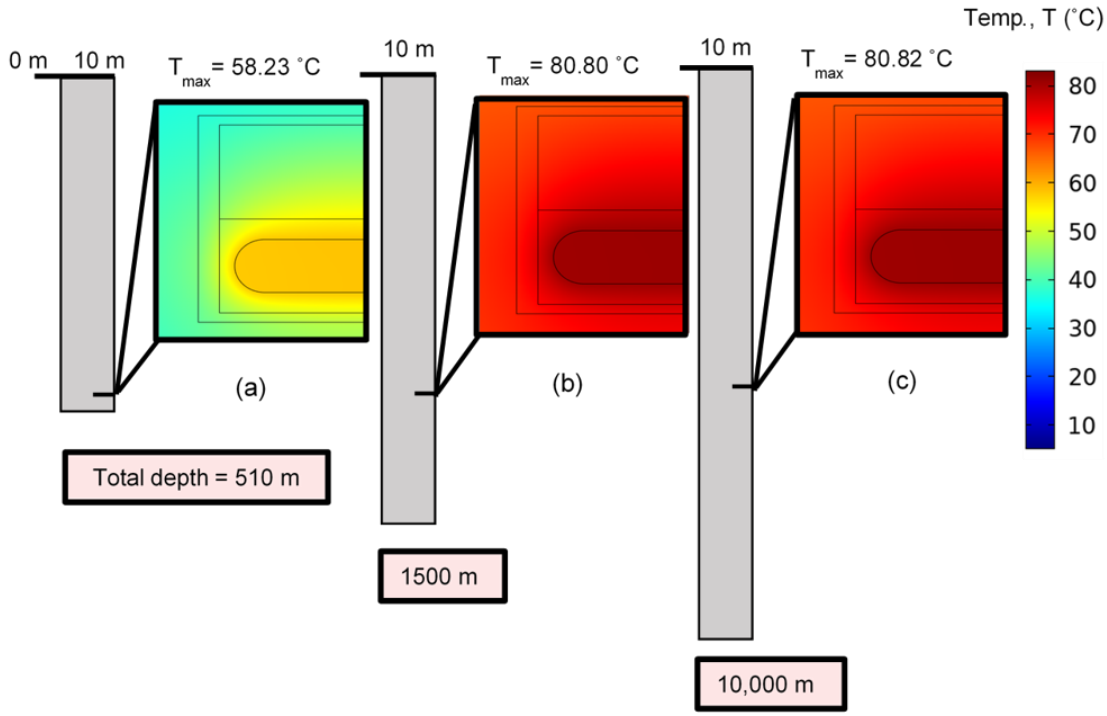

Figure 3.10: Domain depth sensitivity, (a) boundary effect: placing bottom boundary 10 m below the EBS underpredicted the UFC temperature, (b & c) UFC temperature rose to the expected value (i.e., maximum temperature above 80 ˚C) when bottom boundary was moved away from the EBS. Note that the figures are not to scale.

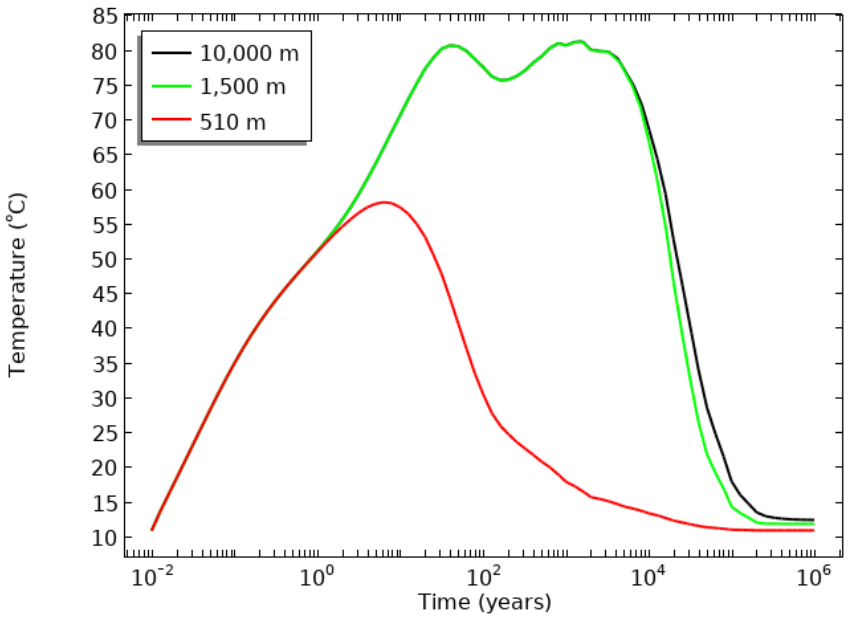

Figure 3.11: Temperature profiles in different depth models

3.4.1.2 Pressure Boundary Conditions

The original model developed by Briggs and Krol (2018) used a Type 2 (no-flow) boundary condition. This boundary condition meant that no water entered the system during saturation, which created an anomalous low-pressure region at late-times (e.g., after 630 years in Figure 3.12a). Therefore, Type 1 (pressure head) boundary conditions were implemented for the current model (Figure 3.12b). Type 1 boundary conditions resulted in a decreased time to full saturation (from approximately 2000 to 20 years) as water was able to enter the model domain from the boundaries. Although this phenomenon is dependent on soil pressure-saturation parameters, the resulting pressure build up is a common result when using the no flow boundary conditions. Therefore, the constant head boundary condition is a better representation of the expected DGR behaviour during saturation.

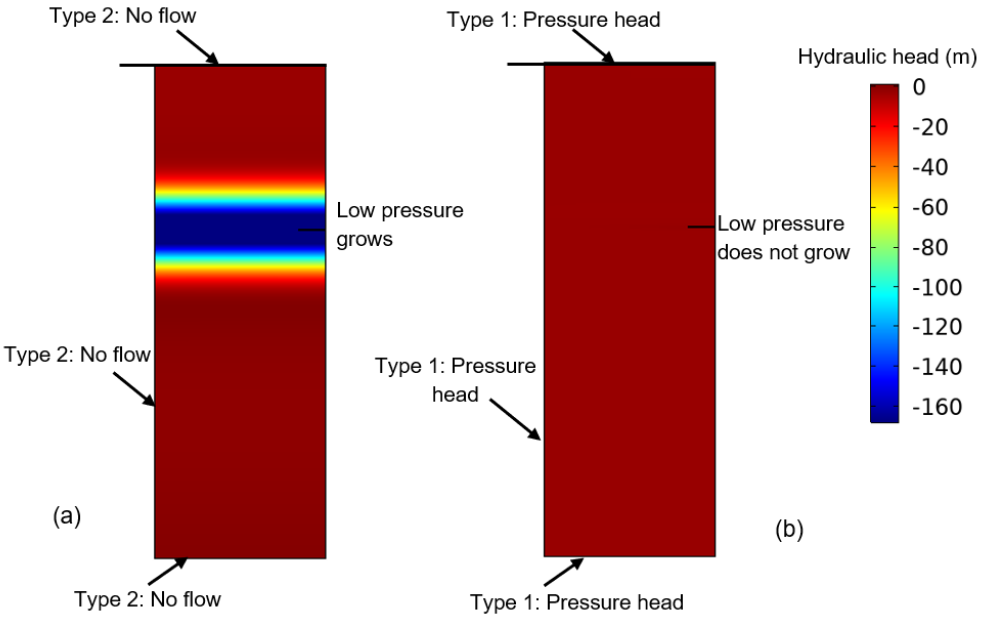

Figure 3.12: Flow boundary conditions sensitivity for: (a) Type 2: No flow boundary conditions (b) Type 1: Pressure head boundary conditions. Results are shown at 630 years.

3.4.1.3 Heat Source

The heat output from the UFC (Tait et al. 2000) can be implemented into COMSOL over a boundary or a domain. For the 2-D model, a boundary heat source (Figure 3.13a) was compared to a domain heat source (Figure 3.13b), and it was found that the latter overpredicted the UFC temperature. This overprediction occurred because the domain heat source was distributed over a 3-D volume and when applied to a 2-D model it overpredicted the heat flux throughout the selected domain. In comparison, when the heat source boundary defined the flux over the selected boundary (area), the 2-D model better approximated the anticipated heat flux into the domain. In the 3-D model, the heat flux was defined over the 3-D volume using a UFC heat rate that is divided by the UFC volume. This correctly approximated the anticipated heat flux into the domain and the temperature output aligned well with expected results (Guo, 2017).

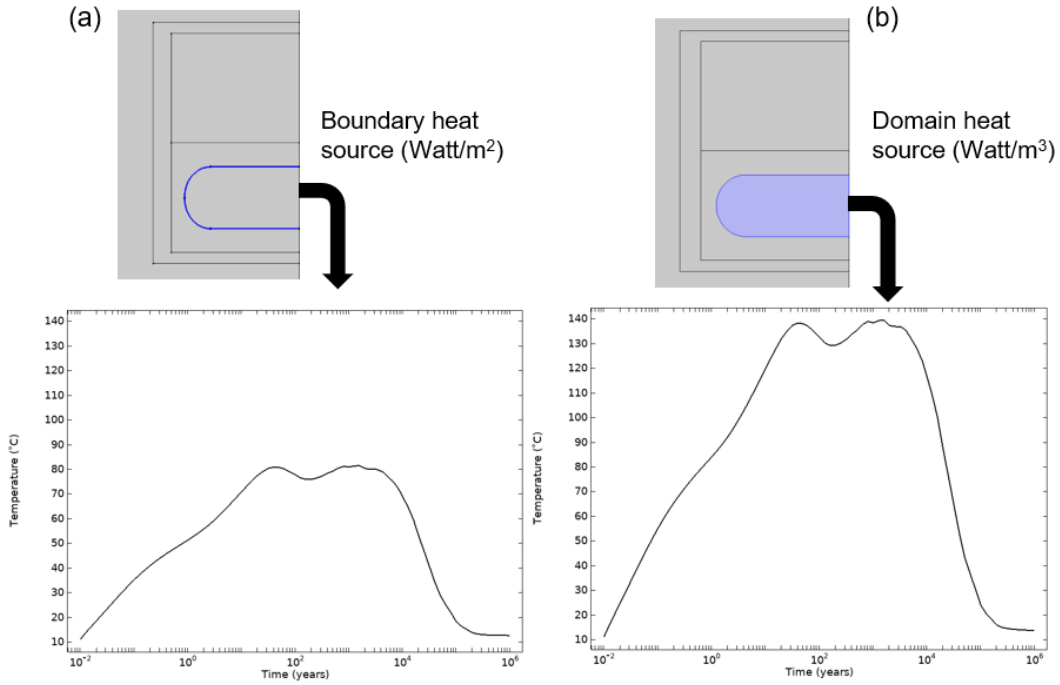

Figure 3.13: Heat source sensitivity using a: (a) boundary heat source, and (b) domain heat source for a 2-D model. Total domain depth of 10,000 m was used in both cases.

The discrepancies described in these sections, highlight how slight differences in model assumptions can lead to errors or inaccurate results; therefore, boundary conditions and initial conditions need to be chosen carefully.

3.4.2 Saturation Time

The 2-D THC model was run for a reference period of 1 million years with an initial bentonite saturation of 67% and fully saturated rock. Figure 3.14 shows water saturation in the crystalline DGR after 2, 5, and 15 years. The HCB near the hemispherical ends of the UFC saturates first within 5 years. Full saturation occurs after 20 years for a host rock permeability of $4.08\times10^{-17}m^2$(reference case for the crystalline rock, Table 3.2). This result compares well with other studies assuming similar host rock conditions, i.e., 10's-100's of years (Millard et al. 2004, Nguyen and Jing 2005). Saturation evolution in the sedimentary DGR is slower than the crystalline DGR, as seen in Figure 3.15 due to lower rock permeability. In addition, the saturation front is not as pronounced in the sedimentary DGR due to the relative permeability of the rock with respect to bentonite. In the crystalline domain, the rock has a higher permeability compared to bentonite while in the sedimentary DGR the rock has a lower permeability (Table 3.2). However, since the rock permeability in the sedimentary domain is lower than in the crystalline, full saturation occurs later - after 160 years for a host rock horizontal permeability of $2\times10^{-21}m^2$ and vertical permeability of $2\times10^{-22}m^2$ (reference case for the sedimentary rock, Table 3.2). Capturing this difference in saturation evolution is important to delineate the oxic and anoxic corrosion. However, this saturation evolution may also be affected by other variables in the host rock, e.g., natural permeability heterogeneity, salinity, and excavation induced fractures.

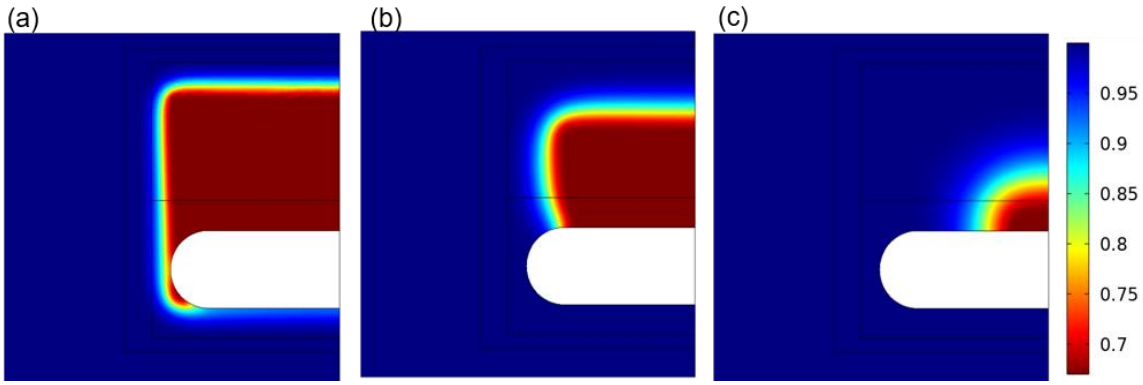

Figure 3.14: Water saturation in the crystalline DGR after a) 2 years, b) 5 years, and c) 15 years. Average permeability of rock and bentonite are 4.08×10^{-17} m^2 and 6×10^{-21} m^2, respectively.

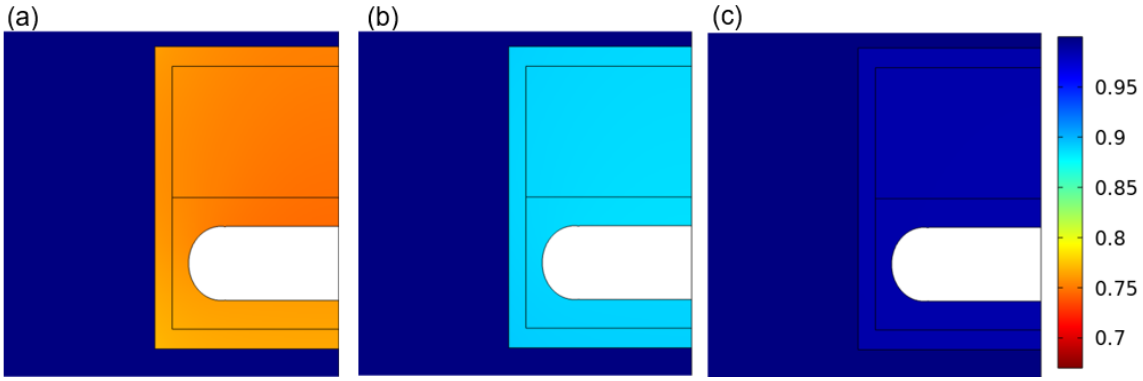

Figure 3.15: Water saturation in the sedimentary DGR after a) 15 years, b) 50 years, and c) 100 years. Horizontal and vertical permeabilities of rock are 2×10^{-21} m^2 and 2×10^{-22} m^2, respectively. Average bentonite permeability is 1×10^{-19} m^2.

Figure 3.16 shows sensitivity in saturation profiles due to varying rock permeability. Typically, increasing rock permeability decreases bentonite saturation time. However, the saturation times are insensitive to the rock permeability when it is higher than the bentonite permeability. This insensitivity is seen in the saturation profiles in the crystalline DGR, which do not vary significantly with rock permeability of greater than 10^{-19} m^2 due to the lower bentonite permeability ($6\times10^{-21}m^2$, Table 2) and results in a consistent saturation time for all crystalline rock permeabilities (20 years, Figure 3.16a). In addition,

saturation time will also be affected by the soil van Genuchten parameters which govern initial saturation condition and soil water characteristic curve of the bentonite (Van Genuchten 1980, Baumgartner 2006).

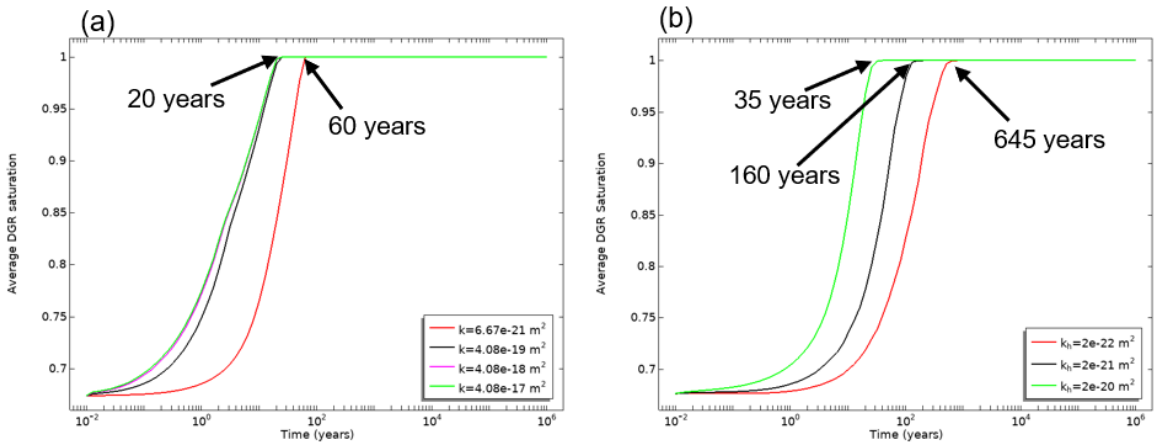

Figure 3.16: Average water saturation over the estimated life span of the DGR for varying a) average permeabilities of the crystalline rock (bentonite k= 6×10^{-21} m^2), b) horizontal permeabilities of the sedimentary rock while keeping the vertical permeability unchanged (bentonite k= 1×10^{-19} m^2).

3.4.3 Bisulfide Flux and MIC Depth

Bisulfide fluxes were examined in the crystalline DGR after 2, 5, and 15 years (Figure 3.17) and the sedimentary DGR after 15, 50, and 100 years (Figure 3.18). The effective bisulfide diffusion coefficient was kept at $1\times10^{-11}m^2\ s^{-1}$ in both models. The MIC depth, d_{corr} at a given time at the UFC is a function of bisulfide flux and Equation 3.1 and was calculated following SKB (2010):

$$d_{corr}=\frac{N_{HS}f_{HS}M_{cu}}{A_{corr}\rho_{cu}} \qquad (3.11)$$

N_{HS}/A_{corr} is the bisulfide flux computed from the model, f_{HS} is the stoichiometric factor (with a value of 2 from the stoichiometry of Eq. 3.1), M_{cu} is the molar mass of copper, and ρ_{cu} is the density of copper. The MIC rate can be calculated at the UFC. Initially, the MIC rate is zero since no bisulfide is present at the UFC. Bisulfide diffusion occurs from the host rock as the bentonite becomes saturated. More bisulfide enters through the bottom boundary (Figure 3.17a) as the sharp saturation front saturates the bentonite near the bottom boundary first compared to other parts (Figure 3.14a). The maximum bisulfide flux occurs at the hemi-spherical UFC end caps due to EBS and UFC geometry (Briggs et al, 2017). The maximum MIC rate in the crystalline DGR is 2 nm.year^{-1}ppm bisulfide^{-1}after 1653 years. The maximum MIC rate in the sedimentary DGR is 2.54 nm.year^{-1}ppm bisulfide^{-1}after 1267 years. It is important to note that the MIC rate is solely based on bisulfide diffusion and not on the rate of bisulfide production due to SRB activity (microbial reactions are not considered in this model).

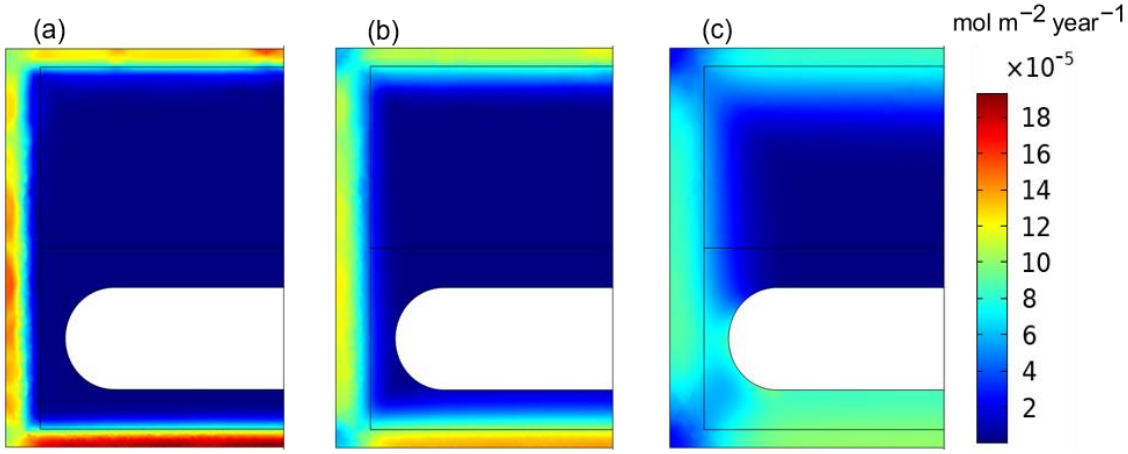

Figure 3.17: Bisulfide flux in the crystalline DGR after a) 2 years, b) 5 years, and c) 15 years

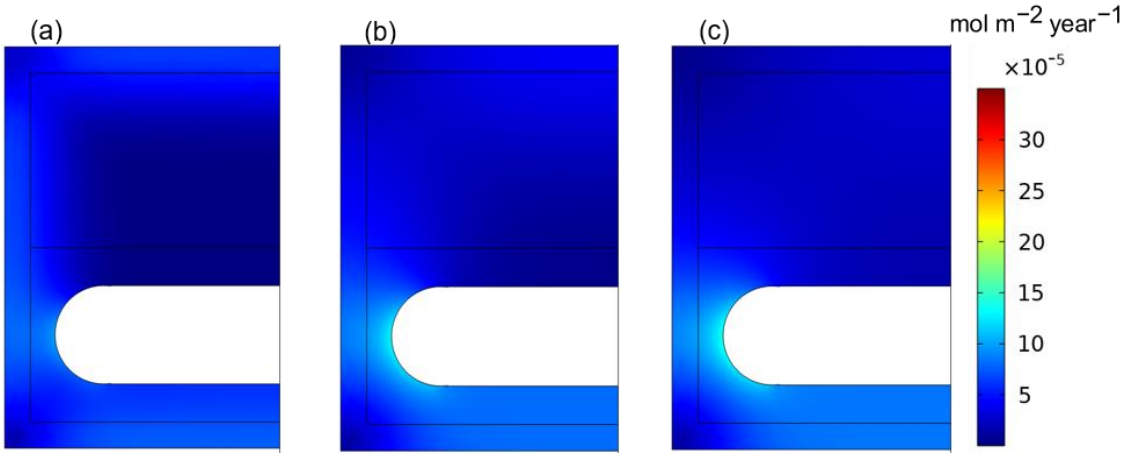

Figure 3.18: Bisulfide flux in the sedimentary DGR after a) 15 years, b) 50 years, and c) 100 years

3.4.4 THC versus Other Models

The previous study (Briggs and Krol 2018) assessed the effects of saturation and temperature on MIC using separate models. These models simulated: (*i*) Chemical (Diffusion) processes (referred to as the "C model", Figures 3.19a, and 3.20a), (*ii*) Hydraulic-Chemical (Diffusion) processes (referred to as the "HC model", Figures 3.19b, and 3.20b), and (*iii*) Thermal-Chemical (Diffusion) processes (referred to as the "TC model", Figures 3.19c, and 3.20c). This current work (the "THC model", Figures 3.19d, and 3.20d) explores the combined effects of saturation, diffusion, and temperature in one model, to improve MIC estimations.

Figure 3.19e compares maximum MIC rates from different models set in the crystalline DGR. As the bisulfide diffusion rate is dependent on saturation and temperature (Eqs. 3.5, and 3.6), the MIC rate is also controlled by hydraulic and thermal conditions. In the TC model, bisulfide enters the system after year "one" and the diffusion rate increases with temperature (Figures 3.19c, and e). In comparison, bisulfide transport starts later in

the HC model (approximately 3 years) and the THC model (approximately 1.5 years) once water has infiltrated the bentonite (Figures 3.19b, d, and e). Bisulfide transport starts after 3 years in the C model as temperature does not affect the diffusion rate in an isothermal system (Figures 3.19a, and e). Therefore, bisulfide travel time is mostly affected by temperature, followed by saturation of the system in the crystalline domain.

All models reach steady-state MIC rates when UFC heat has fully dissipated, and temperature returns to the background level (approximately after 2×10^5 years). MIC rates in TC and THC models are very similar (Figure 3.19e) as saturation in the THC model is fast (Figure 3.14) and does not significantly delay the onset of bisulfide diffusion. In addition, the total MIC depth as estimated using Equation 11 (Table 3.3), shows that the MIC rates with and without variable saturation (i.e., THC vs. TC) are also nearly identical, whereas the MIC rate in isothermal conditions are lower showing that temperature has a bigger impact on bisulfide diffusion than saturation in the crystalline domain. It should be noted that these MIC estimates are conservative as these models assume there is no sorption or reactions within the bentonite, no evaporation or gaseous transport is simulated, and bentonite swelling is assumed to occur instantaneously (bentonite permeability is given for swelled conditions).

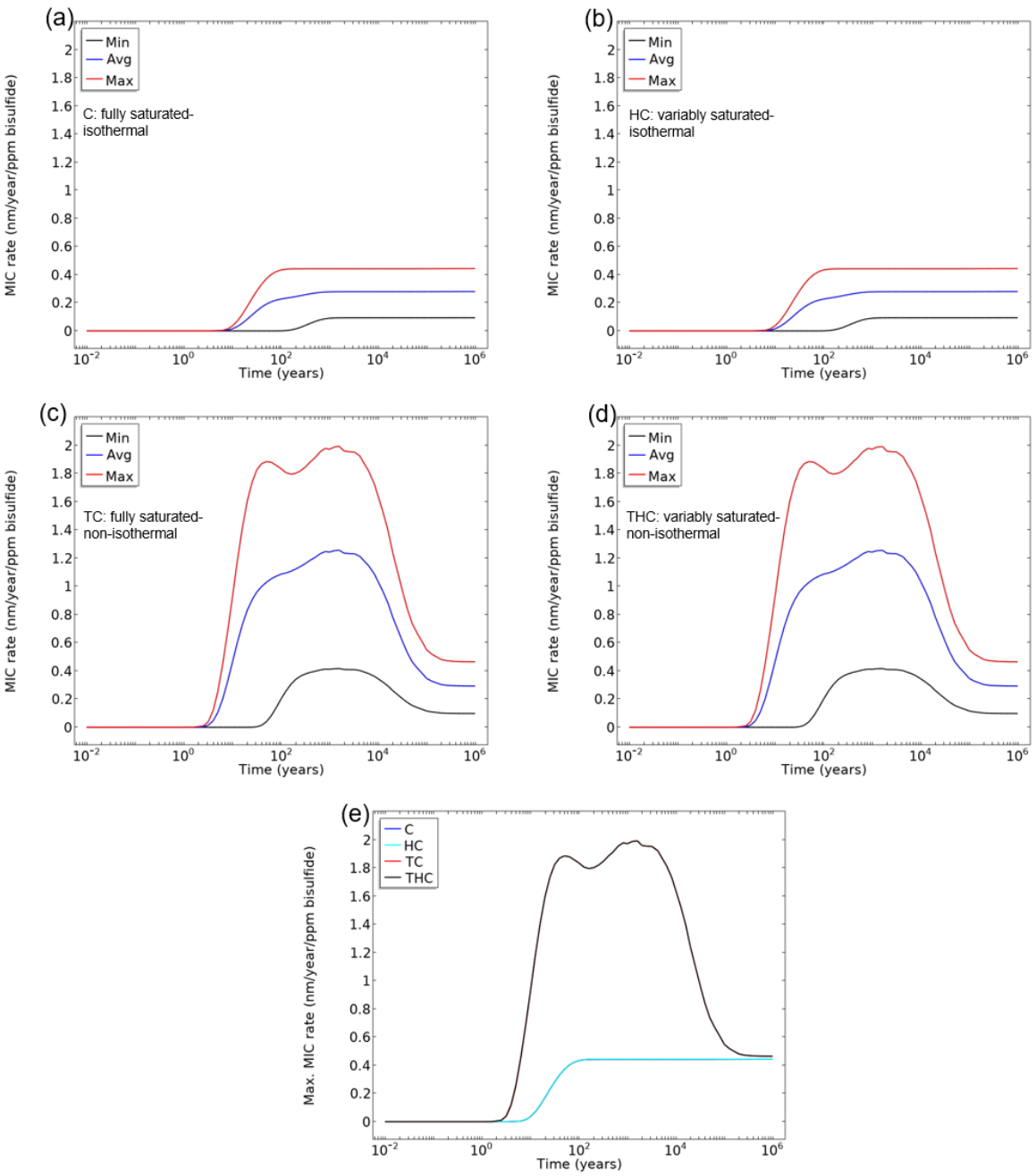

Figure 3.19: MIC rates (max, min, average) in the crystalline DGR under different conditions a) C model simulates bisulfide diffusion under fully saturated-isothermal conditions, b) HC model simulates bisulfide diffusion under variably saturated-isothermal conditions, c) TC model simulates bisulfide diffusion under fully saturated-non-isothermal conditions, d) THC model simulates bisulfide diffusion under variably saturated-non-isothermal conditions, and e) maximum MIC rates in all the different models

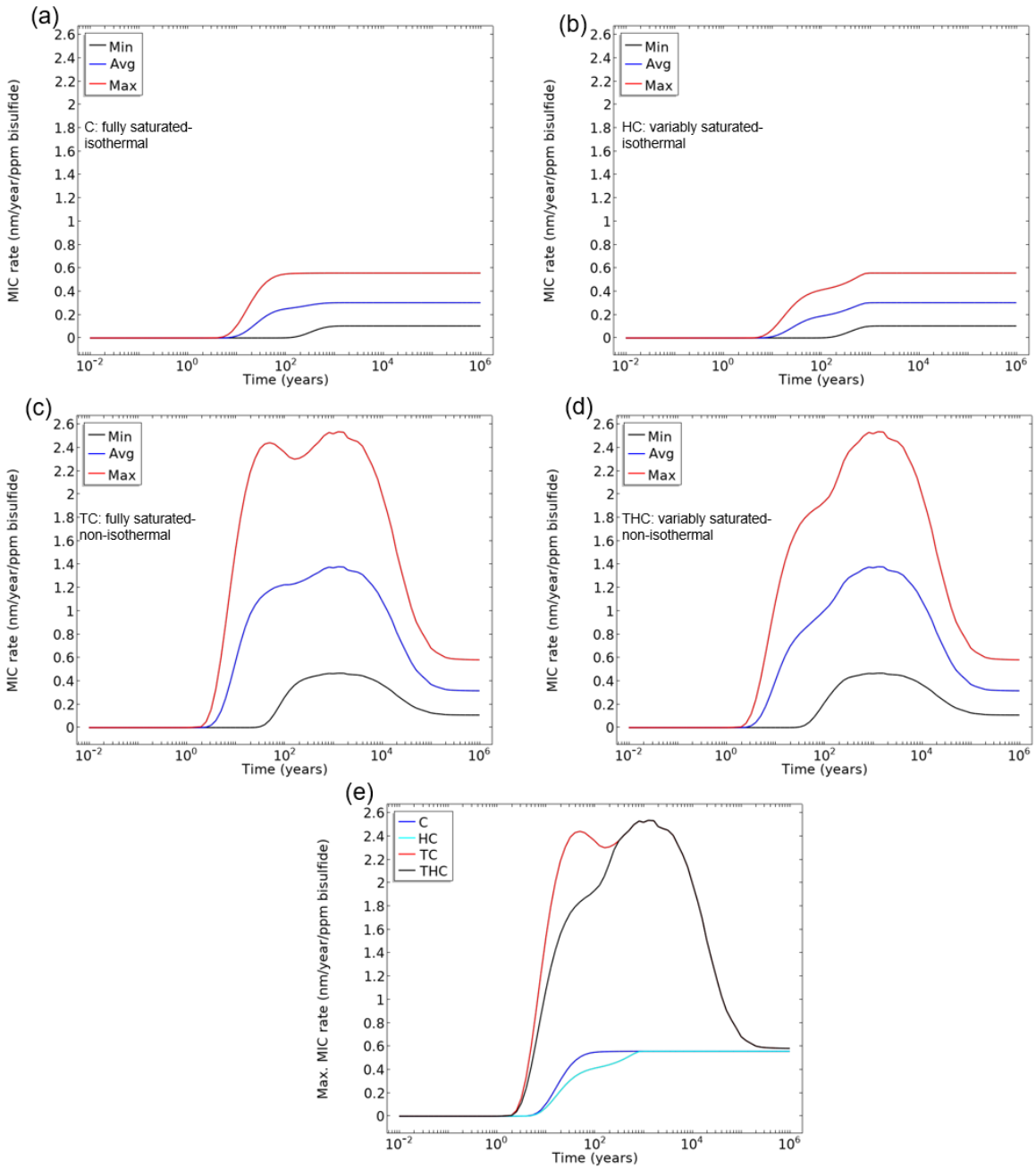

Figure 3.20: MIC rates (max, min, average) in the sedimentary DGR models under different conditions a) C model simulates bisulfide diffusion under fully saturated-isothermal conditions, b) HC model simulates bisulfide diffusion under variably saturated-isothermal conditions, c) TC model simulates bisulfide diffusion under fully saturated-non-isothermal conditions, d) THC model simulates bisulfide diffusion under variably saturated-non-isothermal conditions, and e) maximum MIC rates in all the different models

Figure 3.20e compares maximum MIC rates from different models set in the sedimentary DGR. Like crystalline DGR, bisulfide enters the system after year “one” in the TC model and diffusion rate increases with temperature (Figures 3.20c, and e). In comparison, bisulfide transport starts later in the HC model (after ~5 years) and THC model (after ~2 years) after water has infiltrated the bentonite (Figures 3.20b, d, and e). Bisulfide transport starts after 2 years in the C model as temperature does not affect diffusion rate in an isothermal system (Figures 3.20a, and e). Unlike the crystalline domain, MIC rates in TC and THC models are different (Figure 3.20e) as saturation of the domain in the THC model delays the onset of bisulfide diffusion as it transports through the water filled fraction of the pore space; however, the peak MIC rates are similar (Figure 3.20e). The same is seen for the C and HC models (Figure 3.20e). Like the crystalline DGR, the total MIC depths (Table 3.3) are nearly identical for the THC and TC models, suggesting that the transient MIC rates last for a short time compared to the overall DGR lifespan.

Table 3. 3: Total maximum MIC depths calculated by the various models

Model	**Total maximum MIC depth (mm)**	
	Crystalline	**Sedimentary**
C	0.443	0.556
HC	0.443	0.556
TC	0.517	0.645
THC	0.517	0.645

To demonstrate this, Figure 3.21 shows maximum MIC rates plotted against a linear time scale. This figure shows that the MIC rates driven by changes in saturation and UFC temperature (that impact bisulfide diffusion rates), only occur during the initial life span of the DGR (i.e., before 200,000-400,000 years). After this time, the DGR conditions are fully saturated and isothermal. Therefore, the comparisons in Figure 3.21 help to

understand the relative importance of including different processes in the model and how the system behaves over time due to coupling these processes.

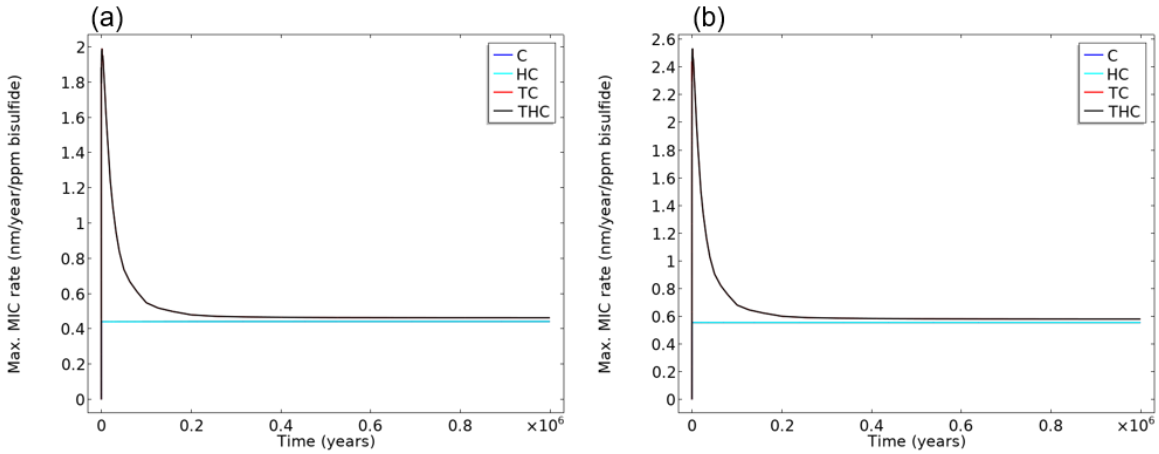

Figure 3.21: Maximum MIC rates in different models, plotted against a linear time scale, a) crystalline DGR, and b) sedimentary DGR

3.4.5 Predicted DGR Environmental Conditions

The THC model was also used to show the predicted environmental conditions and bisulfide flux distribution in the crystalline and sedimentary DGRs (Figure 3.22). The initial bentonite saturation is assumed to be 67% in both DGRs; however, full saturation occurs at different times due to the differences in rock permeability. The normalized air content is calculated as $(1-S_e)/(1-S_{e,0})$, which is assumed to correspond to the evolution of oxic/anoxic conditions in the DGR. However, these models do not simulate the free and dissolved oxygen mass balance or oxygen movement within the DGR. Instead, the influence of key physical processes affecting bisulfide flux (i.e., saturation and heating) are highlighted. The low degree of saturation lowers bisulfide flux (seen most clearly in Figure 3.22b), as bisulfide is assumed to transfer through the water-filled fraction in the pore space. The peak bisulfide flux occurs under high UFC temperatures when the DGR is fully saturated (Figure 3.22).

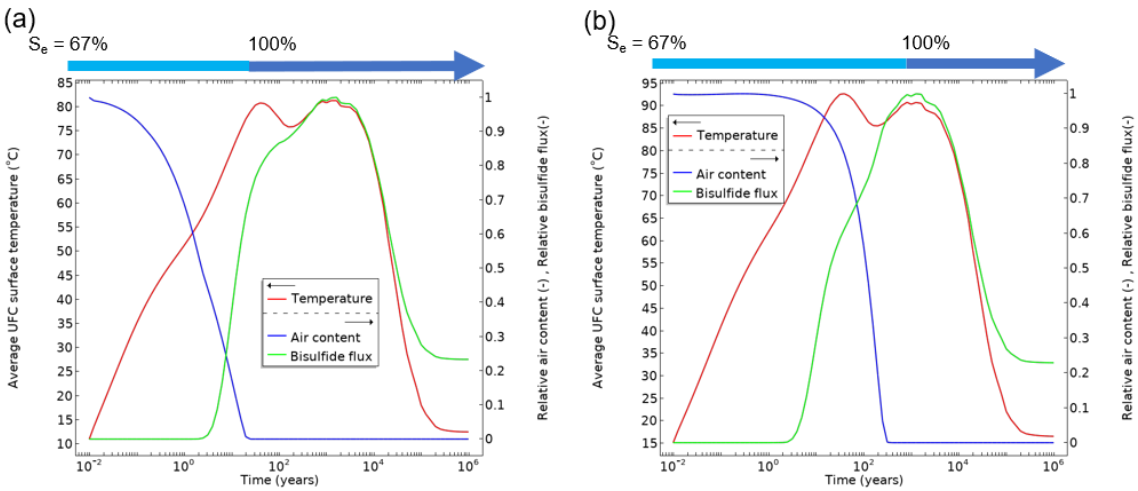

Figure 3.22: Predicted environmental conditions from the THC models in the a) crystalline DGR, and b) sedimentary DGR. Note that the average bentonite air content and bisulfide flux values are normalized.

3.5 3-D THC Model

The previous results were given for the 2-D model therefore Figure 3.23 compares maximum MIC rates, temperature, maximum bisulfide flux, and average DGR saturation in the 2-D and 3-D THC models set in the crystalline DGR. As seen in Figure 3.23a, maximum MIC rates in the 2-D and 3-D THC models are not the same. The total MIC depth in the 3-D THC model is 0.59 mm (Figure 3.26) while the 2-D THC model estimates 0.517 mm (Table 3). This difference occurs due to 3-D geometry (also observed by Briggs and Krol (2018)), which captures MIC rates in the third dimension that are not included in the 2-D model. However, the characteristic UFC temperature (Figure 3.23b) and degree of saturation (Figure 3.23c) are very similar between the 2-D and 3-D models. In addition, the trends and sensitivities discussed in Section 3.4 are the same for the 2-D and 3-D models. This can be seen in the results from the 3-D crystalline and sedimentary DGR models (Figures 3.24, 3.25, and 3.26).

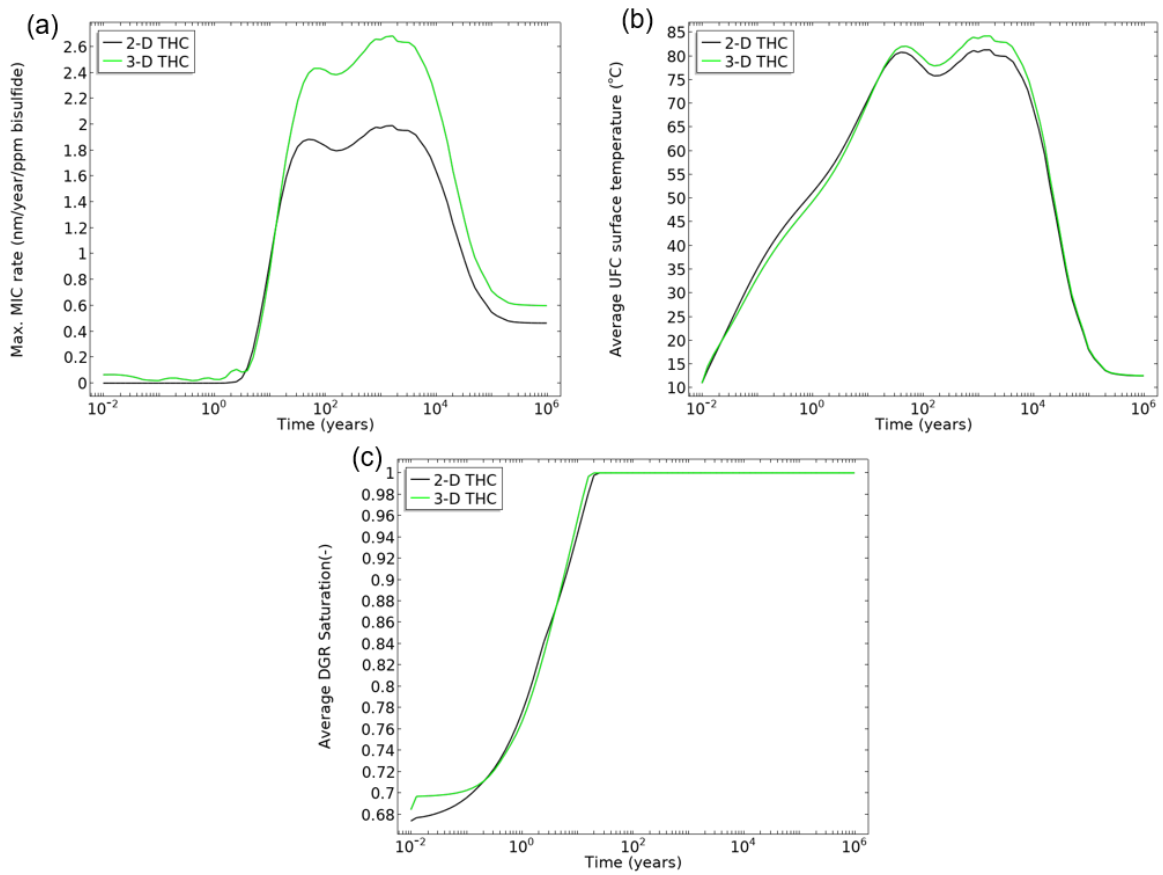

Figure 3.23: 2-D THC versus 3-D THC models of the crystalline DGR, a) maximum MIC rates, b) temperature, and c) average DGR saturation

Figures 3.24a and 3.24 b show sensitivity in saturation profiles due to varying rock permeability in the 3-D crystalline and sedimentary DGR, respectively. The results in these Figures of the 3-D DGR models show the same trend in saturation profiles observed in the 2-D DGR models' saturation profiles in Figure 3.16. Figures 3.24c and 3.24d show UFC temperature evolution in the crystalline and sedimentary DGR, respectively**.** These figures show that temperature evolution is insensitive to hydrogeological properties, as evaporation and condensation processes are not considered.

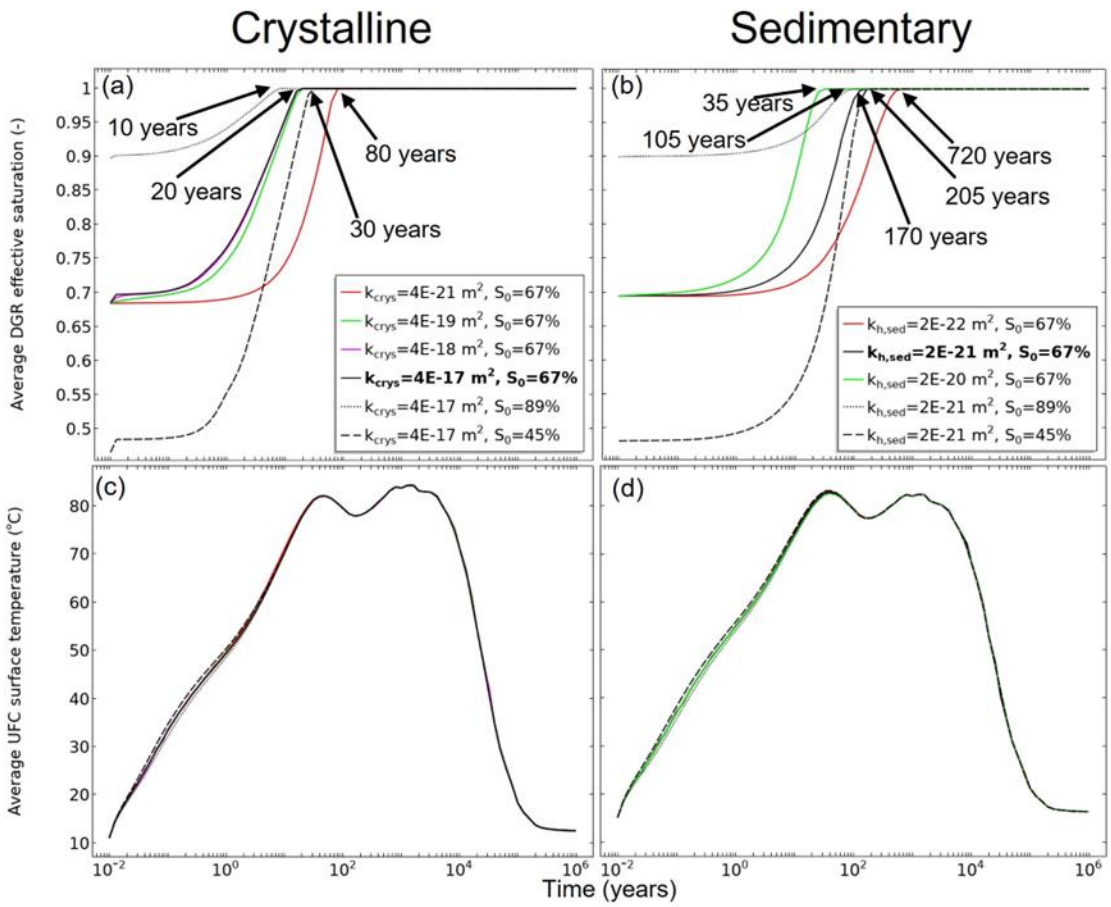

Figure 3.24: (a, b) average DGR effective saturation and (c, d) average UFC surface temperature from varying the initial saturation, isotropic rock permeabilities (in the crystalline model in frames a and c), and horizontal rock permeabilities (in the sedimentary model in frames b and d). The base case scenarios are bolded (Rashwan et al. 2022).

Figures 3.25a and 3.25b show relative bisulfide flux over time in the crystalline and sedimentary domains under different modelling conditions (C, HC, TC, and THC). Figures 3.25c and 3.25d show simulated DGR conditions. The results in these Figures of the 3-D DGR models show the same trend in bisulfide flux and DGR conditions observed in Figures 3.19e, 3.20e, and 3.22 for the 2-D models.

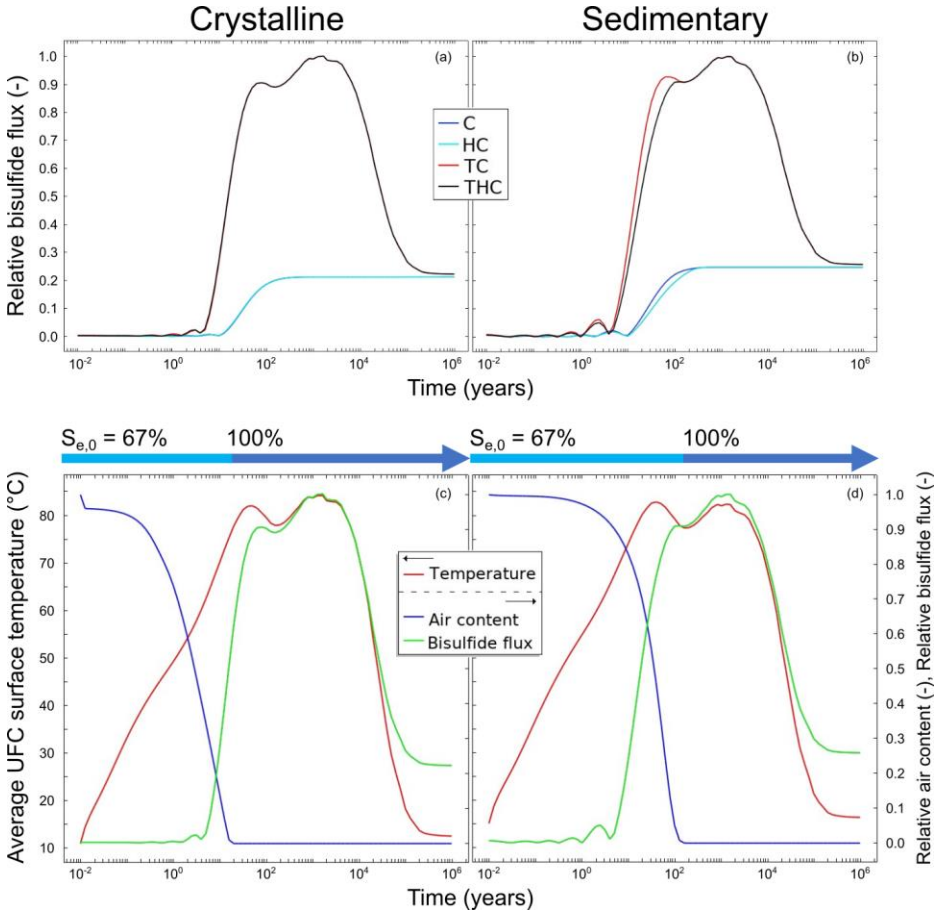

Figure 3.25: Relative bisulfide fluxes estimated at UFC surface (upper end-caps) in (a) crystalline and (b) sedimentary DGR models under different modelling conditions. C model simulates bisulfide diffusion under fully saturated-isothermal conditions, HC model simulates bisulfide diffusion under variably saturated-isothermal conditions, TC model simulates bisulfide diffusion under fully saturated-non-isothermal conditions, THC model simulates bisulfide diffusion under variably saturated-non-isothermal conditions. (c and d) Prediction hydrogeological conditions in the crystalline and sedimentary domains. Note that the average bentonite air content and bisulfide flux values are normalized (Rashwan et al. 2022).

Figure 3.26 shows that bisulfide corrosion depths are identical in the models as saturation has negligible impact (<1%). Heating only increases bisulfide flux by less than 20%, which occurs during the initial life span of the DGR. The highest bisulfide corrosion is below the NWMO HS corrosion depth tolerance, 0.8 mm, reported in Hall et al. (2021).

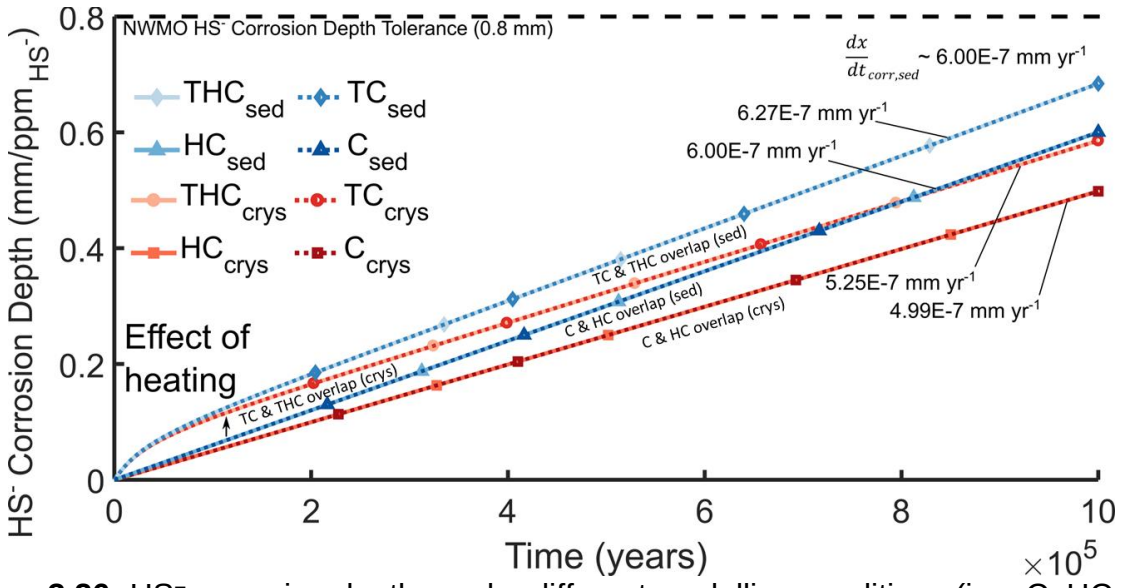

Figure 3.26: HS^- corrosion depths under different modelling conditions (i.e., C, HC, TC, and THC) in the crystalline or sedimentary domains. The slopes are calculated from 200,000 to 1,000,000 years in each model using linear regression analyses. Note that the horizontal axis represents a linear timescale (Rashwan et al. 2022). The HS^- corrosion depth tolerance is reported in Hall et a. (2021).

3.6 Theoretical and Numerical Bisulfide Flux

Figure 3.24 compares bisulfide fluxes from a simplified 1-D analytical and 1-D, 2-D, and 3-D numerical C models, set in the crystalline DGR. The 1-D models consider the transient diffusion from the centre of the UFC end cap to the rock-bentonite interface. As seen in Figure 3.27, bisulfide fluxes from the 1-D analytical and 1-D numerical models are identical. In addition, bisulfide fluxes from the 2-D and 3-D numerical C models match well with the 1-D analytical flux in the early times (i.e., during the first 30 years). The early matching reveals that the onset of bisulfide diffusion occurs through 1-D transport path (i.e., the shortest distance from the rock-bentonite interface to the UFC end cap/caps). The difference in bisulfide fluxes after 30 years indicates multidimensional transport, which was not considered in the 1-D analytical model. Therefore, the similarity in bisulfide evolution in the analytical and numerical models further confirms that the numerical

approximation used in the DGR models is appropriate and the model is properly developed.

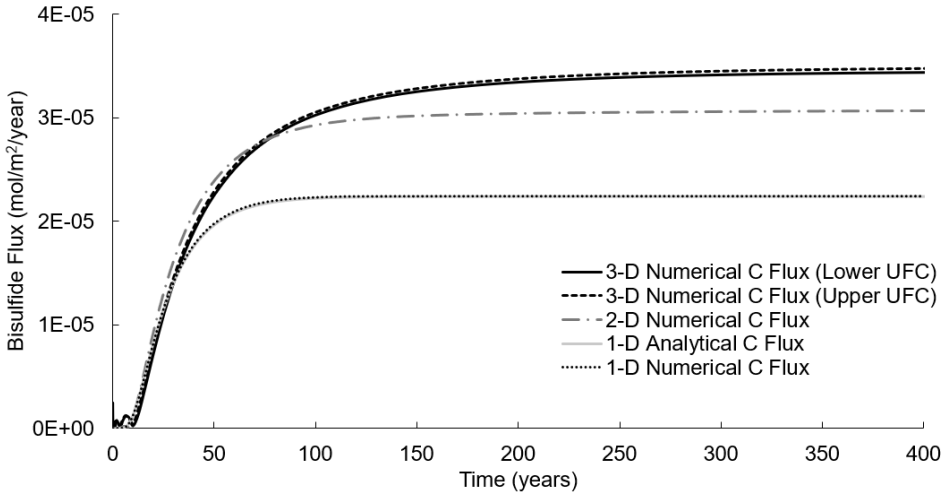

Figure 3.27: Comparison of bisulfide fluxes from an analytical model and numerical C models of the crystalline DGR

3.7 Conclusions

This chapter outlines the long-term conditions anticipated in the DGR, conceptual models of the processes affecting MIC, and results of the newly coupled 2-D and 3-D Thermal-Hydraulic-Chemical (Diffusion) model (referred to as the "THC model"). The THC model can simulate bisulfide diffusion through the bentonite in the DGR under variably saturated and non-isothermal conditions. Moreover, the specific implementation and verification procedures have been documented. The parameters used in the model are obtained from NWMO case studies (Sykes et al. 2011, Gobien et al. 2016, 2018, Guo 2016, 2018, Dixon et al. 2018, Dixon 2019), and other sources (Baumgartner 2006, SKB 2010b). This model is designed to be flexible and accommodate site-specific information as it becomes available; however, many of the key trends elucidate characteristic evolution expected in the DGR and its influence on MIC.

A range of verification and validation procedures were conducted to develop confidence in the THC model. For example, a mesh convergence study was performed to ensure the model was properly discretized in space. In addition, a sensitivity study on various boundary conditions was performed to ensure boundary assumptions were not leading to spurious, unrealistic results. A domain depth of 10,000 m was used as it provided the expected temperature profile without increasing computational time. In addition, constant pressure head conditions were used at the model flow boundaries to simulate realistic flow conditions and avoid anomalous low-pressure zones that developed at late-times with no-flow boundaries. Around the UFC, a boundary heat source was chosen to model the heat generated by the used nuclear fuel, as a domain heat source overpredicted the UFC temperature due to geometry and modelling inputs. The host rock was assumed to be fully saturated; the HCB was initially at 67% saturation and a constant, 1 ppm bisulfide concentration boundary condition was assumed at the rock-bentonite interface. The 2-D THC model was compared with previous models developed by Briggs and Krol (2018) and the 3-D THC model was developed and compared with the 2-D THC model and two 1-D C models (analytical and numerical) for verification purposes. Lastly, the robustness of the numerical approximation used in the model was confirmed through good agreement between numerical and theoretical solutions.

The mass transport and thermal processes were validated by Briggs and Krol (2018), while the hydraulic process (Richard's equation) verification is presented in this chapter. As no 2-D experiments have been completed, the saturation process was verified by

developing a 1-D saturation model which reproduced a quasi-1-D experiment of water infiltration into clay. Upon verification, the THC model was run for both DGR domains and it predicted 20 years and 160 years for full saturation in the crystalline and sedimentary host rock models, respectively. These saturation times are comparable to the results from other HCB saturation studies assuming similar host rock conditions, i.e., 10's-100's of years (e.g., DECOVALEX III project results). Bentonite saturation is slower in the sedimentary rock compared to the crystalline rock due to lower rock permeabilities. In addition, the saturation front is not as sharp in the sedimentary domain due to the relative magnitude of permeability of the rock and bentonite. Typically, increasing rock permeability would decrease bentonite saturation time. However, the saturation times are insensitive to rock permeability when the rock permeability is higher than the bentonite permeability, making the bentonite the governing transport layer (as seen in the crystalline domain). Capturing this difference in saturation evolution is important to delineate the oxic and anoxic corrosion. However, this saturation evolution may be affected by many variables in the host rock and bentonite, e.g., permeability, salinity, and excavation induced fractures. The estimation of saturation time is also controlled by the van Genuchten parameters which govern initial saturation condition and soil water characteristic curve of the bentonite.

This chapter also provides a model comparison between the THC model and previous models developed by Briggs and Krol (2018)). This analysis reveals that the MIC is driven by changes in saturation and UFC temperature that impact bisulfide diffusion rates, which only occurs during the initial life span of the DGR (i.e., before 200,000 - 400,000 years).

After this time, bisulfide diffusion occurs in a saturated system under isothermal conditions. In addition, the 3-D THC model, set in the crystalline DGR, results in a total MIC depth of 0.671 mm, compared to 0.517 mm using the 2-D THC model. This difference in MIC depths is due to the 3-D geometry which includes bisulfide flux from an additional dimension and shows the importance of using 3-D simulation to estimate corrosion depth.

As bisulfide transport is diffusion dominated, and no gaseous transport is assumed, bisulfide transport starts as the EBS pore space becomes saturated. The maximum bisulfide flux occurs at the hemi-spherical end caps of the UFC as water contacts the caps first due to UFC and EBS geometry. The total maximum MIC depths are 0.645 mm and 0.517 mm in million years in the sedimentary and crystalline DGR, respectively. However, this MIC estimate is conservative due to several assumptions, such as:

- no sorption, geochemical reactions or microbial processes are assumed to be occurring within the bentonite; including these reactions would decrease the amount of bisulfide that would be transported to the UFC
- bentonite is assumed to swell instantly, and bentonite permeability is assumed to be constant throughout the simulation; including bentonite swelling may increase bisulfide transport in the early times due to higher bentonite permeability; this would have a bigger impact in the crystalline domain as the bentonite permeability has a more controlling impact on diffusion
- No vapour transport or evaporation or condensation is modelled in the system; including these processes would lead to cooling of the system resulting in lower bisulfide transport

In summary, the THC model has been robustly developed to aid in the performance assessment of the Canada's DGR. The developed THC model is designed to be flexible to accommodate additional processes and site-specific information as it becomes available. Future work will include sorption and geochemical reactions, vapour transport, bentonite swelling, corrosion equations, microbial reactions, and biochemical modelling.

Chapter 4 Assessment of Hydrogen Gas Formation Using Numerical Modelling Under Deep Geological Repository Environments

4.1 Introduction

The Canadian Nuclear Waste Management Organization (NWMO) is responsible for the design and implementation of Canada's high level nuclear waste deep geological repository (DGR). The NWMO has proposed a DGR design, which consists of copper coated used fuel containers (UFCs) being placed within a highly compacted bentonite (HCB) buffer surrounded by natural host rock (either crystalline or sedimentary) (Figure 4.1a). Hydrogen (H_2) may be generated in Canada's high level nuclear waste DGR through various pathways. The primary scenario of H_2 generation in the rock is via radiolysis (e.g., radiolysis of water), which will occur following the slow radioactive decay of uranium within the host rock itself, as this will produce reducing (i.e. hydrogen-dominated) conditions at depth in the "far-field" (Sherwood Lollar 2011).

$$H_2O + \alpha\beta\gamma \rightarrow OH^{\cdot}_{(aq)}, H^{+}_{(aq)}, e^{-}, H^{\cdot}_{(aq)}, H_2O_{2(aq)}, H_{2(g)}, HO^{\cdot}_{2(aq)} \quad (4.1)$$

It is worth mentioning that the concentration of radioactive elements varies in different rocks (Jędrzejek et al. 2022). The H_2 may also be produced in the DGR due to steel corrosion, used for repository construction:

$$3Fe_{(aq)} + 4H_2O \rightarrow Fe_3O_{4(s)} + 4H_{2(g)} \quad (4.2)$$

Among different plausible H_2 production scenarios that may affect the UFCs and bentonite (i.e., within the "near-field"), microbiologically influenced corrosion (MIC) of the UFC copper coating is most likely. However, MIC will depend on the availability of HS^- at

the container surface, which will depend on many factors, including: (*i*) the availability of a sulfate (SO_4^{2-}) inventory, (*ii*) groundwater chemistry (e.g., HS^- production in acidic or alkaline media), and (*iii*) microbial growth conditions (e.g., availability of organic compounds and H_2, which may be available from radiolysis of water (Eq. 4.1 or repository steel corrosion (Eq. 4.2). In the far-field, sulfate-reducing bacteria (SRB) could use H_2 (Eq. 4.3 or organic compounds (e.g., lactate) (Eq. 4.4 as electron donors to reduce sulfate and produce HS^- in the host rock (Abrahamsen-Mills and Small 2019):

$$4H_{2(g)} + SO_{4\,(aq)}^{2-} + H^+_{(aq)} \rightarrow HS^-_{(aq)} + 4H_2O \quad (4.3)$$

$$2(CH_2O)_{(aq)} + SO_{4\,(aq)}^{2-} + 2H^+_{(aq)} \rightarrow 2HCO_{3(aq)} + HS^-_{(aq)} + 3H^+_{(aq)} \quad (4.4)$$

The sulfate source may be present in the groundwater due to mineral dissolution (e.g., celestite) in the host rock (Eq. 4.5) or gypsum dissolution in the bentonite (Eq. 4.6):

$$SrSO_{4\,(s)}^{2-} \rightarrow Sr^{2+}_{(aq)} + SO_{4\,(aq)}^{2-} \quad (4.5)$$

$$CaSO_{4(s)} \rightarrow Ca^{2+}_{(aq)} + SO_{4\,(aq)}^{2-} \quad (4.6)$$

However, H_2 consumption by SRB is likely to be competitive with methanogenesis, should methanogens also be present in the far-field. These methanogens will consume H_2 through methane formation (CH_4) (Behazin et al. 2021):

$$CO_{2(g)} + 2H_{2(g)} \rightarrow CH_{4(g)} + 2H_2O \quad (4.7)$$

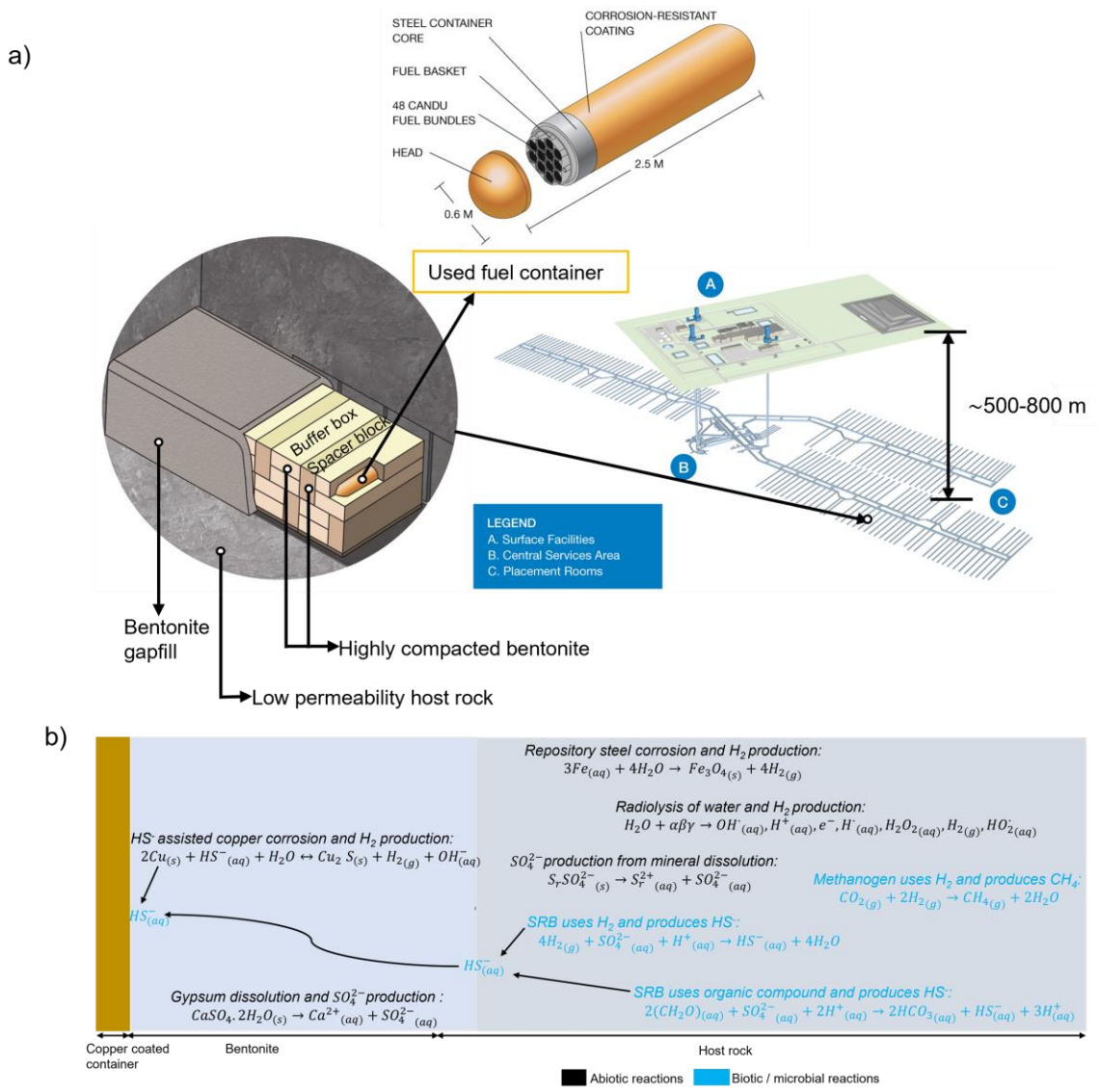

Figure 4.1: a) Proposed multiple barrier system in Canadian DGR (adapted from Hall et al. 2021) and b) Conceptual model of key processes relevant to H_2 production and consumption in Canada's proposed DGR.

The produced HS^- in the host rock (Eqs. 4.3-4.4) could transport through the HCB to the UFC surface and corrode the copper coating in acidic (Eq. 4.8) or alkaline (Eq. 4.9) media (Cloet et al. 2017, Hall et al. 2021):

$$2Cu_{(s)} + HS^-_{(aq)} + H^+ \leftrightarrow Cu_2S_{(s)} + H_{2(g)} \quad (4.8)$$

$$2Cu_{(s)}+HS^-_{(aq)}+H_2O\leftrightarrow Cu_2S_{(s)}+H_{2(g)}+OH^-_{(aq)} \quad (4.9)$$

As seen in Eqs. 4.8-4.9, H_2 is a by-product of the MIC reaction. In laboratory test cells, H_2 production from reaction between copper and hydrogen sulfide (H_2S, another form of HS^-) is shown to be slow ($\approx 10^{-6}$ moles after 4 years) and generated in the aqueous phase (Senior et al. 2020). However, H_2 production from MIC may be influenced by many different processes throughout the DGR design life (1 million years). A conceptual model of the key processes relevant to H_2 production and consumption is presented in Figure 4.1b.

The produced H_2 will be dissolved in the water saturated pore space due to the confining pressures at the DGR level (i.e., 500-800 m below surface) increasing its solubility limit (Muhammed et al. 2022). Subsequently if the produced H_2 accumulates and surpasses the H_2 solubility limit, it may also partition from the aqueous to gaseous phase over the DGR design-life (i.e., one million years).

Aqueous H_2 may become trapped in the DGR's HCB or transported through the DGR to the surrounding host rock (King 2012), which will be governed by rock and clay diffusive properties or fractures (e.g., which would act as preferential pathways). Gaseous H_2 may also create preferential pathways in the HCB that may compromise UFC protection (King 2012). Therefore, H_2 poses numerous risks in a DGR, and it is important to understand its dynamics over the long DGR design-life. Many researchers have studied DGR gas generation to evaluate effects of gases on the DGR safety (Moreno and Neretnieks 2013, Calder 2014, Suckling et al. 2015, Diomidis et al. 2016, Scully et al. 2016, Silva et al.

2019a, 2019b, Vikman et al. 2019, NWMO 2021). While these studies provide valuable insight into gas generation processes, long-term H_2 dynamics due to MIC is not well-quantified.

This study presents a H_2 model (referred to as the THC-H_2 model), which is based on a previously published Thermal-Hydraulic-Chemical (THC) DGR transport model to estimate corrosion rates in DGRs (Asad et al. 2022, Rashwan et al. 2022). The objective of this study is to understand if H_2 could accumulate in the DGR and surpass the H_2 solubility limit, which would indicate H_2 gas (bubble) formation. This THC-H_2 model uses generally conservative assumptions around HS^- and H_2 transport and flux conversion (i.e., converted HS^- flux represented the rate of aqueous H_2 accumulation) to identify key parameters relevant to H_2 dynamics and draw implications for long-term impact of H_2 on the engineered barrier system in a DGR.

4.2 Model Approach and Methodology

4.2.1 Model Development

The hydrogen model developed in this study (THC-H_2) is based on the THC model that simulated MIC due to HS^- transport in a DGR under varying thermal and hydraulic conditions (Briggs and Krol 2018, Asad et al. 2022, Rashwan et al. 2022). The DGR was approximated as a 2-D and 3-D system in crystalline rock and all parameters were obtained from NWMO case studies and other reports. The THC model results showed that the UFC heating accelerated MIC through accelerating HS^- transport rate, but the saturation process delayed the onset of MIC. However, both processes did not strongly influence projected MIC over the design life of 1 million years (see Rashwan et al. (2022);

Asad et al. (2022) for additional details). The THC-H_2 model extends the THC model and examines two distinct H_2 dynamics: i). THC-H_2: H_2 is generated at the UFC surface following Eq. 4.8 and ii). THC-H_2 feedback: H_2 is generated at the UFC surface but once it diffuses to the rock-bentonite interface (RBI), it is converted to HS^- following Eq. 4.3. Both models were developed using conservative assumptions presented in Table 4.1.

Table 4. 1: Conservative assumptions made in modelling H_2 dynamics

Model	**Modelled reaction and location**	**Assumptions**
THC-H_2	At UFC: $2Cu_{(s)}+HS^-_{(aq)}+H^+_{(aq)} \leftrightarrow Cu_2S_{(s)}+H_{2(g)}$	Equilibrium condition is constant across space and time. pH was assumed to be 8-11. At the UFC, HS^- flux is converted to H_2 flux. Cu and Cu_2S are immobile. H_2 is assumed to be a dissolved species.
	At RBI: Constant HS^- concentration boundary	
THC-H_2 feedback	At UFC: $2Cu_{(s)}+HS^-_{(aq)}+H^+_{(aq)} \leftrightarrow Cu_2S_{(s)}+H_{2(g)}$	Same as THC-H_2
	At RBI: $4H_{2(g)} + SO^{2-}_{4\,(aq)} + H^+_{(aq)} \leftrightarrow HS^-_{(aq)} + 4H_2O$	Equilibrium condition is constant across space and time. H_2 is assumed to be a dissolved species. At RBI, H_2 flux is converted to HS^- flux based on shown equation. SO_4 is assumed to be a non-limiting species.

An overview of the model domain, geochemical boundaries, and initial conditions for both the THC-H_2 and THC-H_2 feedback models are shown in Figures 4.2 and 4.3, respectively. For all other processes (i.e., thermal, hydraulic, chemical transport), the boundary and

initial conditions are detailed in Asad et al. (2022) (and Supplementary Materials, Figure A.S.1).

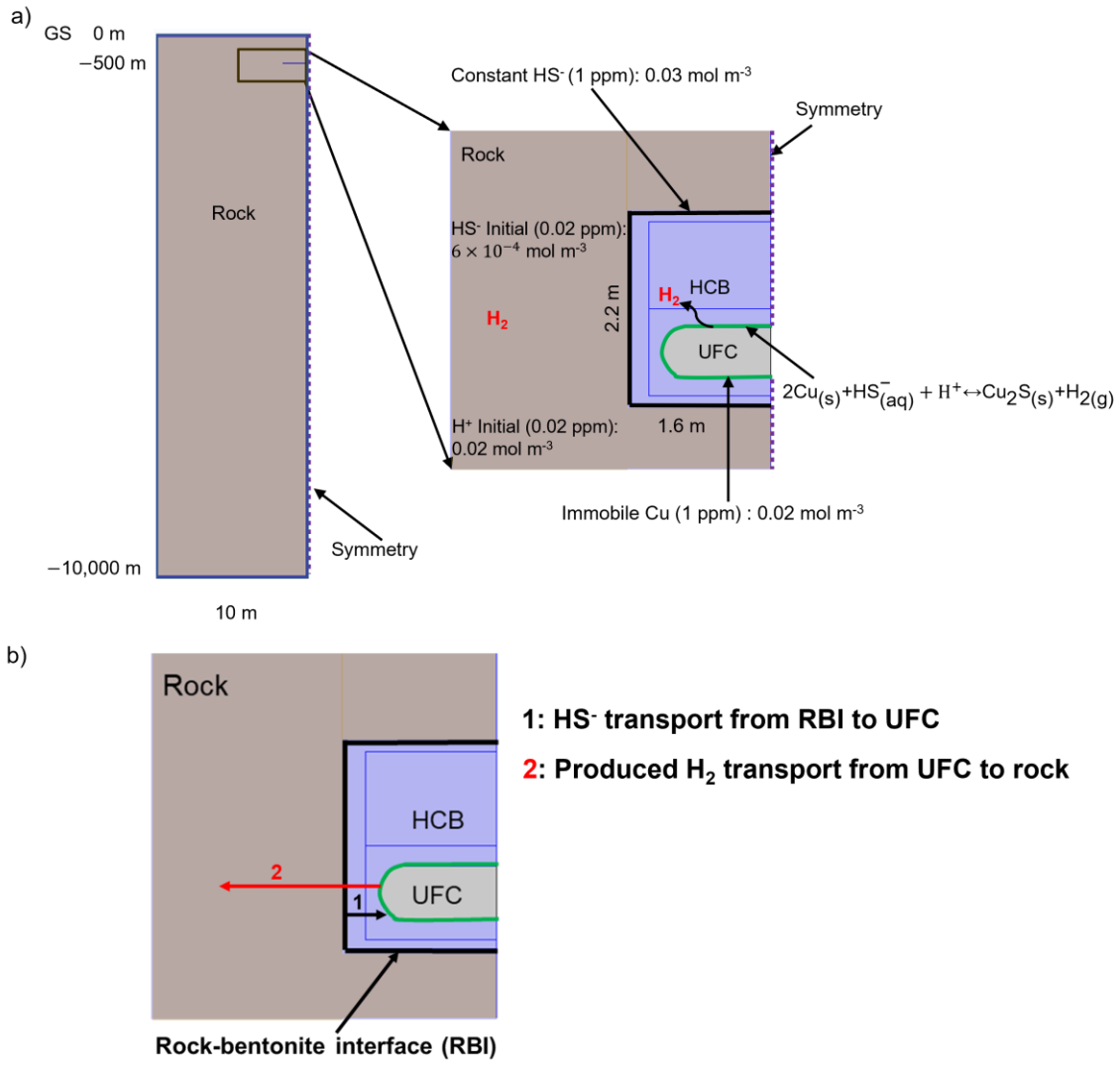

Figure 4.2: a) Key initial and boundary conditions for HS^- and H_2 in the THC-H_2 model and b) Transport directions of HS^- and H_2

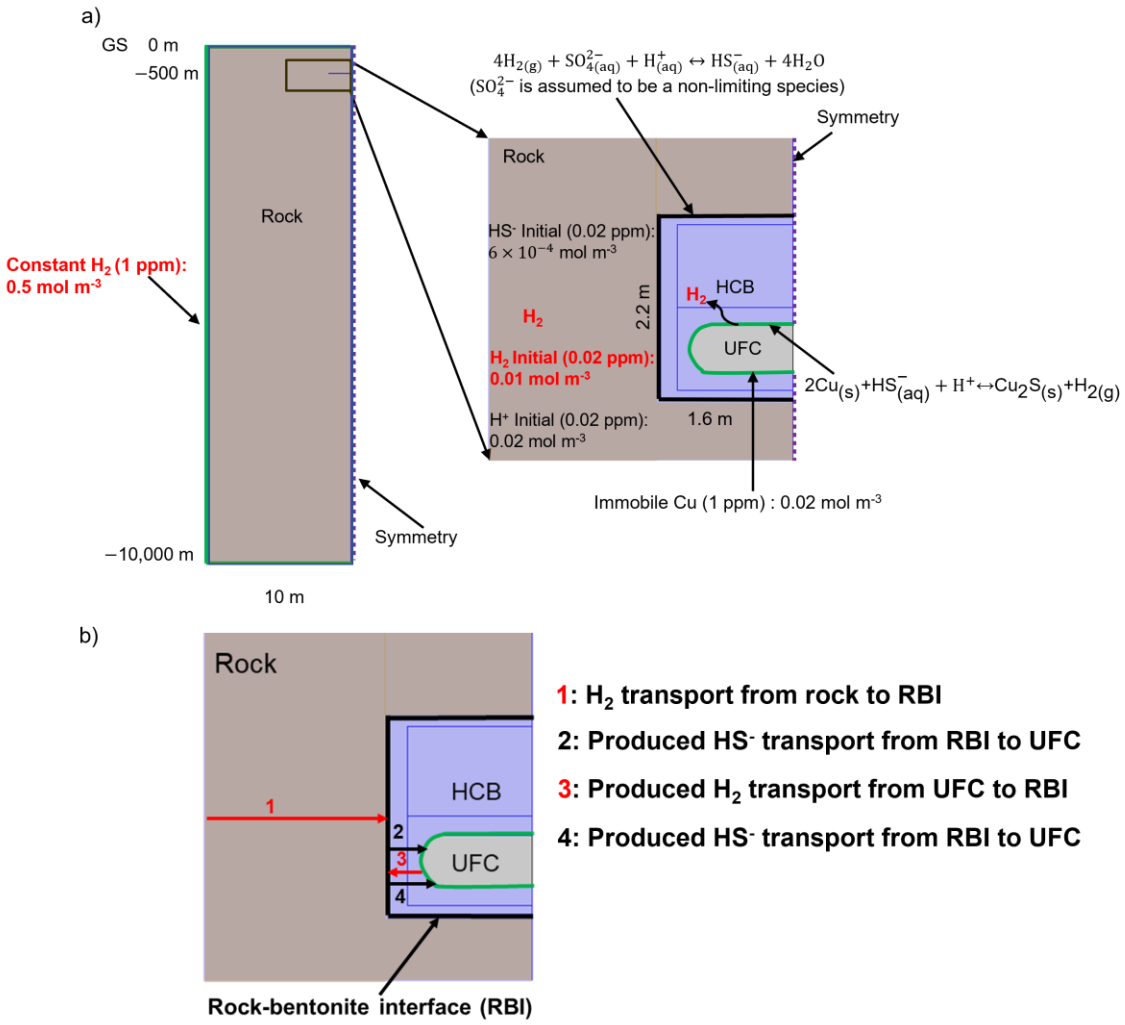

Figure 4.3: Key initial and boundary conditions for HS^- and H_2 in the THC-H_2 feedback model and b) Transport directions of HS^- and H_2

4.2.1.1 THC-H_2 Model Development

The 2-D THC-H_2 model described MIC and H_2 production using Eq. 4.8 at the UFC surface. The species included in the model are copper (Cu), HS^- (assumed pH: 8-11), hydrogen ion (H^+), copper sulfide (Cu_2S), and H_2. The Eq. 4.8 reaction was implemented as a surface equilibrium reaction (SER) (see supplementary materials, Section A.S.2):

$$E = \frac{[H_2]}{[HS^-]\,[H^+]} \tag{4.10}$$

where E is the equilibrium constant. The HS^- concentration at the RBI was assumed to be 1 ppm (0.03 mol m^{-3}) and was implemented as a constant concentration boundary condition (Rashwan et al. 2022). These boundary conditions assumed that HS^- transported from the host rock to the UFC surface and produced H_2, which then transported from the UFC back to the host rock. All transport was assumed to be diffusion-driven (i.e., no advection). The diffusivity for each species was defined independently. The effective diffusivities for HS^- and H_2 in bentonite and rock were defined similarly as a function of: (*i*) species-specific water diffusion coefficients, (*ii*) saturation, (*iii*) temperature, (*iv*) diffusion accessible porosity, and (*v*) tortuosity following Rashwan et al. (2022). Since rock has a much lower porosity than bentonite, the effective HS^- and H_2 rock diffusivities were significantly lower than the effective HS^- and H_2 bentonite diffusivities (Archie 1950) (see Table 4.2).

4.2.1.2 THC-H_2 Feedback Model Development

The THC-H_2 feedback model incorporated H_2 generation from MIC using the same SER approach described above, but also modelled production of HS^- through consumption of moles H_2 via SRB reaction using Eq. 4.3 at the RBI. The SO_4^{2-} was conservatively assumed to be a non-limiting species. Altogether, this H_2 generation approach described a feedback process: i.e., HS^- produced at the RBI from far-field H_2 sources (Eq. 4.3) was transported to the UFC surface to produce H_2 (Eq. 4.8), and then transported from the UFC back to the RBI to produce HS^- (Eq. 4.3). Unlike the THC-H_2 model, the far-field rock boundary was modelled with a constant H_2 boundary condition of 0.5 mol m^{-3} (i.e., 1 ppm H_2) (Sherwood Lollar et al. 1993a, 1993b, Szakálos and Seetharaman 2012) in the THC-H_2 feedback model and a SER boundary condition was implemented at the RBI to convert

HS^- from the H_2 via Eq. 4.3. The constant H_2 boundary condition represented a constant source of H_2 flux through the rock, which was used to produce HS^- flux at the RBI via Eq. 4.3. Although the constant H_2 boundary condition is conservative, it represents H_2 sources that could be due to different processes throughout the rock (see Figure 4.1). The initial background H_2 concentration throughout the DGR was assumed to be 0.01 mol m^{-3} (i.e., 0.02 ppm H_2) (Szakálos and Seetharaman 2012). It is worth noting that previous works (Sherwood Lollar et al. 1993a, 1993b, Sherwood Lollar 2011) reported ≈4 ppb and ≈3 ppm H_2 as the expected H_2 concentrations in Canadian shield and Fennoscandian shield, respectively. As such, the initial H_2 concentration used in this simulation represents a conservative scenario.

4.2.2 Parameters

The key model parameters are shown in Table 4.2. These parameters represent the properties of HCB and rock, as well as the species Cu, HS^- and H_2 in the UFC, HCB, and rock.

Table 4.2: Key parameters for H_2 dynamics

Parameter	Domain	Value
General parameters		
Water, Air[1]	All	Thermophysical properties from COMSOL 5.6 Material Library
Key parameters for H_2 dynamics		
Porosity[2,3,4] (Ø)	HCB	0.382
	Rock	0.003
Density[5,6]	HCB	1700 kg m^{-3}
	Rock	2700 kg m^{-3}
Initial HS^- concentration[8,9] ($[HS^-_{(aq)i}]$)	All	6×10^{-4} mol m^{-3} (0.02 ppm)
HS^- concentration[2,3] ($[HS^-_{(aq)}]$)	RBI	0.03 mol m^{-3} (1 ppm) (THC-H_2)
		Produced HS^- from H_2 consumption (Eq.3) (THC- H_2 feedback)
Initial H^+ concentration[4]	All	0.02 mol m^{-3} (0.02 ppm)
Immobile Cu concentration [Cu]	UFC	0.02 mol m^{-3} (1 ppm)
Initial H_2 concentration[4,7] ($[H_{2(aq)i}]$)	All	0.01 mol m^{-3} (0.02 ppm)
H_2 concentration[4,7] ($[H_{2(aq)}]$)	Rock at far-field	0.5 mol m^{-3} (1 ppm) (THC-H_2 feedback)
HS^- diffusion coefficient in water[10](D_{0HS^-})	All	1×10^{-9} m^2/s
Effective HS^- diffusion coefficient[2,3] (D_e)	HCB	1×10^{-11} m^2/s at full saturation, 20 ˚C
	Rock	1.64×10^{-13} m^2/s at full saturation, 20 ˚C
H_2 diffusion coefficient in water[11] (D_{0H_2})	All	5.13×10^{-9} m^2/s
Effective H_2 diffusion coefficient[12] (D_{eH_2})	HCB	7.5×10^{-10} m^2/s at full saturation, 20 ˚C
	Rock	8.4×10^{-13} m^2/s at full saturation, 20 ˚C

[1](COMSOL 2021b) [2]Rashwan et al. (2022) [3]Asad et al. (2022) [4]Szakálos and Seetharaman (2012) [5](Gobien et al. 2016) [6](Guo 2016, 2018) [7]Sherwood Lollar et al. 1993a,b [8]Gascoyne(1997) [9]Kremer(2017) [10] (SKB 2010b) [11](Hemme and Van Berk 2018) [12]Archie (1950)

4.3 Model Results

4.3.1 Model Confirmation

4.3.1.1 HS^- Concentration Comparison

The THC-H_2 model was verified against the previously published THC model (Asad et al. 2022), where comparisons between modelled HS^- concentration distributions are shown in Figure 4.4. The THC-H_2 results in Figure 4.4a mirror the HS^- profiles from the benchmark 2-D THC model, which used a constant 0 ppm HS^- boundary condition at the UFC surface instead of the reaction in Eq. 4.8. Therefore, the agreement between Figures 4.4a and b confirms that the surface reaction was implemented correctly in the THC-H_2 model, as it effectively modelled a constant zero HS^- concentration boundary condition at the UFC. In other words, all HS^- at the UFC surface was assumed to react immediately

to produce H_2 (see supplementary materials, Section A.S.3 for species conversion rate verification).

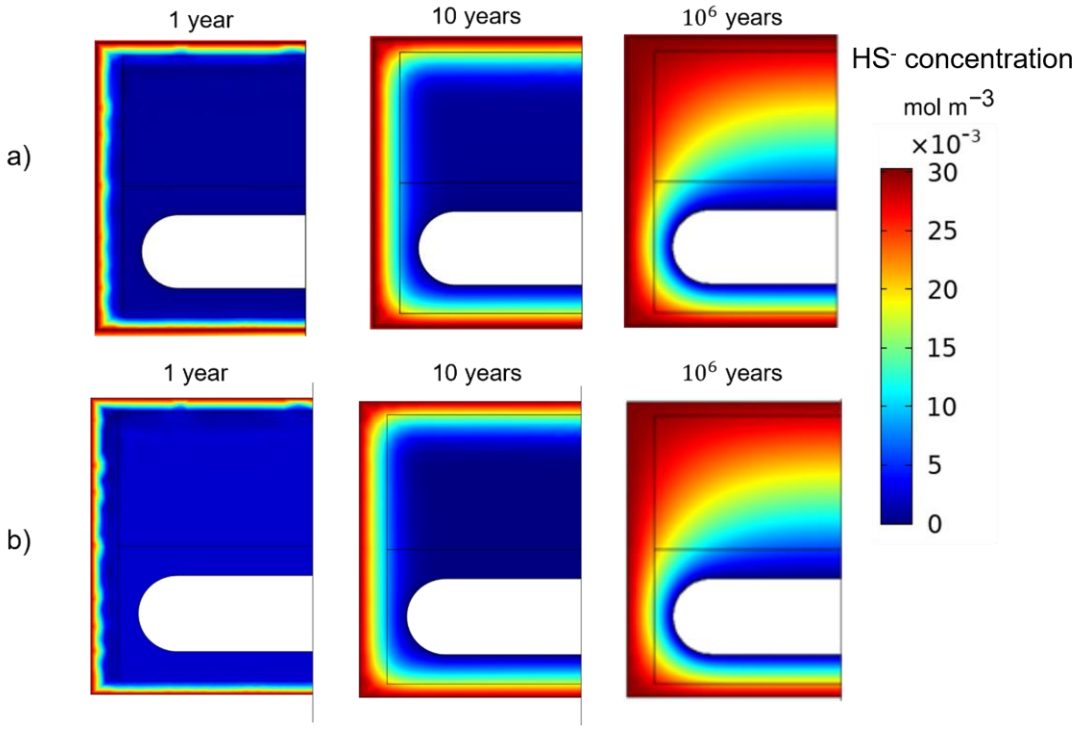

Figure 4.4: HS^- concentration over time in the a) THC-H_2 model and b) THC model

4.3.2 Sensitivity Study

4.3.2.1 Simulated Cases for Sensitivity Analysis

Ten cases were established (Table 4.3) to examine the effect of HS^- and H_2 initial background concentration, constant HS^- RBI concentration, constant H_2 concentration at the far-field rock boundary, and the effective H_2 rock diffusion coefficient on H_2 dynamics in a DGR. For the THC-H_2 model, the base case scenario was Case 1 (C1). The value of HS^- initial concentration in C1 was chosen based on data from previous studies by Gascoyne (1997) and Kremer (2017). C1 was compared to Cases 2 and 3 (C2, C3) where HS^- initial concentrations of 0.5 ppm and 1 ppm were used, respectively, which were 25 and 50 times greater than the C1 HS^- initial concentration, respectively. The value of HS^-

initial concentration in C3 represented an upper bound of the concentration (over an order of magnitude higher than expected HS^- concentrations in Canadian shield), chosen to observe the sensitivity of HS^- initial concentration on H_2 dynamics. The value of constant HS^- RBI concentration in C1 was chosen following previous studies by Gascoyne (1997) and Kremer (2017) who reported 30-90 ppb as the expected HS^- concentrations in Canadian shield, which are over an order of magnitude lower than 1 ppm. Case 4 (C4) used 2 ppm HS^- concentration at the RBI, i.e., double the HS^- concentration used in C1. This value represented an upper bound of the concentration, chosen to observe the sensitivity of HS^- concentration at the RBI on H_2 dynamics.

For the THC-H_2 feedback model, the base case scenario was Case 6 (C6). The H_2 initial concentration in C6 was chosen based on data found from previous study by Szakálos and Seetharaman (2012). Cases 7 and 8 (C7 and C8) used H_2 initial concentrations of 0.5 ppm and 1 ppm, respectively, which were 25 and 50 times greater than the H_2 initial concentration used in C6, respectively. Like the HS^- sensitivity, the H_2 initial concentration value in C8 represented an upper bound of the H_2 concentration (over an order of magnitude higher than expected H_2 concentration in Canadian shield). The value of constant H_2 concentration at the far-field rock boundary in C6 was chosen following previous studies by Sherwood Lollar (2011) and Sherwood Lollar et al. (1993a, b) who reported ≈4 ppb as the expected H_2 concentrations in Canadian shield, which is over an order of magnitude lower than 1 ppm. Case 9 (C9) used a H_2 concentration of 2 ppm at the far-field rock boundary, i.e., double the HS^- concentration used in C6. This value represented an upper bound of concentration to observe the sensitivity of H_2

concentration at the far-field rock boundary on H_2 dynamics. The effective H_2 diffusivity used in C1 and C6 was estimated based on the procedure described in previous studies by Rashwan et al. (2022) and Archie (1950). Cases 5 and 10 (C5 and C10) used an effective host rock H_2 diffusivity of 8.4×10^{-12} m^2 s^{-1}, which was about 10 times greater than the effective H_2 diffusivity used in C1 and C6. C5 and C10 therefore explored the sensitivities to host rock H_2 diffusivity, which could occur due to fractures resulting in preferential flow paths.

Table 4.3: Sensitivity analysis simulations

Model	Case	HS^- initial background concentration (ppm)	Constant HS^- concentration at the RBI (ppm)	H_2 initial background concentration (ppm)	Constant H_2 concentration at the far-field rock boundary (ppm)	Effective H_2 rock diffusivity (m^2 s^{-1})
THC-H_2	C1[a]	0.02	1	0	0	8.4×10^{-13}
THC-H_2	C2[b]	0.5	1	0	0	8.4×10^{-13}
THC-H_2	C3[b]	1	1	0	0	8.4×10^{-13}
THC-H_2	C4[b]	0.02	2	0	0	8.4×10^{-13}
THC-H_2	C5[b]	0.02	1	0	0	$\mathbf{8.4 \times 10^{-12}}$
Feedback	C6[c]	0.02	Produced HS^- from H_2 consumption (Eq. 3)	0.02	1	8.4×10^{-13}
Feedback	C7[d]	0.02	Produced HS^- from H_2 consumption	0.5	1	8.4×10^{-13}
Feedback	C8[d]	0.02	Produced HS^- from H_2 consumption	1	1	8.4×10^{-13}
Feedback	C9[d]	0.02	Produced HS^- from H_2 consumption	0.02	2	8.4×10^{-13}
Feedback	C10[d]	0.02	Produced HS^- from H_2 consumption	0.02	1	$\mathbf{8.4 \times 10^{-12}}$

[a]THC-H_2 base case, [b]THC-H_2 sensitivity case, [c]THC-H_2 feedback base case, [d]THC-H_2 feedback sensitivity case. Note that the effective H_2 diffusivity in bentonite was kept the same in all cases and bold values represent the varied values for the sensitivity study.

4.3.2.2 Effect of HS^- initial Background Concentration (THC-H_2 model)

The effects of HS^- initial background concentration on maximum H_2 concentration and average species conversion rates (i.e., HS^- and H_2 rates) at the UFC are shown in Figure 4.5.

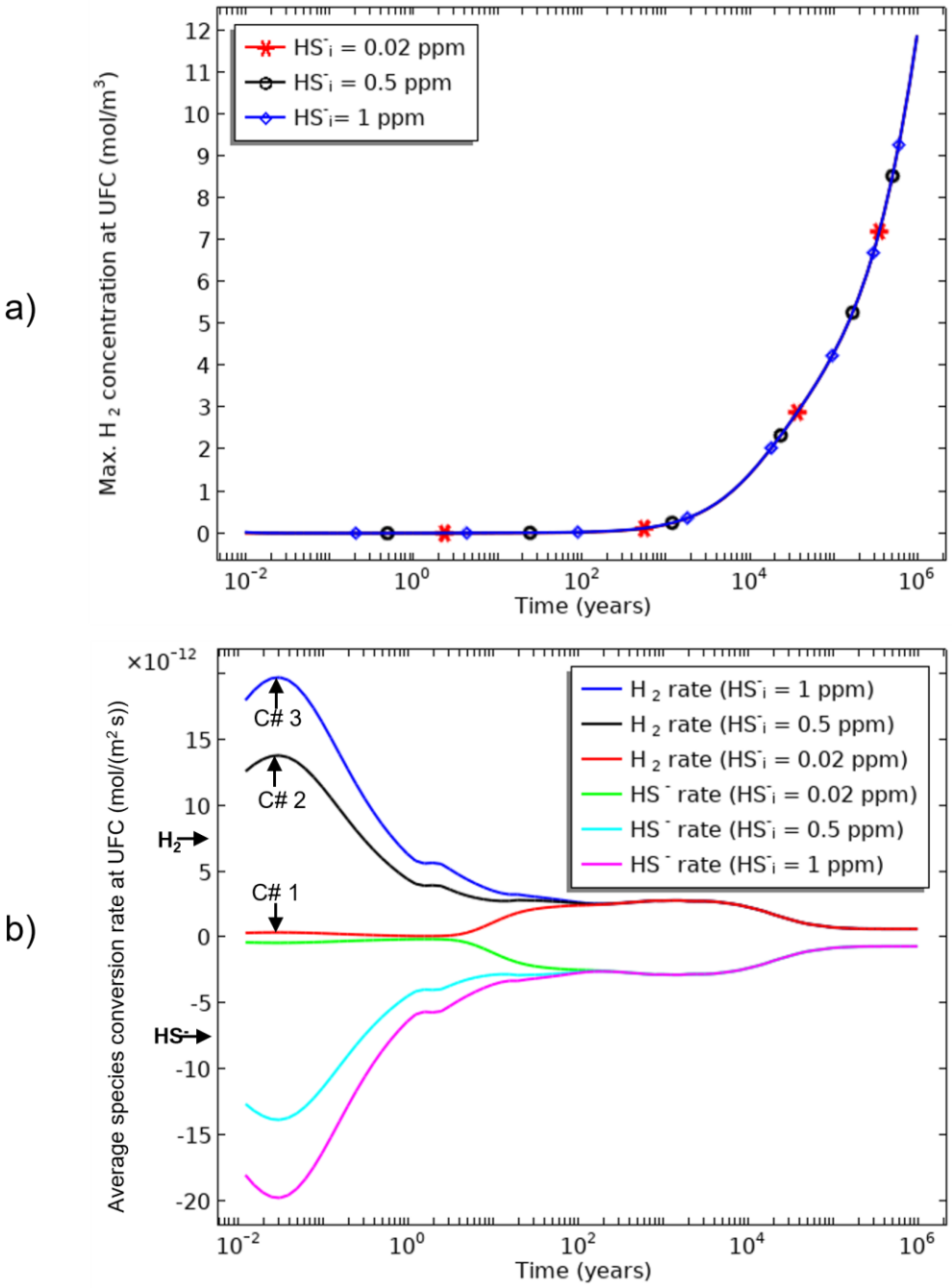

Figure 4.5: Effect of HS^- initial background concentration on a) maximum H_2 concentration at the UFC and b) average species conversion rate at the UFC. Note that the positive and negative species conversion rates indicate species production and consumption, respectively.

Figure 4.5a shows that H_2 concentrations at the UFC were insensitive to changes in HS^- initial concentration (see supplementary materials, Section A.S.5 for little change (0 to

~0.02 mol m^{-3}) in H_2 concentration at the UFC due to changes in HS^- initial concentration). That is, the H_2 rates (Eq. 4.8) increased slightly after year "zero" due to higher HS^- concentrations near the UFC (i.e., due to initial HS^- concentration changes), but decreased over 100 years and converged at common H_2 rates because the initial HS^- used up before 100 years (i.e., converted to H_2 before 100 years). These late-time H_2 rates (i.e., from ~100 – 1,000,000 years) ultimately governed the H_2 concentration trends (Figure 4.5b). In other words, the HS^- initial concentration did not impact long-term H_2 production, as variations of initial HS^- concentrations (C1 to C3) only led to minor, inconsequential initial-effects.

4.3.2.3 Effect of Constant HS^- Concentration at the RBI (THC-H_2 model)

The effects of constant HS^- concentration at the RBI on maximum H_2 concentration and average species conversion rates (i.e., HS^- and H_2 rates) at the UFC are shown in Figure 4.6. Unlike Figure 4.5, Figure 4.6a shows that the H_2 concentration was highly sensitive to constant HS^- concentrations at the RBI, which led to higher conversion rates (Eq. 4.8) after ~4 years that was sustained across the full 1 million years (Figure 4.6b, C4). These rate differences reflect the time-lag, t_{L1}, due to HS^- transport from the RBI to the UFC (see supplementary materials, Section A.S.7 for diffusion time scale analysis). After this time-lag, Figure 4.6 shows H_2 concentrations were controlled by the HS^- transport to the UFC. In other words, variations in the constant HS^- boundary concentration (C1 and C4) varied the HS^- supply to the UFC over the full design life; therefore, an increase in the HS^- boundary concentration increased long-term H_2 production.

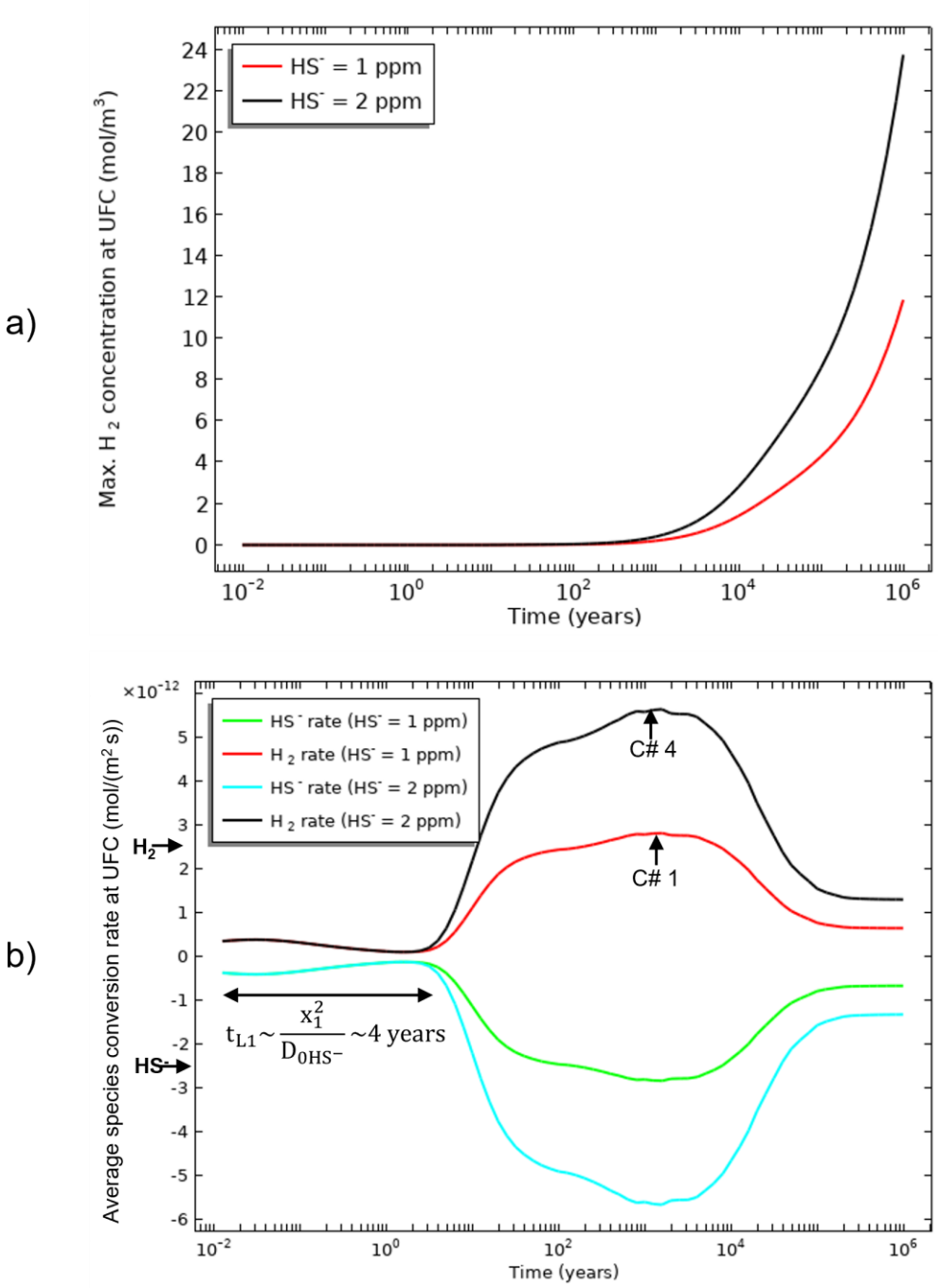

Figure 4.6: Effect of constant HS^- concentration at the RBI on a) maximum H_2 concentration at the UFC and b) average species conversion rate at the UFC. Note that the positive and negative species conversion rates indicate species production and consumption, respectively. Also note that t_{L1} represents time lag due to HS^- transport from the RBI to the UFC and x_1 is the minimum horizontal distance between RBI and UFC cap, 0.343 m.

The maximum aqueous H_2 concentration at the UFC was 23 mol m^{-3} after 1 million years for a constant HS^- concentration of 2 ppm at the RBI and the DGR H_2 solubility limit, 88.9 mol m^{-3} at 20 ˚C at 500 m depth (see supplementary materials, Section S.4) was not surpassed. These results therefore highlight that the long-term H_2 production from MIC may depend on constant supply of HS^- to the UFC. This condition is unlikely to be present in the DGR where HS^- concentration has been found to be quite small, 30-90 ppb (Gascoyne 1997, Kremer 2017)) and resulting from sulfate reduction, which would not lead to a constant concentration condition.

4.3.2.4 Effect of H_2 Initial Background Concentration at the RBI (THC-H_2 Feedback model)

The effects of H_2 initial background concentration on maximum H_2 concentration and average species conversion rates (i.e., HS^- and H_2 rates) at the UFC are shown in Figure 4.7. This figure shows that additional initial H_2 led to higher species conversion rates that were sustained for ~1000 years. There were minimal changes in the H_2 concentrations (Figure 4.7a), and HS^- and H_2 rates at the UFC (Figure 4.7b) until ~4 years. Like Figure 4.6b, this delay partially reflects the time-lag due to HS^- transport from the RBI to the UFC. However, this time-lag also reflects extra HS^- transport to the UFC, which was generated at the RBI due to the transformations of initial H_2 to HS^- (step 4 in Figure 4.3b). That is, H_2 in the bentonite and rock is eventually transported towards the RBI, which maintained a zero H_2 concentration boundary condition due to the H_2 to HS^- conversion assumption (Eq. 3).

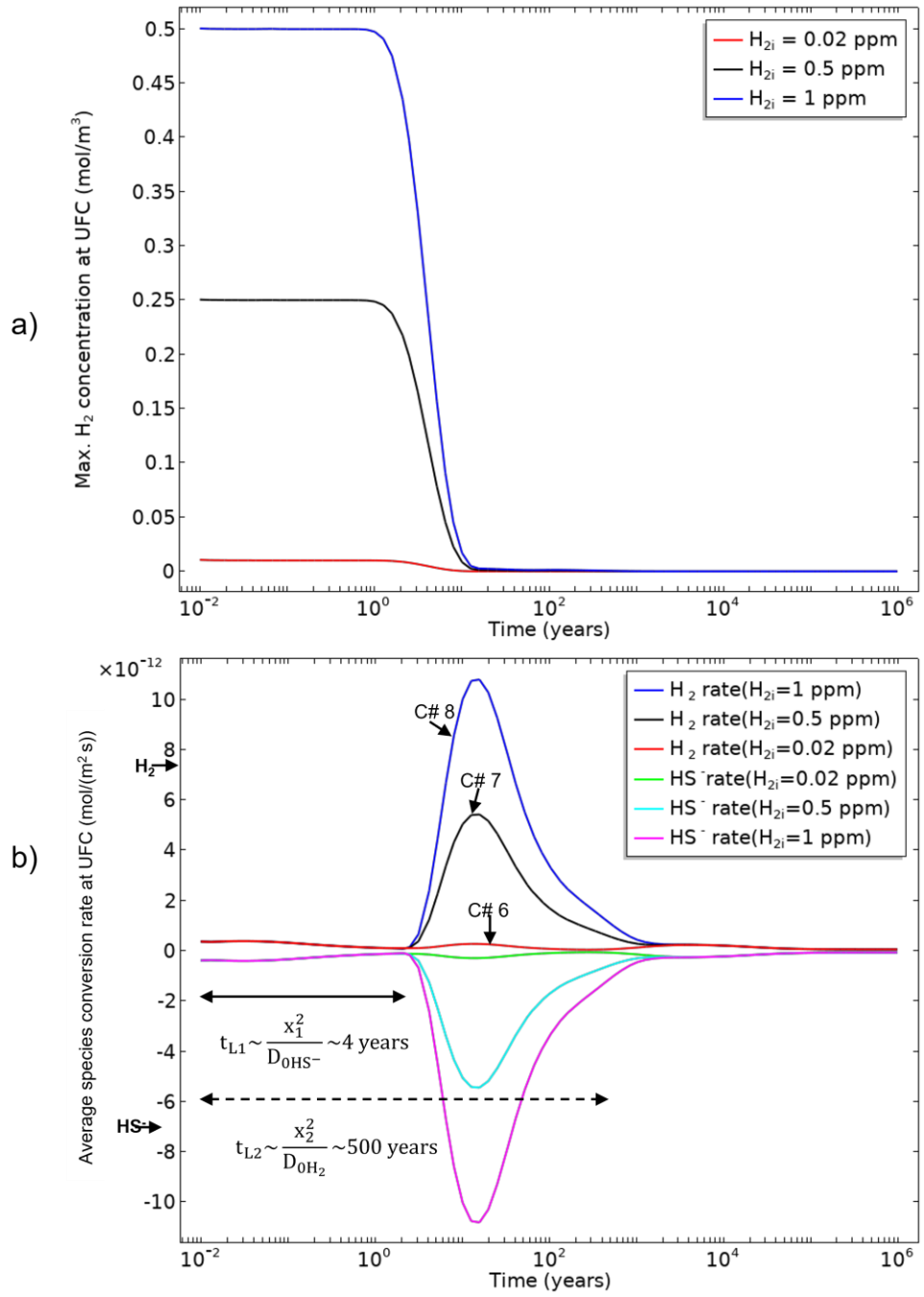

Figure 4.7: Effect of H_2 initial concentration on a) maximum H_2 concentration at the UFC and b) average species conversion rate at the UFC. Note that the positive and negative species conversion rates indicate species production and consumption, respectively. Also note that t_{L1} represents time lag due to HS^- transport from the RBI to the UFC and x_1 is the minimum horizontal distance between RBI and UFC cap, 0.343 m. t_{L2} represents time lag due to H_2 transport from the far-field rock boundary to the RBI where x_2 is the minimum horizontal distance between far-field rock boundary and RBI, 8.4 m.

The H_2 transport through the bentonite (from UFC) to the host rock drove the initial sharp H_2 concentration reductions over the first 10 years, as seen in Figure 4.7a. The H_2 to HS^- conversion led to extra HS^- production and transport to the UFC, which increased H_2 production and concentrations. Ultimately, after the initial H_2 was converted to HS^- (i.e., after ~1000 years), all conversion rates converged to common values (C6-8 rates, Figure 4.7b), which were controlled by the H_2 concentrations at the far-field rock boundary. Note that the influence of the far-field rock boundary was not observed after a time lag of ~500 years as little HS^- was produced (see influence of far-field rock boundary in Figure 4.8). The H_2 concentration at the UFC was 7.8×10^{-5} mol m^{-3} after 1 million years and the DGR H_2 solubility limit, 88.9 mol m^{-3} at 20 ˚C at 500 m depth, was not surpassed.

4.3.2.5 Effect of Constant H_2 Concentration at the Far-field Rock Boundary (THC-H_2 Feedback model)

The sensitivities to the H_2 concentration at the far-field rock boundary on maximum H_2 concentration and average species conversion rates (i.e., HS^- and H_2 rates) at the UFC are shown in Figure 4.8. The H_2 concentration at the UFC increased with increasing H_2 concentration at the far-field rock boundary (Figure 4.8a) as the H_2 conversion rate increased after ~500 years until 1 million years (Figure 4.8b). In other words, the H_2 boundary concentration at the far-field rock moderated the H_2 supply rate to the DGR over its full design life; therefore, the cumulative H_2 concentration near the UFC was slightly sensitive to that boundary condition (Figure 4.8a). Like in Figure 4.7a, the initial decrease in H_2 concentration over the first 10 years in Figure 4.8a reflects the transport of initial H_2 in the bentonite towards the RBI.

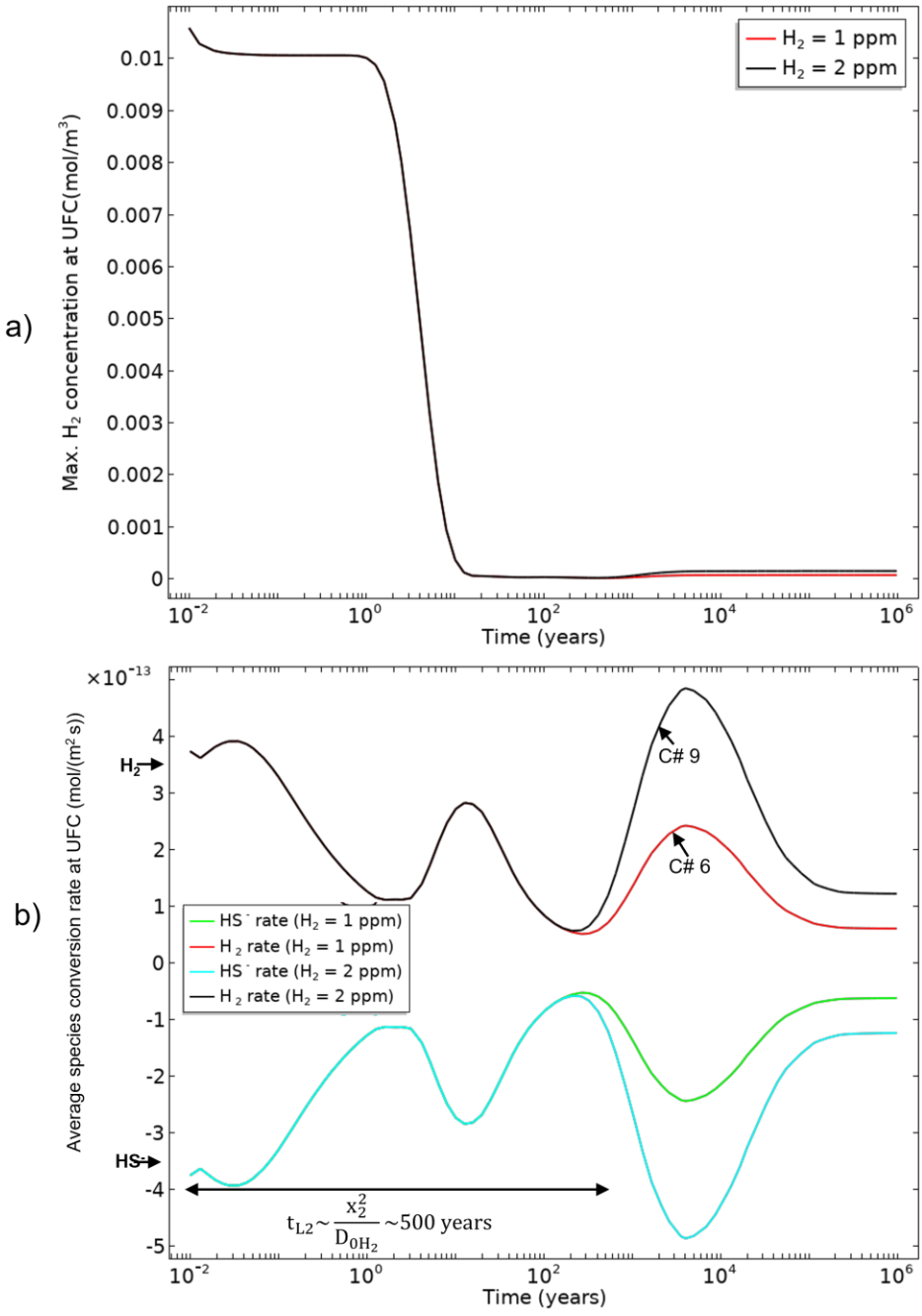

Figure 4.8: Effect of constant H_2 concentration at the far-field rock boundary on a) maximum H_2 concentration at the UFC and b) average species conversion rate at the UFC. Note that the positive and negative species conversion rates indicate species production and consumption, respectively. Also note that t_{L2} represents time lag due to H_2 transport from the far-field rock boundary to the RBI where x_2 is the minimum horizontal distance between far-field rock boundary and RBI, 8.4 m.

The H_2 production time-lag of ~500 years also mirrors the trends in Figure 4.7. Like in Figure 4.7, this ~500 year time-lag was due to H_2 transport from the far-field rock boundary, to the RBI, which produced HS^- that transported to the UFC to drive increased H_2 production rates (Figure 4.8b, C6 and C9) and concentrations (Figure 4.8a) through a small change in rates (2.4×10^{-13} mol m^{-2} s^{-1} to 4.8×10^{-13} mol m^{-2} s^{-1} at 5000 years). The increased H_2 production rate (C9) produced a maximum H_2 concentration 1.6×10^{-4} mol m^{-3} at the UFC surface (one order of magnitude higher than C6 to C8) after 1 million years and the DGR H_2 solubility limit, 88.9 mol m^{-3} at 20 ˚C at 500 m depth was not surpassed. This observation on H_2 production highlights the role of H_2 amount and H_2 transport time-lag on H_2 dynamics in a DGR.

4.3.2.6 Effect of Effective H_2 Rock Diffusivity

4.3.2.6.1 THC-H_2 Model

The effects of effective H_2 rock diffusivity (THC-H_2 model) on maximum H_2 concentration and average species conversion rates (i.e., HS^- and H_2 rates) at the UFC are shown in Figure 4.9. The H_2 concentration at the UFC decreased with increasing the effective H_2 diffusivity in the rock (Figure 4.9a, C1 and C5), even with the same H_2 conversion rates (Figure 4.9b). This is because the increased rock effective H_2 diffusivity increased the transport rate of H_2 out of the bentonite through the rock, which limited H_2 accumulation near the UFC. Therefore, even though HS^- transport conditions were unchanged, increased rock H_2 diffusivity moderated H_2 accumulation in the DGR. Figure 4.10 illustrates the H_2 concentration distribution after 1 million years in both low (Figure 4.10a) and high (Figure 4.10b) H_2 rock diffusivity cases. These figures show how rock H_2 diffusivity controlled H_2 accumulation and dissipation in the DGR. H_2 accumulated due to

low H_2 diffusivity (see accumulation at DGR level in Figure 4.10a) and diffused out of the bentonite due to increased H_2 diffusivity, thereby decreasing the maximum H_2 concentration from 12 mol m^{-3} to 4.1 mol m^{-3}, respectively (Figure 4.10b). These results therefore highlight the role of rock diffusivity on DGR H_2 dynamics.

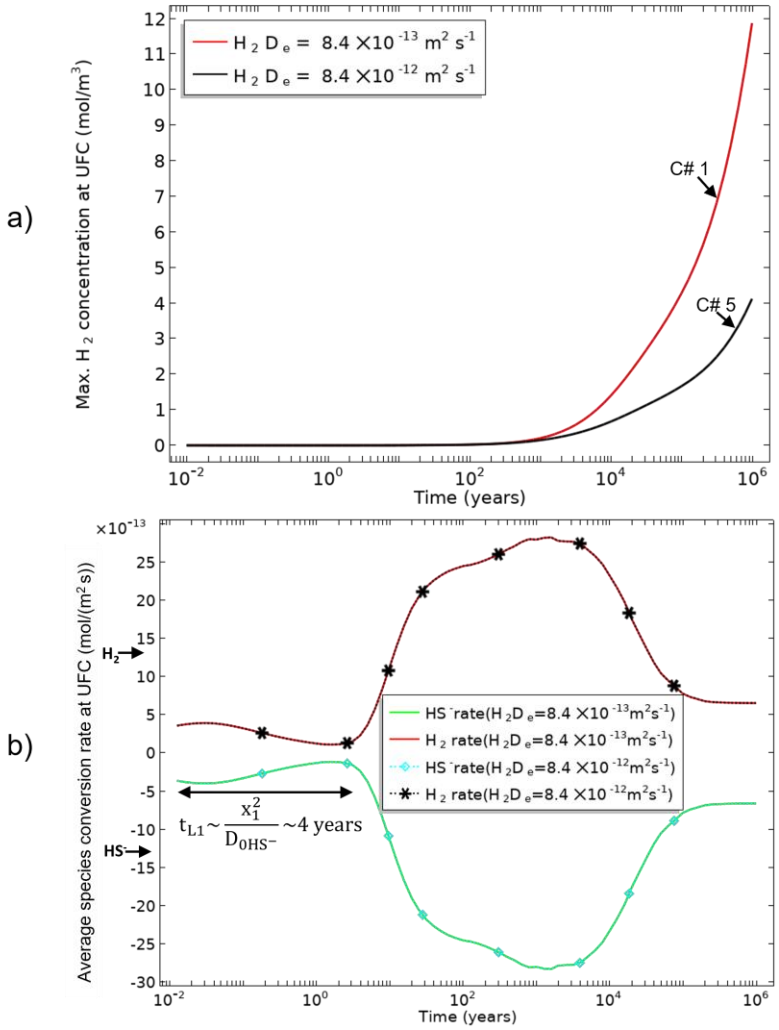

Figure 4.9: Effect of effective H_2 rock diffusivity (THC-H_2 model) on a) maximum H_2 concentration at the UFC and b) average species conversion rate at the UFC. Note that the positive and negative species conversion rates indicate species production and consumption, respectively. Also note that t_{L1} represents time lag due to HS^- transport from the RBI to the UFC and x_1 is the minimum horizontal distance between RBI and UFC cap of 0.343 m.

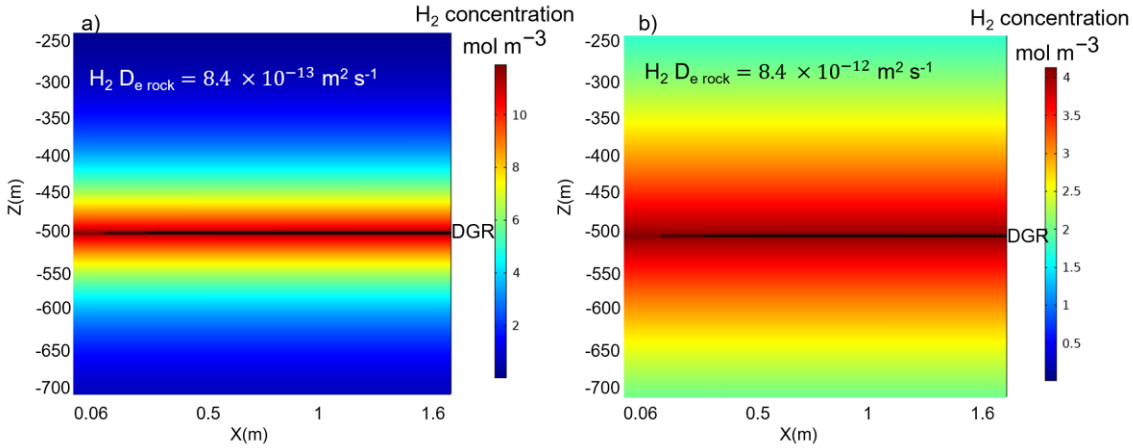

Figure 4.10: H_2 concentration in the DGR after 10^6 years due to different rock H_2 diffusivities a) case 1, effective H_2 rock diffusivity, H_2 $D_{e\ rock}$ = 8.4×10^{-13} m^2s^{-1} and b) case 5, H_2 $D_{e\ rock}$ = 8.4×10^{-12} m^2s^{-1}. Note that the figures are not drawn to correct aspect ratio (DGR is represented by a line), to help to visualize the H_2 accumulation and dissipation. Also note that the effective H_2 bentonite diffusivity was kept the same.

4.3.2.6.2 THC-H_2 Feedback Model

The effects of H_2 rock diffusivity were also explored via the THC-H_2 feedback model. The resulting maximum H_2 concentrations and average HS^- and H_2 conversion rates at the UFC are shown in Figure 4.11. Unlike the THC-H_2 model, H_2 conversion rates and concentrations increased in the THC-H_2 feedback model with increasing effective H_2 rock diffusivity (Figure 4.11, C6 and C10). This is because the HS^- production at the RBI (Eq. 4.3) was greatly controlled by the transport of H_2 from the far-field rock boundary to the RBI. Therefore, by increasing H_2 rock diffusivity, the HS^- production rate at the bentonite-rock interface also increased and more HS^- was available to transport to the UFC surface. Although this increased HS^- flux to the UFC increased H_2 production via the HS^-/H_2 feedback between the UFC and RBI, the DGR H_2 solubility limit, 88.9 mol m^{-3} at 20 ˚C at 500 m depth was not surpassed. The maximum H_2 concentration at the UFC was 7.8×10^{-4} mol m^{-3} after 1 million years for an effective H_2 rock diffusivity of 8.3 x 10^{-12} m^2 s^{-1}. Figure 4.12 shows the H_2 concentration distribution after 1 million years in both low (Figure

4.12a) and high (Figure 4.12b) H_2 rock diffusivity cases. These figures show how H_2 consumption process (Eq. 4.3) impacted H_2 production (Eq. 4.8).

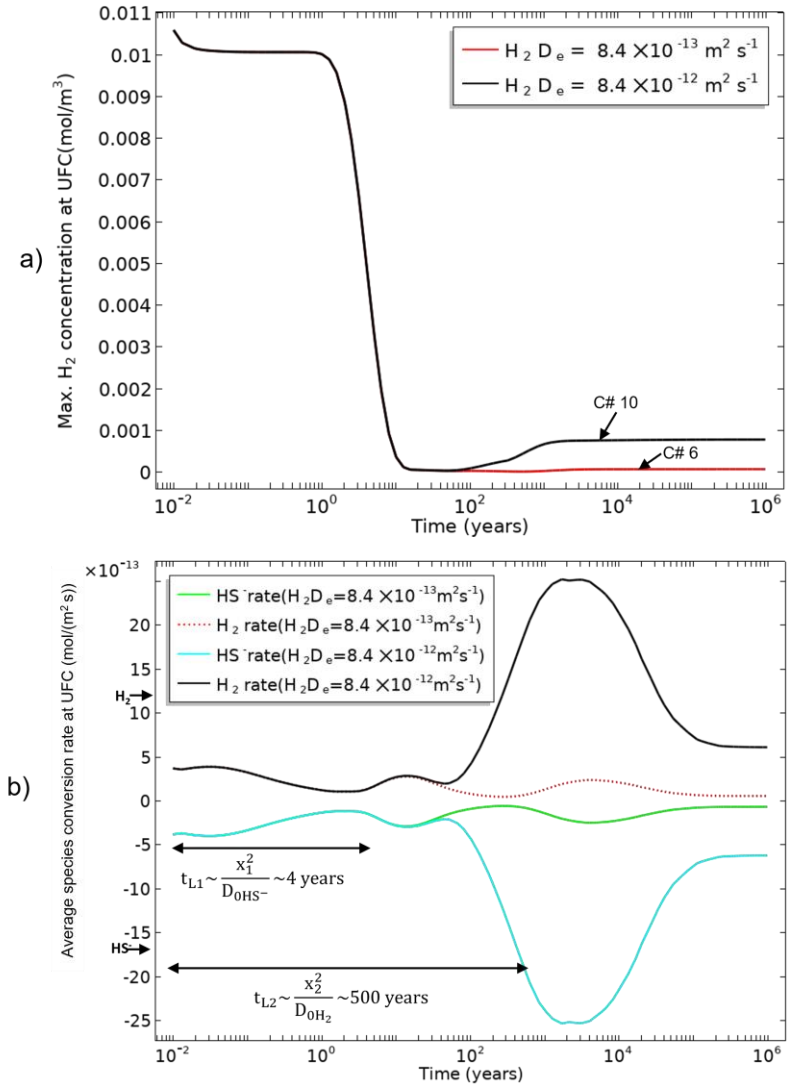

Figure 4.11: Effect of effective H_2 rock diffusivity (THC-H_2 feedback model) on a) maximum H_2 concentration at the UFC and b) average species conversion rate at the UFC. Note that the positive and negative species conversion rates indicate species production and consumption, respectively. Also note that t_{L1} represents time lag due to HS^- transport from the RBI to the UFC where x_1 is the minimum horizontal distance between RBI and UFC cap, 0.343 m. t_{L2} represents time lag due to H_2 transport from the far-field rock boundary to the RBI where x_2 is the minimum horizontal distance between far-field rock boundary and RBI, 8.4 m.

Although the far-field H_2 transport to the RBI increased due to increased transport rate (seen through H_2 rate increase in Figure 4.11), more H_2 (either from the far-field or MIC) was consumed to produce HS^- at the RBI (see supplementary materials, section A.S.8) leaving the overall H_2 accumulation within the DGR almost the same (Figure 4.12). Therefore, consumption of H_2 at the RBI dominated regulating the H_2 concentrations at the UFC surface over rock diffusivity. This observation highlights the importance of H_2 consumption at the rock bentonite interface, which could occur if bacteria was present (e.g., sulfate reducing bacteria (SRB) activity), in reducing H_2 level in a DGR.

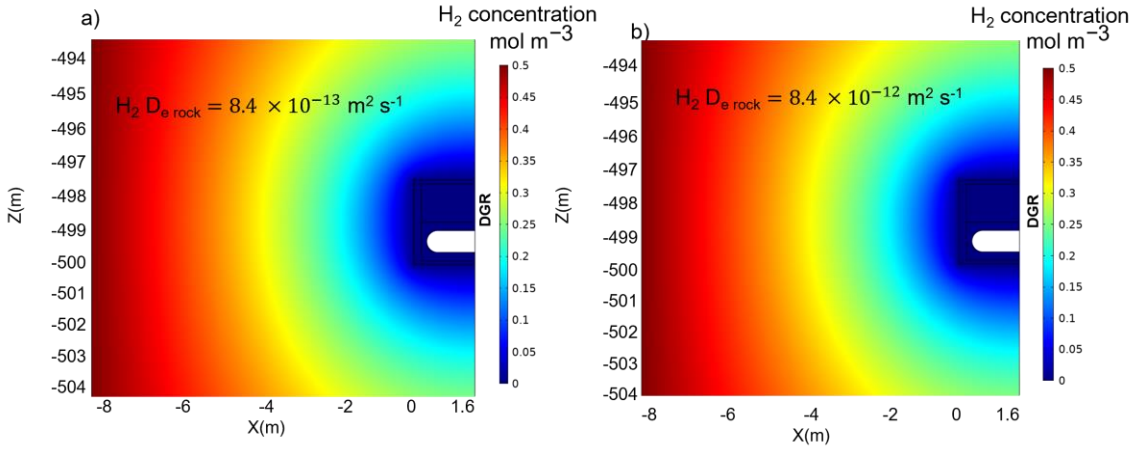

Figure 4.12: H_2 concentration in the DGR after 10^6 years due to different rock H_2 diffusivities a) C6, H_2 $D_{e\ rock} = 8.4\times10^{-13}$ m^2s^{-1} and b) C10, H_2 $D_{e\ rock} = 8.4\times10^{-12}$ m^2s^{-1}. Note that the effective H_2 diffusivity in bentonite was kept the same.

4.3.3 DGR H_2 Concentration from Sensitivity Cases

DGR H_2 concentrations from all modelling scenarios (C1 to C10) are compared in Figure 4.13. The H_2 solubility limit of 88.9 mol m^{-3} at 20 ˚C (and 500m below ground) was not surpassed in any modelling scenario (C1 to C10), signifying that no H_2 gas would be produced under modelling conditions. It is important to note that the H_2 solubility limit varies slightly (88.5-88.9 mol m^{-3}) with DGR temperature (11-81 ˚C) and increases with depth, however the depth of 500 m was chosen as the comparison (see supplementary

materials, Section A.S.6). The effects of bentonite saturation and temperature on maximum H_2 concentration in bentonite using the THC-H_2 model are explored in the next section. TCH-H_2 is used since H_2 concentration was higher than the THC-H_2 model feedback model (Figure 4.13).

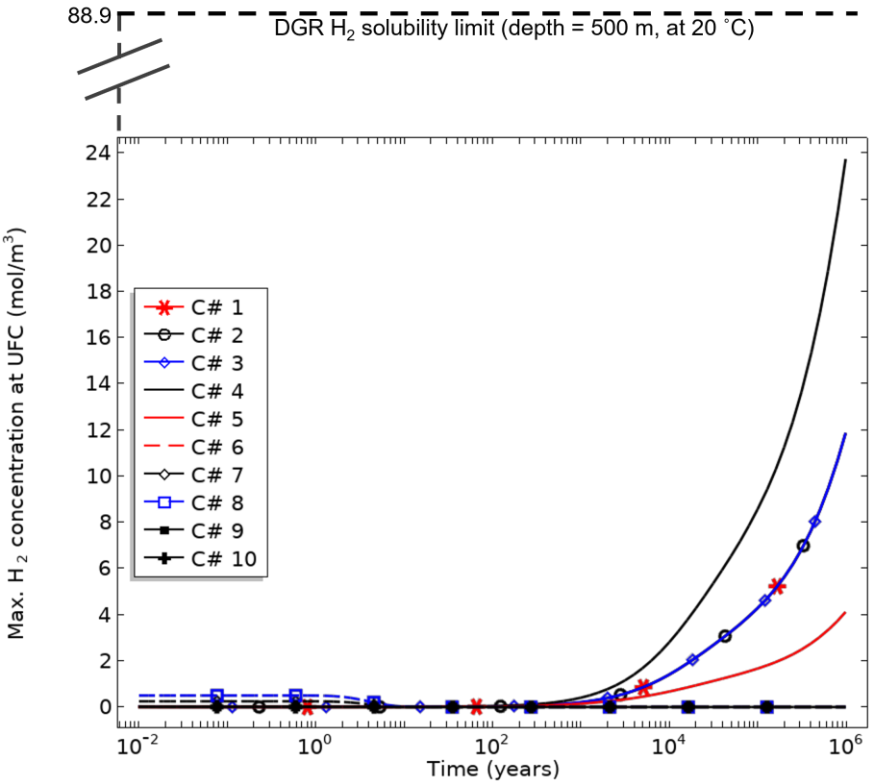

Figure 4.13: Maximum DGR H_2 concentrations obtained from sensitivity cases (C1 to C10)

4.3.4 Effects of Temperature and Saturation

The THC-H_2 model was also decomposed into simpler models to understand effects from saturation and temperature separately. These models simulated (*i*) Chemical (Diffusion) processes-only (referred to as the "C-H_2 model"), (*ii*) Hydraulic-Chemical (Diffusion) processes (referred to as the "HC-H_2 model"), and (*iii*) Thermal-Chemical (Diffusion) processes (referred to as the "TC-H_2 model"). As the diffusion rates are dependent on

bentonite saturation and temperature, the transient effects of these conditions on H_2 dynamics in bentonite were investigated.

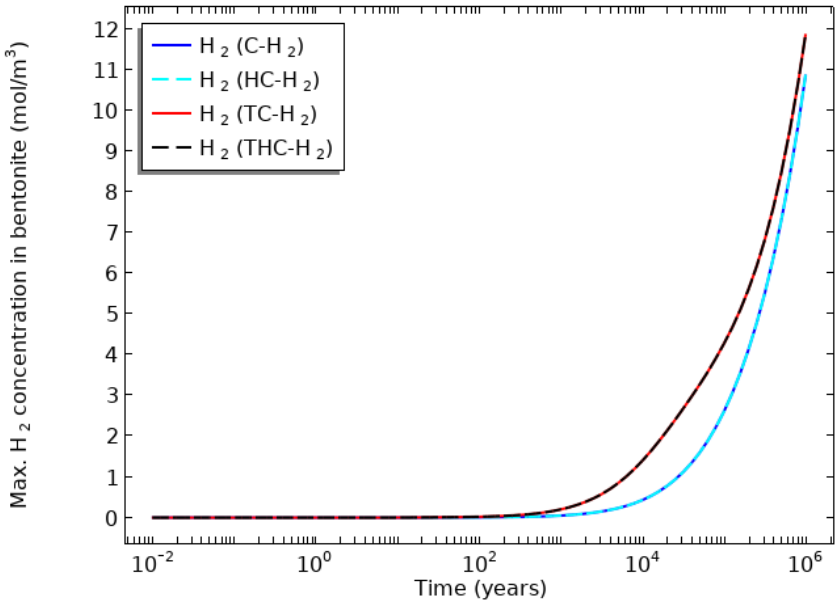

Figure 4.14: Maximum H_2 concentrations in the bentonite under different conditions a) C-H_2 model simulates H_2 dynamics under fully saturated-isothermal conditions, b) HC-H_2 model simulates H_2 dynamics under variably saturated-isothermal conditions, c) TC-H_2 model simulates H_2 dynamics under fully saturated-non-isothermal conditions, d) THC-H_2 model simulates H_2 dynamics under variably saturated-non-isothermal conditions

Figure 4.14 compares maximum H_2 bentonite concentrations over time from these different models. In the THC-H_2 and TC-H_2 models, H_2 production started after ~500 years (Figure 4.14). In comparison, H_2 production started slightly later in the HC-H_2 and C-H_2 models (approximately after ~1500 years). The key differences between the models in Figure 4.14 (i.e., between C-H_2 and HC-H_2 vs. TC-H_2 and THC-H_2) were due to simulating temperature changes, as the saturation process occurred rapidly within the first 20 years and did not noticeably impact H_2 dynamics (Asad et al. 2022). The differences between the models were ultimately due to the temperature dependencies embedded in the

modelled effective diffusivities. That is, the HS^- diffusion rates in bentonite increased with temperature and drove higher H_2 production in the THC-H_2 and TC-H_2 models (when the UFCs were emitting heat) compared to the HC-H_2 and C-H_2 models (which did not consider UFC heating, and only simulated ambient temperatures).

4.4 Conclusions

This study outlines the development, implementation, and results of a novel hydrogen (H_2) dynamics model for a DGR in crystalline rock. However, the model is flexible and can accommodate site-specific information as they become available. This model simulated bisulfide (HS^-) transport and H_2 production due to MIC and biotic H_2 consumption. The objective of this research was to investigate whether the net amount of H_2 would surpass the solubility limit leading to H_2 gas (bubble) formation in a DGR, using generally conservative assumptions of HS^- and H_2 flux (rate) conversion. The results reveal that the long-term H_2 production from MIC depends on HS^- supply to the UFC, H_2 rock diffusivity, H_2 transport time lag, and H_2 biotic consumption. The H_2 can be produced from MIC (using HS^- to H_2 rate conversion at the UFC) as long as HS^- is available in the DGR vicinity. However, the H_2 concentration in a DGR will depend on the H_2 diffusivity and transport time-lag, for example, transport time of electron donor (e.g., H_2) from far-field to DGR vicinity for producing HS^- through microbial activity. The H_2 may diffuse out of the bentonite due to increased H_2 rock diffusivity as observed through a simulation of constant (1 ppm) HS^- transport through the bentonite to the UFC. However, including a HS^-/H_2 feedback mechanism to the model implemented a HS^- production mechanism at the RBI (instead of a constant concentration boundary), which provided novel insight into H_2 dynamics considering H_2 migration and its solubility limit. It was

assumed that microbes at the RBI (i.e., sulfate reducing bacteria (SRB)) consumed both far-field H_2 and H_2 from MIC (sulfate was assumed to be a non-limiting species) to produce HS^- and assist UFC corrosion. Specifically, the HS^-/H_2 feedback mechanism included a feedback of HS^- production at the RBI due to far-field H_2 transport towards the RBI, HS^- transport towards UFC and then MIC driven H_2 transport back to the RBI to produce HS^-. The far-field H_2 transport to the DGR was delayed (~500 years) due to diffusive transport from far-field to the RBI. Although increased transport rate (due to increased diffusivity) increased H_2 supply, both far-field H_2 and H_2 generated due to MIC were consumed at the RBI (assumed by microbial activity (e.g., SRB activity)), which prevented the formation of a distinct H_2 gas phase in a DGR suggesting that, consumption of H_2 at the RBI dominated regulating the H_2 concentrations at the UFC surface over rock diffusivity. This result therefore highlights the significance of biotic processes (e.g., SRB activity, modelled through a simplified approach) which could consume and reduce H_2 levels in a DGR environment. The H_2 solubility limit was not surpassed in any sensitivity cases, albeit with the highest H_2 concentration in C4 where no HS^-/H_2 feedback was modelled. Lastly, the dynamics of H_2 was slightly affected by temperature while the effect of saturation was negligible. Future work may include additional aspects of H_2 fate and transport in a DGR, such as:

- The H_2 and HS^- rock effective diffusivity values were approximated from literature values and would also benefit from laboratory measurements under relevant DGR conditions (e.g., temperature, ionic strength).
- The consequences of copper sulfide production could also be investigated (e.g., in forming a crust that may inhibit corrosion, or in causing local non-uniformities).

- The current model assumes that H_2 was unreactive; however, H_2 may participate in reactions that would limit HS^- production, e.g., kinetic geochemical or microbiological reactions in the bentonite and host rock. In addition, SO_4 may be a rate limiting species through microbial SO_4 reduction (where H_2 may participate as an electron donor), which can affect the H_2/HS^- feedback process.

Overall, this study provides novel insight into H_2 accumulation and transport dynamics in DGR environments.

Chapter 5 Modelling Key Reactive Processes Relevant to Bisulfide Transport through Highly Compacted Bentonite

5.1 Introduction

The Canadian Nuclear Waste Management Organization (NWMO) is responsible for the design and implementation of Canada's plan to manage high level nuclear fuel waste in a deep geological repository (DGR). The NWMO has proposed a DGR design, which consists of copper coated used fuel containers (UFCs) being placed within a highly compacted bentonite (HCB) buffer surrounded by a suitable host rock (see supplementary materials (SM), Figure B.S.1). Although the copper is thermodynamically stable in oxygen-free environments (King et al. 2013; Senior et al. 2020, 2023), it is potentially susceptible to corrosion from bisulfide (HS^-) produced from microbiological metabolic processes within the host rock or at the clay-rock interface during anoxic conditions. Depending on site-specific conditions (e.g., host rock type, groundwater chemistry, microbial growth conditions), HS^- could transport through the HCB to the UFC surface and corrode the copper coating and compromise the long-term performance of UFCs (Hall et al. 2021). The long-term prediction of copper corrosion by HS^- is one of the metrics that helps ensure adequate corrosion allowance of the UFCs (Hall et al. 2021). Therefore, it is vital to understand HS^- transport behaviour through the bentonite to accurately understand HS^- transport mechanisms and assess the extent of corrosion to ensure safe and long-term performance of copper as a corrosion barrier.

The effects of key hydrogeologic properties (e.g., saturation, temperature) on HS^- transport and corrosion have been assessed by using thermal-hydraulic-chemical (THC)

models (Asad et al. 2022; Rashwan et al. 2022; Cloet et al. 2017; King et al. 2020; Briggs and Krol 2018; Wersin et al. 2014, 2017). In addition to hydrogeologic processes, various geochemical reactions (e.g., hydrolysis, cation exchange, complexation, oxidation-reduction, and dissolution-precipitation) (Figure 5.1) can occur within the saturated bentonite, causing changes in the porewater chemistry and pore structure (Villar et al. 2012) with implications for species transport through the bentonite (e.g., mobility, reactivity) (Wersin et al. 2014). One of the key geochemical processes relevant to HS^- transport through bentonite is the formation of iron sulfide species such as mackinawite (FeS) due to a reaction between iron-containing species within the bentonite and HS^-, as observed in experiments (Maanoja et al. 2020; Pedersen et al. 2017; Chowdhury et al. 2021a; Hansel et al. 2015). For example, Pedersen et al. (2017) reported that HS^- may reduce ferric iron, Fe^{3+} (e.g., Fe^{3+} produced due to dissolution of goethite, FeOOH) to ferrous iron, Fe^{2+} (Eq. 1), which could react with the free HS^- (i.e., free HS^- after forming elemental sulphur, S^0) and form FeS (Eq. 2):

$$2Fe^{3+}_{(aq)} + HS^-_{(aq)} \rightarrow 2Fe^{2+}_{(aq)} + S^0_{(s)} + H^+_{(aq)} \quad (5.1)$$

$$Fe^{2+}_{(aq)} + HS^-_{(aq)} \rightarrow FeS_{(s)} + H^+_{(aq)} \quad (5.2)$$

$$2Fe^{3+}_{(aq)} + 2HS^-_{(aq)} \rightarrow Fe^{2+}_{(aq)} + S^0_{(s)} + FeS_{(s)} + 2H^+_{(aq)} \quad (5.3)$$

The above oxidation-reduction reactions show the total reaction as irreversible process through FeS precipitation. However, an equilibrium process may also be considered, where FeS dissolves as Fe^{2+} and HS^-. Iron sulfide solubility was explored in some studies (Behazin et al. 2021; Lemire et al. 2020; Davison 1991; Rickard and Luther 2007) who reported that FeS dissolution is generally unlikely in the geosphere, as the most stable form of iron sulfide is pyrite (FeS_2), which has very low solubility (solubility product

constant Ksp = $10^{-26.89}$ at 25 °C). Its geological precursor is mackinawite, which is more soluble than pyrite, (K_{SP} = 6.5 x 10^{-4} at 25 °C). Geochemical reactions can be modelled either using chemical equilibrium at a specified temperature or a kinetic reaction rate (Pekala et al. 2019; Kiczka et al. 2021).

Figure 5.1 shows how various surface-mediated reactions can complicate HS^- transport through bentonite, e.g., via sorption (i.e., adsorption, desorption, absorption), anion exclusion, surface and/or bentonite interlayer diffusion (Shackelford and Moore 2013; Van Loon et al. 2007). Bentonite exhibits sorption affinity to cations (e.g., cesium, strontium) (Oscarson et al. 1994; Khan et al. 1994, 1995; Norrfors 2011). Since HS^- is an anion, the anion exclusion effect (i.e., where anions are excluded from the pore space due to repulsion from the negatively charged clay particles) controls HS^- sorption behaviour in compacted bentonite (Van Loon et al. 2007; Chowdhury et al. 2024). Due to anion exclusion, HS^- may occupy small part of the pore space in compacted bentonite (i.e., accessible porosity) and, therefore, HS^- sorption onto the compacted clay particles becomes an unlikely process (Tournassat and Appelo 2011; Papry et al. 2023). Hence, the likely process that can lead to retention of HS^- in compacted bentonite is the reaction with iron (Chowdhury et al. 2021b). However, in a DGR safety study, possible processes (likely and unlikely) are included to verify impact of each process. Species sorption can be modelled either using linear or nonlinear relationships between sorbed amount of species and species concentration (Oscarson et al. 1994; Khan et al. 1994). Although the linear approach is simple, it is generally applicable at low species concentrations (note that the expected HS^- concentration in Canadian DGR is 30-90 ppb) (Gascoyne 1997;

Kremer 2017). The transport path of HS^- in bentonite can be constricted if transport of cations through interlayers (i.e., interlayer diffusion) and diffuse double layers (i.e., surface diffusion) is dominant and cations occupy most parts of the pore space (Appelo and Wersin 2007; Shackelford and Moore 2013). It is found that both geochemical reactions (equilibrium and kinetic) and surface mediated processes (linear and nonlinear sorption) have been used by others to explain ionic transport. Although some laboratory studies on HS^- reaction and HS^- sorption are available (Pedersen et al. 2017; Chowdhury et al. 2021a; Papry et al. 2023; Chowdhury et al. 2024), anion/HS^- exclusion effect, which lowers the diffusion accessible porosity, and the effect of surface and/or bentonite interlayer diffusion are not well-understood, as relevant experiments have not been conducted. However, chloride (Cl^-) diffusion through bentonite (Van Loon et al. 2007) provides valuable insight on anion exclusion (e.g., dependency of diffusion coefficient on diffusion accessible porosity). Altogether, it is difficult to delineate the governing mechanisms for HS^- transport through bentonite as many complicated geochemical and surface-mediated reactions (Figure 5.1) may influence HS^- transport.

Numerical modelling is a powerful tool that can be used to improve our understanding of HS^- transport by identifying key processes. For example, the delay of HS^- flux to the UFC due to iron sulfide formation and HS^- sorption reactions can be numerically simulated using various processes and compared to laboratory experiments. In addition, numerical models can be used to predict HS^- transport and assess UFC corrosion over the DGR lifespan. Numerous numerical models have been developed to evaluate bisulfide fluxes through bentonite (Cloet et al. 2017; Kiczka et al. 2021; Wersin et al. 2017; Pekala et al.

2019; Wersin et al. 2014; Sena et al. 2010). While these models include geochemical processes, they do not model the anticipated DGR environment (e.g., varying thermal and hydraulic conditions), which can affect the geochemical evolution. In addition, governing mechanisms for HS^- transport are not well-understood as different processes and conditions are not modelled (e.g., surface-mediated reactions, reaction kinetics).

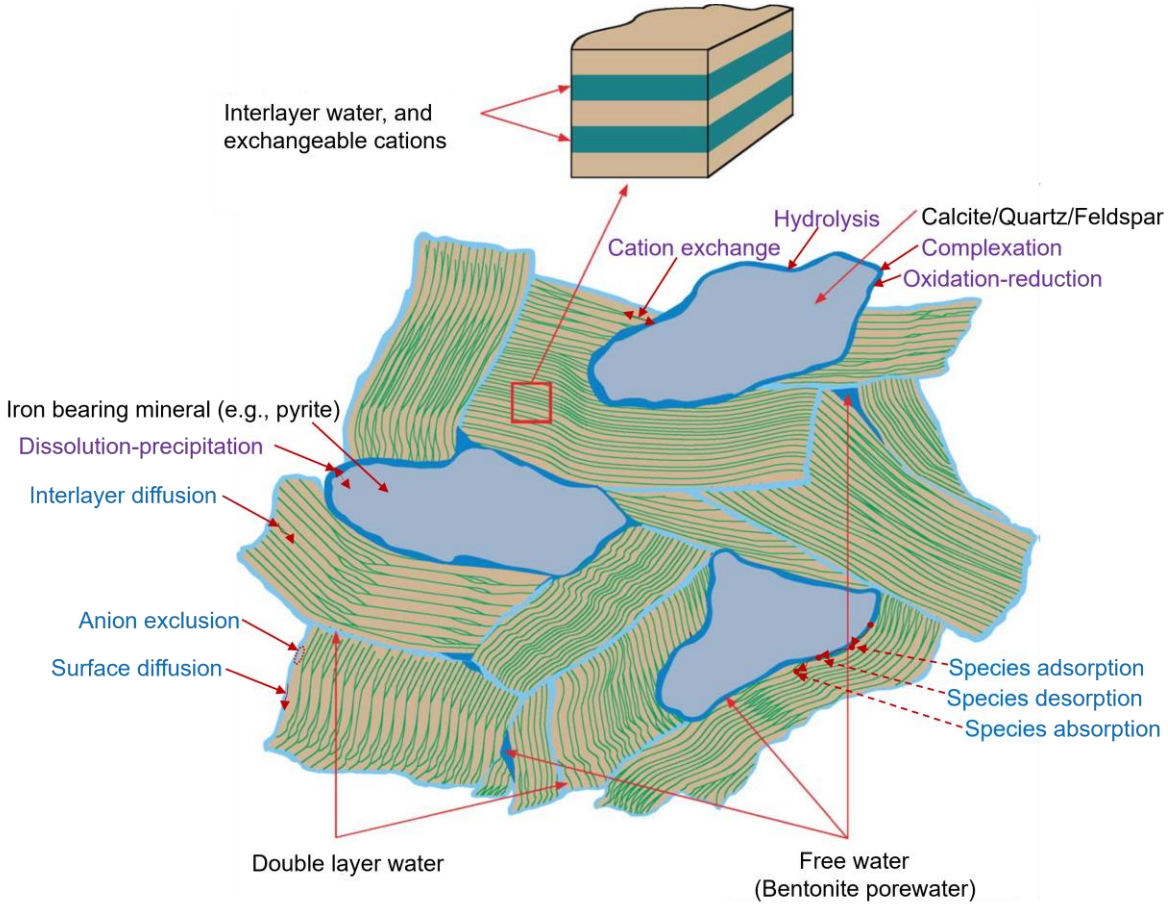

Figure 5.1: A conceptual model of various geochemical (purple) and surface mediated processes (blue) in saturated bentonite clay. Adapted from (Bradbury and Baeyens 2003) with permission of Elsevier.

This study presents three 1-D models (Table 5.1), developed in COMSOL, to understand HS^- transport dynamics. The developed 1-D models coupled HS^- transport with either HS^-

adsorption (i.e., linear and non-linear adsorption) or HS^- reaction models (i.e., kinetically irreversible HS^- and Fe^{2+} reaction). The model outputs were compared to laboratory diffusion tests to understand geochemical evolution relevant to HS^- and Fe^{2+} reaction, explore effects of HS^- adsorption and HS^- reactions on HS^- breakthrough, and to delineate the processes controlling HS^- transport dynamics. Using this comparative approach, the study identified that the three 1-D models (i.e., (i) kinetically irreversible HS^- reaction and (ii) linear and (iii) nonlinear HS^- adsorption models) provided reasonably accurate descriptions of the experimental HS^- transport dynamics. These three models were then coupled individually to a previously published 3-D thermal-hydraulic-chemical (THC) model for bisulfide transport (Rashwan et al. 2022) to understand HS^- transport and reaction evolutions in the DGR. One of the 3-D models coupled HS^- transport with a geochemical reaction between HS^- and iron, Fe^{2+} (i.e., HS^- retardation due to FeS formation) and the others coupled a HS^- adsorption process (as a part of the sorption process). These 3-D coupled models were run for a reference period of 1 million years (i.e., Canadian DGR design life) and HS^- corrosion was quantified. Altogether, this study infers how HS^- adsorption and HS^- reaction with Fe^{2+} influences HS^- transport using a comparative approach between modelled and laboratory HS^- breakthrough profiles and provides important implications for HS^- corrosion in the Canadian DGR.

5.2 Methodology

5.2.1 Model Development

A 1-D HS^- transport model (referred to as the “C model”) was developed to simulate HS^- diffusive transport under fully saturated and isothermal conditions (i.e., using Fick’s second law). The C model does not simulate reactions and does not include advection

(i.e., as Peclet number, Pe << 0.1, see Rashwan et al. (2022)). The Peclet number was calculated as a ratio of advective to diffusive transport ($\mathrm{P_e} = \frac{\mathrm{LU}}{\mathrm{D_e}}$) (Huysmans and Dassargues 2005), where L is the size of pore in bentonite, U is the Darcy velocity using reference bentonite permeability, and $\mathrm{D_e}$ is the effective diffusivity of HS^-. This C model was coupled with either HS^- adsorption models or HS^- reaction model (see Table 5.1).

Table 5.1: Reactive 1-D models

Model	**Abbreviated model name**	**Physics**	**Assumption**
Linear HS^- adsorption	C-S_L	HS^- adsorption	A partitioning coefficient describes adsorption. Absorption and desorption are not modelled.
Non-linear HS^- adsorption	C-S_{NL}	HS^- adsorption	Langmuir parameters describe adsorption. Absorption and desorption are not modelled.
Kinetically irreversible HS^- reaction	C-R_I	HS^- and Fe^{2+} reaction	Irreversible reaction is defined using a reaction rate. FeS is modelled as a relatively immobile aqueous species.

An overview of the model domain, boundary, and initial conditions for the three 1-D models are shown in Figures 5.2b (linear adsorption, C-S_L), 5.2c (non-linear adsorption, C-S_{NL}), and 5.2d (kinetically irreversible reaction, C-R_I). For all the 1-D models, the HS^- concentration at the inlet was set to 1000 ppm (30.2 mol m^{-3}) and was implemented as a constant concentration boundary condition. The outlet was also modelled as a constant concentration boundary condition with a value of 0 mol m^{-3}. The initial concentration of HS^- was set to 0 mol m^{-3}. The diffusivity for each species was defined separately and is

given in Table 2. The effective diffusivity of HS^- was defined as a function of HS^- diffusion accessible porosity (ϵ_{HS^-}) following Van Loon et al. (2007):

$$\epsilon_{HS^-} = \epsilon_{HS^-}^{max} - Ae^{-B[HS^-_{(aq)}]} \quad (5.4)$$

$$D_e = D_w \epsilon_{HS^-}^n \quad (5.5)$$

where $\epsilon_{HS^-}^{max}$ is the interparticle pore space, A and B are density dependent constants, D_e and D_w are HS^- effective diffusion coefficient and HS^- diffusion coefficient in water, respectively, and n is the Archie's law (Archie 1950) tortuosity (τ) dependent exponent. The above definition of effective HS^- diffusivity (Eqs. 5.4 and 5.5) modelled anion/HS^- exclusion in bentonite pore space, which lowers the diffusion accessible porosity (Van Loon et al. 2007). The values of A and B for HS^- transport have not been measured and therefore Cl^- diffusion values were assumed following Van Loon et al. (2007) (Table 5.2). The effective diffusivities for Fe^{2+}, and H^+ were defined following Archie (1950). All boundary and initial concentration conditions were taken from an experiment performed by (Chowdhury et al. 2021b, 2024) (Figure 5.2a) and model boundary conditions were confirmed through accurately simulating a tracer (Cl^-) diffusion experiment (Figure 5.3) .

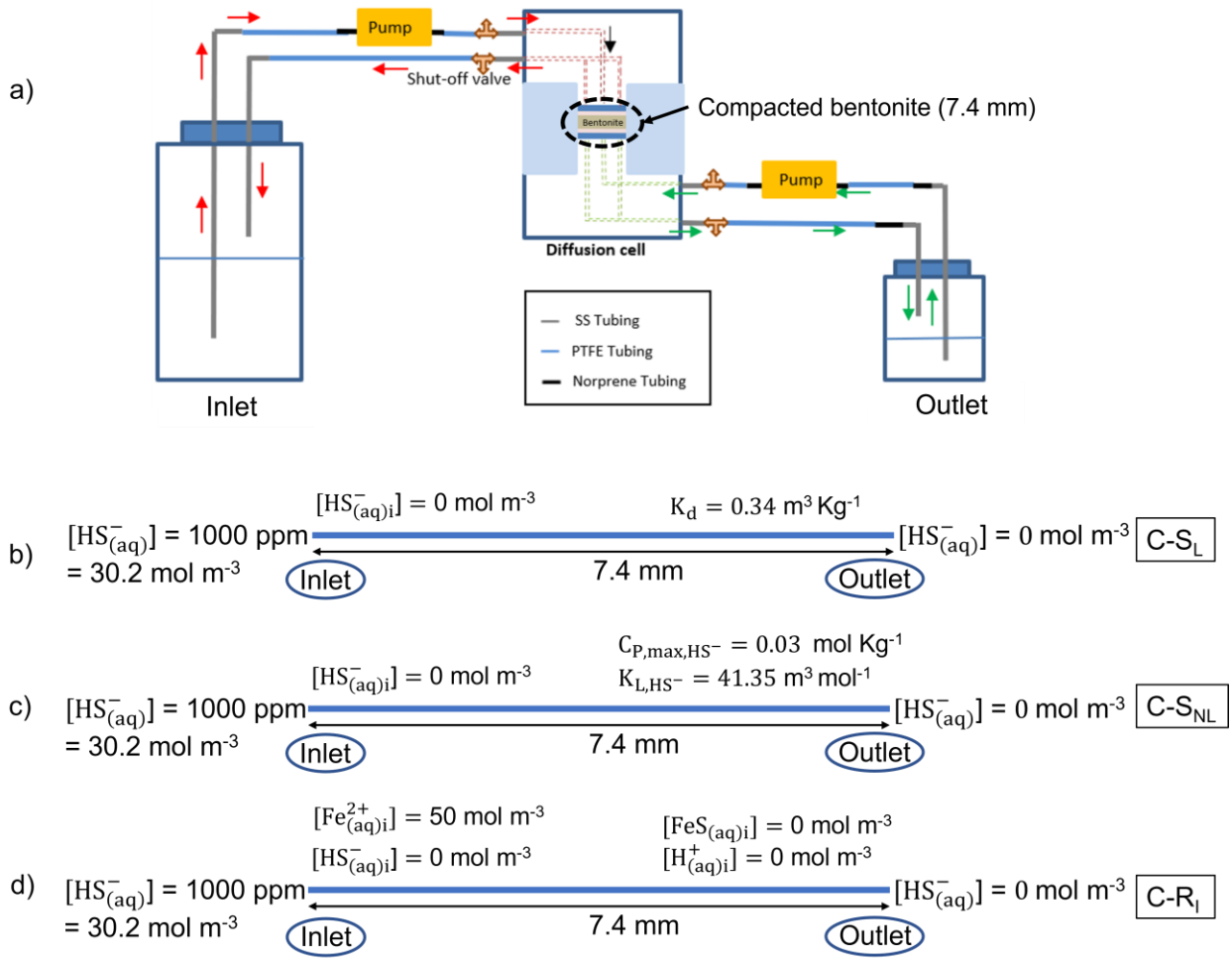

Figure 5.2: a) Experimental setup of HS^- diffusion through 7.4 mm, medium density compacted bentonite (ρ_M=1330 kg m^{-3}) from (Chowdhury et al. 2021b, 2024). b) to d) schematics representing the initial and boundary conditions in the 1-D models: b) Linear HS^- adsorption (C-S_L) model, c) Non-linear HS^- adsorption (C-S_{NL}) model, and d) Kinetically irreversible HS^- reaction (C-R_I) model.

5.2.1.1 HS^- Adsorption Model Development

5.2.1.1.1 Linear HS^- Adsorption (C-S_L) Model Development

The linear HS^- adsorption (C-S_L) model describes HS^- adsorption as follows, using a linear distribution coefficient, K_d:

$$C_{P,HS^-} = K_d\,[HS^-_{(aq)}] \tag{5.6}$$

where C_{P,HS^-} is the adsorbed amount of HS^-. The K_d is the HS^- partitioning coefficient due to adsorption, which represents a linear interaction between HS^- and the bentonite

surface. The value of K_d was initially set to 0.34 m^3 kg^{-1} (representative of powdered bentonite, liquid to solid ratio (L:S) =200, Papry et al. 2023) and K_d of compacted bentonite was determined through fitting HS^- breakthrough curve in compacted bentonite from (Chowdhury et al. 2024) (see section 5.3.2.1).

5.2.1.1.2 Non-linear HS^- Adsorption (C-S_{NL}) Model Development

The non-linear HS^- adsorption (C-S_{NL}) model describes HS^- adsorption following Langmuir isotherm (Langmuir 1917):

$$C_{P,HS^-} = \frac{K_{L,HS^-}\ C_{P,max,HS^-}\ [HS^-_{(aq)}]}{1 + K_{L,HS^-}\ [HS^-_{(aq)}]} \quad (5.7)$$

where K_{L,HS^-} is the Langmuir constant. Like K_d, K_{L,HS^-} represents the extent of interaction between HS^- and bentonite surface, where a relatively larger K_{L,HS^-} value represents a strong interaction between HS^- and bentonite surface while smaller K_{L,HS^-} value represents a weak interaction. The C_{P,max,HS^-} is the adsorption maximum, which represents the capacity up to which HS^- can be adsorbed onto bentonite surface. Unlike the C-S_L model, the C-S_{NL} model (Eq. 5.7) represents a nonlinear HS^- partitioning as the adsorbed and aqueous HS^- are function of both K_{L,HS^-} and C_{P,max,HS^-}. The values of adsorption parameters, C_{P,max,HS^-} and K_{L,HS^-} were initially set to 0.03 mol Kg^{-1} and 41.35 m^3 mol^{-1} (powdered bentonite, L:S=200, Papry et al. 2023) and K_{L,HS^-} and C_{P,max,HS^-} of compacted bentonite were determined through fitting HS^- breakthrough curve in compacted bentonite from (Chowdhury et al. 2024) (see section 5.3.2.1).

5.2.1.2 HS^- Reaction Model Development

5.2.1.2.1 Kinetically Irreversible HS^- Reaction (C-R_I) Model Development

The kinetically irreversible HS^- reaction (C-R_I) model describes irreversible production of FeS with the following reaction:

$$Fe^{2+}_{(aq)} + HS^-_{(aq)} \rightarrow FeS_{(s)} + H^+_{(aq)} \quad (5.8)$$

FeS is modelled to be a relatively immobile aqueous species using a very low FeS diffusivity. The reaction rate (R) is described as a function of reactant's concentration and rate constant (k) following (Rickard 1997; Cloet et al. 2017):

$$R = k\,[Fe^{2+}_{(aq)}]\,[HS^-_{(aq)}] \quad (5.9)$$

$$k = A_h\, e^{\frac{-E_h}{R_g T}} \quad (5.10)$$

The Arrhenius frequency factor (A_h), Arrhenius activation energy (E_h), gas constant (R_g), and temperature (T) are used to define k. Under constant k and $[HS^-_{(aq)}]$, a relatively larger reaction rate indicates iron is available in the bentonite while smaller reaction rate indicates iron is depleting due to reaction between initial Fe^{2+} and HS^- (as $R \propto [Fe^{2+}_{(aq)}]$ in Eq. 5.9). The initial concentrations of reactant HS^- and products FeS and H^+ (Figure 5.2d) were set to 0 mol m^{-3} in the C-R_I model as initial concentrations of HS^-, FeS, and H^+ were not needed to define the reaction rate (Eq. 5.9). The initial estimate of available Fe^{2+} was assumed to be less than the total Fe mass (4% of the total bentonite mass, ≈950 mol m^{-3} for medium density compacted bentonite, ρ_M=1330 kg m^{-3} and reported in Gilmour et al. 2021; Karnland 2010), which was equal to 50 mol m^{-3}.

5.2.2 Parameters

The model parameters are shown in Table 5.2. These parameters represent the properties of bentonite (e.g., porosity) and the compounds (HS^-, Fe^{2+}, FeS, and H^+) in the bentonite. Parameters without a reference are assumed values, as discussed above.

Table 5.2: Model parameters

Parameter		**Value**
Length of bentonite[1](L)		7.4 mm
Compacted bentonite density[1] (ρ_M)		1330 kg m^{-3}
Porosity[1] (ø)		0.4 (-)
Initial HS^- concentration[1,2,3] ($[HS^-_{(aq)i}]$)		0 mol m^{-3}
HS^- constant concentration at inlet[1]($[HS^-_{(aq)}]$)		30.2 mol m^{-3} (1000 ppm)
HS^- constant concentration at outlet[1,2,3] ($[HS^-_{(aq)}]$)		0 mol m^{-3}
Initial Fe^{2+} concentration ($[Fe^{2+}_{(aq)i}]$)		50 mol m^{-3}
Initial FeS concentration ($[FeS_{(aq)i}]$)		0 mol m^{-3}
Initial H^+ concentration ($[H^+_{(aq)i}]$)		0 mol m^{-3}
Interparticle pore space ($\epsilon^{max}_{HS^-}$)[4]		0.226(-)
Density dependent constant[4]	A	0.21(-)
	B	17.9(-)
Archie's law exponent[4]		2 (-)
HS^- diffusion coefficient in water(D_w)[5]		1× 10^{-9} m^2 s^{-1}
Effective Fe^{2+} diffusivity[6] (D_{eFe})		1.05× 10^{-10} m^2 s^{-1} at full saturation, 20 ˚C
Effective FeS diffusivity[6] (D_{eFeS})		1.05× 10^{-15} m^2 s^{-1} at full saturation, 20 ˚C
Effective H^+ diffusivity[6] (D_{eH})		7.5× 10^{-10} m^2 s^{-1} at full saturation, 20 ˚C
Adsorption maximum[7] ($C_{P,\,max,HS^-}$)		0.03 mol kg^{-1}
Langmuir constant[7] ($K_{L,\,HS^-}$)		41.35 m^3 mol^{-1}
HS^- partitioning coefficient[7] (K_d)		0.34 m^3 kg^{-1}
Arrhenius frequency factor[8] (A_h)		0.01 m^3 mol^{-1} s^{-1}
Arrhenius activation energy[8] (E_h)		35 kJ mol^{-1}
Temperature (T)		20 ˚C

[1]Chowdhury et al. (2024) [2]Rashwan et al. (2022) [3]Asad et al. (2022) [4]Van Loon et al. (2007) [5]SKB (2010) [6]Archie (1950) [7]Papry et al. (2023) [8]Rickard (1997)

5.3 Results and Discussion

5.3.1 Influence of Anion Exclusion on Species Diffusion

To explore the influence of anion exclusion on species diffusion and ensure correct boundary conditions were used in the models, a 1-D Cl^- diffusion model was developed and compared to the experimental results from Chowdhury et al. (2021). Because Cl^- is a conservative tracer, mass retardation processes (reaction or sorption) were not included in the Cl^- diffusion model. The Cl^- diffusion model used the same transport conditions of Cl^- (inlet and outlet concentrations) from Chowdhury et al. (2021) and implemented 1,000 mol m^{-3} (1 M Cl^-) and 0 mol m^{-3} Cl^- constant concentration boundary at the inlet and outlet, respectively (see SM, Table S.1). The effective diffusivity of Cl^- was defined as a function of Cl^- diffusion accessible porosity (ϵ_{Cl^-}) following Van Loon et al. (2007):

$$\epsilon_{Cl^-} = \epsilon_{Cl^-}^{max} - Ae^{-B[Cl^-_{(aq)}]} \quad (5.11)$$

$$D_{eCl^-} = D_w \epsilon_{Cl^-}^{n} \quad (5.12)$$

where $\epsilon_{Cl^-}^{max}$ is the interparticle pore space, A and B are density dependent constants, D_{eCl^-} and D_{wCl^-} are Cl^- effective diffusion coefficient and Cl^- diffusion coefficient in water, respectively, and n is the Archie's law (Archie 1950) tortuosity dependent exponent (see SM, Table B.S.1). Above definition of effective Cl^- diffusivity (Eqs. 5.11-5.12) was used to model anion/Cl^- exclusion in bentonite pore space, which lowered the diffusion accessible porosity (Van Loon et al. 2007). The cumulative Cl^- mass at the outlet was compared (Figure 5.3) and a good fit (R^2 = 0.92) between the experimental and numerical Cl^- mass was obtained which indicates proper implementation of boundary conditions in the C model (i.e., 1,000 ppm HS^- constant concentration boundary at the inlet and 0 ppm HS^- constant concentration boundary at the outlet). The incorporation of Cl^- exclusion in the model (i.e., $D_{eCl^-} = f(\epsilon_{Cl^-})$ through Eqs. 5.11-5.12) resulted in a better fit (R^2 =0.92)

between the experimental and numerical Cl^- mass than when no Cl^- exclusion was modelled (i.e., constant $D_{eCl^-} = 1\times 10^{-11}$ m^2 $s^{-1,}$ $R^2 = 0.91$). The better fit indicates that diffusive anion transport through bentonite can be well-predicted when anion exclusion is considered (see SM, Figure B.S.2 for time and space dependent D_{eCl^-} and ϵ_{Cl^-}). In particular, a linear profile was established early when anion exclusion was included (see the inset in Figure 5.3). Altogether, the comparison in Figure 5.3 highlights that the anion exclusion is likely occurring in bentonite.

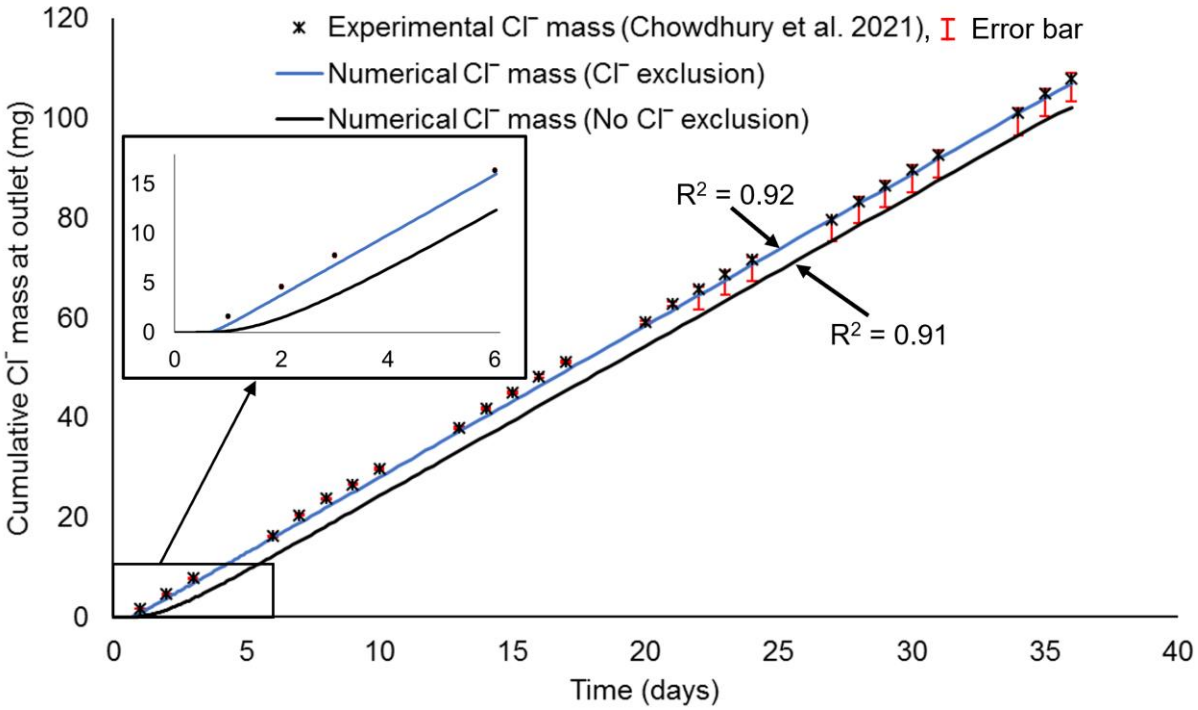

Figure 5.3: The cumulative Cl^- mass from Chowdhury et al. (2021) was compared to the two numerical models. The red bars represented the error bars in the experimental data, which are not visible on most data points because of the small errors.

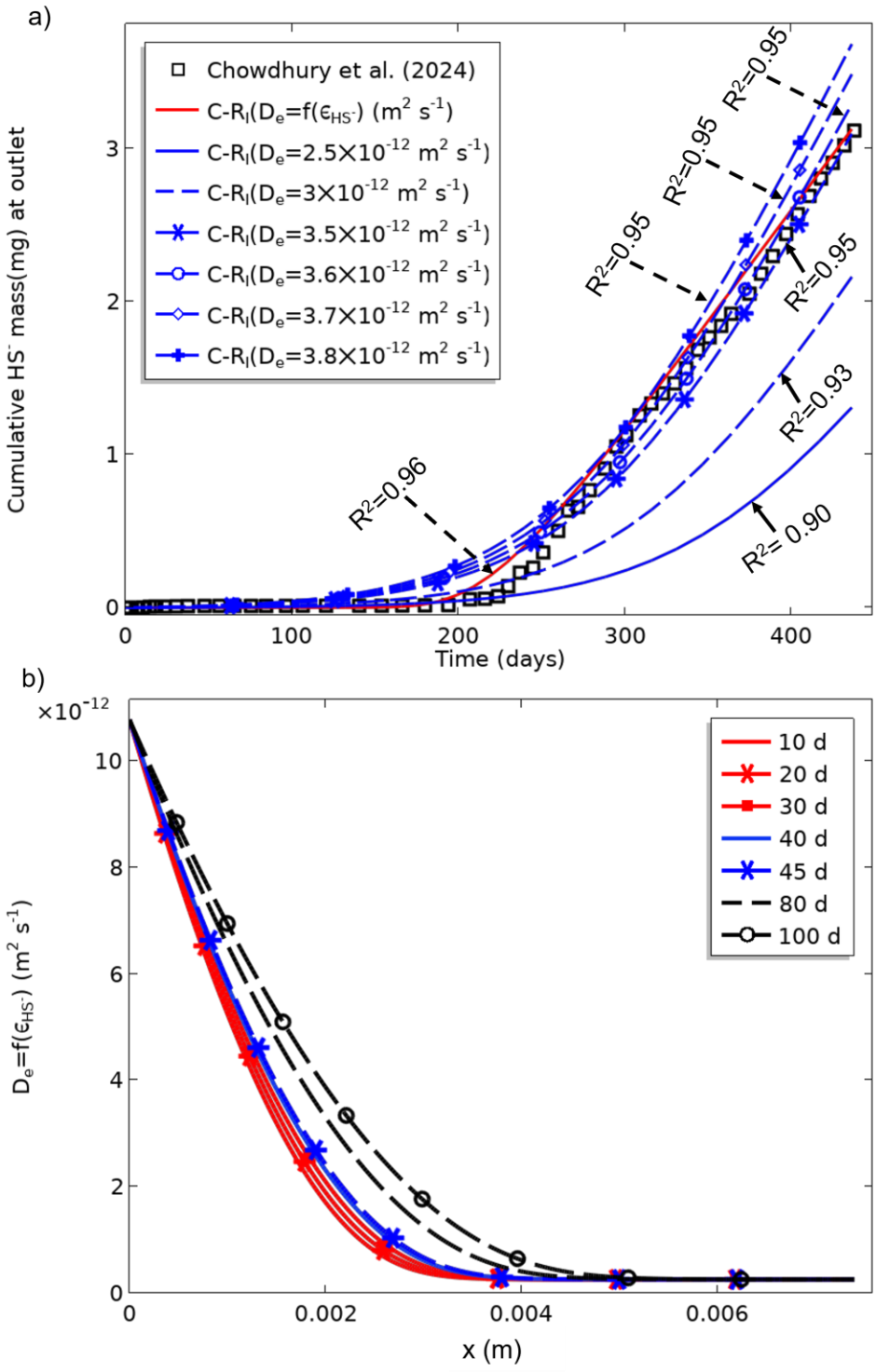

Figure 5.4: a) Cumulative HS^- mass at the compacted bentonite outlet in the C-R_I model for time and space dependent D_e (i.e., Eq. 5) and constant D_e and b) time and space dependent D_e (i.e., Eq. 5.5) in the C-R_I model. Note that the initial Fe^{2+} concentration was kept at 700 mol m^{-3} and x represented the bentonite length.

Since HS^- is also an anion, anion/HS^- exclusion was simulated in all 1-D models. The variation in HS^- diffusion accessible porosity due to anion/HS^- exclusion was implemented through Eq. 5.4 and the variation in HS^- effective diffusivity due to variation in HS^- diffusion accessible porosity was implemented through Eq. 5.5. In other words, HS^- effective diffusivity was implemented as a function of HS^- diffusion accessible porosity (i.e., $D_e=f(\epsilon_{HS^-})$) resulting in diffusion being spatially and temporally dependent. To explore the significance of anion/HS^- exclusion effect, cumulative HS^- mass for time and space dependent D_e (i.e., $D_e=f(\epsilon)$) was compared to the cumulative HS^- mass for various constant D_e values (Figure 5.4a). As seen in Figure 5.4a, constant De values (3.5×10^{-12} $m^2\ s^{-1}$ and 3.6×10^{-12} $m^2\ s^{-1}$) described the laboratory HS^- mass profile well ($R^2 = 0.95$) although still overestimated the diffusion at early times; however, a slight increase in constant D_e (from 3.6×10^{-12} $m^2\ s^{-1}$ to 3.7×10^{-12} $m^2\ s^{-1}$) over estimates the HS^- mass in later times (around 400 days). The HS^- mass profile was well-described when anion/HS^- exclusion effect was included in the model ($R^2 = 0.96$, Figure 5.4a). Therefore, the comparison in Figure 5.4a shows that D_e could be changing spatially and temporally (as seen by simulating anion/HS^- exclusion effect), which creates an effective HS^- diffusion path in bentonite (Figure 5.4b).

5.3.2 HS^- Adsorption Models' Results

The HS^- sorption parameters were fitted to a laboratory HS^- breakthrough curve and these values are compared to parameters measured from batch laboratory experiments, as discussed below.

5.3.2.1 Fitting HS^- Adsorption Parameters

The HS^- sorption parameters for compacted bentonite have not been experimentally determined; as such, the sorption parameters (i.e., K_d, K_{L,HS^-} and C_{P,max,HS^-}) were fitted to an experimental HS^- breakthrough curve from Chowdhury et al. (2024) (see Figure 5.5). The modelled HS^- breakthrough at the compacted bentonite outlet was significantly delayed (i.e., ~11,000 and ~29,000 days) compared to experimental observations when high K_d values were used, which were measured from powdered bentonite sorption experiments from Papry et al. (2023). The range of breakthrough times reflects the varying K_d values at different liquid to solid (L:S) ratios (i.e., K_d = 0.34 $m^3\,kg^{-1}$, L:S=200 and K_d = 0.90 $m^3\,kg^{-1}$, L:S=1000). (Gupt et al. 2019) describes that sorption parameters vary with L:S ratios because of inhibition effects in sorption experiments that limit ion/bentonite interactions – due to the formation of a gel-like consistency – which increases with L:S. Moreover, note that all sorption experiments from Papry et al. (2023) used small aqueous HS^- concentrations (i.e.,$\sim 1 - 6$ ppm starting concentration) compared to the concentrations used in the diffusion experiments from Chowdhury et al. (2024) (i.e., 1000 ppm at the inlet). Therefore, the application of a linear sorption model may not be appropriate at these high concentrations, as the measured K_d values did not account for a maximum number of sorption sites. Consequently, an artificially low sorption

coefficient (i.e., K_d = 0.005 m^3 kg^{-1}) was needed to match the C-S_L model and experimental results.

Like the C-S_L model, the HS^- breakthrough at the compacted bentonite outlet was delayed when using the C-S_{NL} model, although to a lesser extent (~700 days) when the non-linear sorption parameters from experiments with L:S=1000 (K_{L,HS^-}=5.85 m^3mol^{-1} and C_{P,max,HS^-} =0.24 mol kg^{-1}) were used. An earlier HS^- breakthrough was modelled with non-linear sorption parameters measured from experiments with L:S=200 (K_{L,HS^-}=41.35 m^3 mol^{-1} and C_{P,max,HS^-} =0.03 mol kg^{-1}). As mentioned above, this range of sorption behaviour is anticipated to be due to the inhibitory effects, which increased in experiments with decreasing L:S ratios. However, despite this variability in non-linear sorption parameters, Figure 5.5 shows that they provided close predictions of the sorption effects observed in the experiments from Chowdhury et al. (2024). The best fit between experimental and modelled HS^- mass profiles was obtained using: K_d = 0.005 m^3 kg^{-1} in C-S_L model, R^2 = 0.95; K_{L,HS^-} =1 m^3 mol^{-1} and C_{P,max,HS^-} =0.08 mol kg^{-1} in C-S_{NL} model, R^2 =0.96 (see SM for K_d sensitivity and K_{L,HS^-} and C_{P,max,HS^-} sensitivity; Figures B.S.4 a and B.S.4b, respectively).

Additionally, both linear and non-linear sorption parameters estimated through data fitting followed the trend observed in other studies (Tachi et al. 2014; Oscarson et al. 1994), The C-S_{NL} model is more representative of the experimental behaviour than the C-S_L model. This improved model behaviour can be seen in Figure 5.5 as the C-S_{NL} model better matched the HS^- breakthrough at ~200 days than the C-S_L model. Moreover, the

C-S_{NL} model accounted for bentonite's maximum sorption capacity and provided relatively good predictions using measured values from experiments. On the other hand, the C-S_L model required very small sorption parameters relative to those measured from experiments to fit the experimental data (i.e., the fitted K_d was two orders of magnitude smaller than the K_d values measured from experiments).

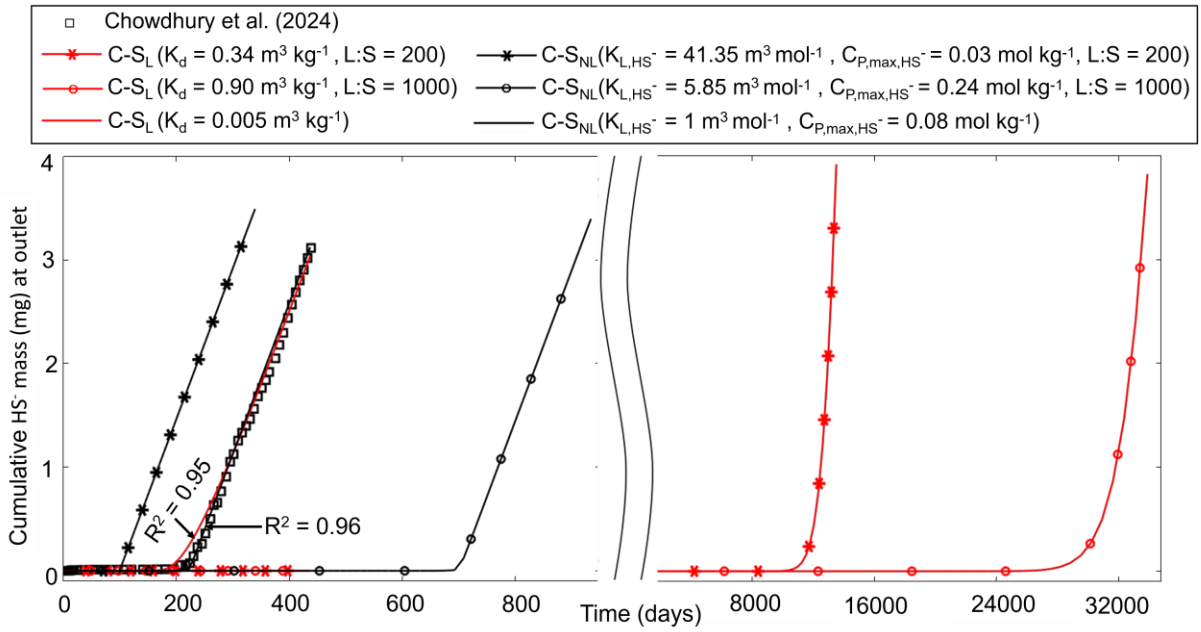

Figure 5.5: Cumulative HS^- mass at the compacted bentonite outlet in the C-S_L and C-S_{NL} models from varying the sorption parameters K_d and K_{L,HS^-} and C_{P,max,HS^-}, respectively. The models were compared to the cumulative HS^- mass breakthrough curve from Chowdhury et al. 2024. Note that the K_d= 0.34 m^3kg^{-1} (L:S=200) and K_d= 0.90 m^3kg^{-1} (L:S=1000); K_{L,HS^-}= 41.35 m^3 mol^{-1} and C_{P,max,HS^-} =0.03 mol kg^{-1} (L:S=200) and K_{L,HS^-}= 5.85 m^3 mol^{-1} and C_{P,max,HS^-} =0.24 mol kg^{-1} (L:S=1000) values were obtained from batch experiments of powdered bentonite (Papry et al. 2023).

5.3.3 HS^- Reaction Model's Results

Since HS^- is a reactive species, the reaction model was implemented and expected trends in species evolution were evaluated (e.g., Fe^{2+} decrease due to FeS formation) (see SM, Figure B.S.5). The initial Fe^{2+} in the C-R_I model was fitted to experimental breakthrough curve and reaction mechanisms were explored which are discussed below.

5.3.3.1 *Sensitivity of HS^- Mass Profile to Initial Available Iron*

Given the potentially central role of Fe^{2+} in governing HS^- flux through bentonite, a sensitivity study for the C-R_I model was undertaken to see how bentonite's Fe^{2+} content impacts the cumulative HS^- mass profile at the outlet and compare that to both a HS^- transport model (C model) and experimental data from (Chowdhury et al. 2024) (Figure 5.6). All C-R_I models exhibited a delayed HS^- mass breakthrough at the outlet compared to the C model as FeS production removed HS^- from the bentonite porewater (Eqs. 5.9 and 5.10). It was observed (Figure 5.6) that increases in initial Fe^{2+} concentration further delayed the onset of HS^- diffusion due to increased reaction rate (Eq. 5.9). An initial Fe^{2+} concentration of 700 mol m^{-3} exhibited the best fit to the experimental HS^- mass from (Chowdhury et al. 2024). The available iron content may be smaller than 700 mol m^{-3} as it was assumed that HS^- retardation is due to HS^- reaction only (i.e., C-R_I model) while other processes (Figure 5.1) do not affect HS^- retardation. Recent laboratory test measured an iron content of 24 mol m^{-3} of extractable (weakly leachable) iron in a MX-80 bentonite sample (ρ_H=1700 kg m^{-3}) when the porewater is free from external species (e.g., HS^-, Cl^-) (Surface Science 2024). However, reactivity of iron in bentonite increases when HS^- is present in excess (~100 mM or 100 mol m^{-3}) (Hadi et al. 2023), which may contribute to increased amount of available iron for reaction in bentonite. It is worth noting that a constant source of 1,000 ppm HS^- (30.2 mol m^{-3}) was used by Chowdhury et al. (2024) in the HS^- diffusion experiment, which is a high HS^- concentration (i.e., many orders of magnitude above the 30-90 ppb anticipated in the Canadian DGR). The best fit initial Fe^{2+} concentration (700 mol m^{-3}) in the bentonite differs from the total iron values calculated as ≈950 mol m^{-3}, respectively, which is 4% of the total bentonite mass (Gilmour et al. 2021; Karnland 2010). Indeed, the 950 mol m^{-3} simulation (Figure 5.6) exhibits an

even greater delay in HS^- outflow. While this may suggest that iron content in bentonite affords some layer of protection against HS^- corrosion, it is worth mentioning that the differences in onset of HS^- diffusion between 700 and 950 mol m^{-3} is likely negligible over the lifespan of the repository (see Section 5.3.5). Even so, the comparison provides insight into available Fe^{2+} content in the bentonite which may help assess long term DGR design relevant to HS^- transport.

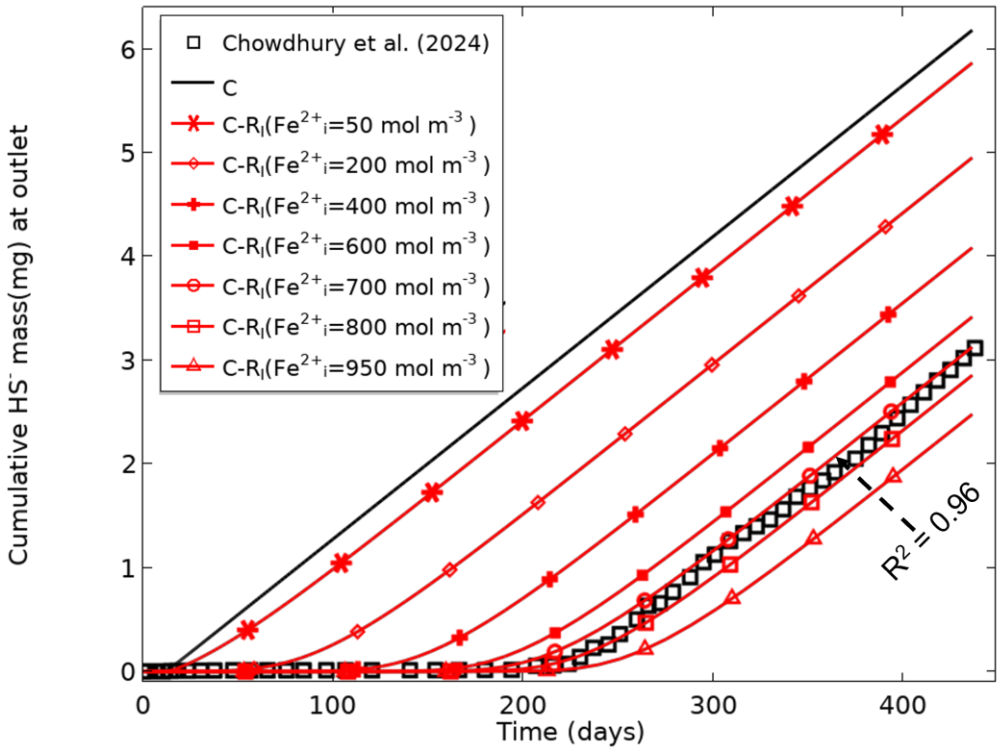

Figure 5.6: Cumulative HS^- mass at the compacted bentonite outlet in the C-R_I model from varying the initial Fe^{2+} concentration compared to the cumulative HS^- mass from Chowdhury et al. 2024.

5.3.3.2 *Reaction Mechanism*

A sensitivity study for the C-R_I model was undertaken to see how the Arrhenius reaction frequency factor, A_h, impacts the cumulative HS^- mass profile at the outlet and compare that to both a HS^- transport model (C model) and experimental data from (Chowdhury et

al. 2024) (Figure 5.7). This sensitivity provided valuable insights on the reaction mechanisms. The Arrhenius activation energy, E_h was kept at 35 kJ mol^{-1} (Rickard 1997; Cloet et al. 2017) as the decrease in rate constant (Eq. 5.10) due to a change in E_h from 5 to 100 kJ mol^{-1} is only ≈3.5 % (under constant A_h), while increase in rate constant due to a change in A_h from 0.01 m^3 mol^{-1} s^{-1} to 0.1 m^3 mol^{-1} s^{-1} is 900% (under constant E_h). As seen in Figure 5.7, the HS^- mass profile in the C-R_I model is only sensitive to low A_h values (e.g., 0.01-1 m^3 mol^{-1} s^{-1}) and does not vary with high A_h values (e.g., 100-10,000 m^3 mol^{-1} s^{-1}). In other words, the FeS formation (Eq. 5.8) occurs instantaneously when a high A_h value is used. This instantaneous FeS formation in the C-R_I model represents an equilibrium state when kinetic reaction rates (Eq. 5.9) do not affect the reaction progress. Therefore, the equilibrium reaction occurs at a rate (see SM, Figure B.S.6 for reaction rates due to high Ah values), which is achieved when reactants (HS^- and Fe^{2+}) react (i.e., collide) immediately through a high collision frequency (A_h). Altogether, these results highlight an equilibrium state (using high A_h) and a kinetic state (using low A_h value) of the FeS formation reaction which could occur in the experiment. In this case, since the experimental work fits the low A_h values, it is likely that FeS formation occurs following a kinetic reaction.

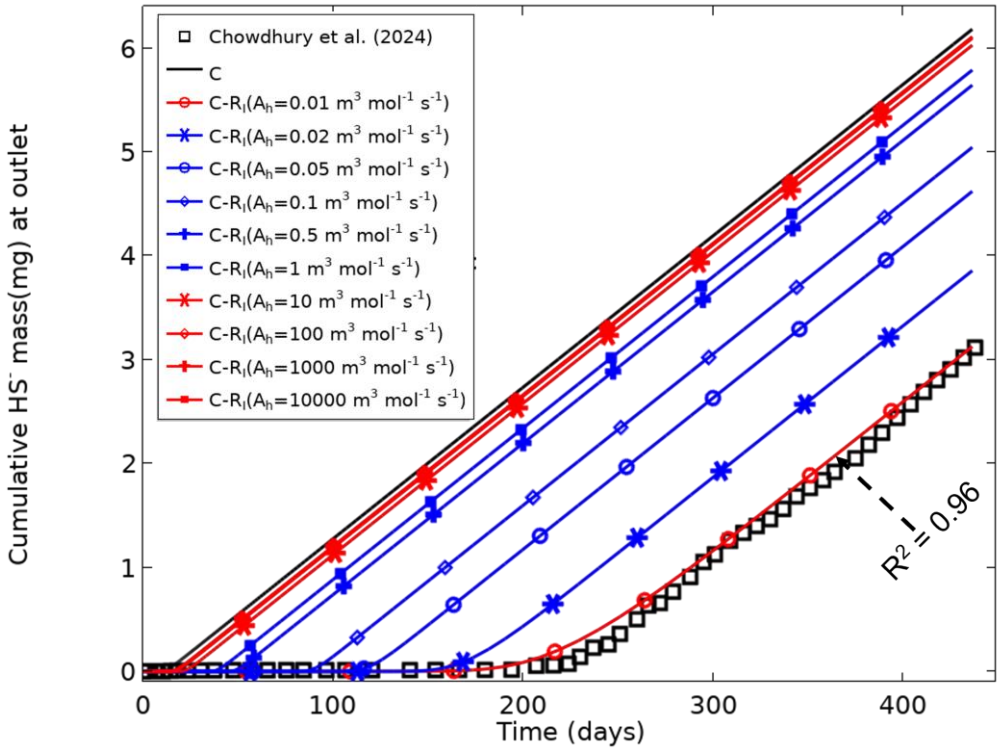

Figure 5.7: Cumulative HS^- mass at the HCB outlet in the C-R_I model from varying the A_h and comparison to the cumulative HS^- mass from Chowdhury et al. 2024. Note that initial Fe^{2+} concentration and E_h were kept at 700 mol m^{-3} and 35 kJ mol^{-1}, respectively.

5.3.4 Modelled HS^- Transport Dynamics

The cumulative HS^- outlet mass for the C-S_L, C-S_{NL}, and C-R_I models was compared to the experimental data (Chowdhury et al. 2024) (Figure 5.8). All 1-D models provided a good correlation with experimental result (R^2=0.95-0.96) suggesting that kinetically irreversible HS^- and Fe^{2+} reaction or HS^- adsorption were influencing the behaviour in the experimental system. Although it is not possible to ascertain which process is actually occurring in the system, the results show that HS^- is definitely being retained by the bentonite. The results also highlight that similar HS^- retardation pattern in compacted bentonite can be obtained using adsorption or reaction models which is helpful to understand influence of reactive transport on HS^- corrosion (Section 5.3.5).

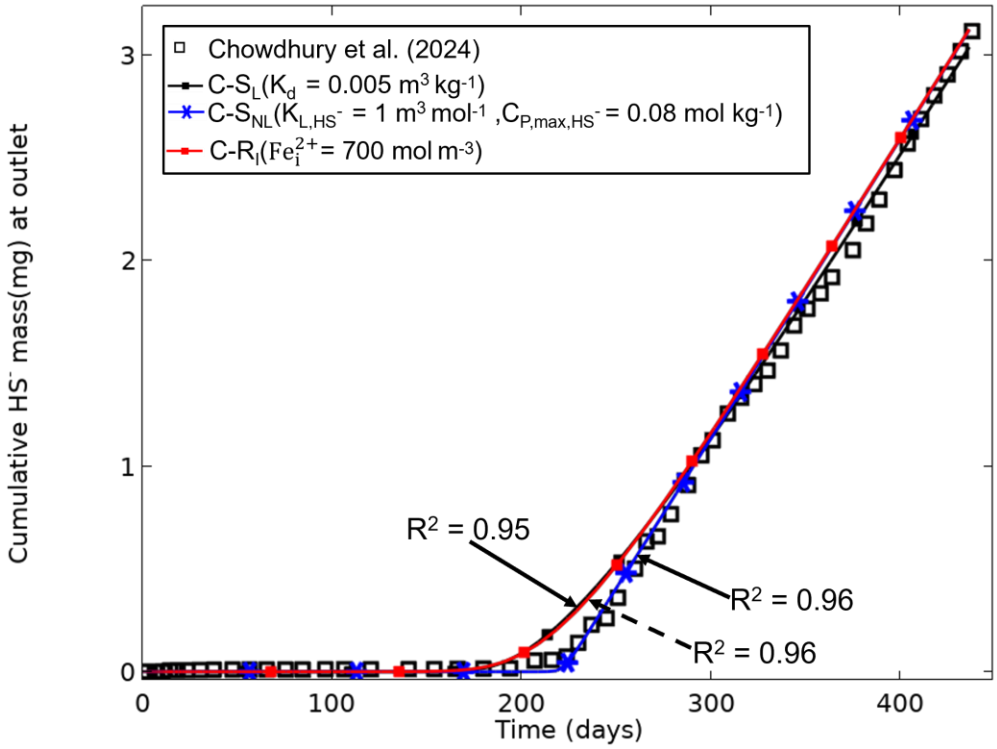

Figure 5.8: Cumulative HS^- mass at the compacted bentonite outlet in the C-S_L, C-S_{NL}, and C-R_I models compared to experimental data from Chowdhury et al. 2024.

5.3.5 3-D HS^- Transport and Reaction Models

While previous sections discuss 1-D reactive transport models, this section uses a 3-D reactive transport model to simulate HS^- transport in the Canadian DGR (crystalline rock host) to understand the influence of reactive transport on UFC corrosion. As the C-S_L, C-S_{NL}, and C-R_I models provided a better description of HS^- transport dynamics (as shown in previous section), they were individually coupled to the THC model for bisulfide transport (these are now referred to as THC-S_L, THC-S_{NL}, and THC-R_I models). The THC model assessed corrosion rates due to HS^- transport (1 ppm constant HS^- source at the rock-bentonite interface) through a DGR under varying thermal and hydraulic conditions utilising parameters relevant to NWMO case studies (Gobien et al. 2016, 2018; Sykes et al. 2011; Dixon 2019; Dixon et al. 2018; Guo 2016, 2018), and other sources (Baumgartner 2006; SKB 2010). The UFC heating accelerated HS^- corrosion through

increasing HS^- diffusivity, but the saturation process delayed the onset of HS^- corrosion. However, neither process strongly influenced the projected HS^- corrosion depth over the design life of 1 million years, as ≈80% of the total corrosion occurred during steady-state conditions (see Rashwan et al. (2022); Asad et al. (2022) for additional details). The THC-S_L, THC-S_{NL}, and THC-R_I models coupled HS^- transport (Rashwan et al. 2022) with linear HS^- adsorption (Eq. 5.6), non-linear HS^- adsorption (Eq. 5.7), and HS^- reaction (Eqs. 5.8-5.10), respectively, in a DGR under varying thermal and hydraulic conditions. In the THC-S_L model, the fitted sorption parameter (K_d = 0.005 $m^3\,kg^{-1}$) was included. In the THC-S_{NL} model, the fitted sorption parameters (K_{L,HS^-} =1 $m^3\,mol^{-1}$ and C_{P,max,HS^-} =0.08 mol kg^{-1}, see section 5.3.2.1) were included. Similarly, in the THC-R_I model, the initial concentration of reactant Fe^{2+} was assumed to be equal to the available iron of 700 mol m^{-3} as obtained from the comparison with the experiments (see section 5.3.3.1). The initial concentrations of reactant HS^- and products FeS and H^+ were set to 0 mol m^{-3}. The effective diffusivity of HS^- was defined following Rashwan et al. (2022). The effective diffusivities for Fe^{2+} and H^+ were defined as a function of species-specific diffusion coefficient in water (which varies with temperature and viscosity), saturation, porosity, and Archie's law tortuosity dependent exponent following Rashwan et al. (2022) and Archie (1950). The effective FeS diffusivity was set as a very low value of 1×10^{-15} $m^2\,s^{-1}$ to prevent migration, assuming immobile solid FeS with low solubility (Behazin et al. 2021). The initial and boundary conditions of the THC-S_L and THC-S_{NL} models simulated HS^- transport through the bentonite under varying thermal and hydraulic conditions and how HS^- was adsorbed based on the fitted sorption parameters (Eq. 5.6 and Eq. 5.7, respectively). The initial and boundary conditions of the THC-R_I model simulated HS^- transport through the bentonite

under varying thermal and hydraulic conditions and simulated FeS production based on the reaction rate (Eq. 5.9).

The THC-S_L, THC-S_{NL}, and THC-R_I models were run for a reference period of 1 million years (i.e., the Canadian DGR design life). To understand the effect of HS^- reaction and HS^- adsorption on HS^- evolution, HS^- flux from the THC model was compared to the THC-S_L,THC-S_{NL}, and THC-R_I models (Figure 5.9). In addition, spatial distribution of HS^- flux was also explored to visually understand HS^- retardation due to HS^- reaction and HS^- adsorption (Figure 5.10). In the THC-S_L model, HS^- adsorption delayed the onset of HS^- diffusion and HS^- did not reach the UFCs until ≈50 years (Figure 5.9 and Figure 5.10b). In other words, aqueous HS^- was reduced due to adsorption until the interaction between HS^- and bentonite surface, modelled by linear adsorption, ceased after ≈50 years. In the THC-S_{NL} model, HS^- adsorption delayed the onset of HS^- diffusion and HS^- did not reach the UFCs until ≈700 years (Figure 5.9 and Figure 5.10c). In other words, aqueous HS^- was reduced until the maximum sorption capacity was reached in ≈700 years. In the THC-R_I model, HS^- reaction delayed the onset of HS^- diffusion and HS^- did not reach the UFCs until ≈800 years (Figure 5.9 and Figure 5.10d) as the HS^- flux reduction and the FeS production continued until ≈800 years as the initial Fe^{2+} decreased over time (Eq. 5.9). The HS^- reaction had no impact on HS^- evolution after ≈800 years. In all the models, HS^- diffusion started after the HS^- retardation period (≈50-800 years) and HS^- reached the UFCs at ≈54 to 804 years (Figures 5.10b-5.10d). In other words, it took additional 4 years (irrespective of models) for HS^- to reach the UFCs after the HS^- retardation period which is approximately equal to the diffusion time lag (t_L) from the rock bentonite interface to

the UFCs (i.e., $t_L \sim \frac{x^2}{D_w} \sim 4 \text{ years}, x = 0.343 \text{ m}$) following Nield and Bejan (2013). The total HS^- corrosion depth, measured using the microbiologically influenced corrosion equation presented in Rashwan et al. (2022), was nearly identical in the THC-S_L,THC-S_{NL}, and THC-R_I models (Figure 5.11) as the HS^- diffusion delays (i.e., ≈50-800 years) are relatively short compared to the million-year timeframe. The results therefore highlight that reactive processes in bentonite do not affect long-term HS^- corrosion due to early cessation of the reactive processes.

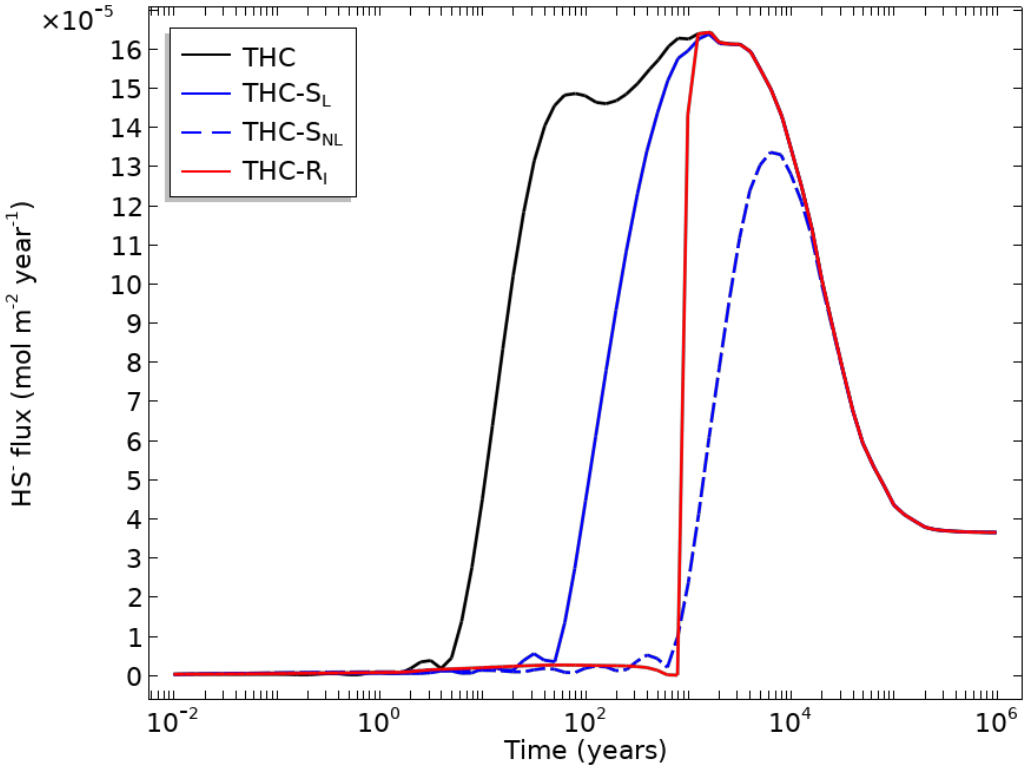

Figure 5.9: Bisulfide flux estimated at upper UFC end cap in the THC, THC-S_L, and THC-S_{NL}, and THC-R_I models.

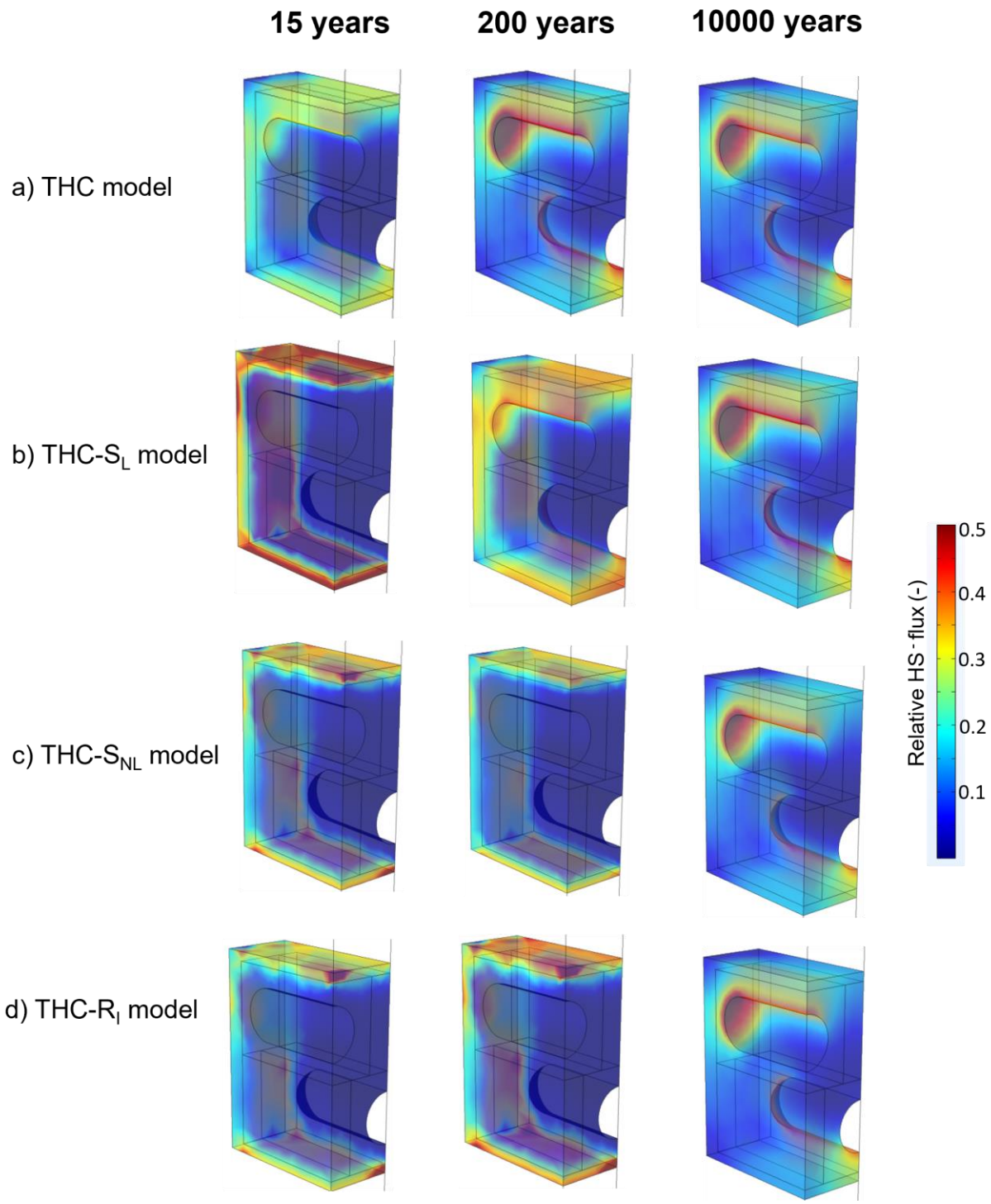

Figure 5.10: The simulated spatial distribution of relative HS^- flux (i.e., HS^- flux ($\dot{N}''_{HS}$) compared to maximum HS^- flux ($\dot{N}''_{HS_{max}}$) or $\dot{N}''_{HS}/\dot{N}''_{HS_{max}}$) over time in the 3-D a) THC model, b) THC-S_L model, c) THC-S_{NL} model, and d) THC-R_I model

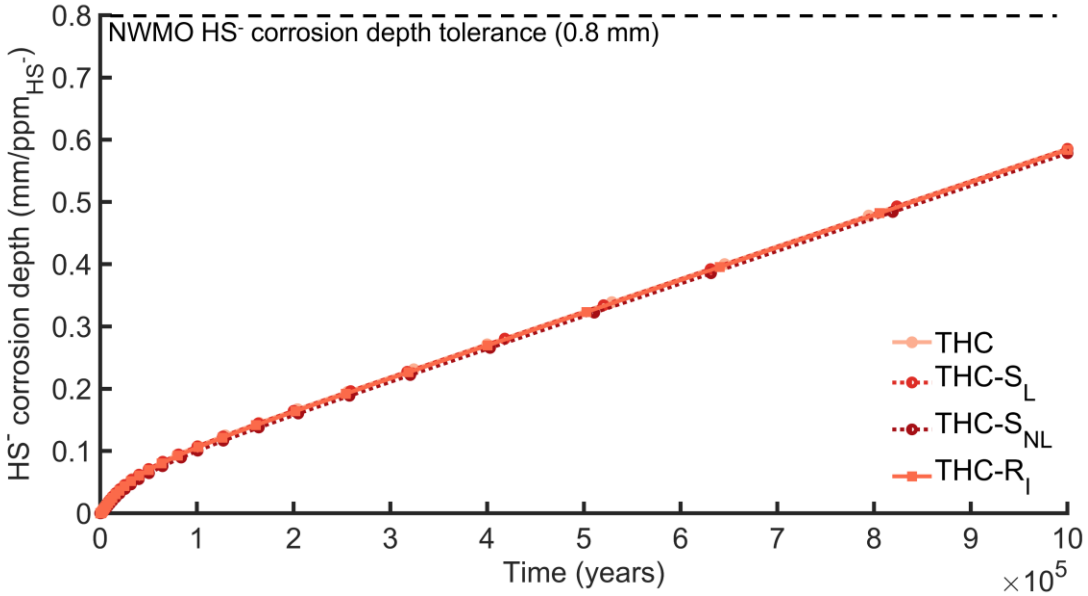

Figure 5.11: HS^- corrosion depths in the THC, THC-S_L, THC-S_{NL}, and THC-R_I models. Note that the horizontal axis represents a linear timescale.

5.4 Conclusions

This study outlined the development, implementation, and results of three 1-D models, which simulate linear and non-linear HS^- adsorption onto the compacted bentonite (referred to as the C-S_L and C-S_{NL} models, respectively) and kinetically irreversible HS^- reaction of HS^- onto compacted bentonite (referred to as the C-R_I model). The C-S_L and C-S_{NL} models simulated HS^- transport and adsorption onto bentonite using linear and non-linear sorption parameters, respectively. The C-R_I model simulated HS^- transport and reaction with available Fe^{2+} in the bentonite (i.e., FeS production) using kinetically irreversible reaction approach. These models were investigated and compared to laboratory data to understand geochemical evolution relevant to HS^- and Fe^{2+} reaction, and explored effects of HS^- adsorption and HS^- reaction on HS^- diffusion breakthrough curves. These three models were then coupled individually to a previously published 3-D thermal-hydraulic-chemical (THC) model for bisulfide transport (Rashwan et al. 2022) and the overall corrosion rate at the UFC was compared. Altogether, this study inferred how

HS^- adsorption and HS^- reaction with Fe^{2+} influence HS^- transport using a comparative approach between modelled and laboratory HS^- diffusion profiles, which uncovered important implications for HS^- corrosion using 3-D THC HS^- transport and reaction model of the Canadian DGR. Altogether, this study provided valuable implications for DGR design, such as:

- Transport of HS^- through bentonite may be governed by anion exclusion effects.
- All 1-D models provided a good correlation with experimental result suggesting that kinetically irreversible HS^- or Fe^{2+} reaction and/or HS^- adsorption were influencing the behaviour in the experimental system. Although it is not possible to ascertain which process is actually occurring in the compacted bentonite, the results show that HS^- is definitely being retained by the bentonite.
- Almost identical HS^- retardation pattern in compacted bentonite was obtained using adsorption or reaction models suggesting that reactive transport of HS^- can be approximated using either adsorption or reaction.
- Although the non-linear HS^- adsorption model is more appropriate as it accounts for bentonite's sorption capacity, both the linear and non-linear HS^- adsorption models showed a similar fit to the experimental HS^- breakthrough curve.
- The iron content in groundwater was assumed to be zero. If there is iron in groundwater, the kinetically irreversible HS^- and Fe^{2+} reaction model could be used to explore effect of additional iron on HS^- transport.
- Although iron content in bentonite and bentonite's sorption affinity (modelled through adsorption) affords some layers of protection against HS^- corrosion through delaying HS^- breakthrough (i.e., by forming FeS due to the reaction

between Fe^{2+} and HS^-, and thereby retarding aqueous HS^- through adsorption), the ≈50-800 years delay is short compared to the lifespan of the repository (1 million years).

- The relatively short HS^- diffusion delay (≈50-800 years) did not impact long-term HS^- corrosion over a million-year timeframe. These results therefore highlight that the reactive processes in bentonite ultimately do not affect HS^- corrosion due to early cessation of the reactive processes.

Chapter 6 Discussion and Conclusions

6.1 Discussion

The deep geological repository (DGR) design involves an engineered barrier system (EBS) within a low permeability host rock that serves as a natural barrier (Hall et al. 2021). The EBS includes copper coated steel used fuel containers (UFCs) within highly compacted bentonite (HCB). The repository is designed to last many thousands of years to ensure people and the environment are protected. Over that timespan , different hydrogeological and geochemical conditions can evolve in the repository (King et al. 2017). These include bentonite saturation and swelling (as water infiltrates into bentonite from the host rock), heating (as used fuel generates heat), phase change (i.e., evaporation and condensation), geochemical reactions, and microbial sulphate reduction. Although the copper is thermodynamically stable in oxygen-free environments (King et al. 2013, Senior et al. 2020, 2023), it is potentially susceptible to corrosion from bisulfide (HS^-) produced from microbiological metabolic processes within the host rock or at the clay-rock interface during anoxic conditions (microbial sulphate reduction). Depending on site-specific conditions (e.g., host rock type, groundwater chemistry, microbial growth conditions), HS^- could transport through the HCB to the UFC surface, corrode the copper coating, and compromise the long term performance of UFCs (Hall et al. 2021):

$$2Cu_{(s)} + HS^-_{(aq)} + H^+ \leftrightarrow Cu_2S_{(s)} + H_{2(g)} \quad (6.1)$$

As HS^- transport through bentonite may occur over long periods, long term hydrogeological and geochemical conditions may affect HS^- transport and understanding

the effect of these conditions can help ensure safe and long-term performance of copper as a corrosion barrier.

In addition, hydrogen (H_2), produced from HS^- corrosion (Eq. 6.1) may also affect DGR integrity. The produced H_2 will be dissolved in the water saturated pore space as the confining pressures at the DGR level (i.e., 500-800 m below surface) increases its solubility limit (Muhammed et al. 2022). Subsequently if the produced H_2 accumulates and surpasses the H_2 solubility limit, it may also partition to gaseous phase over the DGR design-life (i.e., one million years). Aqueous H_2 may become trapped in the DGR's HCB or transported through the DGR to the surrounding host rock (King 2012), which will be governed by rock and clay diffusive properties or fractures (e.g., which would act as preferential pathways). Gaseous H_2 may also create preferential pathways in the HCB that may compromise UFC protection (King 2012). Therefore, H_2 poses numerous risks in a DGR, and it is important to understand its dynamics over the long DGR design-life. Altogether, bisulfide and hydrogen transport assessment are complex and require robust numerical models.

Therefore, the objective of this research is to estimate bisulfide corrosion over the DGR lifespan (1 million years), and to better understand how DGR hydrogeological and geochemical processes influence bisulfide corrosion. In addition, this research also examines hydrogen transport in the DGR. Towards these goals, numerical models in COMSOL were developed to answer these key research questions (RQs):

1. *How long will it take to fully saturate the bentonite (Chapter 3)?*

2. *How do various hydrogeological properties affect key processes in the DGR (Chapter 3)?*
3. *What is the overall influence of saturation and temperature (heating from used fuel) on HS^- transport and corrosion (Chapter 3)?*
4. *How does H_2 from HS^- corrosion* evolve *in the DGR (Chapter 4)?*
5. *Does produced H_2 from HS^- corrosion form gas (Chapter 4)?*
6. *How do geochemical reactions (HS^- adsorption, HS^- and Fe^{2+} reaction) affect HS^- transport and corrosion (Chapter 5)?*

These research questions are answered through numerical models presented in chapters of this dissertation. Chapter 3 includes a model of bisulfide transport under thermal (T), hydraulic (H), and chemical (C) species transport (diffusion) conditions - referred to as the thermal- hydraulic-chemical (THC) model. Chapter 4 includes a model of hydrogen transport, which is based on the THC model and referred to as the THC-H_2 model. Chapter 5 includes models of bisulfide transport and adsorption or geochemical reactions, which are termed as the THC-S or THC-R models, respectively. Therefore, chapter 4 (THC-H_2) and chapter 5 (THC-S or THC-R) are connected to chapter 3 (THC). The key results from these chapters are discussed in the next sections.

6.2 Key Results from THC, THC-S, THC-R, and THC-H_2 Models (Chapters 3, 4, and 5)

This section discusses key results from the THC, THC-S, THC-R models and connected to the research questions (RQs) stated above.

6.2.1 3-D THC Model

6.2.1.1 Assumptions in the THC Model

The THC model has been robustly developed to aid in the performance assessment of the Canada's DGR. The developed THC model is designed to be flexible to accommodate additional processes and site-specific information as it becomes available. The processes highlighted in red in Figure 6.1 represent the processes which are modelled in the THC study.

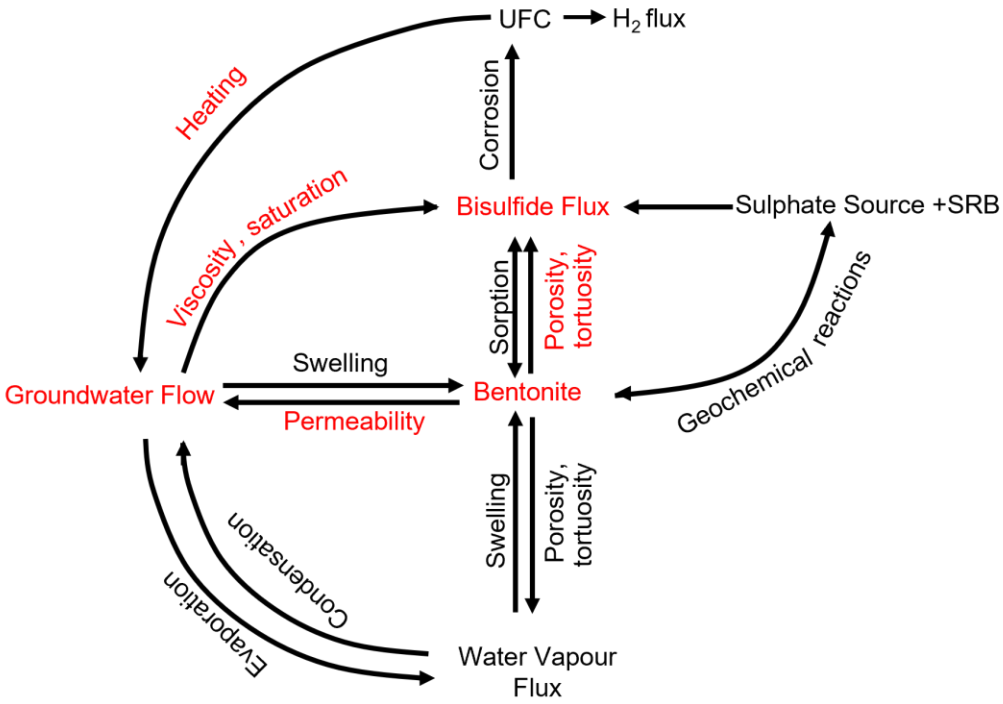

Figure 6.1: Coupled hydrogeological and geochemical processes governing HS^- corrosion; red font indicates modelled processes in the THC model

The HS^- corrosion estimate from the THC model is conservative due to some assumptions, such as:

- Bisulfide concentration is conservatively chosen to be a constant concentration of 1 ppm. Previous studies by Gascoyne (1997) and Kremer (2017) reported 30-90

ppb as the expected HS^- concentrations in Canadian shield, which are over an order of magnitude lower than 1 ppm. Decreasing the HS^- concentration will lower HS corrosion. It is also unlikely that the concentration would be constant over the timeframe modelled.

- No sorption and geochemical reactions, or microbial processes are assumed to be occurring within the bentonite; including these reactions would decrease the amount of bisulfide that would be transported to the UFC.
- Bentonite is assumed to swell instantly, and bentonite permeability is assumed to be constant throughout the simulation. Including bentonite swelling process may increase bisulfide transport in the early times due to higher bentonite permeability; this would have a bigger impact in the crystalline domain as the bentonite permeability has a more controlling impact on diffusion
- No vapour transport or evaporation or condensation is modelled in the system; including these processes would lead to cooling of the system resulting in lower bisulfide transport.

Adsorption (as a part of sorption) and a geochemical reaction were included in the THC-S and THC-R models, respectively, and discussed in section 6.2.2.

6.2.1.2 3-D THC Model Results

The THC model was run for a reference period of 1 million years with an initial bentonite saturation of 67% and fully saturated rock. Figures 6.2 and 6.2b show sensitivity in saturation profiles due to varying rock permeability in the crystalline and sedimentary DGR, respectively. Figures 6.2b and 6.2c show UFC temperature evolution in the crystalline and sedimentary DGR**.** As seen in Figures 6.2a and 6.2b, saturation time is

sensitive to rock type, rock permeability, and bentonite initial saturation. The model predicted 20 years and 170 years for full saturation in the crystalline and sedimentary DGR (RQ 1), respectively, using reference saturation cases (bold text in the legend, Figures 6.1a and b). These saturation times are comparable to the results from other bentonite saturation studies assuming similar host rock conditions (Millard et al. 2004, Nguyen and Jing 2005). Temperature evolution is insensitive to hydrogeological properties, as evaporation and condensation are not considered (see assumptions of the THC model in section 6.2.1.1).

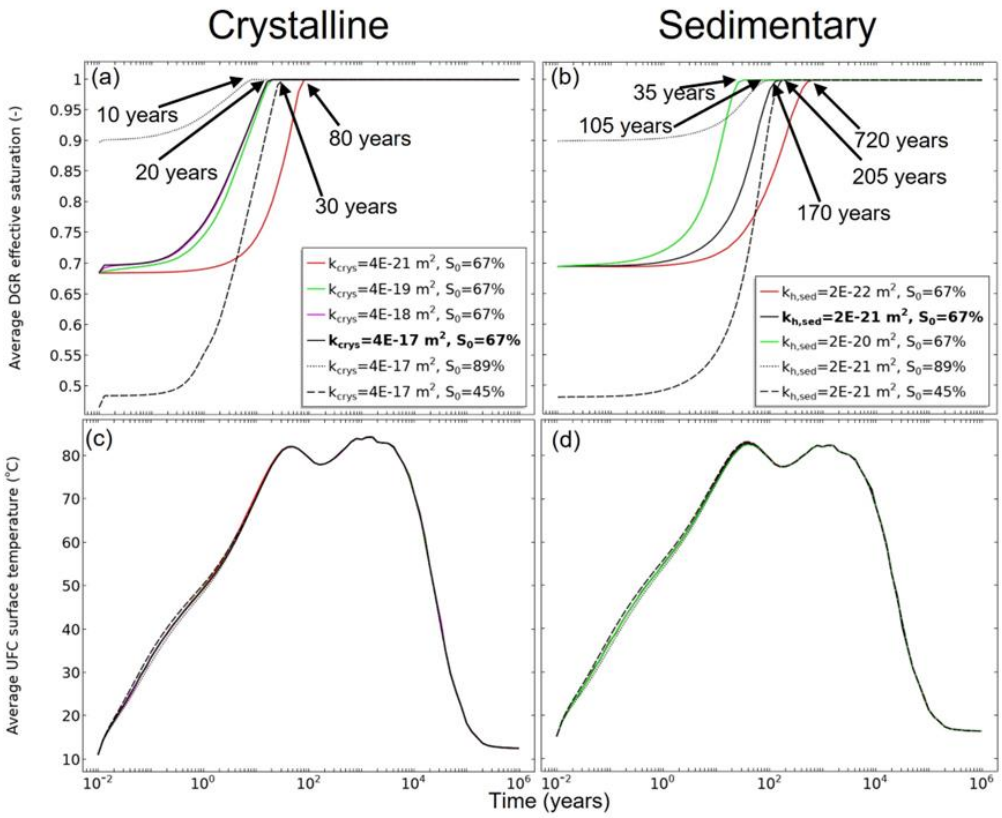

Figure 6.2: (a, b) average DGR effective saturation and (c, d) average UFC surface temperature from varying the initial saturation, isotropic rock permeabilities (in the crystalline model in frames a and c), and horizontal rock permeabilities (in the sedimentary model in frames b and d). The base case scenarios are bolded (Rashwan et al. 2022).

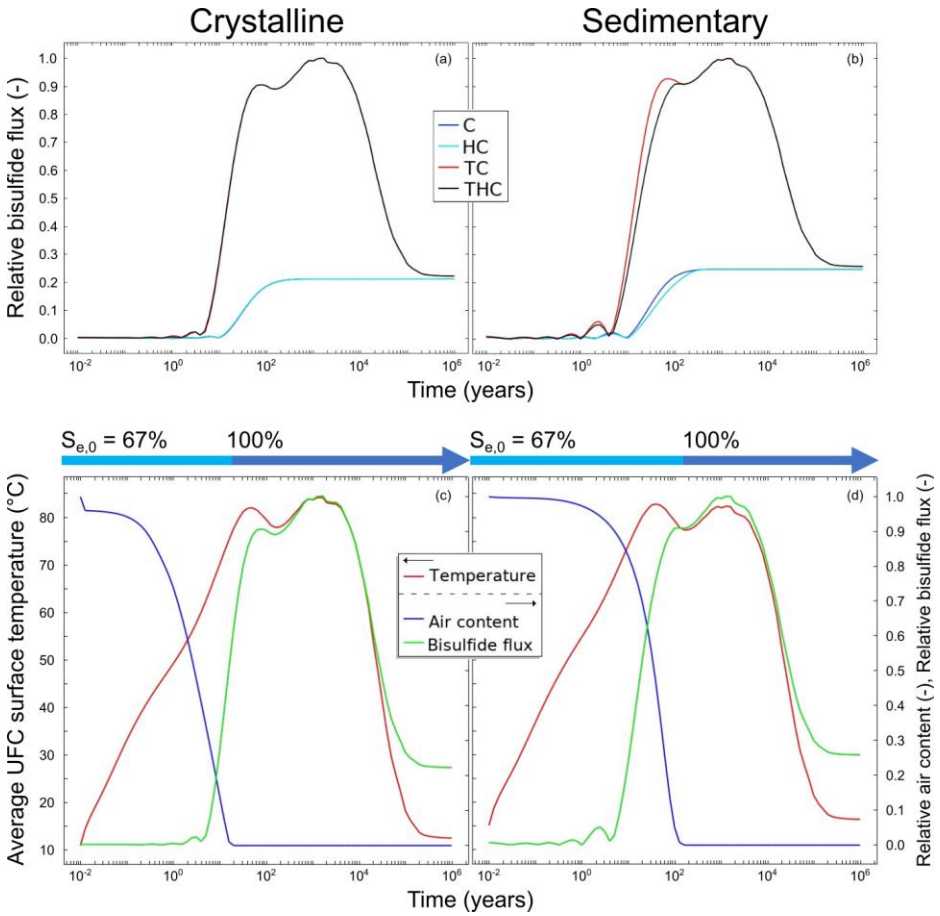

Figure 6.3: Relative bisulfide fluxes estimated at UFC surface (upper end-caps) in (a) crystalline and (b) sedimentary DGR models under different modelling conditions. C model simulates bisulfide diffusion under fully saturated-isothermal conditions, HC model simulates bisulfide diffusion under variably saturated-isothermal conditions, TC model simulates bisulfide diffusion under fully saturated-non-isothermal conditions, THC model simulates bisulfide diffusion under variably saturated-non-isothermal conditions. (c and d) Prediction hydrogeological conditions in the crystalline and sedimentary domains. Note that the average bentonite air content and bisulfide flux values are normalized (Rashwan et al. 2022).

Figures 6.3a and 6.3b show relative bisulfide flux over time in the crystalline and sedimentary domains under different modelling conditions (C, HC, TC, and THC). Figures 6.3c and 6.3d show simulated DGR conditions. As the bisulfide diffusion rate is dependent on saturation and temperature, bisulfide flux is also controlled by hydraulic and thermal conditions. Effects of these two variables (i.e., saturation and temperature) on bisulfide

flux is seen through model comparisons in Figures 6.3a and 6.3b. Results show that temperature increases bisulfide diffusion rate through bentonite (RQ 2) and saturation delays the onset of bisulfide diffusion as it transports through the water filled fraction of the pore space (see Figures 6.3 c and 6.3d) (RQ 2). However, the delay is not pronounced in the crystalline DGR as crystalline saturation is relatively fast. As seen in Figures 6.3 c and 6.3d, full saturation occurs at different times due to the differences in rock permeability while initial saturation is kept constant. The peak bisulfide flux occurs under high UFC temperatures (Figure 6.3) and bisulfide flux is low when the degree of saturation is low (seen most clearly in Figure 6.3d).

The copper corrosion rate is a function of the bisulfide flux over the UFC, stoichiometric factor, and copper mass characteristics. Bisulfide corrosion depths are identical in the models as saturation negligibly affected the bisulfide evolution (<1%) (RQ 3). The effect of heating on bisulfide corrosion is pronounced during the initial phase of the DGR only as temperature decreases after 10,000 years. Due to this, 20% increase in bisulfide flux occurs due to heating (RQ 3). The highest bisulfide corrosion is below the NWMO HS^- corrosion depth tolerance, 0.8 mm, reported in Hall et al. (2021). Additionally, bisulfide corrosion estimate in the THC model is conservative due to assumptions such as: no swelling, evaporation and condensation and, no geochemical reactions (see assumptions of the THC model in section 6.2.1.1).

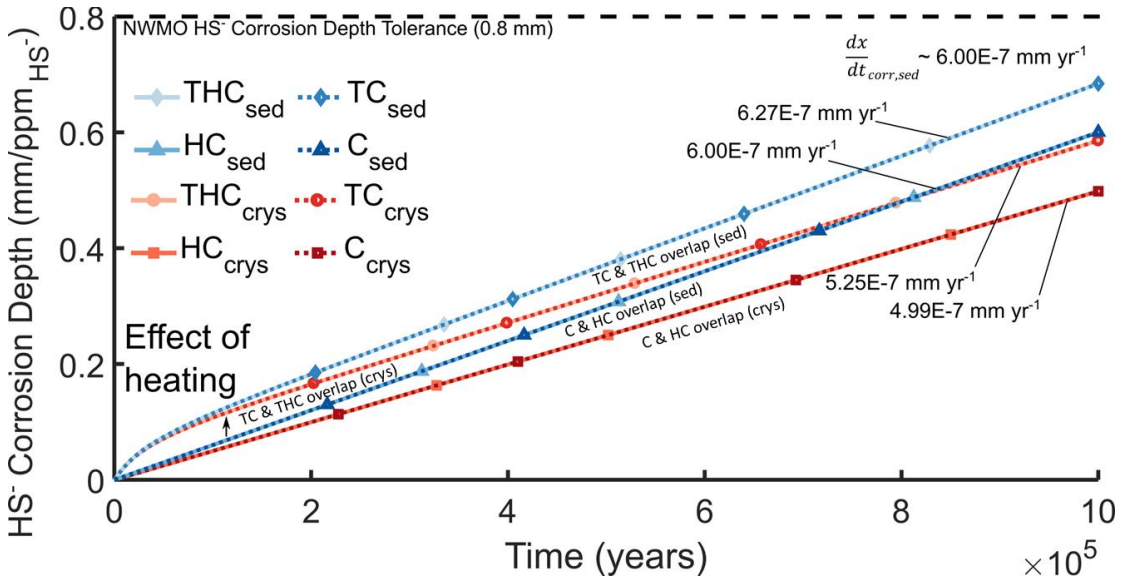

Figure 6.4: HS^- corrosion depths under different modelling conditions (i.e., C, HC, TC, and THC) in the crystalline or sedimentary domains. The slopes are calculated from 200,000 to 1,000,000 years in each model using linear regression analyses. Note that the horizontal axis represents a linear timescale (Rashwan et al. 2022). The HS^- corrosion depth tolerance is reported in Hall et a. (2021).

6.2.2 3-D THC-S and THC-R Models

6.2.2.1 Assumptions in the THC-S and THC-R Models

The processes highlighted in red in Figure 6.5 represent the processes which are modelled in the THC-S and THC-R studies. Like the THC model, the HS^- corrosion estimate from the THC-S and THC-R models is conservative due to some assumptions, such as:

- Only bisulfide adsorption is modelled (no desorption). Desorption would increase bisulfide concentration in the pore space. However, laboratory batch experiments showed that HS^- desorption is unlikely (Papry et al. 2023).
- Bisulfide retardation due to a reaction between HS^- and available Fe^{2+} in the bentonite (i.e., FeS formation) is modelled. Including other reactions (e.g., cation exchange, complexation, and hydrolysis) would impact HS transport rate and retardation. For example, cation exchange process would increase bentonite

permeability (as swelling capacity is reduced due to reduction of interlayer space) (Karnland and Birgersson 2006, Appelo 2013, Xiang et al. 2020) and HS^- concentration, thereby increasing reaction rate (as $R \propto [Fe^{2+}_{(aq)}]\,[HS^-_{(aq)}]$), which would use up available Fe^{2+} at a faster rate and enable early cessation of the reaction. Including aqueous complexation reaction, such as the aqueous complex of calcium chloride in bentonite (Savage et al. 2010, 2011) would reduce bentonite permeability through increasing swelling capacity (i.e., decreasing ionic strength through transferring Cl^- to complex state) and decrease HS^- concentration, thereby decreasing reaction rate (as $R \propto [Fe^{2+}_{(aq)}]\,[HS^-_{(aq)}]$), which would use up available Fe^{2+} at a slower rate and delay cessation of the reaction. In contrast, including hydrolysis reaction (Savage et al. 2010, 2011) would have the opposite effect as it can break the complexation and increase ionic strength through releasing Cl^- in the pore space.

- No microbial processes are assumed to be occurring within the bentonite; including these reactions would decrease the amount of bisulfide that would decrease the reaction rate (as $R \propto [Fe^{2+}_{(aq)}]\,[HS^-_{(aq)}]$) and amount of HS^- adsorption.
- Similar to the THC model, bentonite is assumed to swell instantly, and no vapour transport or evaporation or condensation is modelled in the system;

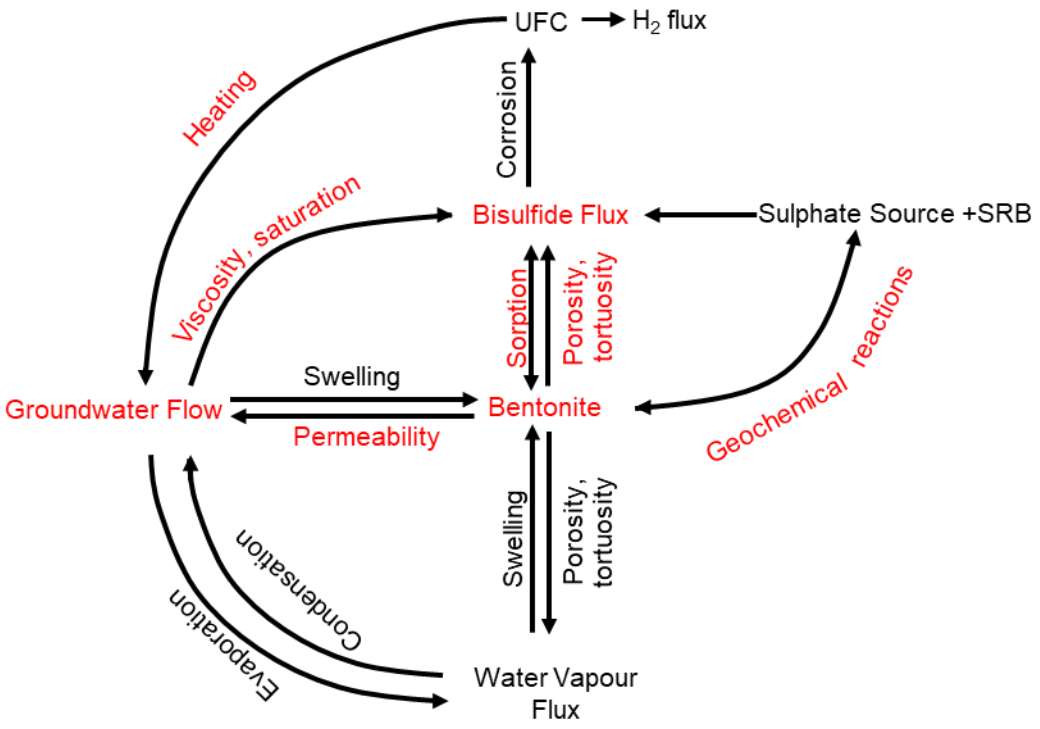

Figure 6.5: Coupled hydrogeological and geochemical processes governing HS^- corrosion; red font indicates modelled processes in the THC-S_L and THC-S_{NL} models (i.e., adsorption as a part of sorption), and THC-R_I (i.e., a reaction between Fe^{2+} and HS^-)

6.2.2.2 3-D THC-S and THC-R Model Results

The THC-S and THC-R models used three 1-D models (two 1-D adsorption models, (C-S_L and C-S_{NL}) and 1-D reaction model (C-R_I)) that were fitted to experimental bisulfide diffusion profiles to estimate adsorption and reaction parameters for compacted bentonite. HS^- transport and adsorption onto bentonite using linear and non-linear adsorption parameters was simulated in the C-S_L and C-S_{NL} models, respectively. HS^- transport and reaction with available Fe^{2+} in the bentonite (i.e., FeS production) using kinetically irreversible reaction approach was simulated the C-R_I model. These three 1-D models were also investigated to explore geochemical evolution relevant to HS^- and Fe^{2+} reaction and effects of HS^- adsorption and HS^- reaction on HS^- diffusion breakthrough curves. These three models were then coupled individually to the 3-D THC model in the

crystalline domain and the overall corrosion rate at the UFC was compared. Bisulfide adsorption and reaction were not explored in the sedimentary domain.

Figure 6.6 shows comparison of cumulative HS^- outlet mass from the C-S_L, C-S_{NL}, and C-R_I models and experiment results (Chowdhury et al. 2024). Almost identical HS^- retardation pattern in compacted bentonite is obtained using adsorption or reaction models. This identical pattern in HS^- retardation does not ascertain the relative influence of HS^- and Fe^{2+} reaction or HS^- adsorption but confirms HS^- retention in compacted bentonite.

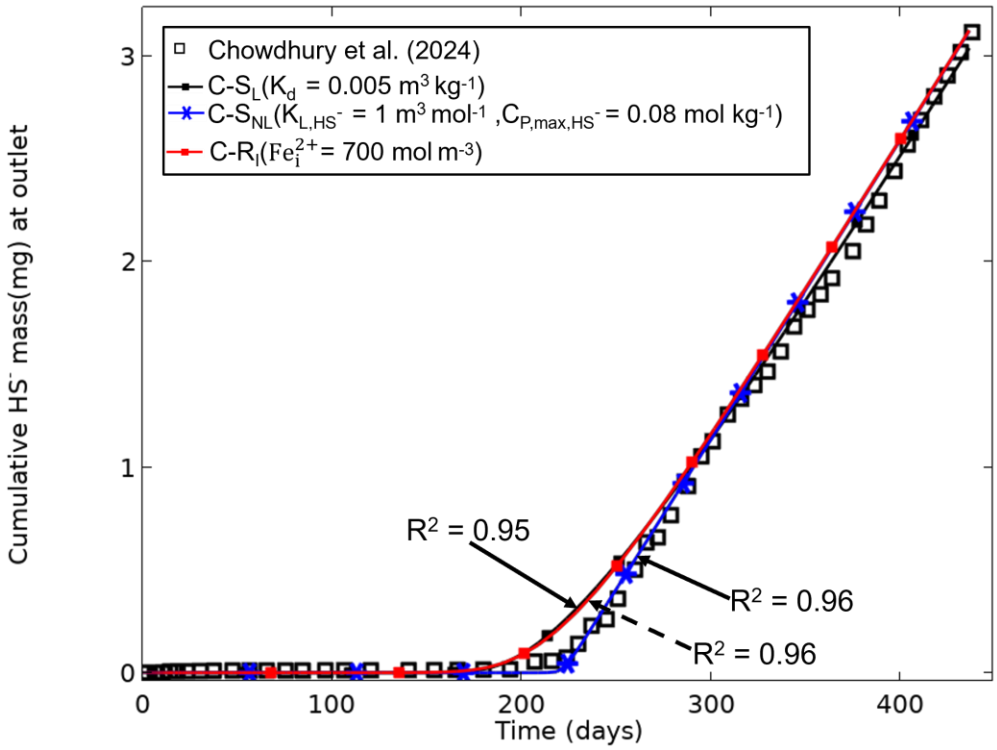

Figure 6.6: Cumulative HS^- mass at the compacted bentonite outlet in the C-S_L, C-S_{NL}, and C-R_I models compared to experimental data from Chowdhury et al. 2024.

The THC-S_L, THC-S_{NL}, and THC-R_I models were run for a reference period of 1 million years (i.e., the Canadian DGR design life). HS^- flux from the THC model was compared to the THC-S_L, THC-S_{NL}, and THC-R_I models to understand the effect of HS^- reaction and HS^- adsorption on HS^- evolution (Figure 6.7). Spatial distribution of HS^- flux was also explored to visually understand HS^- retardation due to HS^- reaction and HS^- adsorption (Figure 6.8). In all the models, HS^- diffusion is delayed due to either HS^- adsorption or reaction (RQ 6). However, the HS^- diffusion delays (i.e., ≈50-800 years) are relatively short compared to the million-year DGR lifespan. Due to this relatively short diffusion delays, the total HS^- corrosion depth is nearly identical (Figure 6.9). Altogether, the long-term HS^- corrosion is unaffected due to early cessation of the HS^- adsorption or reaction processes (RQ 6).

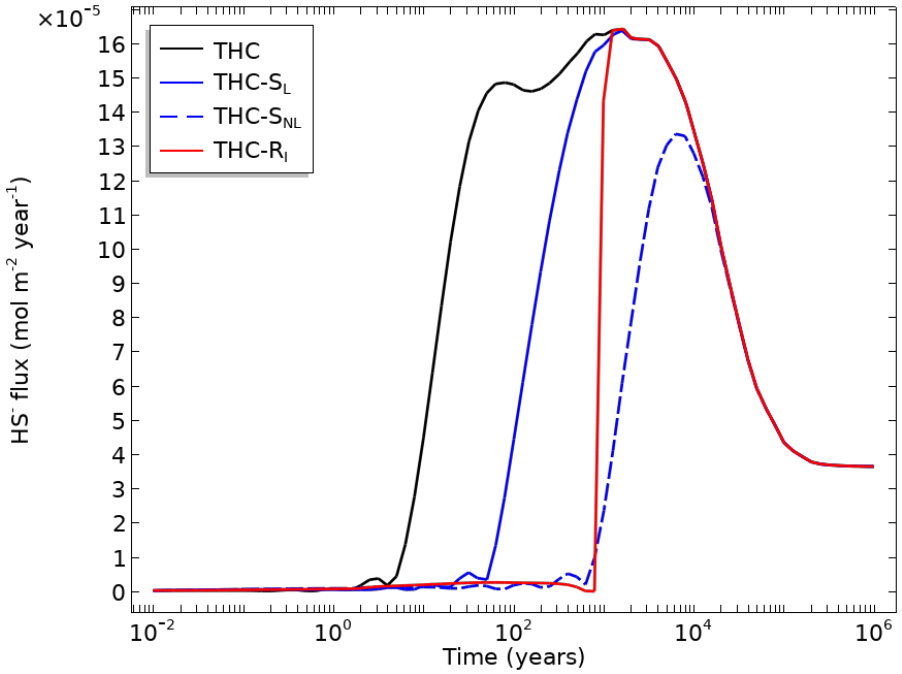

Figure 6.7: Bisulfide flux estimated at upper UFC end cap in the THC, THC-S_L, and THC-S_{NL}, and THC-R_I models.

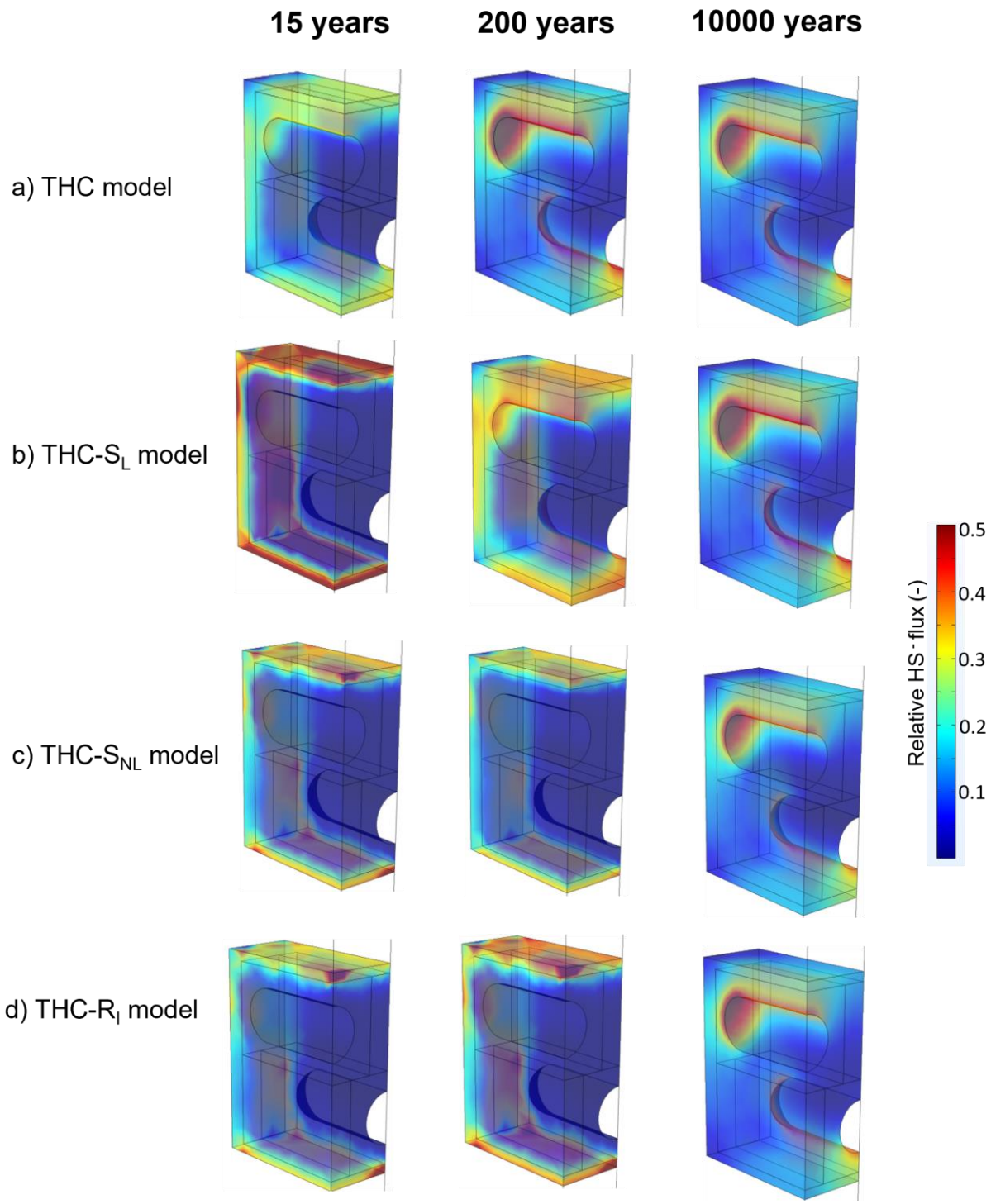

Figure 6.8: The simulated spatial distribution of relative HS^- flux (i.e., HS^- flux ($\dot{N}''_{HS}$) compared to maximum HS^- flux ($\dot{N}''_{HS_{max}}$) or $\dot{N}''_{HS}/\dot{N}''_{HS_{max}}$) over time in the 3-D a) THC model, b) THC-S_L model, c) THC-S_{NL} model, and d) THC-R_I model

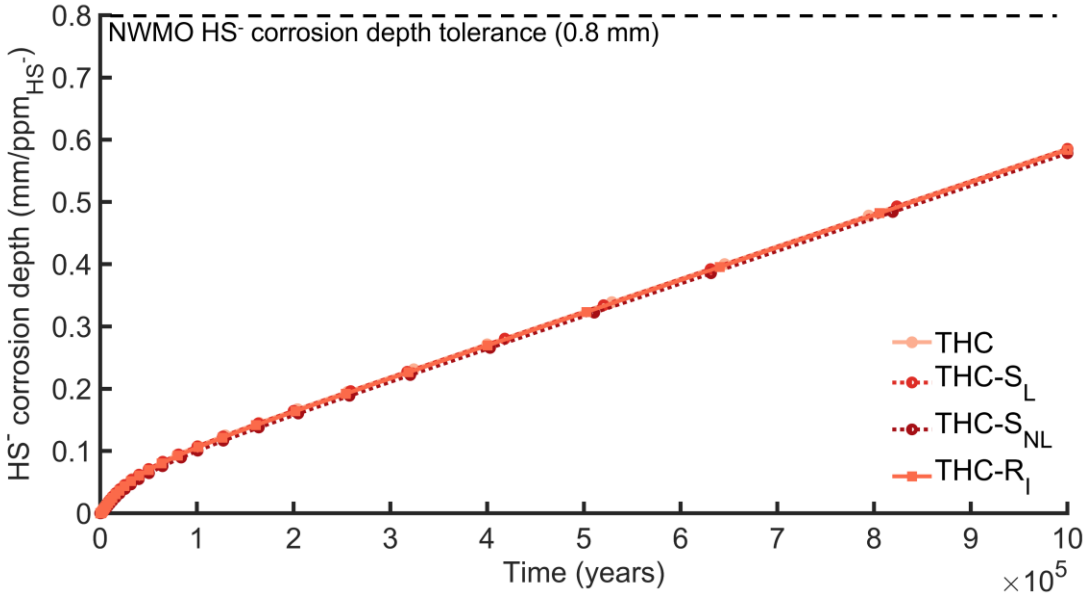

Figure 6.9: HS^- corrosion depths in the THC, THC-S_L, THC-S_{NL}, and THC-R_I models. Note that the horizontal axis represents a linear timescale.

6.2.3 2-D THC-H_2 Model

6.2.3.1 Assumptions in the 2-D THC-H_2 Model

The processes highlighted in red in Figure 6.10 represent the processes which are modelled in the THC-H_2 study. Like the THC model, H_2 evolution model is conservative due to some assumptions, such as:

- The H_2 and HS^- rock effective diffusivity values are conservative as literature values are used.
- H_2 is unreactive in the THC-H_2 model. However, use of H_2 in kinetic geochemical or microbiological reactions in the bentonite and host rock would HS^- production via SRB reaction.
- In the THC-H_2 model, SO_4 is assumed to be non rate limiting species for HS^- production. Including SO_4 as a rate limiting species in microbial SO_4 reduction (where H_2 may participate as an electron donor) would affect the H_2/HS^- feedback process.

Overall, this study provides novel insight into H_2 accumulation and transport dynamics in DGR environments.

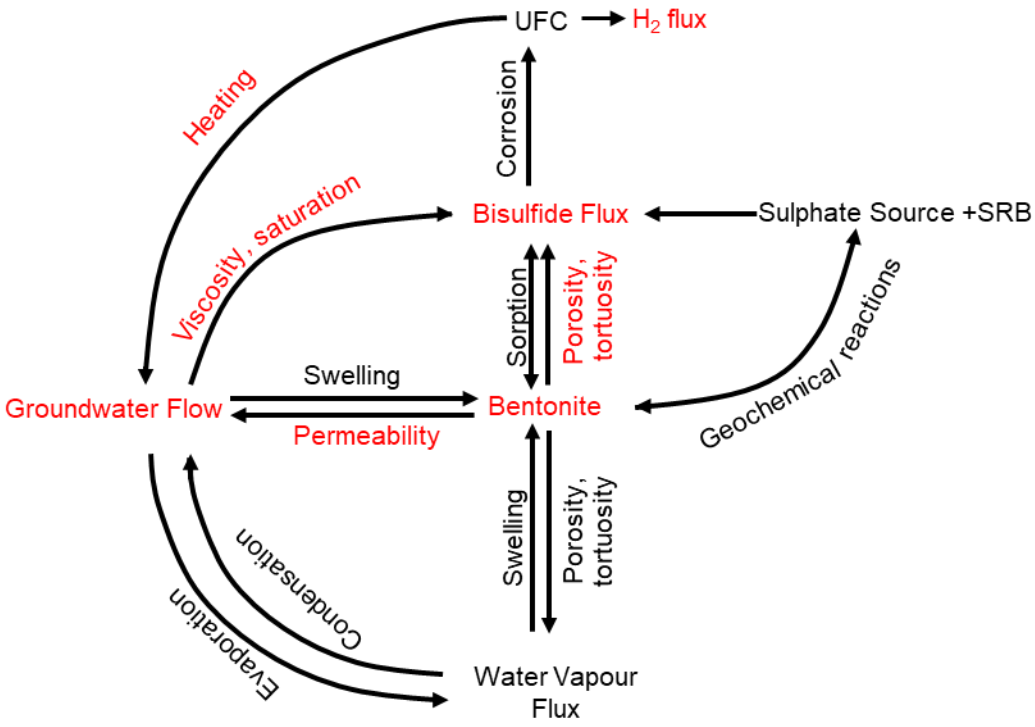

Figure 6.10: Coupled hydrogeological and geochemical processes governing HS^- corrosion; red font indicates modelled processes in the THC-H_2 model

6.2.3.2 2-D THC-H_2 Model Results

The 2-D hydrogen (H_2) model (referred to as the THC-H_2 model) is based on the 2-D THC model in the crystalline domain (Asad et al. 2022). The H_2 evolution was not explored in the sedimentary domain as results would be similar. In this study, the possibility of H_2 gas (bubble) formation in the DGR was explored by comparing DGR H_2 concentration to DGR H_2 solubility limit under various modelling conditions (Table 6.1). A H_2 feedback model was also developed.

The THC-H_2 model assumed a constant supply of HS^- at the RBI which diffused to the UFC and produced H_2 following the reaction showed in Figure 6.11a. In the THC-H_2 feedback model, a H_2 source was assumed in the far-field rock (modelled through a constant 1 ppm H_2 boundary condition) and H_2 diffused to the RBI, where HS^- was produced (Figure 6.11b).

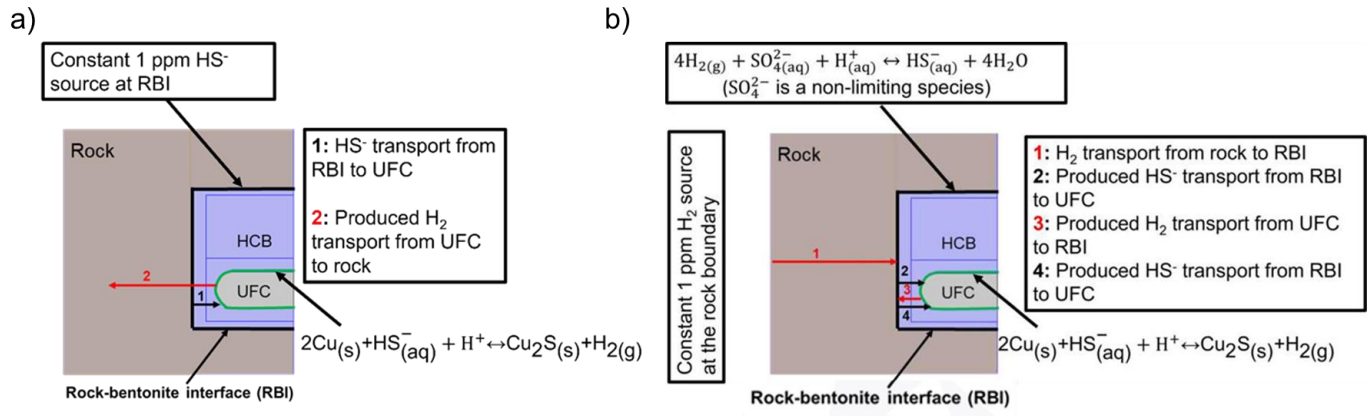

Figure 6.11: Boundary conditions in the a) THC-H_2 model and b) THC-H_2 feedback model. Note that arrows indicate transport directions of HS^- and H_2

Ten cases were explored to examine the effect of various parameters as shown in Table 6.1. Case 1 (C1) was the base case for the THC-H_2 model and case 6 (C6) was the base case for the THC-H_2 feedback model. In the THC-H_2 model, H_2 concentration at the UFC with changing effective H_2 rock diffusivity was examined, where the H_2 concentration decreased with increasing diffusivity (Figure 6.12). This decrease in H_2 concentration was a result of the increased H_2 transport rate out of the bentonite and through the rock due to increasing the effective H_2 rock diffusivity which resulted in limited H_2 accumulation near the UFC. Due to the feedback effect, H_2 production rates

(i.e., rate is of the order of 10^{-13}) and concentrations (i.e., concentration is of the order of 10^{-4} in Fig. 6.12) were both very low. These low rates and concentrations highlight the significance of H_2 consumption at the RBI in reducing DGR H_2 levels, which could be through sulfate reducing bacteria, SRB activity (RQs 4-5). In addition, a comparison of DGR H_2 concentrations from all modelling cases show that DGR H_2 solubility limit is not surpassed, which indicates that H_2 gas bubble would not be formed under the modeling conditions (RQs 4-5) (Figure 6.13).

Table 6.1: Sensitivity analysis simulations

Model	Case	HS^- initial background concentration (ppm)	Constant HS^- concentration at the RBI (ppm)	H_2 initial background concentration (ppm)	Constant H_2 concentration at the far-field rock boundary (ppm)	Effective H_2 rock diffusivity ($m^2\ s^{-1}$)
THC-H_2	C1[a]	0.02	1	0	0	8.4×10^{-13}
THC-H_2	C2[b]	0.5	1	0	0	8.4×10^{-13}
THC-H_2	C3[b]	1	1	0	0	8.4×10^{-13}
THC-H_2	C4[b]	0.02	2	0	0	8.4×10^{-13}
THC-H_2	C5[b]	0.02	1	0	0	$\mathbf{8.4 \times 10^{-12}}$
Feedback	C6[c]	0.02	Produced HS^- from H_2 consumption (Eq. 3)	0.02	1	8.4×10^{-13}
Feedback	C7[d]	0.02	Produced HS^- from H_2 consumption	0.5	1	8.4×10^{-13}
Feedback	C8[d]	0.02	Produced HS^- from H_2 consumption	1	1	8.4×10^{-13}
Feedback	C9[d]	0.02	Produced HS^- from H_2 consumption	0.02	2	8.4×10^{-13}
Feedback	C10[d]	0.02	Produced HS^- from H_2 consumption	0.02	1	$\mathbf{8.4 \times 10^{-12}}$

[a]THC-H_2 base case, [b]THC-H_2 sensitivity case, [c]THC-H_2 feedback base case, [d]THC-H_2 feedback sensitivity case. Note that the effective H_2 diffusivity in bentonite was kept the same in all cases and bold values represent the varied values for the sensitivity study.

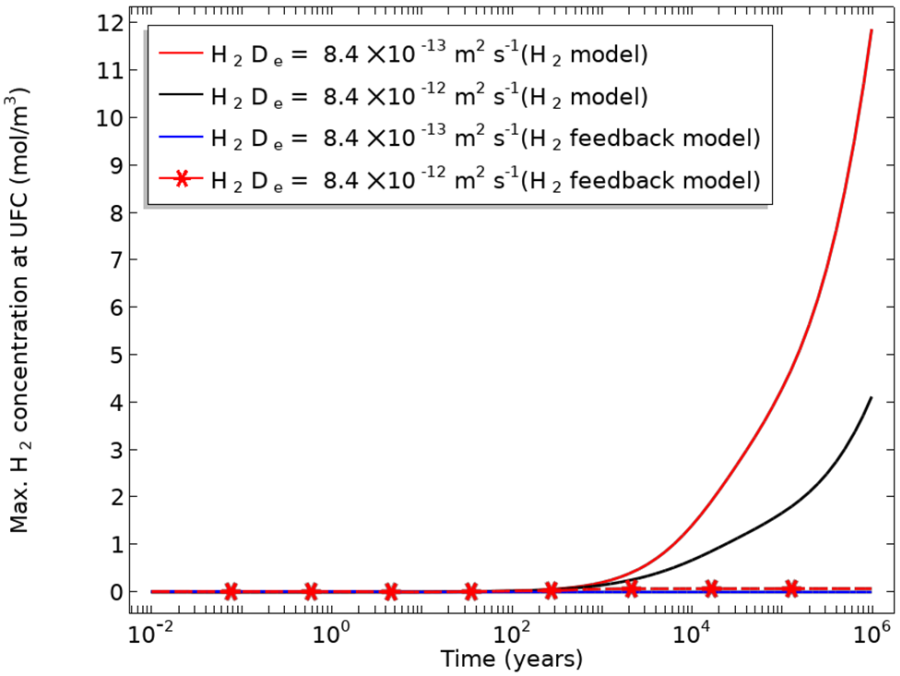

Figure 6.12: Maximum H_2 concentration at the UFC using hydrogen and hydrogen feedback models, at different rock diffusivity values.

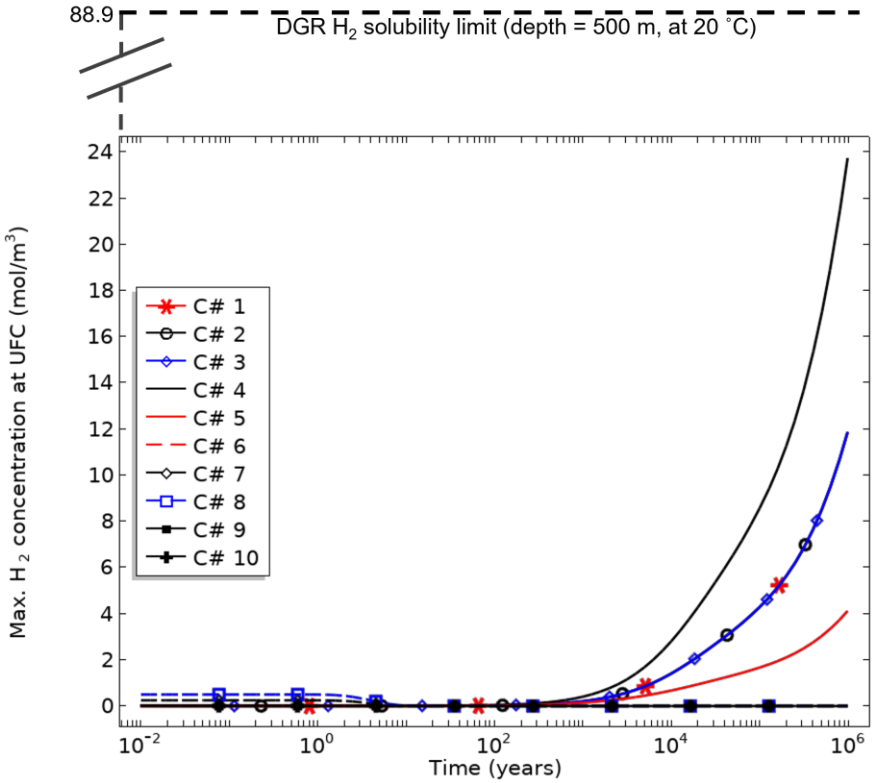

Figure 6.13: Maximum DGR H_2 concentrations obtained from sensitivity cases (C1 to C10)

6.3 Conclusions

In this research, the effects of hydrogeological conditions on HS^- corrosion was examined by developing numerical models. A HS^- transport model was developed which described bisulfide diffusion through the bentonite in the DGR under variably saturated and non-isothermal conditions. The repository was approximated as a 2-D and 3-D system and all parameters were obtained from NWMO case studies and other studies. A range of verification and validation procedures (e.g., mesh convergence study, boundary conditions sensitivity, numerical and theoretical comparison) were conducted to develop confidence in the HS^- transport model. The model was then employed to explore bentonite saturation time, UFC heating, and effects of heating and saturation on HS^- corrosion. A H_2 evolution model was also developed adding surface equilibrium reaction approach to the HS^- transport model. The H_2 model was used to understand role of different properties (i.e., HS^- initial and constant boundary concentrations, H_2 initial and constant boundary concentrations, and effective H_2 diffusivity in rock) on H_2 evolution (due to HS^- corrosion) and gas generation. Lastly, a reaction model (i.e., geochemical model) was developed and coupled with the HS^- transport model. The HS^- transport and reaction model was explored to understand the effect of geochemical reaction (HS^- adsorption or HS^- and Fe^{2+} reaction) on HS^- corrosion. The processes highlighted in red in Figure 6.14 represent the processes which are modelled in this research using THC, THC-H_2, THC-S, and THC-R models. The HS^- corrosion estimate from these models is conservative due to assumptions, such as: conservative HS^- concentration, no swelling, no evaporation and condensation, neglecting some geochemical reactions, e.g., cation exchange, and no microbial processes in bentonite.

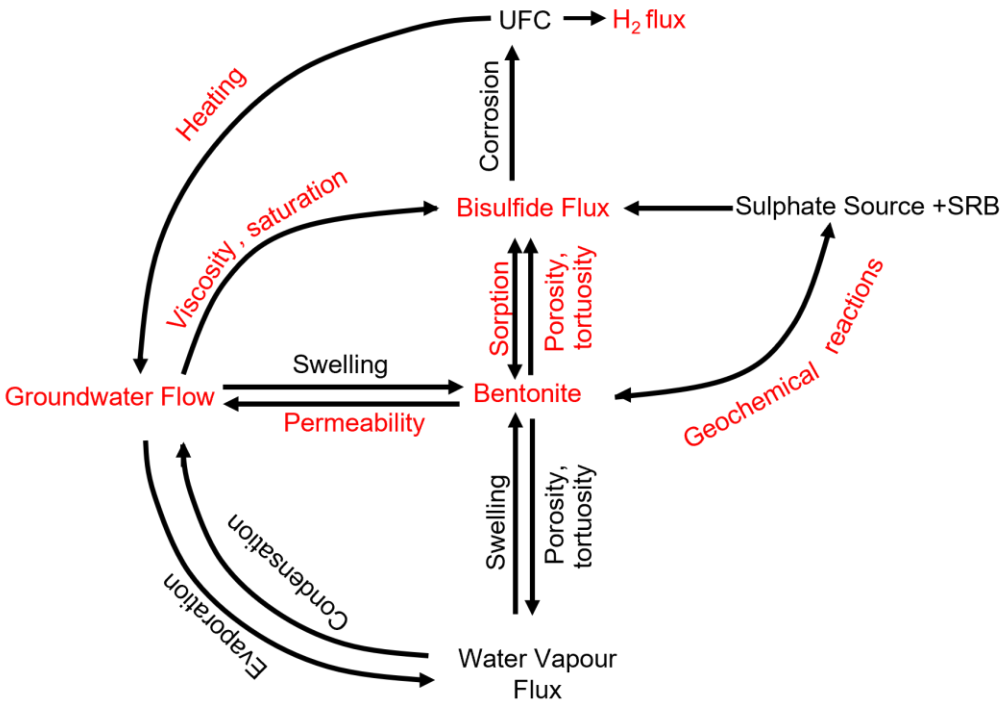

Figure 6.14: Coupled hydrogeological and geochemical processes governing HS^- corrosion; red font indicates modelled processes in this research

The work presented in this thesis demonstrates that the transient DGR hydrogeological and geochemical conditions (i.e., saturation, heating, and geochemical reaction) do not strongly influence HS^- corrosion over the DGR design life. The key conclusions from this research are:

- Heating accelerates HS^- transport and saturation delays it.
- However, over the design life, both processes do not strongly influence projected HS^- corrosion.
- Heating increased HS^- corrosion by < 20%.
- Saturation had a negligible impact on HS^- corrosion.
- The long-term H_2 production from HS^- corrosion depends on HS^- supply to the UFC, H_2 transport properties, and biotic H_2 consumption processes.

- Biotic H_2 consumption process (modelled through HS^-/H_2 feedback) was found to control the accumulation of H_2 in DGR.
- The H_2 solubility limit was never surpassed, indicating that H_2 gas pressure build-up in a DGR is unlikely under the studied conditions.
- HS^- diffusion is delayed (~ 50 to 800 years) due to HS^- adsorption or HS^- and Fe^{2+} reaction (i.e., FeS formation).
- HS^- diffusion starts after the retardation period and continues for rest of simulation.
- However, HS^- diffusion delays are relatively short compared to the million-year timeframe and does not impact long term HS^- corrosion.

6.4 Implications and Research Novelty

The findings of this research are significant. The model's total depth and saturation boundary conditions were found to be important factors to accurately predict long term UFC temperature and bentonite saturation profiles. In addition, the model predicted slower saturation evolution in the sedimentary DGR due to the rock's low permeability compared to the crystalline DGR. The slower saturation evolution in the sedimentary DGR delayed bisulfide transport and therefore HS^- corrosion. Capturing the rock's influence on HS^- corrosion timing was an important outcome which can help NWMO identify appropriate DGR sites. To the author's knowledge, this is one of the only numerical studies where DGR transient environmental conditions were predicted which can play an important role in the Canadian DGR safety assessment. As the model simulated coupled hydrogeological processes, the relative importance of including different processes was highlighted and system behaviour over time due to inclusion of new processes was understood. For example, heating accelerated bisulfide transport while unsaturated

bentonite and bisulfide reaction limited the transport. In addition, the combined effects of saturation, temperature, and bisulfide reaction were not pronounced over the long DGR life span. HS^- transport was simulated for the entire DGR lifespan and was found to be delayed (≈50-800 years) due to a geochemical reaction or adsorption. However, the HS^- diffusion delays were found to be relatively short in a DGR lifespan (1 million years) and did not impact long term HS^- corrosion. Amongst various modelling scenarios, the H_2 solubility limit was never surpassed, indicating the unlikelihood of H_2 gas pressure build-up in a DGR under explored modelling conditions. These findings support the ongoing efforts in planning for Canada's DGR as they provide valuable insights into the expected DGR performance under a wide range of conditions.

This research resulted in the following new numerical models for the use in DGR conditions:

1. Thermal-Hydraulic-Chemical (HS^- Diffusion) (THC) Model
2. Thermal-Hydraulic-Chemical (HS^- Diffusion)-Adsorption (THC-S) Model
3. Thermal-Hydraulic-Chemical (HS^- Diffusion)-Reaction (THC-R) Model
4. Thermal-Hydraulic-Chemical (HS^- and H_2 Diffusion)-Reaction (THC- H_2) Model

Although the models were built to assess the performance of the Canadian DGR they can also be used in other DGR scenarios, as well as other subsurface applications such as geothermal explorations, carbon capture dynamics, and thermal remediation.

Using these models, the following novel results to the body of knowledge regarding Canadian DGRs:

1. Considering all key HS^- transport processes and assuming 1 ppm constant bisulfide source in the DGR (30-90 ppb HS^- in Canadian DGR which would not

lead to a constant source), the highest bisulfide corrosion calculated using the model is below the NWMO HS^- corrosion depth tolerance.

2. HS^- retardation due to iron sulfide formation (i.e., modelled geochemical reaction between HS^- and Fe^{2+}) does not continue for long term (only ≈50-800 years in a million years DGR lifespan) and therefore dos does not protect UFC from long term HS^- corrosion.
3. The H_2 solubility limit was never surpassed even if the worst-case scenarios for HS^- corrosion and H_2 production were modelled. This result indicates the unlikelihood of H_2 gas pressure build-up in Canadian DGR under explored modelling conditions.

6.5 Recommendations for Future Work

The HS^- transport and reaction model has been robustly developed to aid in the performance assessment of the Canada's DGR. The developed model is designed to be flexible to accommodate additional processes and site-specific information as it becomes available. Future work may include additional aspects, such as:

- The THC-R model can be extended by including other geochemical reactions (e.g., cation exchange) that may occur in bentonite. This would result in making the effect of HS^- reaction with Fe^{2+} negligible. Cation exchange would increase bentonite permeability, thus HS^- concentration, and thereby increasing reaction rate as $R \propto [HS^-]$, which would use up Fe^{2+} faster and enable early cessation of reaction.

- Time dependant bentonite swelling behaviour can be included. This would only increase HS^- transport in the early times.
- Vapour transport and evaporation-condensation behaviour can be included. This would lead to cooling of the system, resulting in lower bisulfide transport.
- HS^- production due to microbial sulfate reduction could be modelled using laboratory derived data.
- In the THC-H_2 model, the consequences of copper sulfide production could also be investigated (e.g., in forming a crust that may inhibit corrosion, or in causing local non-uniformities).
- Given the large data variability and uncertainty in many processes in the DGR, machine learning models can help assess DGR safety. Application of machine learning approach for DGR safety assessment is promising, as site specific data grows and becomes available.

References

Abarca, E., Idiart, A., Manuel de Vries, L., Silva, O., Molinero, J., and von Schenck, H. 2013. Flow modelling on the repository scale for the safety assessment SR-PSU.

Abarca, E., Sampietro, D., and Miret, M. 2016. Initial modelling of the near-field hydrogeology – Exploring the influence of host rock characteristics and barrier properties – Report for the safety evaluation SE-SFL. R-16-02. © 2016 Svensk Kärnbränslehantering AB,: 137.

Abarca, E., Sampietro, D., Molinero, J., and Schenck, H. von. 2019. Modelling of the near-field hydrogeology – temperate climate conditions. SKB R-19-03 © 2019 Svensk Kärnbränslehantering AB.

Abrahamsen-Mills, L., and Small, J. 2019. State of Science Review: Modelling microbial effects to assess long-term performance of a DGR. Nuclear Waste Management Organization Report NWMO-TR-2019-15. Toronto, Canada.

Adeloju, S., and Duan, Y.Y. 1994. Influence of Bicarbonate Ions on the Stability of Copper Oxides and Copper Pitting Corrosion. British Corrosion Journal, 29: 315–320. doi:10.1179/000705994798267520.

Åkesson, M., Kristensson, O., Börgesson, L., Dueck, A., and Hernelind, J. 2010. THM modelling of buffer, backfill and other system components - Critical processes and scenarios. : 369.

Al-abidi, A.A., Bin Mat, S., Sopian, K., Sulaiman, M.Y., and Mohammed, A.Th. 2013. CFD applications for latent heat thermal energy storage: a review. Renewable and Sustainable Energy Reviews, 20: 353–363. doi:10.1016/j.rser.2012.11.079.

Albinsson, Y., Andersson, K., Börjesson, S., and Allard, B. 1996. Diffusion of radionuclides in concrete and concrete-bentonite systems. Journal of Contaminant Hydrology, 21(1): 189–200. doi:10.1016/0169-7722(95)00046-1.

Alexander, W.R., and McKinley, L. 2011. Deep Geological Disposal of Radioactive Waste. Elsevier.

AMEC. 2012. CONNECTFLOW Release 10.4 Technical summary document. AMEC/ENV/CONNECTFLOW/15, AMEC, UK.

An, W., Zhu, T., and Yin, L.-J. 2011. Improved iterative convergence of the finite element method in the solution of the second-order radiative transfer equation by modified diffusion synthetic acceleration. Numerical heat transfer, Part B: Fundamentals, 59(5): 409–420. Taylor & Francis. doi:10.1080/10407790.2011.572726.

Andra. 2015. Andra Technology Transfer Identification and Quantification of Potential Benefits | RWM Tools, ANDRA.398.B. Available from https://rwm.nda.gov.uk/publication/andra-technology-transfer-identification-and-quantification-of-potential-benefits/. [accessed 24 March 2019].

Appelo, C. a. J. 2013. A review of porosity and diffusion in bentonite. Posiva Oy.

Apted, M.J., and Ahn, J. 2017. Geological Repository Systems for Safe Disposal of Spent Nuclear Fuels and Radioactive Waste. Woodhead Publishing.

Archie, G.E. 1950. Introduction to Petrophysics of Reservoir Rocks. AAPG Bulletin, 34. doi:10.1306/3D933F62-16B1-11D7-8645000102C1865D.

Asad, A., Rashwan, T., Molnar, I., and Krol, M. 2022. Modelling Bisulfide Transport through the Engineered Barrier System under Repository Conditions: Coupling Unsaturated Flow and Refining Boundary Conditions. Nuclear Waste Management Organization Report NWMO-TR-2022-06. Toronto, Canada.

Avis, J., Walsh, R., and Calder, N. 2012. Corrosion-Generated Hydrogen Gas from Steel Used Fuel Containers and the Postclosure Pressure within a Deep Geological Repository. Nuclear Waste Management Organization Report APM-03640-T10. Toronto, Canada.

Barnichon, J.-D., Dauzères, A., and De Windt, L. 2018. Understanding oxidizing transient conditions in clayey rocks. Applied Geochemistry, 98: 435–447. doi:10.1016/j.apgeochem.2018.09.018.

Bath, A. 2012. Groundwater Chemistry in SKB's Safety Assessment SR-Site: Initial Review.

Baumgartner, P. 2006. Generic Thermal-Hydraulic-Mechanical (THM) Data for Sealing Materials, Volume 1: Soil-Water Relationship. Atomic Energy of Canada Ltd. Report AECL-06819. Pinawa, Canada. 06819-REP-01300-10122-R00. Ontario Power Generation, Nuclear Waste Management Division. Toronto, Ontario.

Baxter, S., Carta, G., and Holton, D. 2018. Modelling of resaturation in the Bentonite-Rock Interaction Experiment with conditioning to dismantling data - Task 8F of SKB Task Forces EBS and GWFTS.

Baxter, S., Holton, D., and Hoch, A. 2017. Modelling bentonite resaturation in the Bentonite Rock Interaction Experiment (BRIE) – Task 8C of SKB Task Forces EBS and GWFTS. P-17-14. © 2017 Svensk Kärnbränslehantering AB,: 135.

Behazin, M., Pedersen, K., Li, L., Abrahamsen-Mills, L., Boylan, A., and Bryan, N. 2021. State of Science Review of Sulfide Production in Deep Geological Repositories for Used Nuclear Fuel. Nuclear Waste Management Organization Report NWMO-TR-2021-18. Toronto, Canada.

Bejan, A., and Kraus, A.D. 2003. Heat Transfer Handbook. John Wiley & Sons.

Bergstroem, U., Pers, K., and Almen, Y. 2011. International perspective on repositories for low level waste. Sweden.

Bianchi, M., Liu, H.-H., and Birkholzer, J.T. 2015. Radionuclide transport behavior in a generic geological radioactive waste repository. Ground Water, 53(3): 440–451. doi:10.1111/gwat.12171.

Bodansky, D. 2004. Nuclear Energy: Principles, Practices, and Prospects. *In* 2nd edition. Springer-Verlag, New York.

Börgesson, L., Hedström, M., Holton, D., Metcalfe, R., and Sandén, T. 2020. Contractor Report to RWM Bentonite in a High-temperature Environment Bentonite Erosion. Radioactive Waste Management (RWM) Report.

Brachman, R.W.I., Rowe, R.K., Baral, A., Hosney, M.S., Su, G., Nguyen, T.S., Brown, J., and Lange, K. 2021. Bentonite swelling characteristics with a hypersaline multi-component pore fluid. Canadian Geotechnical Journal,. NRC Research Press 1840 Woodward Drive, Suite 1, Ottawa, ON K2C 0P7. doi:10.1139/cgj-2019-0558.

Bradbury, M.H., and Baeyens, B. 2002. Porewater Chemistry in Compacted Re-Saturated MX-80 Bentonite: Physico-Chemical Characterisation and

Geochemical Modelling. Nuclear Energy and Safety Research Department Waste Management Laboratory,Paul Scherrer Inst.
Bradbury, M.H., and Baeyens, B. 2003. Porewater chemistry in compacted re-saturated MX-80 bentonite. Journal of Contaminant Hydrology, 61(1): 329–338. doi:10.1016/S0169-7722(02)00125-0.
Brich, K., Keech, P., and Boyle, C. 2013. NWMO Fifth Case Study Reference Data. Nuclear Waste Management Organization Internal Document (Private Collection). Toronto, Canada.
Brich, K., and Yang, T. 2021a. 2021 Safety Assessment-Engineered Sealing Materials Data, South Bruce. Nuclear Waste Management Organization Internal Document (Private Collection). Toronto, Canada.
Brich, K., and Yang, T. 2021b. 2021 Safety Assessment-Engineered Sealing Materials Data, Revell Batholith. Nuclear Waste Management Organization Internal Document (Private Collection). Toronto, Canada.
Briggs, S., and Krol, M. 2018. Diffusive Transport Modelling of Corrosion Agents through the Engineered Barrier System in a Deep Geological Repository for Used Nuclear Fuel. Nuclear Waste Management Organization Report NWMO TR-2018-06. Toronto, Canada.
Briggs, S., McKelvie, J., Sleep, B., and Krol, M. 2017. Multi-dimensional transport modelling of corrosive agents through a bentonite buffer in a Canadian deep geological repository. Science of the total environment, 599–600: 348–354. doi:10.1016/j.scitotenv.2017.04.242.
Calder, N. 2014. FORGE Benchmark Modelling: Cell, Module and Repository Scale Gas Migration in a Hypothetical Repository. Nuclear Waste Management Organization Report NWMO-TR-2014-06. Toronto, Canada.
CEW. 2017. What to do with the nuclear waste – the storage question, Clean Energy Wire (CEW), Journalism for the energy transition. Available from https://www.cleanenergywire.org/factsheets/what-do-nuclear-waste-storage-question. [accessed 7 April 2019].
Chen, Y.-S., Huang, C., Liu, P.-Y., Yen, H.-W., Niu, R., Burr, P., Moore, K.L., Martínez-Pañeda, E., Atrens, A., and Cairney, J.M. 2024. Hydrogen trapping and embrittlement in metals – A review. International Journal of Hydrogen Energy,. doi:10.1016/j.ijhydene.2024.04.076.
Chowdhury, F., Rashwan, T.L., Mondal, P., Behazin, M., Keech, P.G., Sharma, J.S., and Krol, M. 2024. Effect of compaction on bisulfide diffusive transport through MX-80 bentonite. Journal of Contaminant Hydrology, 264: 104341. doi:10.1016/j.jconhyd.2024.104341.
Chowdhury, F., Rashwan, T.L., Papry, S.A., Behazin, M., Keech, P.G., Mondal, P., Sharma, J., and Krol, M. 2021. Measuring Key Parameters Governing Anion Transport Through Mx-80 Bentonite. *In* Proceedings of the Canadian Society of Civil Engineering Annual Conference 2021. *Edited by* S. Walbridge, M. Nik-Bakht, K.T.W. Ng, M. Shome, M.S. Alam, A. el Damatty, and G. Lovegrove. Springer Nature, Singapore. pp. 547–558.
Cloet, V., Pekala, M., Smith, P., Wersin, P., and Diomidis, N. 2017. An Evaluation of Sulphide Fluxes in the Near Field of a HLW Repository. Nagra Report-TR-17-04. Wettingen, Switzerland.

COMSOL. 2021a. Subsurface flow module user's guide, Stockholm, Sweden.
COMSOL, M. v. 5. 6. 2021b. www.comsol.com. COMSOL AB, Stockholm, Sweden, 2021.
Cong, H., Michels, H.T., and Scully, J.R. 2008. Passivity and Pit Stability Behavior of Copper as a Function of Selected Water Chemistry Variables. Journal of The Electrochemical Society, 156(1): C16. IOP Publishing. doi:10.1149/1.2999351.
Craig, T.J., Calais, E., Fleitout, L., Bollinger, L., and Scotti, O. 2023. Time-variable strain and stress rates induced by Holocene glacial isostatic adjustment in continental interiors. Tectonophysics, 854: 229815. doi:10.1016/j.tecto.2023.229815.
Crusset, D., Deydier, V., Necib, S., Gras, J.-M., Combrade, P., Féron, D., and Burger, E. 2017. Corrosion of carbon steel components in the French high-level waste programme: evolution of disposal concept and selection of materials. Corrosion Engineering, Science and Technology, 52(sup1): 17–24. Taylor & Francis. doi:10.1080/1478422X.2017.1344416.
Cui, L.-Y., Ye, W.-M., Wang, Q., Chen, Y.-G., and Cui, Y.-J. 2023. A model for describing advective and diffusive gas transport through initially saturated bentonite with consideration of temperature. Engineering Geology, 323: 107215. doi:10.1016/j.enggeo.2023.107215.
Davison, W. 1991. The solubility of iron sulphides in synthetic and natural waters at ambient temperature. Aquatic Sciences, 53(4): 309–329. doi:10.1007/BF00877139.
De Windt, L., Marsal, F., Corvisier, J., and Pellegrini, D. 2014. Modeling of oxygen gas diffusion and consumption during the oxic transient in a disposal cell of radioactive waste. Applied Geochemistry, 41: 115–127. doi:10.1016/j.apgeochem.2013.12.005.
Dessirier, B., Frampton, A., and Jarsjö, J. 2017. Two-phase flows during re-saturation of sparsely fractured bedrock and bentonite around canisters for deep storage of spent nuclear fuel – Modelling Task 8 of SKB Task Forces GWFTS and EBS. P-17-02. © 2017 Svensk Kärnbränslehantering AB,: 48.
Dessirier, B., Jarsjö, J., and Frampton, A. 2014. Modeling Two-Phase-Flow Interactions across a Bentonite Clay and Fractured Rock Interface. Nuclear Technology, 187(2): 147–157. doi:10.13182/NT13-77.
Diederichs, M.S., and Day, J.J. 2021. An Illustrative Study of the Potential Sensitivity, of Predicted Long-Term EDZ Development, to Internal Fabric of Argillaceous Limestone. Rock Mechanics and Rock Engineering,. doi:10.1007/s00603-021-02602-z.
Diomidis, N., Cloet, V., Leupin, O.X., Marschall, P., Poller, A., and Stein, M. 2016. Production, consumption and transport of gases in deep geological repositories according to the Swiss disposal concept. Radioactive Waste, National Cooperative for the Disposal of Radioactive Waste (NAGRA), Switzerland, Technical Report 16-03: 148.
Dixon, D., Man, A., Rimal, S., Stone, J., and Siemens, G. 2018. Bentonite Seal Properties in Saline Water. Nuclear Waste Management Organization Report NWMO-TR-2018-20. Toronto, Canada.
Dixon, D.A. 2019. Review of the T-H-M-C Properties of MX-80 Bentonite. Nuclear Waste Management Organization Report NWMO-TR-2019-07. Toronto, Canada.

Dodd, J., Tsitsopoulos, V., Hoch, A., Holton, D., and Åkesson, M. 2019. Modelling water transport in bentonite pellets: Task 10 of the EBS Task Force. Wood report 204127-AA-UA00-00001-06-1, Wood, UK.
Dueck, A., and Börgesson, L. 2007. Model suggested for an important part of the hydro-mechanical behaviour of a water unsaturated bentonite. Engineering Geology, 92(3): 160–169. doi:10.1016/j.enggeo.2007.04.004.
Dwivedi, S.K., and Vishwakarma, M. 2018. Hydrogen embrittlement in different materials: A review. International Journal of Hydrogen Energy, 43(46): 21603–21616. doi:10.1016/j.ijhydene.2018.09.201.
Earle, S. 2019. Environmental Geology.
Einstein, A. 1905. Über die von der molekularkinetischen theorie der wärme geforderte bewegung von in ruhenden flüssigkeiten suspendierten teilchen. Annalen der physik, 322(8): 549–560. doi:https://doi.org/10.1002/andp.19053220806.
Erfani, H., Karadimitriou, N., Nissan, A., Walczak, M.S., An, S., Berkowitz, B., and Niasar, V. 2021. Process-Dependent Solute Transport in Porous Media. Transport in Porous Media, 140(1): 421–435. doi:10.1007/s11242-021-01655-6.
Eriksson, P. 2019. Development of thermo-hydraulic model for pellet fillings. SKB P-19-12.
European Commission (*Editor*). 2004. Geological disposal of radioactive wastes produced by nuclear power: from concept to implementation. Office for Official Publications of the European Communities, Luxembourg.
Faybishenko, B., Birkholzer, J., Sassani, D., and Swift, P. 2016. International Approaches for Nuclear Waste Disposal in Geological Formations: Geological Challenges in Radioactive Waste Isolation—Fifth Worldwide Review.
Feiveson, H., Mian, Z., Ramana, M.V., and von Hippel, F. 2011. Managing spent fuel from nuclear power reactors: Experience and lessons from around the world. International Panel on Fissile Materials,.
Fetter, C.W., Boving, T., and Kreamer, D. 1993. Contaminant Hydrogeology: Third Edition. Waveland Press.
Fick, A. 1855. Ueber diffusion. Annalen der physik, 170(1): 59–86. doi:10.1002/andp.18551700105.
Freundlich, H. 1907. Über die Adsorption in Lösungen. Zeitschrift für Physikalische Chemie – Stöchiometrie und Verwandschaftslehre. 57 (4),385–470.
Garitte, B., Weber, H., and Müller, H. 2015. EU Project LUCOEX - Requirements, manufacturing and QC of the buffer components of WP 2 (FE Experiment).
Gascoyne, M. 1997. Evolution of redox conditions and groundwater composition in recharge-discharge environments on the Canadian shield. Hydrogeology Journal, 5(3): 4–18. doi:10.1007/s100400050253.
Geier, J., Thatcher, K.E., Newson, R.K., Benbow, S.J., and Dessirier, B. 2018. Research on Resaturation of Bentonite Buffer. Swedish Radiation Safety Authority, SSM 2018:21: 158.
Gelet, R., Loret, B., and Khalili, N. 2012. A thermo-hydro-mechanical coupled model in local thermal non-equilibrium for fractured HDR reservoir with double porosity. Journal of Geophysical Research: Solid Earth, 117(B7). doi:10.1029/2012JB009161.

Gelet, R., Loret, B., and Khalili, N. 2013. Thermal recovery from a fractured medium in local thermal non-equilibrium. International Journal for Numerical and Analytical Methods in Geomechanics, 37(15): 2471–2501. doi:10.1002/nag.2145.
Gérard, F., Clément, A., and Fritz, B. 1998. Numerical validation of a Eulerian hydrochemical code using a 1D multisolute mass transport system involving heterogeneous kinetically controlled reactions. Journal of Contaminant Hydrology, 30(3): 201–216. doi:10.1016/S0169-7722(97)00047-8.
Giroud, N., Tomonaga, Y., Wersin, P., Briggs, S., King, F., Vogt, T., and Diomidis, N. 2018. On the fate of oxygen in a spent fuel emplacement drift in Opalinus Clay. Applied geochemistry, 97: 270–278. Elsevier.
Gobien, M., Garisto, F., Kremer, E., and Medri, C. 2016. Sixth Case Study: Reference Data and Codes. Nuclear Waste Management Organization Report NWMO-TR-2016-10. Toronto, Canada.
Gobien, M., Garisto, F., Kremer, E., and Medri, C. 2018. Seventh Case Study: Reference Data and Codes. Nuclear Waste Management Organization Report NWMO-TR-2018-10. Toronto, Canada.
Graham, J., Halayko, K.G., Hume, H., Kirkham, T., Gray, M., and Oscarson, D. 2002. A capillarity-advective model for gas break-through in clays. Engineering Geology, 64(2): 273–286. doi:10.1016/S0013-7952(01)00106-5.
Guo, G., and Fall, M. 2019. Modelling of preferential gas flow in heterogeneous and saturated bentonite based on phase field method. Computers and Geotechnics, 116: 103206. doi:10.1016/j.compgeo.2019.103206.
Guo, M., Chen, J., Lilja, C., Dehnavi, V., Behazin, M., Noël, J.J., and Shoesmith, D.W. 2020. The anodic formation of sulfide and oxide films on copper in borate-buffered aqueous chloride solutions containing sulfide. Electrochimica Acta, 362: 137087. doi:10.1016/j.electacta.2020.137087.
Guo, R. 2016. Thermal Response of a Mark II Conceptual Deep Geological Repository in Crystalline Rock. Nuclear Waste Management Organization Report NWMO-TR-2016-03. Toronto, Canada.
Guo, R. 2017. Thermal response of a Canadian conceptual deep geological repository in crystalline rock and a method to correct the influence of the near-field adiabatic boundary condition. Engineering Geology, 218: 50–62. doi:10.1016/j.enggeo.2016.12.014.
Guo, R. 2018. Thermal Response of a Mark II Conceptual Deep Geological Repository in Sedimentary Rock. Nuclear Waste Management Organization Report NWMO-TR-2018-09. Toronto, Canada.
Guzina, Z.R.-, Riahi, A., and Damjanac, B. 2015. Long-Term Stability Analysis of APM Conceptual Repository Design in Sedimentary and Crystalline Rock Settings. NWMO-TR-2015-27, Itasca Consultant Group, Inc.
Hale, S., Ries, X., Jaeggi, D., and Blum, P. 2021. Mechanical and hydraulic properties of the excavation damaged zone (EDZ) in the Opalinus Clay of the Mont Terri rock laboratory, Switzerland. Solid Earth, 12(7): 1581–1600. Copernicus GmbH. doi:10.5194/se-12-1581-2021.
Hall, D.S., Behazin, M., Jeffrey Binns, W., and Keech, P.G. 2021. An evaluation of corrosion processes affecting copper-coated nuclear waste containers in a deep

geological repository. Progress in materials science, 118: 1–28. doi:10.1016/j.pmatsci.2020.100766.
Hall, D.S., and Keech, P.G. 2017. An overview of the Canadian corrosion program for the long-term management of nuclear waste. Corrosion Engineering, Science and Technology, 52(sup1): 2–5. doi:10.1080/1478422X.2016.1275419.
Hall, D.S., Standish, T.E., Behazin, M., and Keech, P.G. 2018. Corrosion of copper-coated used nuclear fuel containers due to oxygen trapped in a Canadian deep geological repository. Corrosion engineering, science and technology, 53(4): 309–315. Taylor & Francis. doi:10.1080/1478422X.2018.1463009.
Harrington, J.F., and Horseman, S.T. 2003. Gas migration in KBS-3 buffer bentonite Sensitivity of test parameters to experimental boundary conditions. Sweden.
Hartley, L., Hoch, A., Jackson, P., Joyce, S., McCarthy, R., Rodwell, W., Swift, B., and Marsic, N. 2006. Groundwater flow and transport modelling during the temperate period for the SR-Can assessment Forsmark area - version 12. Sweden.
He, X., Sinan, M., Kwak, H., and Hoteit, H. 2021. A corrected cubic law for single-phase laminar flow through rough-walled fractures. Advances in Water Resources, 154: 103984. doi:10.1016/j.advwatres.2021.103984.
Heinze, T., and Pastore, N. 2023. Velocity-dependent heat transfer controls temperature in fracture networks. Nature Communications, 14: 362. doi:10.1038/s41467-023-36034-w.
Hemme, C., and Van Berk, W. 2018. Hydrogeochemical Modeling to Identify Potential Risks of Underground Hydrogen Storage in Depleted Gas Fields. Applied Sciences, 8(11): 2282. Multidisciplinary Digital Publishing Institute. doi:10.3390/app8112282.
Huysmans, M., and Dassargues, A. 2005. Review of the use of Péclet numbers to determine the relative importance of advection and diffusion in low permeability environments. Hydrogeology Journal, 13(5): 895–904. doi:10.1007/s10040-004-0387-4.
IAEA. 1993. Report on Radioactive Waste Diposal,Technical Reports Series No. 349, IAEA, Vienna. Text, IAEA. Available from https://www.iaea.org/publications/1453/report-on-radioactive-waste-diposal. [accessed 17 May 2020].
IAEA. 2003. Scientific and Technical Basis for the Geological Disposal of Radioactive Wastes,Technical Reports Series No. 413, IAEA, Vienna. Text, IAEA. Available from https://www.iaea.org/publications/6568/scientific-and-technical-basis-for-the-geological-disposal-of-radioactive-wastes. [accessed 17 May 2020].
IAEA. 2006. Geological Disposal of Radioactive Waste Safety Requirements, Safety Standards Series No. WS-R-4, IAEA, Vienna. Text, IAEA. Available from https://www.iaea.org/publications/7277/geological-disposal-of-radioactive-waste. [accessed 17 May 2020].
IAEA. 2011. Geological Disposal Facilities for Radioactive Waste Specific Safety Guide, IAEA Safety Standards Series No. SSG-14, IAEA, Vienna. Text, IAEA. Available from https://www.iaea.org/publications/8535/geological-disposal-facilities-for-radioactive-waste. [accessed 17 May 2020].
IAEA. 2017. Selection of Technical Solutions for the Management of Radioactive Waste, IAEA TECDOC No. 1817,IAEA, Vienna. Text, IAEA. Available from

https://www.iaea.org/publications/12217/selection-of-technical-solutions-for-the-management-of-radioactive-waste. [accessed 17 May 2020].
IAEA. 2018. Status and Trends in Spent Fuel and Radioactive Waste Management, IAEA Nuclear Energy Series NW-T-1.14, ,IAEA, Vienna. Text, IAEA. Available from https://www.iaea.org/publications/11173/status-and-trends-in-spent-fuel-and-radioactive-waste-management. [accessed 17 May 2020].
IAEA. 2020. Development of a Common Framework for Addressing Climate and Environmental Change in Post-closure Radiological Assessment of Solid Radioactive Waste Disposal, IAEA TECDOC No. 1904, IAEA, Vienna. Text, IAEA. Available from https://www.iaea.org/publications/13642/development-of-a-common-framework-for-addressing-climate-and-environmental-change-in-post-closure-radiological-assessment-of-solid-radioactive-waste-disposal. [accessed 17 May 2020].
Ichikawa, Y., and Selvadurai, A.P.S. 2012. Transport Phenomena in Porous Media: Aspects of Micro/Macro Behaviour. Springer Science & Business Media.
Idiart, A., Laviña, M., and Coene, E. 2019. Modelling of concrete degradation – Hydro-chemo-mechanical processes. Report for the safety evaluation SE-SFL.Swedish Nuclear Fuel and Waste Management Co Report SKB-R-19-11. Stockholm, Sweden.
Idiart, A., and Pekala, M. 2016. Models for Diffusion in Compacted Bentonite. *In* TR-15-06. © 2015 Svensk Kärnbränslehantering AB.
Ikonen, K. 2003. Thermal analyses of KBS-3H type repository. Posiva, Olkiluoto.
Ikonen, K., and Raiko, H. 2015. Thermal analyses of KBS-3H repository. Posiva, Olkiluoto.
Itälä, A. 2009. Chemical Evolution of Bentonite Buffer in a Final Repository of Spent Nuclear Fuel During the Thermal Phase. VTT PUBLICATIONS 721, Finland.
Jędrzejek, F., Szarłowicz, K., and Stobiński, M. 2022. A Geological Context in Radiation Risk Assessment to the Public. International Journal of Environmental Research and Public Health, 19(18): 11750. doi:10.3390/ijerph191811750.
Jofré, S.A.B., Mayer, K.U., and MacQuarrie, K.T.B. 2011. Modelling Reactive Transport in Sedimentary Rock Environments - Phase II;MIN3P code enhancements and illustrative simulations for a glaciation scenario. Nuclear Waste Management Organization, (NWMO TR-2011-13): 172.
Johannesson, L.-E., Kristensson, O., Åkesson, M., Eriksson, P., and Hedin, M. 2014. Tests and simulations of THM processes relevant for the buffer installation. : 72.
Johansson, A.J., Svensson, D., Gordon, A., Pahverk, H., Karlsson, O., Brask, J., Lundholm, M., Malmström, D., and Gustavsson, F. 2020. Corrosion of Copper After 20 years Exposure in the Bentonite Field Tests LOT S2 and A3. Swedish Nuclear Fuel and Waste Management Co Report SKB-TR-20-14. Stockholm, Sweden.
Johnson, P.J., Otto, S., Weaver, D.J., Dozier, B., Miller, T.A., Jordan, A.B., Hayes-Rich, N.G., and Stauffer, P.H. 2019. Heat-Generating Nuclear Waste in Salt: Field Testing and Simulation. Vadose Zone Journal, 18(1): 180160. doi:10.2136/vzj2018.08.0160.

Karlsdóttir, S.N. 2012. 7.08 - Corrosion, Scaling and Material Selection in Geothermal Power Production. *In* Comprehensive Renewable Energy. *Edited by* A. Sayigh. Elsevier, Oxford. pp. 241–259.

Karnland, O., and Birgersson, M. 2006. Montmorillonite stability. With special respect to KBS-3 conditions.

Karnland, O., Olsson, S., Dueck, A., Birgersson, M., Nilsson, U., Hernan-Haakansson, T., Pedersen, K., Goeteborg Univ., D. of C. and M.B., Nilsson, S., Eriksen, T.E., and Rosborg, B. 2009. Long term test of buffer material at the Aespoe Hard Rock Laboratory, LOT project. Final report on the A2 test parcel.

Keto, P., Dixon, D., Jonsson, E., Gunnarsson, D., Börgesson, L., and Hansen, J. 2009. Assessment of backfill design for KBS-3V repository. SKB, R-09-52, Stockholm, Sweden,: 119.

Khan, S.A., Riaz-ur-Rehman, and Ali Khan, M. 1994. Sorption of cesium on bentonite. Waste Management, 14(7): 629–642. doi:10.1016/0956-053X(94)90035-3.

Khan, S.A., Riaz-ur-Rehman, and Khan, M.A. 1995. Sorption of strontium on bentonite. Waste Management, 15(8): 641–650. doi:10.1016/0956-053X(96)00049-9.

Kiczka, M., Pekala, M., Maanoja, S., Muuri, E., and Wersin, P. 2021. Modelling of solute transport and microbial activity in diffusion cells simulating a bentonite barrier of a spent nuclear fuel repository. Applied Clay Science, 211: 106193. doi:10.1016/j.clay.2021.106193.

Kim, C.S. 2017. Evaluation of coupled hydro-mechanical (HM) behaviour of in situ shaft sealing components for used nuclear fuel. : 273.

King, F. 2005. Overview of the Corrosion Behaviour of Copper and Steel Used Fuel Containers in a Deep Geologic Repository in the Sedimentary Rock of the Michigan Basin, Ontario. Ontario Power Generation, Nuclear Waste Management Division Report No: 06819-REP-01300-10101-R00. Toronto, Canada.

King, F. 2007. Overview of a Carbon Steel Container Corrosion Model for a Deep Geological Repository in Sedimentary Rock. Nuclear Waste Management Technical Report NWMO TR-2007-01. Toronto, Canada.

King, F. 2008. Theory Manual for the Copper Corrosion Model for Uniform Corrosion in Sedimentary Rock CCM-UC.1.1. Nuclear Waste Management Organization Report NWMO TR-2008-07. Toronto, Canada.

King, F. 2009. Microbiologically Influenced Corrosion of Nuclear Waste Containers. Corrosion, 65(4): 233–251. doi:10.5006/1.3319131.

King, F. 2012. Gaseous hydrogen issues in nuclear waste disposal. *Edited by* R.P. Gangloff and B.P. Somerday. pp. 126–148.

King, F., Hall, D.S., and Keech, P.G. 2017. Nature of the near-field environment in a deep geological repository and the implications for the corrosion behaviour of the container. Corrosion engineering, science and technology, 52(sup1): 25–30. doi:10.1080/1478422X.2017.1330736.

King, F., and Kolar, M. 2006. Consequences of microbial activity for corrosion of copper used fuel containers – analyses using the CCM-MIC. 0.1 code. Ontario Power Generation, Nuclear Waste Management Division Report No: 06819-REP-01300-10120-R00, Toronto, Ontario, Canada.

King, F., Kolàř, M., Briggs, S., Behazin, M., Keech, P., and Diomidis, N. 2024. Review of the Modelling of Corrosion Processes and Lifetime Prediction for HLW/SF Containers—Part 1: Process Models. Corrosion and Materials Degradation, 5(2): 124–199. Multidisciplinary Digital Publishing Institute. doi:10.3390/cmd5020007.

King, F., Kolar, M., and Gascoyne, S.S. 2002. Theory Manual for the Microbiological Copper Corrosion Model CCM-MIC.0. Ontario Power Generation, Nuclear Waste Management Division Report No: 06819-REP-01200-10091-R00. Toronto, Canada.

King, F., Kolar, M., and Maak, P. 2008. Reactive-transport model for the prediction of the uniform corrosion behaviour of copper used fuel containers. Journal of nuclear materials, 379(1): 133–141. doi:10.1016/j.jnucmat.2008.06.017.

King, F., Kolar, M., and Shoesmith, D.W. 1996. Modelling the effects of porous and semi-permeable layers on corrosion processes.

King, F., Lilja, C., and Vähänen, M. 2013. Progress in the understanding of the long-term corrosion behaviour of copper canisters. Journal of Nuclear Materials, 438(1): 228–237. doi:10.1016/j.jnucmat.2013.02.080.

Kolditz, O., Bauer, S., Bilke, L., Böttcher, N., Delfs, J.O., Fischer, T., Görke, U.J., Kalbacher, T., Kosakowski, G., McDermott, C.I., Park, C.H., Radu, F., Rink, K., Shao, H., Shao, H.B., Sun, F., Sun, Y.Y., Singh, A.K., Taron, J., Walther, M., Wang, W., Watanabe, N., Wu, Y., Xie, M., Xu, W., and Zehner, B. 2012. OpenGeoSys: an open-source initiative for numerical simulation of thermo-hydro-mechanical/chemical (THM/C) processes in porous media. Environmental Earth Sciences, 67(2): 589–599. doi:10.1007/s12665-012-1546-x.

Kosakowski, G. 2004. Time-dependent Flow andTransport Calculations for Project Opalinus Clay (Entsorgungsnachweis). TECHNICAL REPORT 03-10, NAGRA.

Kouhail, Y., Rinderknecht, F., Geyer, F., Soballa, E., Schild, D., Quinto, F., Metz, V., Schäfer, T., and Geckeis, H. 2021. Long term bentonite erosion experiments: Radionuclide diffusion in FEBEX bentonite.

Kremer, E.P. 2017. Durability of the Canadian used fuel container. Corrosion engineering, science and technology, 52(sup1): 173–177. Taylor & Francis. doi:10.1080/1478422X.2017.1330024.

Kröhn, K.-P. 2003. New conceptual models for the resaturation of bentonite. Applied Clay Science, 23(1): 25–33. doi:10.1016/S0169-1317(03)00083-8.

Kröhn, K.-P. 2004. Modelling the re-saturation of bentonite in final repositories in crystalline rock: final report. GRS, Köln Garching b. München Berlin Braunschweig.

Kröhn, K.-P. 2011. Code Viper: theory and current status. Gesellschaft für Anlagen und Reaktorsicherheit, Köln.

Kröhn, K.-P. 2017. Bentonite re-saturation: different conceptual models – similar mathematical descriptions. *In* Radioactive Waste Confinement: Clays in Natural and Engineered Barriers. *Edited by* S. Norris, J. Bruno, M. van Geet, and E. Verhoef. Geological Society of London. p. 0.

Kröhn, K.-P. 2019. Re-saturation of compacted bentonite under repository-relevant flow conditions. Geomechanics for Energy and the Environment, 17: 115–122. doi:10.1016/j.gete.2018.09.003.

Kronberg, M., Johannesson, L.-E., and Eriksson, P. 2020. Strategy, adaptive design and quality control of bentonite materials for a KBS-3 repository.
Kursten, B., Druyts, F., Macdonald, D.D., Smart, N.R., Gens, R., Wang, L., Weetjens, E., and Govaerts, J. 2011. Review of corrosion studies of metallic barrier in geological disposal conditions with respect to Belgian Supercontainer concept. Corrosion Engineering, Science and Technology, 46(2): 91–97. Taylor & Francis. doi:10.1179/1743278210Y.0000000022.
Lang, L.Z., Tripathy, S., Baille, W., Schanz, T., and Sridharan, A. 2019. Linkage between swelling pressure, total suction of saturated bentonites and suction of saturating aqueous solutions. Applied Clay Science, 171: 82–91. doi:10.1016/j.clay.2019.02.007.
Langmuir, I. 1917. The Adsorption of Gases on Plane Surfaces of Glass, Mica and Pt. doi:10.1021/ja02242a004.
Lanyon, G., Senger, R., and Marschall, P. 2009. A Structured Approach to the Derivation of Effective Properties for Combined Water and Gas Flow in the EDZ.
Lanyon, G.W. 2011. Excavation Damaged Zones Assessment.
Lanyon, G.W., and Senger, R. 2011. A Structured Approach to the Derivation of Effective Properties for Combined Water and Gas Flow in the EDZ. Transport in Porous Media, 90(1): 95–112. doi:10.1007/s11242-011-9716-y.
Lee, A., Zivkovic, S., Doyle, D., Brich, K., and Kremer, E. 2016. NWMO Sixth Case Study Reference Data. Nuclear Waste Management Organization Internal Document (Private Collection). Toronto, Canada.
van der Lee, J., De Windt, L., Lagneau, V., and Goblet, P. 2003. Module-oriented modeling of reactive transport with HYTEC. Computers & Geosciences, 29(3): 265–275. doi:10.1016/S0098-3004(03)00004-9.
Lemire, R.J., Palmer, D.A., TAYLOR, P., and Schlenz, H. 2020. CHEMICAL THERMODYNAMICS OF IRON: PART 2-Chemical Thermodynamics Volume 13b. uclear Energy Agency of the OECD (NEA), Paris, France.
Li, W., Chen, M., Jin, Y., Lu, Y., Gao, J., Meng, H., Zhang, Y., and Tan, P. 2018. Effect of local thermal non-equilibrium on thermoporoelastic response of a borehole in dual-porosity media. Applied Thermal Engineering, 142: 166–183. doi:10.1016/j.applthermaleng.2018.06.055.
Li, Z., Su, G., Zheng, Q., and Nguyen, T.S. 2020. A dual-porosity model for the study of chemical effects on the swelling behaviour of MX-80 bentonite. Acta Geotechnica, 15(3): 635–653. doi:10.1007/s11440-019-00762-5.
Liang, S.-Y., Lin, W.-S., Lin, G.-F., Liu, C.-W., and Fan, C. 2021. The Effect of Porosity Change in Bentonite Caused by Decay Heat on Radionuclide Transport through Buffer Material. Applied Sciences, 11(17): 7933. Multidisciplinary Digital Publishing Institute. doi:10.3390/app11177933.
Lichtner, P.C., Hammond, G.E., Lu, C., Karra, S., Bisht, G., Andre, B., Mills, R., and Kumar, J. 2015. PFLOTRAN User Manual: A Massively Parallel Reactive Flow and Transport Model for Describing Surface and Subsurface Processes.
Liu, Y., Ma, L., Ke, D., Cao, S., Xie, J., Zhao, X., Chen, L., and Zhang, P. 2014. Design and validation of the THMC China-Mock-Up test on buffer material for HLW disposal. Journal of Rock Mechanics and Geotechnical Engineering, 6(2): 119–125. doi:10.1016/j.jrmge.2014.01.004.

Löfman, J., and Keto, V. 2007. FEFTRATM. Verification. (VTT RESEARCH NOTES 2385): 118.
Löfman, J., Pitkaenen, P., Meszaros, F., Keto, V., and Ahokas, H. 2009. Modelling of groundwater flow and solute transport in Olkiluoto. Update 2008. Posiva Oy.
Logan, D.L. 2007. First Course in the Finite Element Method. Thomson Engineering.
Lu, Y., Wang, Z., Parker, T., Yang, R., Shen, S., Sun, P., and Wang, Q. 2020. Experimental studies on influencing factors of stress corrosion in rectifying column. Process Safety and Environmental Protection, 144: 123–132. doi:10.1016/j.psep.2020.07.029.
Luo, Y., Zhang, J., Zhou, Z., Aguilar-Lopez, J.P., Greco, R., and Bogaard, T. 2023. Effects of dynamic changes of desiccation cracks on preferential flow: experimental investigation and numerical modeling. Hydrology and Earth System Sciences, 27(3): 783–808. Copernicus GmbH. doi:10.5194/hess-27-783-2023.
Maanoja, S., Lakaniemi, A.-M., Lehtinen, L., Salminen, L., Auvinen, H., Kokko, M., Palmroth, M., Muuri, E., and Rintala, J. 2020. Compacted bentonite as a source of substrates for sulfate-reducing microorganisms in a simulated excavation-damaged zone of a spent nuclear fuel repository. Applied Clay Science, 196: 105746. doi:10.1016/j.clay.2020.105746.
Marquie, C., Richard, B., Dauzeres, A., and Nahas, G. 2019. Concrete aging in containment building and deep geological disposal facilities: the odoba project.
Marsal, F. 2007. Modelling of long term geochemical evolution of the bentonite buffer of a KBS-3 repository. French Institute for Radiological Protection and Nuclear Safety (IRSN) Report. : 83.
Marschall, P., Giger, S., De La Vassière, R., Shao, H., Leung, H., Nussbaum, C., Trick, T., Lanyon, B., Senger, R., Lisjak, A., and Alcolea, A. 2017. Hydro-mechanical evolution of the EDZ as transport path for radionuclides and gas: insights from the Mont Terri rock laboratory (Switzerland). Swiss Journal of Geosciences, 110(1): 173–194. SpringerOpen. doi:10.1007/s00015-016-0246-z.
Marshall, M.H.M., McKelvie, J.R., Simpson, A.J., and Simpson, M.J. 2015. Characterization of natural organic matter in bentonite clays for potential use in deep geological repositories for used nuclear fuel. Applied Geochemistry, 54: 43–53. doi:10.1016/j.apgeochem.2014.12.013.
Martín, M., Cuevas, J., and Leguey, S. 2000. Diffusion of soluble salts under a temperature gradient after the hydration of compacted bentonite. Applied clay science, 17(1): 55–70. doi:10.1016/S0169-1317(00)00006-5.
Mayer, K., Amos, R., Molins, S., and Gérard, F. 2012. Reactive transport modeling in variably saturated media with MIN3P: Basic model formulation and model enhancements. *In* Groundwater Reactive Transport Models. pp. 187–212.
Mayer, K.U., Frind, E.O., and Blowes, D.W. 2002. Multicomponent reactive transport modeling in variably saturated porous media using a generalized formulation for kinetically controlled reactions. Water Resources Research, 38(9): 13-1-13–21. doi:https://doi.org/10.1029/2001WR000862.
McEvoy, F.M., Schofield, D.I., Shaw, R.P., and Norris, S. 2016. Tectonic and climatic considerations for deep geological disposal of radioactive waste: A UK perspective. The Science of the Total Environment, 571: 507–521. doi:10.1016/j.scitotenv.2016.07.018.

Millard, A., Rejeb, A., Chijimatsu, M., Jing, L., De Jonge, J., Kohlmeier, M., Nguyen, T.S., Rutqvist, J., Souley, M., and Sugita, Y. 2004. Evaluation of THM coupling on the safety assessment of a nuclear fuel waste repository in a homogeneous hard rock. *In* Elsevier Geo-Engineering Book Series. pp. 211–216.
Montes-H, G., Fritz, B., Clement, A., and Michau, N. 2005. Modelling of geochemical reactions and experimental cation exchange in MX80 bentonite. Journal of Environmental Management, 77(1): 35–46. doi:10.1016/j.jenvman.2005.03.003.
Moore, R. 1939. Water conduction from shallow water tables. Hilgardia, 12(6): 383–426. University of California, Agriculture and Natural Resources.
Moreno, L., and Neretnieks, I. 2013. Impact of gas generation on radionuclide release – comparison between results for new and old data. Swedish Nuclear Fuel and Waste Management Co Report SKB-R-19-06. Stockholm, Sweden. : 52.
Mota-Heredia, C., Cuevas, J., and Fernández, R. 2024. Effect of Iron Chloride (II) on Bentonites under Hydrothermal Gradients: A Comparative Study between Sodium Bentonite and Calcium Bentonite. Minerals, 14(2): 132. Multidisciplinary Digital Publishing Institute. doi:10.3390/min14020132.
Muhammed, N.S., Haq, B., Shehri, D.A., Al-Ahmed, A., Rahman, M.M., and Zaman, E. 2022. A review on underground hydrogen storage: Insight into geological sites, influencing factors and future outlook. Energy Reports, 8: 461–499. Elsevier.
Müller, H.R., Garitte, B., Vogt, T., Köhler, S., Sakaki, T., Weber, H., Spillmann, T., Hertrich, M., Becker, J.K., Giroud, N., Cloet, V., Diomidis, N., and Vietor, T. 2017. Implementation of the full-scale emplacement (FE) experiment at the Mont Terri rock laboratory. Swiss journal of geosciences, 110(1): 287–306. doi:10.1007/s00015-016-0251-2.
NAS. 1957. The Disposal of Radioactive Waste on Land. National Academy of Sciences (NAS)-National Research Council, Washington, D. C.
Nasir, O., Fall, M., and Evgin, E. 2014. A simulator for modeling of porosity and permeability changes in near field sedimentary host rocks for nuclear waste under climate change influences. Tunnelling and Underground Space Technology, 42: 122–135. doi:10.1016/j.tust.2014.02.010.
Natural Resources Canada. 2019. Natural Resoruce Canada:Inventory of radioactive waste in Canada.
NDA. 2010. Geological Disposal: Summary of generic designs. *In* NDA Report NDA/RWMD/054. Nuclear Decommissioning Authority.
NEA. 1999. Geological Disposal of Radioactive Waste: Review of Developments in the Last Decade, OECE Nuclear Energy Agency, Paris. Text. Available from https://www.oecd-ilibrary.org/nuclear-energy/geological-disposal-of-radioactive-waste_9789246180547-en. [accessed 17 May 2020].
NEA. 2021. Radioactive Waste Management and Decommissioning. OECD. pp. 240–270.
Nemes, A., Schaap, M.G., Leij, F.J., and Wösten, J.H.M. 2001. Description of the unsaturated soil hydraulic database UNSODA version 2.0. Journal of Hydrology, 251(3): 151–162. doi:10.1016/S0022-1694(01)00465-6.
Nguyen, T.S., and Jing, L. 2005. DECOVALEX III/BENCHPAR PROJECTS Implications of Thermal-Hydro-Mechanical Coupling on the Near-Field Safety of a Nuclear Waste Repository in a Homogeneous Rock Mass. SKI Report 2005:25. Available

from https://drive.google.com/file/d/0Bzn-bWq-69-4RFYtQUFaVzc3R0NBQVpEcHJfNzdQdVQ2YmZ3/edit?usp=sharing&usp=embed_facebook. [accessed 18 August 2020].
Nield, D.A., and Bejan, A. 2013. Convection in Porous Media. *In* Convection in Porous Media. *Edited by* D.A. Nield and A. Bejan. Springer International Publishing, Cham. pp. 1–35.
Noronha, J. 2016. Deep geological repository conceptual design report crystalline / sedimentary rock environment. Nuclear Waste Management Organization, APM-REP-00440-0015 R001: 191.
Norrfors, K.K. 2011. Stability and sorption capacity of montmorillonite colloids. TRITA-CHE Report 2015:8: 1–91.
NWMO. 2019. RD 2019 – NWMO's Program for Research and Development for Long-Term Management of Used Nuclear Fuel. Nuclear Waste Management Organization Report. Toronto, Canada.
NWMO. 2021. Technical Program for Long-Term Management of Canada's Used Nuclear Fuel – Annual Report 2020. Nuclear Waste Management Organization Report NWMO-TR-2021-01. Toronto, Canada.
NWMO. 2024. Site selection : About the site selection process.
Olivella, S., and Alonso, E.E. 2008. Gas flow through clay barriers. Géotechnique, 58(3): 157–176. ICE Publishing. doi:10.1680/geot.2008.58.3.157.
Oscarson, D.W., Hum, H.B., and King, F. 1994. Sorption of Cesium on Compacted Bentonite.
Palomäki, J., and Ristimäki, L. 2013. Facility Description 2012 Summary Report of the Encapsulation Plant and Disposal Facility Designs.
Papry, S.A., Rashwan, T.L., Mondal, P.K., Behazin, M., Keech, P.G., and Krol, M.M. 2023. Investigating bisulfide sorption onto bentonite through laboratory batch experiments. Applied Geochemistry, 152: 105626. doi:10.1016/j.apgeochem.2023.105626.
Parkhurst, D.L., and Appelo, C. a. J. 2013. Description of input and examples for PHREEQC version 3: a computer program for speciation, batch-reaction, one-dimensional transport, and inverse geochemical calculations. *In* Techniques and Methods. U.S. Geological Survey.
Parkhurst, D.L., Kipp, K.L., Engesgaard, P., and Charlton, S.R. 2016. PHAST--A program for simulating groundwater flow, solute transport, and multicomponent geochemical reactions. Available from https://pubs.usgs.gov/tm/2005/tm6A8/. [accessed 7 April 2019].
Patankar, S.V. 2018. Numerical heat transfer and fluid flow. CRC Press, Boca Raton.
Patel, R., Punshon, C., Nicholas, J., Bastid, P., Zhou, R., Schneider, C., Bagshaw, N., Howse, D., Hutchinson, E., Asano, R., and King, F. 2012. Canister Design Concepts for Disposal of Spent Fuel and High Level Waste. Radioactive Waste,: 245.
Pati, S., Borah, A., Boruah, M.P., and Randive, P.R. 2022. Critical review on local thermal equilibrium and local thermal non-equilibrium approaches for the analysis of forced convective flow through porous media. International Communications in Heat and Mass Transfer, 132: 105889. doi:10.1016/j.icheatmasstransfer.2022.105889.

Pedersen, K. 2010. Analysis of copper corrosion in compacted bentonite clay as a function of clay density and growth conditions for sulfate-reducing bacteria. Journal of applied microbiology, 108(3): 1094–1104. doi:10.1111/j.1365-2672.2009.04629.x.

Pekala, M., Smith, P., Wersin, P., Diomidis, N., and Cloet, V. 2020. Comparison of models to evaluate microbial sulphide generation and transport in the near field of a SF/HLW repository in Opalinus Clay. Journal of Contaminant Hydrology, 228: 103561. doi:10.1016/j.jconhyd.2019.103561.

Pekala, M., Wersin, P., Cloet, V., and Diomidis, N. 2019. Reactive transport calculations to evaluate sulphide fluxes in the near-field of a SF/HLW repository in the Opalinus Clay. Applied Geochemistry, 100: 169–180. doi:10.1016/j.apgeochem.2018.11.006.

Pernicova, R., Citek, D., Dobias, D., Kolisko, J., Mandlik, T., and Hausmannova, L. 2023. Development of a Low-pH Concrete Intended for Deep Geological Repository for Radioactive Waste. Buildings, 13(1): 182. Multidisciplinary Digital Publishing Institute. doi:10.3390/buildings13010182.

Pintado, X., Md. Mamunul, H., and Martikainen, J. 2012. Thermo-hydromechanical tests of buffer materials.

Posiva. 2020. General Time Schedule for Final Disposal. Available from http://www.posiva.fi/en/final_disposal/general_time_schedule_for_final_disposal. [accessed 17 May 2020].

Poteri, A., and Laitinen, M. 1999. Site-to-canister scale flow and transport in Haestholmen, Kivetty, Olkiluoto and Romuvaara. Finland.

Pruess, K., Oldenburg, C., and Moridis, G. 2012. TOUGH2 USER'S GUIDE, VERSION 2. Earth Sciences Division, Lawrence Berkeley National Laboratory University of California, Berkeley, California.,: 210.

Pusch, R. 1980. Permeability of highly compacted bentonite. SKB Technical Report 80-16, SKB.

Radeisen, E., Shao, H., Hesser, J., Naumov, D., Wang, W., and Kolditz, O. 2024. Modelling of preferential gas flow in saturated bentonite using a bimodal, strain-dependent pore model. Applied Clay Science, 249: 107232. doi:10.1016/j.clay.2023.107232.

Rashwan, T.L., Asad, M.A., Molnar, I.L., Behazin, M., Keech, P.G., and Krol, M.M. 2022. Exploring the governing transport mechanisms of corrosive agents in a Canadian deep geological repository. Science of The Total Environment,: 1–43.

Richards, L.A. 1931. Capillary conduction of liquids through porous mediums. Cornell University,.

Rickard, D. 1997. Kinetics of pyrite formation by the H2S oxidation of iron (II) monosulfide in aqueous solutions between 25 and 125°C: The rate equation. Geochimica et Cosmochimica Acta, 61(1): 115–134. doi:10.1016/S0016-7037(96)00321-3.

Rickard, D., and Luther, G.W. 2007. Chemistry of Iron Sulfides. Chemical Reviews, 107(2): 514–562. American Chemical Society. doi:10.1021/cr0503658.

Rutqvist, J., Bäckström, A., Chijimatsu, M., Feng, X.-T., Pan, P., Hudson, J., Jing, L., Kobayashi, A., Koyama, T., Lee, H.S., Huang, X.-H., Rinne, M., and Shen, B. 2008. A multiple-code simulation study of the long-term EDZ evolution of

geological nuclear waste repositories. Environmental Geology, 57: 1313–1324. doi:10.1007/s00254-008-1536-1.
RWM. 2017. Geological Disposal: Concept Status Report | RWM Tools. Available from https://rwm.nda.gov.uk/publication/geological-disposal-concept-status-report/. [accessed 23 December 2021].
RWM. 2018. Geological Disposal Concept Selection Process. Radioactive Waste Managment (RWM), Nuclear decommissioning Authority, The United Kingdom.
Salas, J., Sena, C., and Arcos, D. 2014. Hydrogeochemical evolution of the bentonite buffer in a KBS-3 repository for radioactive waste. Reactive transport modelling of the LOT A2 experiment. Applied Clay Science, 101: 521–532. doi:10.1016/j.clay.2014.09.016.
Savage, D., Arthur, R., Watson, C., Wilson, J., and Strömberg, B. 2011. Testing geochemical models of bentonite pore water evolution against laboratory experimental data. Physics and Chemistry of the Earth, Parts A/B/C, 36(17): 1817–1829. doi:10.1016/j.pce.2011.07.025.
Savage, D., Watson, C., Wilson, J., and Arthur, R. 2010. An Evaluation of Models of Bentonite Pore Water Evolution. Sweden.
Schaetzl, R.J., and Thompson, M.L. 2015. Soils: Genesis and Geomorphology. Cambridge University Press.
Schenck, H. von. 2018. Thermal evolution of the repository – the effect of heat generating waste – Report for the safety evaluation SE-SFL. : 20.
Schwartz, M.O. 2019. Groundwater contamination associated with a potential nuclear waste repository at Yucca Mountain, USA. Bulletin of Engineering Geology and the Environment, 79(2): 1125–1136. doi:10.1007/s10064-019-01591-2.
Scully, J.R., Féron, D., and Hänninen, H. 2016. Review of the NWMO Copper Corrosion Program. Nuclear Waste Management Organization Report NWMO-TR-2016-11. Toronto, Canada.
Selvadurai, A.P.S., and Najari, M. 2017. The thermo-hydro-mechanical behavior of the argillaceous Cobourg Limestone. Journal of geophysical research: Solid earth, 122(6): 4157–4171. doi:https://doi.org/10.1002/2016JB013744.
Sena, C., Salas, J., and Arcos, D. 2010. Thermo-Hydro-Geochemical Modelling of the Bentonite Buffer – LOT A2 Experiment. Swedish Nuclear Fuel and Waste Management Co Report SKB-TR-10-65. Stockholm, Sweden.
Senger, R., Lanyon, G., and Marschall, P. 2014. Modeling the Hydraulic and Two-phase Flow Behaviour of the Heterogeneous, Fractured EDZ in the Opalinus Clay During the HG-A Experiment at the Mont Terri URL. doi:10.3997/2214-4609.20140044.
Senior, N., Martino, T., Binns, W., and Keech, P. 2020. The anoxic corrosion behaviour of copper in the presence of chloride and sulphide. Materials and Corrosion, 72. doi:10.1002/maco.202011783.
Senior, N., Martino, T., Keech, P.G., Binns, W.J., Diomidis, N., and Lilja, C. 2023. The use of hydrogen in monitoring the anoxic corrosion of copper. Materials and Corrosion, 74(11–12): 1645–1655. doi:10.1002/maco.202313769.
Seyedi, D.M., Plúa, C., Vitel, M., Armand, G., Rutqvist, J., Birkholzer, J., Xu, H., Guo, R., Thatcher, K.E., Bond, A.E., Wang, W., Nagel, T., Shao, H., and Kolditz, O. 2021. Upscaling THM modeling from small-scale to full-scale in-situ experiments

in the Callovo-Oxfordian claystone. International Journal of Rock Mechanics and Mining Sciences, 144: 104582. doi:10.1016/j.ijrmms.2020.104582.
Shackelford, C., and Moore, S. 2013. Fickian diffusion of radionuclides for engineered containment barriers: Diffusion coefficients, porosities, And complicating issues. Engineering geology, 152: 133–147. doi:10.1016/j.enggeo.2012.10.014.
Sharma, V.K., and Millero, F.J. 1988. The oxidation of Cu(I) in electrolyte solutions. Journal of Solution Chemistry, 17(6): 581–599. doi:10.1007/BF00651464.
Sherwood Lollar, B. 2011. Far-field Microbiology Considerations Relevant to a Deep Geological Repository – State of Science Review. Nuclear Waste Management Organization Report NWMO-TR-2011-09. Toronto, Canada.
Sherwood Lollar, B., Frape, S.K., Fritz, P., Macko, S.A., Welhan, J.A., Blomqvist, R., and Lahermo, P.W. 1993a. Evidence for bacterially generated hydrocarbon gas in Canadian shield and fennoscandian shield rocks. Geochimica et Cosmochimica Acta, 57(23): 5073–5085. doi:10.1016/0016-7037(93)90609-Z.
Sherwood Lollar, B., Frape, S.K., Weise, S.M., Fritz, P., Macko, S.A., and Welhan, J.A. 1993b. Abiogenic methanogenesis in crystalline rocks. Geochimica et Cosmochimica Acta, 57(23): 5087–5097. doi:10.1016/0016-7037(93)90610-9.
Silva, O., Coene, E., Molinero, J., Laviña, M., and Idiart, A. 2019a. Gas release from the BHK vault – Multiphase flow modelling of the near-field. Swedish Nuclear Fuel and Waste Management Co Report SKB-R-19-06. Stockholm, Sweden.
Silva, O., Sáinz-García, A., and Molinero, J. 2019b. Gas release from the SFL repository and migration through the geosphere. Swedish Nuclear Fuel and Waste Management Co Report SKB-R-19-07. Stockholm, Sweden.
Singhal, B.B.S., and Gupta, R.P. 2010. Applied Hydrogeology of Fractured Rocks: Second Edition. *In* 2nd edition. Springer Netherlands.
SKB. 2010a. Design and production of the KBS-3 repository. Swedish Nuclear Fuel and Waste Management Company (SKB). : 56.
SKB. 2010b. Corrosion Calculations Report for the Safety Assessment SR-Site. Swedish Nuclear Fuel and Waste Management Co Report SKB-TR-10-66. Stockholm, Sweden.
SKB. 2011. Site selection – siting of the final repository for spent nuclear fuel.
Smith, P.A., Brommundt, J., Mayer, G., Koskinen, L., Poteri, A., Nordman, H., Pulkkanen, V.-M., Cormenzana, J.L., Hjerpe, T., and Snellman, M.V. 2012. Modelling Strategy Report, Working Report 2012-06. POSIVA OY FI-27160 OLKILUOTO, FINLAND.
Sobola, D., and Dallaev, R. 2024. Exploring Hydrogen Embrittlement: Mechanisms, Consequences, and Advances in Metal Science. Energies, 17(12): 2972. Multidisciplinary Digital Publishing Institute. doi:10.3390/en17122972.
Soler, J.M., Neretnieks, I., Moreno, L., Liu, L., Meng, S., Svensson, U., Trinchero, P., Iraola, A., Ebrahimi, H., Molinero, J., and Vidstrand, P. 2019. Evaluation and modelling report of Task 9A based on comparisons and analyses of predictive modelling results for the REPRO WPDE experiments. Swedish Nuclear Fuel and Waste Management Co Report SKB-R-17-10. Stockholm, Sweden. : 156.
Standish, T., Chen, J., Jacklin, R., Jakupi, P., Ramamurthy, S., Zagidulin, D., Keech, P., and Shoesmith, D. 2016. Corrosion of copper-coated steel high level nuclear

waste containers under permanent disposal conditions. Electrochimica acta, 211: 331–342. doi:10.1016/j.electacta.2016.05.135.
Steefel, C.I., Appelo, C.A.J., Arora, B., Jacques, D., Kalbacher, T., Kolditz, O., Lagneau, V., Lichtner, P.C., Mayer, K.U., Meeussen, J.C.L., Molins, S., Moulton, D., Shao, H., Šimůnek, J., Spycher, N., Yabusaki, S.B., and Yeh, G.T. 2015. Reactive transport codes for subsurface environmental simulation. Computational Geosciences, 19(3): 445–478. doi:10.1007/s10596-014-9443-x.
Stroes-Gascoyne, S., Hamon, C.J., Maak, P., and Russell, S. 2010. The effects of the physical properties of highly compacted smectitic clay (bentonite) on the culturability of indigenous microorganisms. Applied clay science, 47(1): 155–162. doi:10.1016/j.clay.2008.06.010.
Suckling, p., Avis, J., Calder, N., Nasir, O., Humphreys, P., King, F., and Walsh, R. 2015. T2GGM Version 3.2: Gas Generation and Transport Code. Nuclear Waste Management Organization Report NWMO-TR-2015-13. Toronto, Canada.
Sun, H., Scaringi, G., Mašín, D., and Najser, J. 2022. An experimental investigation on the swelling behavior of compacted B75 bentonite. Engineering Geology, 296: 106452. doi:10.1016/j.enggeo.2021.106452.
Suzuki, Y., and Hisamatsu, Y. 1981. Stress corrosion cracking of pure copper in dilute ammoniacal solutions. Corrosion Science, 21(5): 353–368. doi:10.1016/0010-938X(81)90072-X.
Svensson, U., and Ferry, M. 2010. Darcy Tools version 3.4 – User's Guide. Svensk Kärnbränslehantering AB, (SKB R-10-72): 157.
Sykes, J.F., Normani, S.D., and Yin, Y. 2011. Hydrogeologic Modelling. Nuclear Waste Management Organization Report NWMO-TR-2011-16. Toronto, Canada.
Szakálos, P., and Seetharaman, S. 2012. Corrosion of copper canister. Swedish Radiation Safety Authority Report 2012:17.Stockholm, Sweden.
Tachi, Y., Yotsuji, K., Suyama, T., and Ochs, M. 2014. Integrated sorption and diffusion model for bentonite. Part 2: porewater chemistry, sorption and diffusion modeling in compacted systems. Journal of Nuclear Science and Technology, 51(10): 1191–1204. Taylor & Francis. doi:10.1080/00223131.2014.914453.
Taheri, S., and El-Zein, A. 2023. Desiccation cracking of polymer-bentonite mixtures: An experimental investigation. Applied Clay Science, 238: 106945. doi:10.1016/j.clay.2023.106945.
Tait, J.C., Roman, H., and Morrison, C.A. 2000. Characteristic and Radionuclide Inventories of Used Fuel from OPG Nuclear Generation Stations. Volume 1 – Main report; and Volume 2 – Radionuclide inventory data. Ontario Power Generation, Nuclear Waste Management Division Report No: 06819-REP-01200-10029-R00. Toronto, Canada.
Tamayo-Mas, E., Harrington, J.F., Damians, I.P., Olivella, S., Radeisen, E., Rutqvist, J., and Wang, Y. 2024. Advective gas flow in bentonite: Development and comparison of enhanced multi-phase numerical approaches. Geomechanics for Energy and the Environment, 37: 100528. doi:10.1016/j.gete.2023.100528.
Tanaka, S. 2022. Bentonite barrier performance affected by precipitation of secondary minerals: Diffusivities of water and iodide ions in the presence of calcium carbonate. Applied Geochemistry, 146: 105448. doi:10.1016/j.apgeochem.2022.105448.

Thouvenot, P., Bildstein, O., Munier, I., Cochepin, B., Poyet, S., Bourbon, X., and Treille, E. 2013. Modeling of concrete carbonation in deep geological disposal of intermediate level waste. EPJ Web of Conferences, 56: 05004. EDP Sciences. doi:10.1051/epjconf/20135605004.
Tournassat, C., and Appelo, C.A.J. 2011. Modelling approaches for anion-exclusion in compacted Na-bentonite. Geochimica et Cosmochimica Acta, 75(13): 3698–3710. doi:10.1016/j.gca.2011.04.001.
Trotignon, L., Devallois, V., Peycelon, H., Tiffreau, C., and Bourbon, X. 2007. Predicting the long term durability of concrete engineered barriers in a geological repository for radioactive waste. Physics and Chemistry of the Earth, Parts A/B/C, 32(1): 259–274. doi:10.1016/j.pce.2006.02.049.
Tufenkji, N. 2007. Modeling Microbial Transport in Porous Media: Traditional Approaches and Recent Developments. Advances in Water Resources, 30: 1455–1469. doi:10.1016/j.advwatres.2006.05.014.
U.S. DOE. 2002. Yucca Mountain Science and Engineering Report Technical Information Supporting Site Recommendation Consideration. DOE/ RW-0539 Rev. 1; Department of Energy, Office of Civilian Radioactive Waste Management.: Las Vegas.
Van Genuchten, M.T. 1980. A closed-form equation for predicting the hydraulic conductivity of unsaturated soils 1. Soil science society of America journal, 44(5): 892–898.
Van Loon, L.R., Glaus, M.A., and Müller, W. 2007. Anion exclusion effects in compacted bentonites: Towards a better understanding of anion diffusion. Applied Geochemistry, 22(11): 2536–2552. doi:10.1016/j.apgeochem.2007.07.008.
Vaunat, J., and Olivella, S. 2009. CODE_BRIGHT User's Guide: A 3-D program for thermo-hydro-mechanical analysis in geological media.
Verhoeven, B., Bogaerts, W., Van Aken, P., Gaggiano, R., Baeyens, J., Rossi, B., and Dewil, R. 2022. Pitting and General Corrosion Susceptibilities of Materials for High Level Radioactive Waste (HLW) Disposal. Materials, 15(18): 6464. Multidisciplinary Digital Publishing Institute. doi:10.3390/ma15186464.
Vidstrand, P., Stigsson, M., Åkesson, M., and Fransson, Å. 2017. SKB Task Forces EBS and GWFTS - Modelling the interaction between engineered and natural barriers - A compilation of Task 8 descriptions. SVENSK KÄRNBRÄNSLEHANTERING AB, (P-16-05): 143.
Vieno, T. 2000. Groundwater salinity at Olkiluoto and its effects on a spent fuel repository. POSIVA OY.
Vikman, M., Marjamaa, K., Nykyri, M., Small, J.S., Miettinen, H., Heikinheimo, L., Haavisto, T., and Itävaara, M. 2019. The biogeochemistry of gas generation from low-level nuclear waste: Microbiological characterization during 18 years study under in situ conditions. Applied Geochemistry, 105: 55–67. doi:10.1016/j.apgeochem.2019.04.002.
Villar, M.V., Gutiérrez-Álvarez, C., and Campos, G. 2023. Bentonite swelling into a void under suction or water flow. Acta Geotechnica, 18(3): 1495–1513. doi:10.1007/s11440-022-01702-6.
Villar, M.V., Martín, P.L., Bárcena, I., García-Siñeriz, J.L., Gómez-Espina, R., and Lloret, A. 2012. Long-term experimental evidences of saturation of compacted

bentonite under repository conditions. Engineering geology, 149–150: 57–69. doi:10.1016/j.enggeo.2012.08.004.
Walke, R.C., Kirchner, G., Xu, S., and Dverstorp, B. 2015. Post-closure biosphere assessment modelling: comparison of complex and more stylised approaches. Journal of Environmental Radioactivity, 148: 50–58. doi:10.1016/j.jenvrad.2015.06.006.
Walsh, R., Nasir, O., Leung, H., and Avis, J. 2015. Numerical characterization of the excavation damaged zone in the HG-A experiment. : 702–709.
Wersin, P. 2003. Geochemical modelling of bentonite porewater in high-level waste repositories. Journal of Contaminant Hydrology, 61(1): 405–422. doi:10.1016/S0169-7722(02)00119-5.
Wersin, P., Alt-Epping, P., Pekala, M., Pitkänen, P., and Snellman, M. 2017. Modelling Sulfide Fluxes and Cu Canister Corrosion Rates in the Engineered Barrier System of a Spent Fuel Repository. Procedia Earth and Planetary Science, 17: 722–725. doi:10.1016/j.proeps.2016.12.183.
Wersin, P., Alt-Epping, P., Pitkänen, P., Román-Ross, G., Trinchero, P., Molinero, J., Smith, P., Snellman, M., Filby, A., and Kiczka, M. 2014. Sulphide Fluxes and Concentrations in the Spent Nuclear Fuel Repository at Olkiluoto. Posiva Oy Report POSIVA 2014-01. Eurajoki, Finland.
Wersin, P., Johnson, L.H., Schwyn, B., Berner, U., and Curti, E. 2003. Redox conditions in the near field of a repository for SF/HLW and ILW in Opalinus Clay. Switzerland.
Wieland, E. 2001. Experimental studies on the inventory of cement-derived colloids in the pore water of a cementitious backfill material.
Wiest, R.J.M.D. 1966. On the storage coefficient and the equations of groundwater flow. Journal of Geophysical Research (1896-1977), 71(4): 1117–1122. doi:10.1029/JZ071i004p01117.
Williams, M. 2021. Self-sealing processes in Opalinus Clay shale identified within excavation damaged zones at the Mont Terri Underground Rock Laboratory (Switzerland). Doctoral Thesis, ETH Zurich.
WIPP. 2019. Current status of Waste Isolation Pilot Plant (WIPP). Available from https://www.wipp.energy.gov/. [accessed 7 April 2019].
WNA. 2024. International Nuclear Waste Disposal Concepts. Available from https://world-nuclear.org/information-library/nuclear-fuel-cycle/nuclear-waste/international-nuclear-waste-disposal-concepts.
Wu, M., Behazin, M., Nam, J., and Keech, P. 2019. Internal Corrosion of Used Fuel Container. Nuclear Waste Management Organization,NWMO-TR-2019-02.
Xiang, G., Ye, W., Xu, Y., and Jalal, F.E. 2020. Swelling deformation of Na-bentonite in solutions containing different cations. Engineering Geology, 277: 105757. doi:10.1016/j.enggeo.2020.105757.
Xu, L., Ye, W., Wang, Q., and Luo, H. 2023. Experimental Study on the Intrusion/Erosion Behavior of GMZ Bentonite Considering Fracture Aperture Effects. *In* Proceedings of the 23rd Pacific Basin Nuclear Conference, Volume 1. *Edited by* C. Liu. Springer Nature, Singapore. pp. 872–886.

Xu, T., Sonnenthal, E., Spycher, N., and Pruess, K. 2005. TOURGHREACT: A Simulation Program for Non-isothermal MultiphaseReactive Geochemical Transport in Variably Saturated GeologicMedia. Computer & Geosciences, 32(2).

Yoon, S., Lee, G.-J., Park, T.-J., Lee, C., and Cho, D.-K. 2022. Thermal conductivity evaluation for bentonite buffer materials under elevated temperature conditions. Case Studies in Thermal Engineering, 30: 101792. doi:10.1016/j.csite.2022.101792.

Yu, Y.-C., Lee, I.-H., Ni, C.-F., Shen, Y.-H., Tong, C.-Z., Wu, Y.-C., and Lo, E. 2021. Numerical Assessment of the Hybrid Approach for Simulating Three-Dimensional Flow and Advective Transport in Fractured Rocks. Applied Sciences, 11(22): 10792. Multidisciplinary Digital Publishing Institute. doi:10.3390/app112210792.

Zheng, L., and Fernández, A.M. 2023. Prediction of Long-Term Geochemical Change in Bentonite Based on the Interpretative THMC Model of the FEBEX In Situ Test. Minerals, 13(12): 1522. Multidisciplinary Digital Publishing Institute. doi:10.3390/min13121522.

Zheng, L., and Samper, J. 2008. A coupled THMC model of FEBEX *mock-up* test. Physics and Chemistry of the Earth, Parts A/B/C, 33: S486–S498. doi:10.1016/j.pce.2008.10.023.

Appendix A: Supplementary Materials for "Assessment of Hydrogen Gas Formation Using Numerical Modelling Under Deep Geological Repository Environments"

A.S.1 Boundary and Initial Conditions of the THC Model

Boundary and initial conditions and mesh of the THC model are shown in Figure A.S.1. The engineered barrier system (EBS) was placed at 500 m below the ground surface and the total domain depth was 10 000 m. The hydraulic, thermal, and chemical transport processes were simulated using Richards' equation, heat transfer equation, and Fick's 2nd law, respectively. A hydrostatic equilibrium was established setting pressure head at top, sides, and bottom boundaries (Avis et al. 2012). The crystalline host rock was assumed to be fully saturated while 67% initial saturation was implemented for bentonite (HCB) and gap fill (GF) (6th case study). An isothermal condition was established at the top and bottom boundaries using geothermal gradient (Guo 2016, 2018). A boundary heat source was implemented to model UFC heating and an adiabatic symmetry condition was implemented on the outside vertical boundary to model infinite number of UFCs. A constant 1 ppm bisulfide (HS^-) concentration was implemented at the host rock-GF(bentonite) interface while a constant 0 ppm HS^- concentration was applied at the UFC, which assumed that corrosion occurs instantaneously at the UFC (Briggs and Krol 2018). The model used an extremely fine mesh at the UFC end cap due to complex geometry. A finer mesh was applied around the UFC (i.e., the region of interest)

and a progressively larger mesh was applied towards the host rock to reduce computation cost. The results of the 2-D THC model are discussed in Asad et al. (2022).

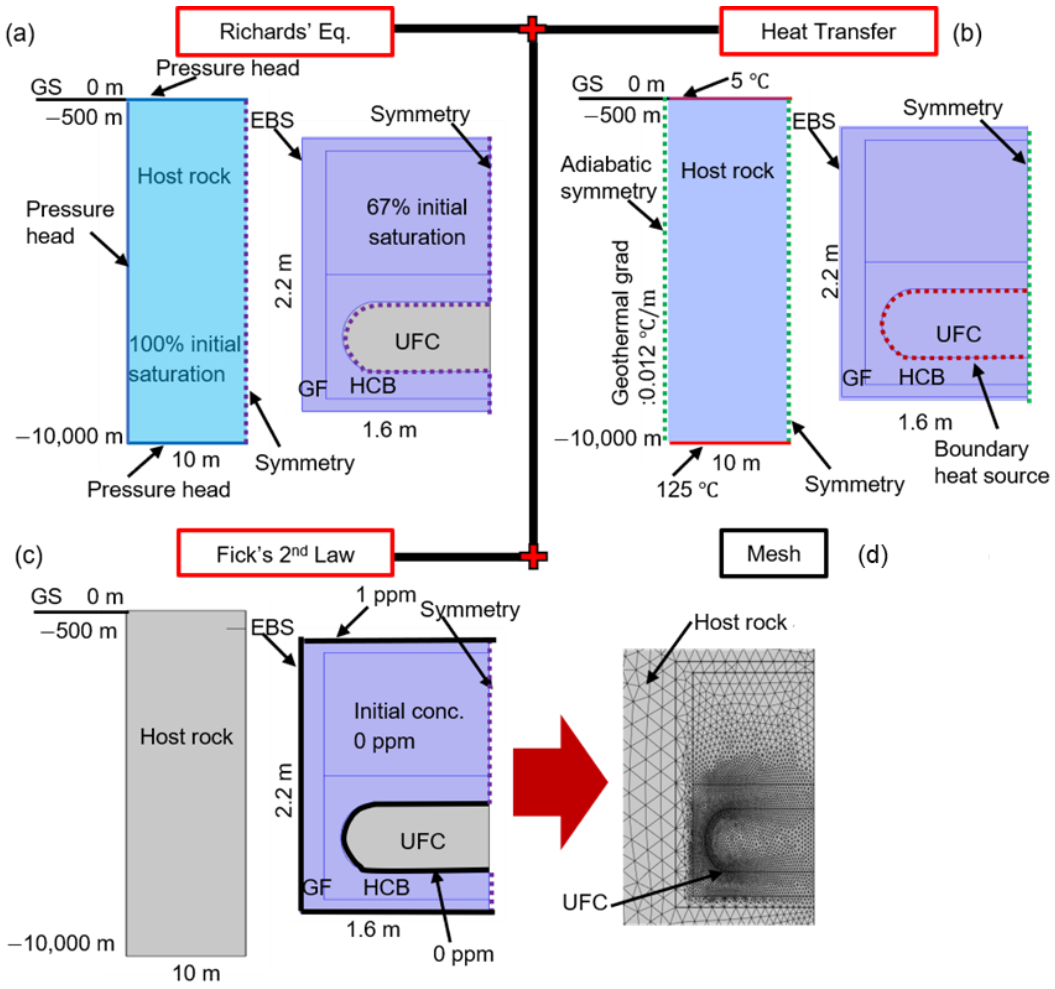

Figure A.S.1: Boundary and initial conditions of the THC model for: (a) hydraulic, (b) thermal, and (c) chemical transport processes and (d) triangular mesh. Adapted from (Asad et al. 2022).

A.S.2 THC-H_2 Model Implementation

The 2-D THC-H_2 model described copper corrosion and H_2 production using Eq. A.S.1 at the UFC surface.

$$2Cu_{(s)}+HS^-_{(aq)}+H^+ \leftrightarrow Cu_2S_{(s)}+H_{2(g)} \quad \text{(A.S.1)}$$

The species included immobile copper (Cu), HS^- (assumed pH: 8-11), hydrogen ion (H^+), immobile copper sulfide (Cu_2S), and H_2. The Eq. A.S.1 reaction was described as a surface equilibrium reaction (SER) which is:

$$E = \frac{[H_2][Cu_2S]}{[Cu]^2\,[HS^-]\,[H^+]} \quad \text{(A.S.2)}$$

where E is the equilibrium constant. The SER approach was chosen since it was assumed the reactions were very fast relative to transport and so the reaction kinetics were not considered. Altogether, the SER approach solved for the flux of the products and reactants using Eq. A.S.2 and fulfilled the equilibrium condition at all times and space coordinates (COMSOL 2019). The initial background concentration of reactant H^+ was assumed to be 0.02 mol m^{-3} (i.e., 0.02 ppm H^+) (Szakálos and Seetharaman 2012) and the initial concentrations of reactants HS^- and Cu were set to 6×10^{-4} mol m^{-3} (i.e., 0.02 ppm HS^-) and 0 mol m^{-3}, respectively. The UFC surface was modelled with a constant Cu concentration boundary condition of 0.02 mol m^{-3} (i.e., 1 ppm Cu). To represent the solid state of Cu and Cu_2S, they were modelled as immobile aqueous species by using zero and very

low (1×10^{-15} m^2 s^{-1}) diffusivities, respectively. Using Cu and Cu_2S immobility, H_2 production was implemented as a function of aqueous species only:

$$E = \frac{[H_2]}{[HS^-]\,[H^+]} \qquad \text{(A.S.3)}$$

In other words, the model correctly implemented Eq. A.S.1 as solid species does not affect equilibrium.

A.S.3 Species Conversion Rate Comparison

To ensure that the SER and boundary conditions were implemented correctly, species conversion rates were computed for varying equilibrium constants and compared to the HS^- consumption rates from the THC model (Asad et al. 2022). The positive and negative species conversion rates indicate species production and consumption, respectively (Figure A.S.2). The H_2 production and HS^- consumption rates were initially the same across all equilibrium constants (10^0-10^{80}) due to HS^- to H_2 conversion, which simulated a constant zero HS^- concentration boundary condition at the UFC. However, the high equilibrium constants of $10^{40} - 10^{80}$ maintained the constant zero HS^- concentration boundary condition until 1 million years as all incoming HS^- was converted to H_2 at the UFC. This is because the high equilibrium constants of $10^{40} - 10^{80}$ forced the conversion of HS^- to H_2 at all times and space coordinates (COMSOL 2019). In other words, all HS^- that reached the UFC was consumed (Eq. 8) when high equilibrium constants were used (see Section A.S.4). In contrast, HS^- was fully

consumed after 100 years (i.e., HS^- reached steady state) with a comparatively low equilibrium constant ($E=10^6$), which ceased HS^- to H_2 conversion (Figure A.S.2). Altogether, the use of the high equilibrium constant is a conservative approach used to model the maximum amount of aqueous H_2 that could be produced based on HS^- transport to the UFC (Eq. 8); therefore, the benchmark equilibrium constant was set to 10^{40}.

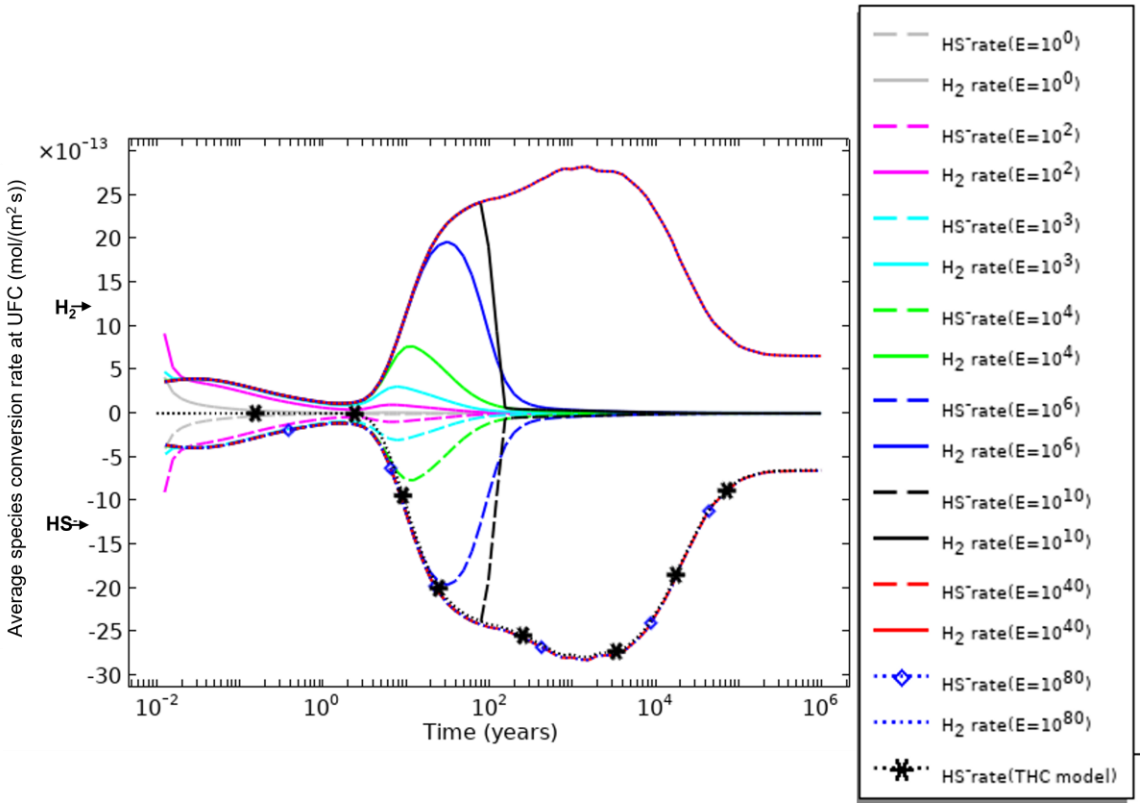

Figure A.S.2: Average species conversion rates at the UFC in the THC-H_2 model with varying equilibrium constants. The positive and negative species conversion rates indicate species production and consumption, respectively. The average HS^- rate from the THC model (Asad et al. 2022) is also shown.

A.S.4 Species Concentration in the THC-H_2 Model

To explore H_2 production and HS^- consumption at the UFC, species concentrations were computed for two equilibrium constants (Figure A.S.3). A constant Cu concentration was implemented at the UFC. The initial background H^+ depleted over time. The HS^- was the only species which always had a flux towards the UFC as constant HS^- concentration was maintained at the rock bentonite interface. As seen in Figure A.S.3, the given equilibrium constant (ratio of products to reactants) was always maintained using varying concentrations of products and reactants. An E= 10^6 was maintained by the ratio of products and reactants, i.e., constant Cu concentration, depleting H^+, and steady HS^- after 100 years (Figure A.S.3a). However, an E= 10^{40} implemented an instantaneous use of HS^- and all H^+ was used up within 100 years. Therefore, the greater E value of 10^{40} was greatly maintained using reactant HS^- at all times and space coordinates (Figure A.S.3b). A greater amount of Cu_2S was produced compared to H_2 as immobile Cu_2S accumulated at the UFC while H_2 diffused out of the bentonite.

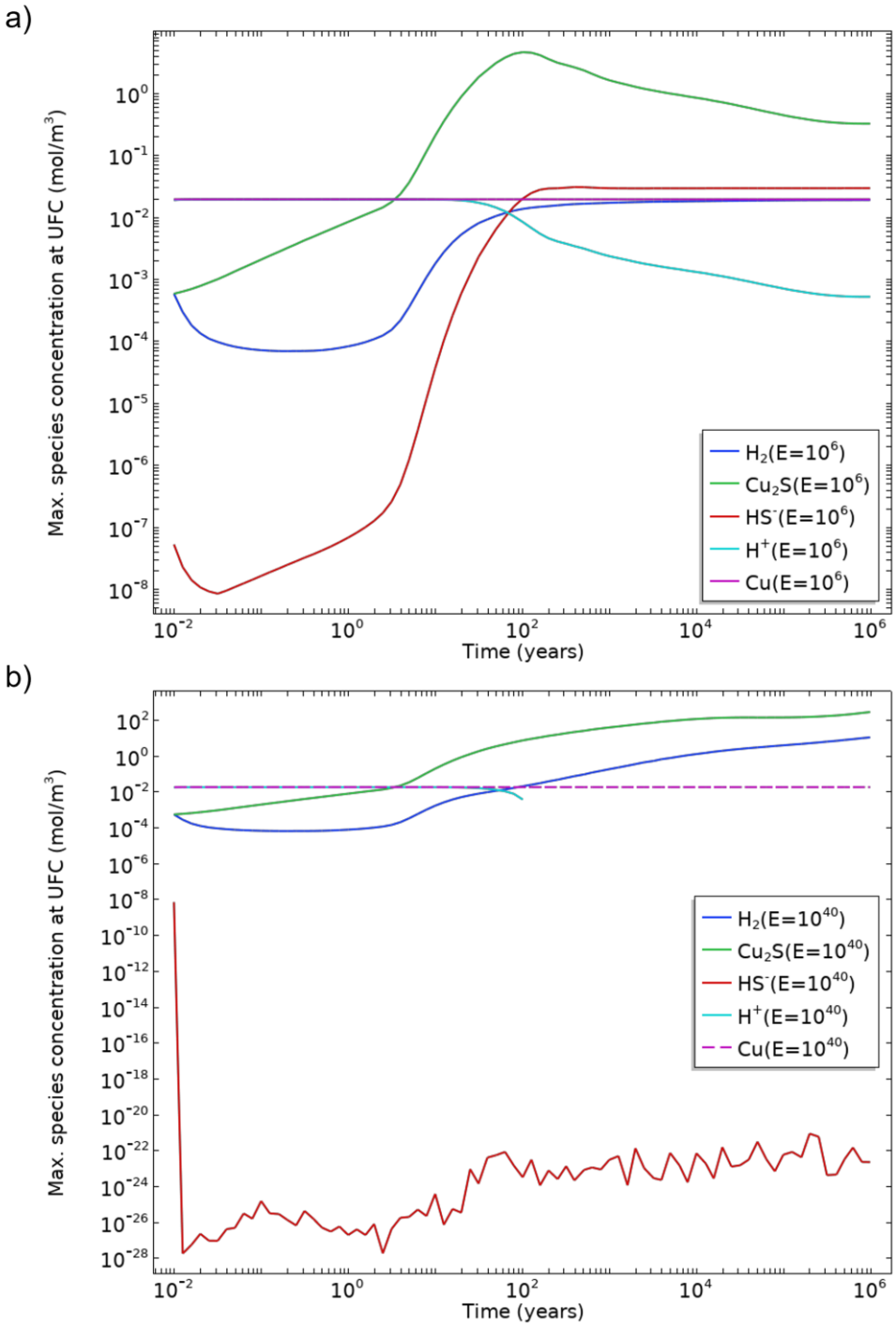

Figure A.S.3: Maximum species concentration over time a) $E=10^6$ and b) $E=10^{40}$. Note that the results are shown for THC-H_2 base case (i.e., C1).

A.S.5 Species Concentration in the THC-H_2 Model

The effect of HS^- initial background concentration on maximum H_2 concentration at the UFC is shown in Figure A.S.4. The maximum H_2 concentration at the UFC is plotted up to 815 years (instead of 1 million years) to explore little change in H_2 concentration due to change in HS^- initial background concentration. This little change in H_2 concentration at the UFC cannot be observed if plotted up to 1 million years due to relatively high H_2 concentration at the UFC after 1 million years (i.e., 12 mol m^{-3} vs. ~0.02 mol m^{-3}).

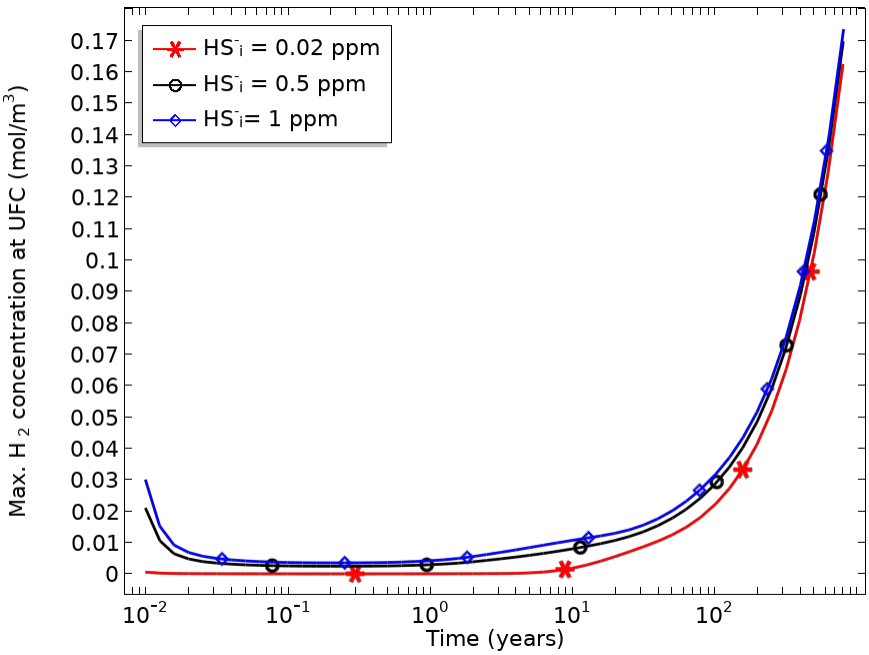

Figure A.S.4: Effect of HS^- initial concentration on a) maximum H_2 concentration at the UFC plotted up to 815 years.

A.S.6 DGR Level H_2 Solubility

The H_2 gas would evolve in the DGR if the H_2 gas pressures exceed the confining pressures at the DGR level (i.e., ~500-800 m below surface). The DGR level H_2 solubility limit was estimated equalling the total gas pressures (partial, P_{H_2} and vapour pressure, P_{vp}) to total confining pressures (atmospheric, P_a ,hydrostatic, P_w ,and capillary pressure, P_C):

$$P_{H_2}+P_{vp}=P_a+P_w+P_C \quad \text{(A.S.4)}$$

The P_{H_2} can be described using Henry's law:

$$C_{H_2}= k_{H_2}P_{H_2} \quad \text{(A.S.5)}$$

$$P_{H_2}=\frac{C_{H_2}}{k_{H_2}}\ \text{atm} \quad \text{(A.S.6)}$$

where C_{H_2} is the H_2 concentration (mol m^{-3}), $k_{H_2}$is the H_2 solubility constant (mol m^{-3} atm^{-1}). The H_2 solubility constant is 0.790 mol m^{-3} atm^{-1} (Kaye and Laby 1986). The P_{vp} can be described using Antoine equation:

$$P_{vp}=(10^{A-\frac{B}{C+T}})\times 0.00131579\ \text{atm} \quad \text{(A.S.7)}$$

where T is the temperature (˚C), and A, B, and C are constants. The values of A, B, and C are 8.07131, 1730.63, and 233.426, respectively (Lide 2004). The P_w can be described as follows:

$$P_w=\rho g h \times 9.87\times 10^{-6}\ \text{atm} \quad \text{(A.S.8)}$$

where ρ is the water density (kg m^{-3}), g is the acceleration due to gravity (m s^{-2}), and h is the DGR depth. The P_C was estimated following (Harrington and Horseman 2003; Lassin et al. 2011) which is 63. 2 atm. Using Eq. A.S.4, the DGR

H_2 solubility limit, C_{H_2}(at 20 ˚C) is 88.9 mol m^{-3} and 111.9 mol m^{-3} at 500 m and 800 m below surface, respectively. The DGR H_2 solubility limit varies slightly with DGR temperature (Figure A.S.5).

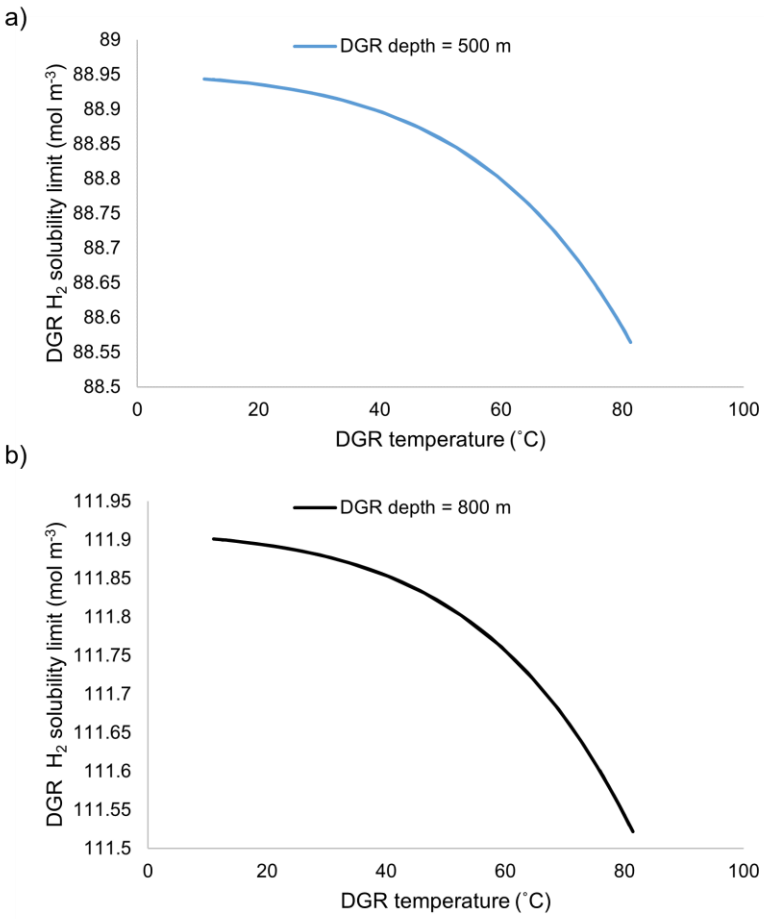

Figure A.S.5: Variation of DGR H_2 solubility limit with temperature at a DGR depth of a) 500 m and b) 800 m. Note that the DGR temperature was taken from THC-H_2 model of (Asad et al. 2022)

A.S.7 Diffusion Time Scale Analysis

The transport of aqueous species through soil is described by Fick's 2nd law (Fick 1855):

$$\phi \frac{\partial c}{\partial t} = D_e \frac{\partial^2 c}{\partial x^2} \qquad \text{(A.S.9)}$$

The variables include aqueous species concentration (c), time (t), and distance (x). The constants are porosity (ϕ) and effective diffusion coefficient (D_e) as the species transport is assumed under fully saturated and isothermal conditions. Therefore, Eq. S.9 represents a simplified transport model (i.e., C model, a transport only model). The maximum concentration is C after time t_L (i.e., diffusion time) over a test section of length L. To find out the scale of diffusion, relative variables (i.e., dimensionless variables) are used in Eq. S.9 following (Nield and Bejan 2013; Aït-Mokhtar et al. 2007) which are:

$$c_R = \frac{c}{C} \; ; \; t_R = \frac{t}{t_L} \; ; \; x_R = \frac{x}{L} \qquad \text{(A.S.10)}$$

and then Eq. S.9 becomes:

$$\frac{\phi C}{t_L} \frac{\partial c_R}{\partial t_R} = \frac{D_e C}{L^2} \frac{\partial^2 c_R}{\partial x_L^2} \qquad \text{(A.S.11)}$$

The dimensionless form of the equation A.S.11 is obtained through dividing both sides by $\frac{D_e C}{L^2}$:

$$\frac{\phi L^2}{D_e t_L} \quad \frac{\partial c_R}{\partial t_R} = \frac{\partial^2 c_R}{\partial x_L^2} \qquad \text{(A.S.12)}$$

For steady diffusion where the dominant force is concentration gradient, the perfector term $\emptyset L^2/D_e t_L \sim 1$ (Nield and Bejan 2013). Therefore, the diffusion time is:

$$t_L \sim \frac{\emptyset L^2}{D_e} \quad \text{(A.S.13)}$$

The D_e is described using aqueous diffusion coefficient (D_0), effective porosity ($\emptyset_e$), and tortuosity (τ) (Shackelford and Moore 2013):

$$D_e = \frac{\emptyset_e}{\tau} D_0 \quad \text{(A.S.14)}$$

Using the relation (Eq. A.S.14) in Eq. A.S.13:

$$t_L \approx \frac{\emptyset L^2}{\frac{\emptyset_e}{\tau} D_0} \quad \text{(A.S.15)}$$

In Eq. A.S.15, $\frac{\emptyset}{\frac{\emptyset_e}{\tau}}$ is roughly in the order of 1 (i.e., $\frac{\emptyset}{\frac{\emptyset_e}{\tau}} \sim 1$) which relates diffusion time to diffusion length and aqueous diffusion coefficient only:

$$t_L \approx \frac{L^2}{D_0} \quad \text{(A.S.16)}$$

Therefore, the transport time of aqueous species from one location to another can be approximated using Eq. A.S.16.

A.S.8 Average Species Conversion Rate at Rock-Bentonite Interface

The average species conversion rate at the rock-bentonite interface (RBI) in the hydrogen feedback model is shown in Figure A.S.6. More H_2 (either from the far-

field or produced from UFC corrosion) was consumed in the hydrogen feedback model at the RBI through MIC and to produce HS^- (e.g., 12×10^{-11} mol $m^{-2}s^{-1}$ of H_2 flux was converted to 3×10^{-11} mol $m^{-2}s^{-1}$ of HS^- flux at the RBI as seen through Figure A.S.6).

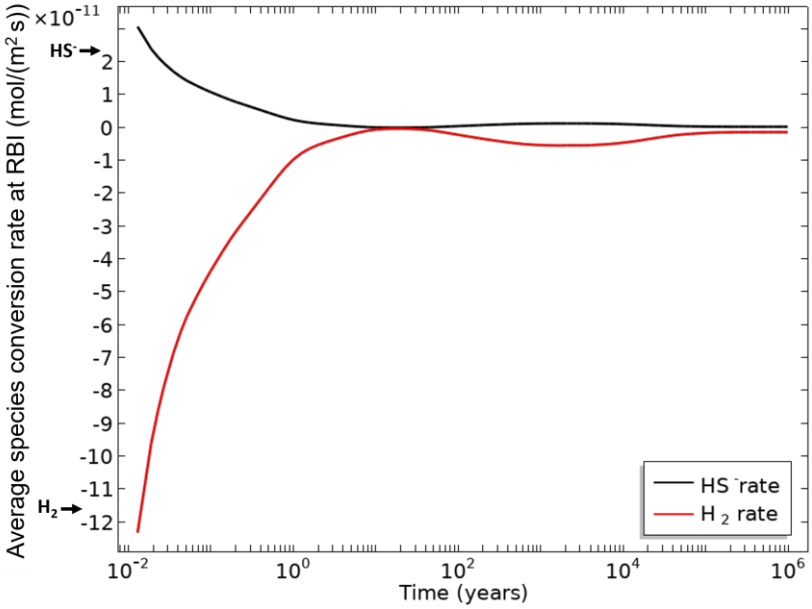

Figure A.S. 6: Average species conversion rate at the RBI in the hydrogen feedback model. The positive and negative species conversion rates indicate species production and consumption, respectively.

A.S.9 References

Aït-Mokhtar, A., O. Millet and O. Amiri. 2007. Electrodiffusion in porous media. Revue Européenne de Génie Civil, 11, 775–785.

Asad, A., T. Rashwan, I. Molnar and M. Krol. 2022. Modelling Bisulfide Transport through the Engineered Barrier System under Repository Conditions: Coupling Unsaturated Flow and Refining Boundary Conditions. Nuclear Waste Management Organization Report NWMO-TR-2022-06. Toronto, Canada.

Avis, J., R. Walsh and N. Calder. 2012. Corrosion-Generated Hydrogen Gas from Steel Used Fuel Containers and the Postclosure Pressure within a

Deep Geological Repository. Nuclear Waste Management Organization Report APM-03640-T10. Toronto, Canada.
Briggs, S. and M. Krol. 2018. Diffusive Transport Modelling of Corrosion Agents through the Engineered Barrier System in a Deep Geological Repository for Used Nuclear Fuel. Nuclear Waste Management Organization Report NWMO TR-2018-06. Toronto, Canada.
Fick, A. 1855. Ueber diffusion. Annalen der physik, 170, 59–86.
Guo, R. 2016. Thermal Response of a Mark II Conceptual Deep Geological Repository in Crystalline Rock. Nuclear Waste Management Organization Report NWMO-TR-2016-03. Toronto, Canada.
Guo, R. 2018. Thermal Response of a Mark II Conceptual Deep Geological Repository in Sedimentary Rock. Nuclear Waste Management Organization Report NWMO-TR-2018-09. Toronto, Canada.
Harrington, J.F. and S.T. Horseman. 2003. Gas migration in KBS-3 buffer bentonite. Sensitivity of test parameters to expereimental boudary conditions. Swedish Nuclear Fuel and Waste Management Co Report SKB-TR-03-03. Stockholm, Sweden.
Kaye, G.W.C. and T.H. Laby. 1986. Tables of physical and chemical constants. 15th Edition.
Lassin, A., M. Dymitrowska and M. Azaroual. 2011. Hydrogen solubility in pore water of partially saturated argillites: Application to Callovo-Oxfordian clayrock in the context of a nuclear waste geological disposal. Physics and Chemistry of the Earth, Parts A/B/C, 36, 1721–1728.
Lide, D.R. 2004. CRC Handbook of Chemistry and Physics, 85th Edition. p. 2904, CRC Press.
Nield, D.A. and A. BejanD. A. Nield and A. Bejan, Editors. 2013. Convection in Porous Media. Convection in Porous Media D. A. Nield and A. Bejan, Editors, p. 1–35, Springer International Publishing Cham. doi:10.1007/978-3-319-49562-0_1.
Shackelford, C. and S. Moore. 2013. Fickian diffusion of radionuclides for engineered containment barriers: Diffusion coefficients, porosities, And complicating issues. Engineering geology, 152, 133–147.

Appendix B: Supplementary Materials for "Modelling Key Reactive Processes Relevant to Bisulfide Transport Through the Highly Compacted Bentonite"

B.S.1 Proposed Design of Canadian DGR

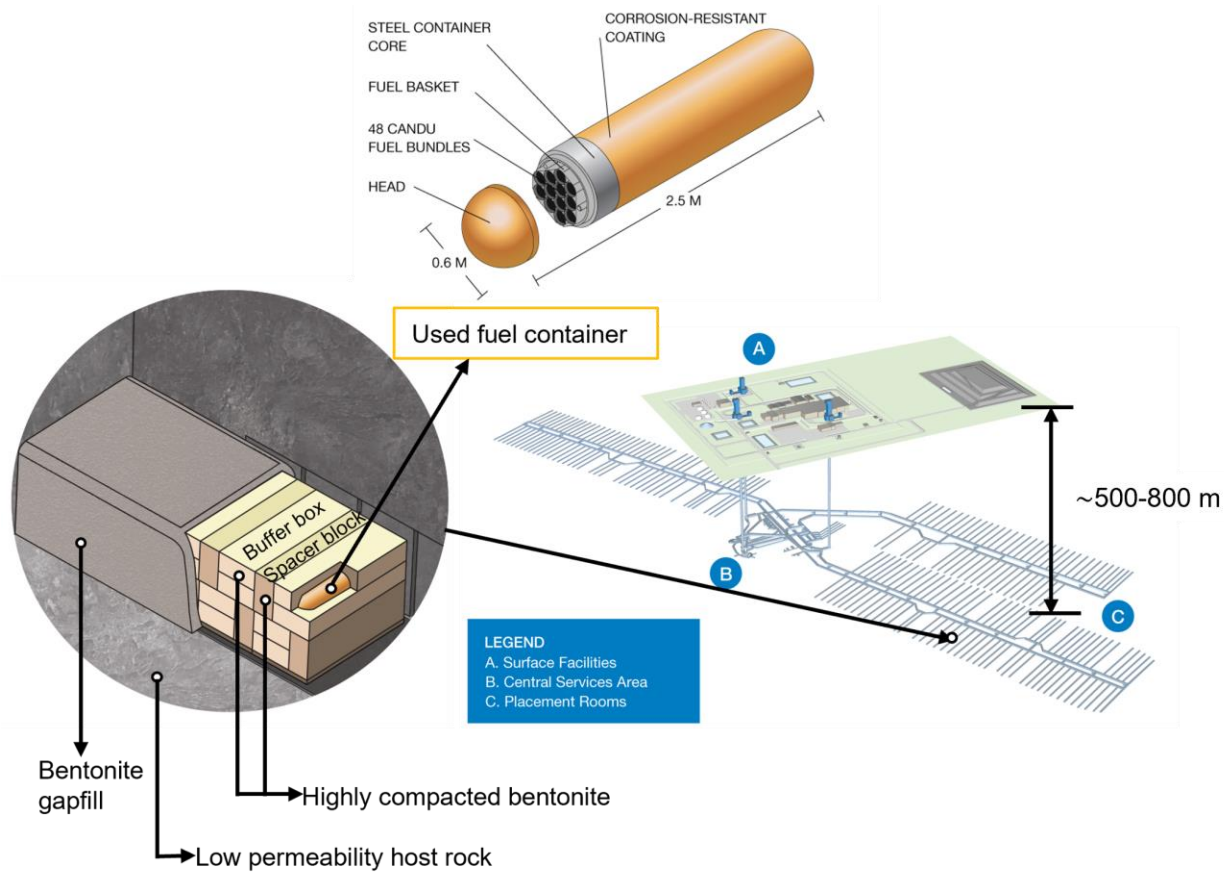

Figure B.S.1: Proposed multiple barrier system in Canadian DGR (adapted from Hall et al. (2021))

B.S.2 Diffusivity and Accessible Porosity in the Cl^- Diffusion Model

In the Cl^- diffusion model, the Cl^- effective diffusivity was implemented as a function of Cl^- diffusion accessible porosity (i.e., $D_{eCl^-}=f(\epsilon_{Cl^-})$). The Cl^- effective diffusivity and Cl^- diffusion accessible porosity at different locations in the bentonite are shown in Figures B.S.2a and B.S.2b, respectively. The Cl^- diffusion model parameters are shown in Table B.S.1.

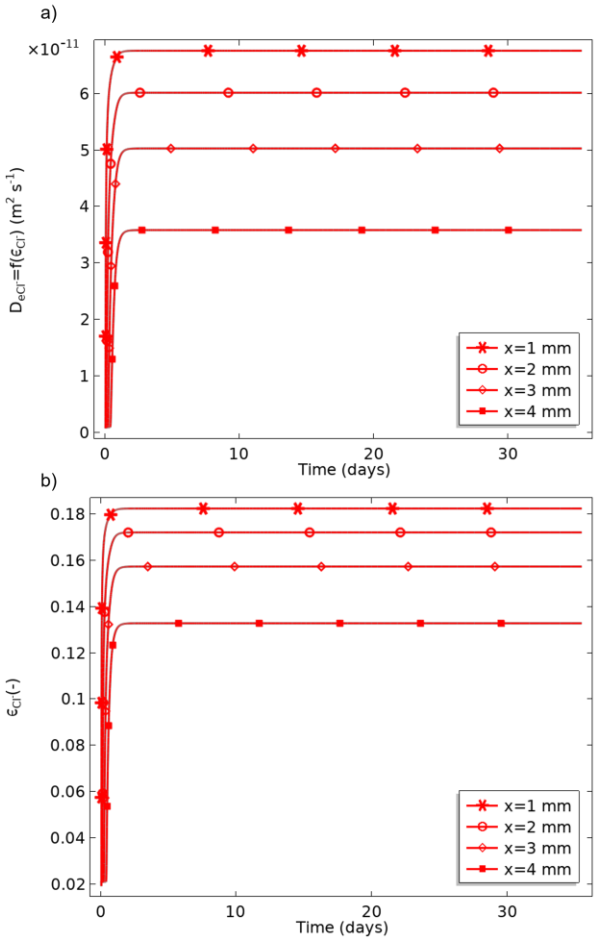

Figure B.S.2: a) Time and space dependent D_{eCl^-} in the Cl^- diffusion model and b) Time and space dependent ϵ_{Cl^-} in the Cl^- diffusion model. Note that x represented the measured points in bentonite.

Table B.S.1: Cl^- Diffusion Model Parameters

Parameter		**Value**
Length of bentonite[1](L)		5 mm
Bentonite density[1](ρ)		1500 kg m^{-3}
Porosity[1] (∅)		0.4 (-)
Initial Cl^- concentration[1] ($[Cl^-_{(aq)i}]$)		0 mol m^{-3}
Cl^- constant concentration at inlet[1]($[Cl^-_{(aq)}]$)		1000 mol m^{-3}
Cl^- constant concentration at outlet[1] ($[Cl^-_{(aq)}]$)		0 mol m^{-3}
Interparticle pore space ($\epsilon^{max}_{Cl^-}$)[2]		0.230 (-)
Density dependent constant[2]	A	0.209 (-)
	B	1.66(-)
Archie's law exponent[4]		2 (-)
Cl^- diffusion coefficient in water(D_{wCl^-})[3]		1× 10^{-9} m^2 s^{-1}

[1]Chowdhury et al. (2021) [2]Van Loon et al. 2007) [3]SKB 2010)

B.S.3 HS^- Adsorption Confirmation

To ensure that the HS^- adsorption was implemented correctly, cumulative HS^- mass at the outlet from the C, C-S_L, and C-S_{NL} models was compared. The onset of HS^- diffusion was delayed in the C-S_L, and C-S_{NL} models compared to the C model (Figure B.S.3). In other words, HS^- was adsorbed onto bentonite; the HS^- flux ceased in the C-S_L, and C-S_{NL} models as expected, verifying that transport and adsorption had been properly coupled.

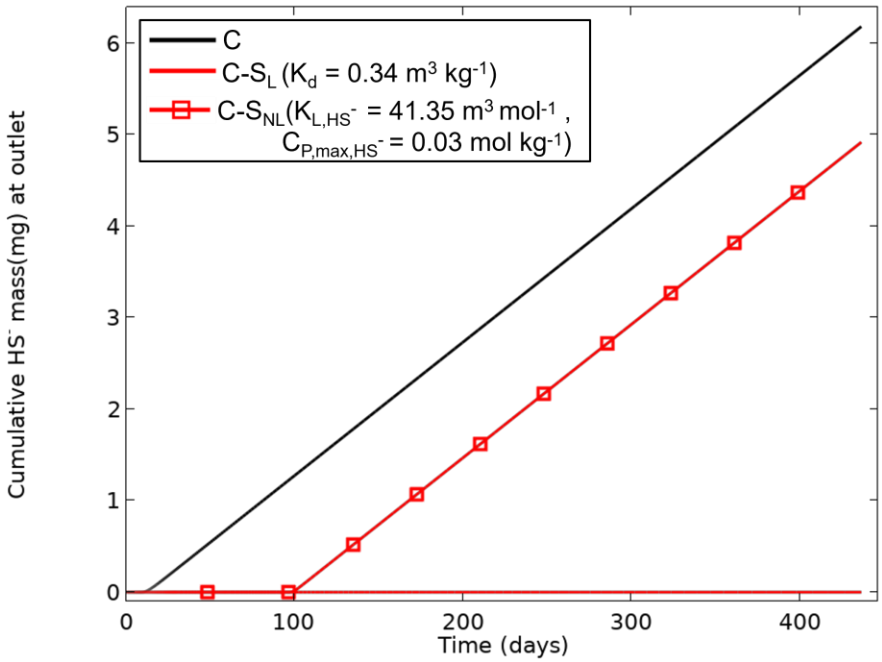

Figure B.S.3: Comparison of cumulative HS^- mass from the C, C-S_L, and C-S_{NL} models.

B.S.4 Fitting HS^- Adsorption Parameters through Varying Data

To ensure a best fit between experimental and modelled HS^- mass profiles, adsorption parameters K_d and K_{L,HS^-} and C_{P,max,HS^-} were varied in the C-S_L and C-S_{NL} models, respectively (Figure B.S.4). A best fit between experimental and modelled HS^- mass profiles was obtained using K_d = 0.005 $m^3\ kg^{-1}$, and K_{L,HS^-} =1 $m^3\ mol^{-1}$ and C_{P,max,HS^-} =0.08 mol kg^{-1} in the C-S_L and C-S_{NL} models, respectively (R^2=0.95 and R^2=0.96, respectively). As seen in Figure B.S.4b, the HS^- mass profiles were very sensitive to C_{P,max,HS^-} values. For example, HS^- breakthrough was differed by ≈120 days due to change in C_{P,max,HS^-} from 0.03 mol kg^{-1} to 0.08 mol kg^{-1} (keeping K_{L,HS^-} at 1 $m^3\ mol^{-1}$). In contrast, the cumulative HS mass profiles

were nearly identical due to a change in K_{L,HS^-} from 41.35 $m^3\,mol^{-1}$ to 1 $m^3\,mol^{-1}$ (keeping C_{P,max,HS^-} at 0.03 mol kg^{-1}).

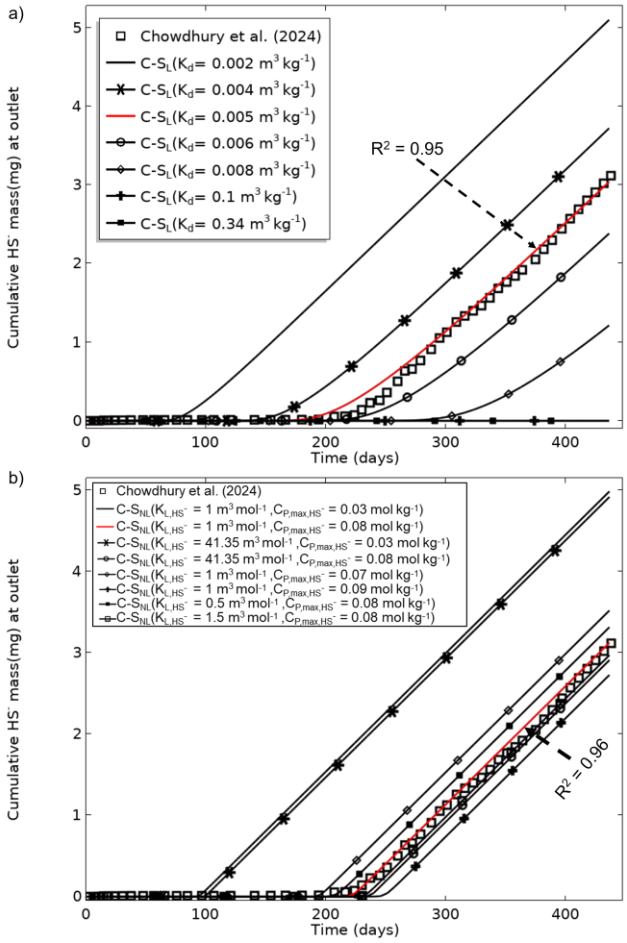

Figure B.S.4: a) Cumulative HS^- mass at the compacted bentonite outlet in the C-S_L model from varying K_d. and b) Cumulative HS^- mass at the compacted bentonite outlet in the C-S_{NL} model from varying K_{L,HS^-} and C_{P,max,HS^-}. The models were compared to the cumulative HS^- mass breakthrough curve from Chowdhury et al. (2024). Note that K_d= 0.34 m^3kg^{-1}, K_{L,HS^-}= 41.35 $m^3\,mol^{-1}$ and C_{P,max,HS^-} =0.03 mol kg^{-1} values were obtained from batch experiment of granular bentonite (Papry et al. 2023).

B.S.5 Kinetically Irreversible HS^- Reaction (C-R_I) Model Confirmation

To ensure that the HS^- reaction was implemented correctly, species concentrations and reaction rate after 5 days were compared to 250 days. The model was run for a period of 438 days (i.e., experimental duration). The FeS was produced as the HS^- reacted with the Fe^{2+}(Figures B.S.5a and B.S.5b). Although the HS^- maintained a constant concentration boundary, reaction rate decreased (Figures B.S.5c and B.S.5d) as the initial Fe^{2+} decreased over time. However, the amount of FeS increased after 250 days (Figure B.S.5 b) because of the continuous reaction between HS^- and initial Fe^{2+} before 250 days.

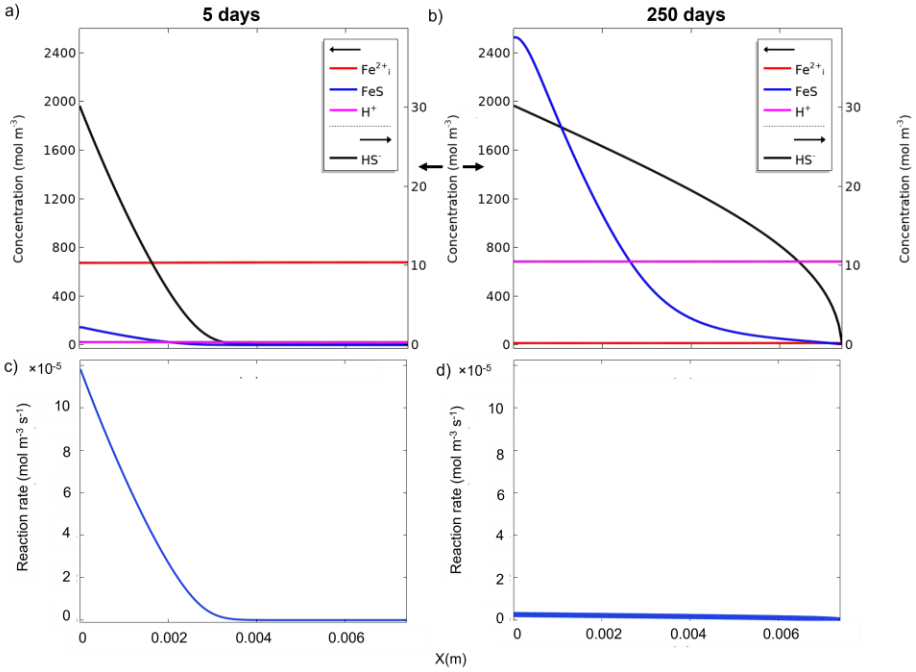

Figure B.S.5: The modelled evolutions of: (a, b) species concentrations, (c, d) reaction rate in the C-R_I model. Note that X represented the bentonite length and initial Fe^{2+} was kept at 700 mol m^{-3}

B.S.6 Sensitivity of Reaction Rate to Arrhenius Frequency Factor

A sensitivity study for the C-R_I model was undertaken to see how the Arrhenius reaction frequency factor, A_h impacts the reaction rate (Figure B.S.6). The Arrhenius activation energy, E_h was kept at 35 kJ mol^{-1} (Rickard 1997; Cloet et al. 2017) as the decrease in rate constant due to a change in E_h from 5 to 100 kJ mol^{-1} is only ≈3.5 % (under constant A_h), while increase in rate constant due to a change in A_h from 0.01 m^3 mol^{-1} s^{-1} to 0.1 m^3 mol^{-1} s^{-1} is 900% (under constant E_h).

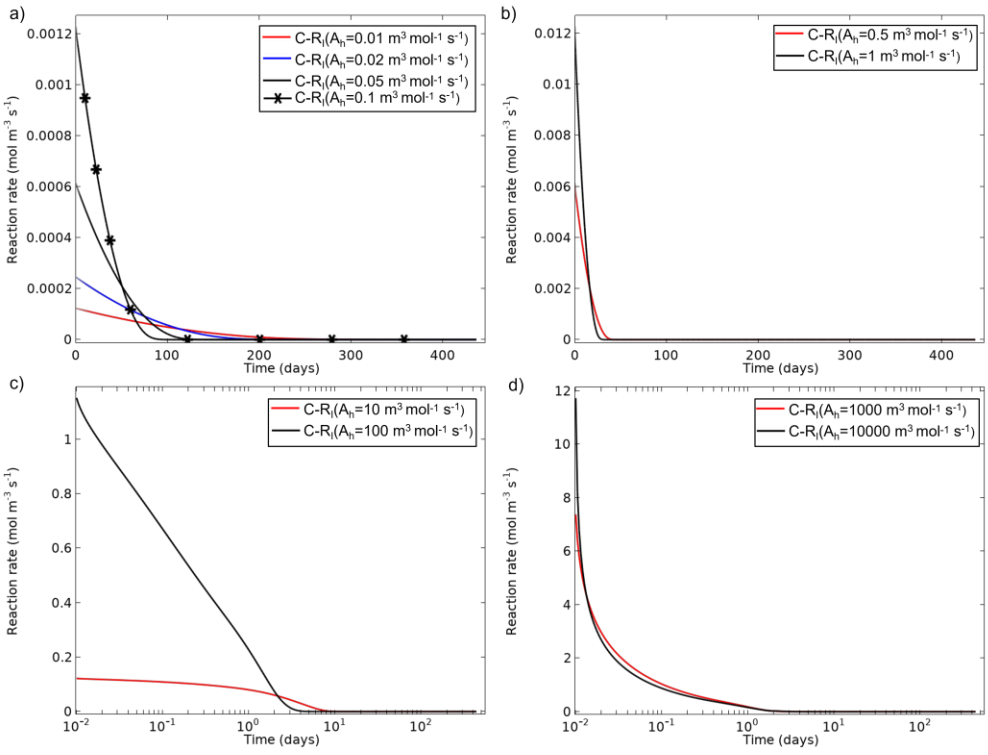

Figure B.S.6: Reaction rates in the C-R_I model from varying the A_h from a) 0.01-0.1 mol m^{-3} s^{-1}, b) 0.5-1 mol m^{-3} s^{-1}, c) 10-100 mol m^{-3} s^{-1}, and d)1000-10000 mol m^{-3} s^{-1}. Note that the horizontal axis is shown in log scale in Figures B.S.6c and B.S.6d to explore rates around 0-10 days.

As seen in Figure B.S.6, low reaction rates are produced due to low A_h values (e.g., 0.01-1 m^3 mol^{-1} s^{-1}) which vary up to 150 days (Figure B.S.6a), while the reaction rates become higher and vary only initially when higher A_h values are used (Figures B.S.6b-B.S.6d). In other words, reaction rate increases instantaneously due to higher A_h value.

B.S.7 References

Chowdhury, F., T.L. Rashwan and M.M. Krol. 2024. Bisulfide diffusion through highly compacted bentonite [unpublished data].

Chowdhury, F. et al.S. Walbridge et al., Editors. 2021. Measuring Key Parameters Governing Anion Transport Through Mx-80 Bentonite. Proceedings of the Canadian Society of Civil Engineering Annual Conference 2021 Lecture Notes in Civil Engineering. S. Walbridge et al., Editors, p. 547–558, Springer Nature Singapore. doi:10.1007/978-981-19-0503-2_44.

Hall, D.S., M. Behazin, W. Jeffrey Binns and P.G. Keech. 2021. An evaluation of corrosion processes affecting copper-coated nuclear waste containers in a deep geological repository. Progress in materials science, 118, 1–28.

Papry, S.A., T.L. Rashwan, P.K. Mondal, M. Behazin, P.G. Keech and M.M. Krol. 2023. Investigating bisulfide sorption onto bentonite through laboratory batch experiments. Applied Geochemistry, 152, 105626.

SKB. 2010. Design and production of the KBS-3 repository. Swedish Nuclear Fuel and Waste Management Company (SKB). 56.

Van Loon, L.R., M.A. Glaus and W. Müller. 2007. Anion exclusion effects in compacted bentonites: Towards a better understanding of anion diffusion. Applied Geochemistry, 22, 2536–2552.

Appendix C: Reproduction Licenses

RightsLink

An evaluation of corrosion processes affecting copper-coated nuclear waste containers in a deep geological repository

Author: David S. Hall,Mehran Behazin,W. Jeffrey Binns,Peter G. Keech

Publication: Progress in Materials Science

Publisher: Elsevier

Date: May 2021

Creative Commons

This is an open access article distributed under the terms of the Creative Commons CC-BY license, which permits unrestricted use, distribution, and reproduction in any medium, provided the original work is properly cited.

You are not required to obtain permission to reuse this article.

To request permission for a type of use not listed, please contact Elsevier Global Rights Department.

Are you the author of this Elsevier journal article?

Chemical Evolution of Bentonite Buffer in a Final Repository of Spent Nuclear Fuel During the Thermal Phase

Author: Aku Itälä, Markus Olin
Publication: Nuclear Technology
Publisher: Taylor & Francis
Date: Apr 10, 2017

ELSEVIER LICENSE
TERMS AND CONDITIONS

May 12, 2024

This Agreement between Mr. MD ABDULLAH ASAD ("You") and Elsevier ("Elsevier") consists of your license details and the terms and conditions provided by Elsevier and Copyright Clearance Center.

License Number	5786641454887
License date	May 12, 2024
Licensed Content Publisher	Elsevier
Licensed Content Publication	Journal of Nuclear Materials
Licensed Content Title	Reactive-transport model for the prediction of the uniform corrosion behaviour of copper used fuel containers
Licensed Content Author	F. King,M. Kolar,P. Maak
Licensed Content Date	Sep 30, 2008
Licensed Content Volume	379

Licensed Content Issue	1-3
Licensed Content Pages	9
Start Page	133
End Page	141
Type of Use	reuse in a thesis/dissertation
Portion	figures/tables/illustrations
Number of figures/tables/illustrations	1
Format	both print and electronic
Are you the author of this Elsevier article?	No
Will you be translating?	No
Title of new work	MODELLING LONG TERM CONDITIONS IN CANADIAN DEEP GEOLOGICAL REPOSITORY
Institution name	York University

Expected presentation date	Aug 2024
Portions	Figure 3
Requestor Location	Mr. MD ABDULLAH ASAD York University TORONTO, ON M3J 1P3 Canada Attn: Mr. MD ABDULLAH ASAD
Publisher Tax ID	GB 494 6272 12
Total	0.00 CAD

Terms and Conditions

INTRODUCTION

1. The publisher for this copyrighted material is Elsevier. By clicking "accept" in connection with completing this licensing transaction, you agree that the following terms and conditions apply to this transaction (along with the Billing and Payment terms and conditions established by Copyright Clearance Center, Inc. ("CCC"), at the time that you opened your RightsLink account and that are available at any time at https://myaccount.copyright.com).

GENERAL TERMS

2. Elsevier hereby grants you permission to reproduce the aforementioned material subject to the terms and conditions indicated.

3. Acknowledgement: If any part of the material to be used (for example, figures) has appeared in our publication with credit or acknowledgement to another source, permission

must also be sought from that source. If such permission is not obtained then that material may not be included in your publication/copies. Suitable acknowledgement to the source must be made, either as a footnote or in a reference list at the end of your publication, as follows:

"Reprinted from Publication title, Vol /edition number, Author(s), Title of article / title of chapter, Pages No., Copyright (Year), with permission from Elsevier [OR APPLICABLE SOCIETY COPYRIGHT OWNER]." Also Lancet special credit - "Reprinted from The Lancet, Vol. number, Author(s), Title of article, Pages No., Copyright (Year), with permission from Elsevier."

4. Reproduction of this material is confined to the purpose and/or media for which permission is hereby given. The material may not be reproduced or used in any other way, including use in combination with an artificial intelligence tool (including to train an algorithm, test, process, analyse, generate output and/or develop any form of artificial intelligence tool), or to create any derivative work and/or service (including resulting from the use of artificial intelligence tools).

5. Altering/Modifying Material: Not Permitted. However figures and illustrations may be altered/adapted minimally to serve your work. Any other abbreviations, additions, deletions and/or any other alterations shall be made only with prior written authorization of Elsevier Ltd. (Please contact Elsevier's permissions helpdesk here). No modifications can be made to any Lancet figures/tables and they must be reproduced in full.

6. If the permission fee for the requested use of our material is waived in this instance, please be advised that your future requests for Elsevier materials may attract a fee.

7. Reservation of Rights: Publisher reserves all rights not specifically granted in the combination of (i) the license details provided by you and accepted in the course of this licensing transaction, (ii) these terms and conditions and (iii) CCC's Billing and Payment terms and conditions.

8. License Contingent Upon Payment: While you may exercise the rights licensed immediately upon issuance of the license at the end of the licensing process for the transaction, provided that you have disclosed complete and accurate details of your proposed use, no license is finally effective unless and until full payment is received from you (either by publisher or by CCC) as provided in CCC's Billing and Payment terms and conditions. If full payment is not received on a timely basis, then any license preliminarily granted shall be deemed automatically revoked and shall be void as if never granted. Further, in the event that you breach any of these terms and conditions or any of CCC's Billing and Payment terms and conditions, the license is automatically revoked and

shall be void as if never granted. Use of materials as described in a revoked license, as well as any use of the materials beyond the scope of an unrevoked license, may constitute copyright infringement and publisher reserves the right to take any and all action to protect its copyright in the materials.

9. Warranties: Publisher makes no representations or warranties with respect to the licensed material.

10. Indemnity: You hereby indemnify and agree to hold harmless publisher and CCC, and their respective officers, directors, employees and agents, from and against any and all claims arising out of your use of the licensed material other than as specifically authorized pursuant to this license.

11. No Transfer of License: This license is personal to you and may not be sublicensed, assigned, or transferred by you to any other person without publisher's written permission.

12. No Amendment Except in Writing: This license may not be amended except in a writing signed by both parties (or, in the case of publisher, by CCC on publisher's behalf).

13. Objection to Contrary Terms: Publisher hereby objects to any terms contained in any purchase order, acknowledgment, check endorsement or other writing prepared by you, which terms are inconsistent with these terms and conditions or CCC's Billing and Payment terms and conditions. These terms and conditions, together with CCC's Billing and Payment terms and conditions (which are incorporated herein), comprise the entire agreement between you and publisher (and CCC) concerning this licensing transaction. In the event of any conflict between your obligations established by these terms and conditions and those established by CCC's Billing and Payment terms and conditions, these terms and conditions shall control.

14. Revocation: Elsevier or Copyright Clearance Center may deny the permissions described in this License at their sole discretion, for any reason or no reason, with a full refund payable to you. Notice of such denial will be made using the contact information provided by you. Failure to receive such notice will not alter or invalidate the denial. In no event will Elsevier or Copyright Clearance Center be responsible or liable for any costs, expenses or damage incurred by you as a result of a denial of your permission request, other than a refund of the amount(s) paid by you to Elsevier and/or Copyright Clearance Center for denied permissions.

LIMITED LICENSE

The following terms and conditions apply only to specific license types:

15. **Translation**: This permission is granted for non-exclusive world **English** rights only unless your license was granted for translation rights. If you licensed translation rights you may only translate this content into the languages you requested. A professional translator must perform all translations and reproduce the content word for word preserving the integrity of the article.

16. **Posting licensed content on any Website**: The following terms and conditions apply as follows: Licensing material from an Elsevier journal: All content posted to the web site must maintain the copyright information line on the bottom of each image; A hyper-text must be included to the Homepage of the journal from which you are licensing at http://www.sciencedirect.com/science/journal/xxxxx or the Elsevier homepage for books at http://www.elsevier.com; Central Storage: This license does not include permission for a scanned version of the material to be stored in a central repository such as that provided by Heron/XanEdu.

Licensing material from an Elsevier book: A hyper-text link must be included to the Elsevier homepage at http://www.elsevier.com . All content posted to the web site must maintain the copyright information line on the bottom of each image.

Posting licensed content on Electronic reserve: In addition to the above the following clauses are applicable: The web site must be password-protected and made available only to bona fide students registered on a relevant course. This permission is granted for 1 year only. You may obtain a new license for future website posting.

17. **For journal authors:** the following clauses are applicable in addition to the above:

Preprints:

A preprint is an author's own write-up of research results and analysis, it has not been peer-reviewed, nor has it had any other value added to it by a publisher (such as formatting, copyright, technical enhancement etc.).

Authors can share their preprints anywhere at any time. Preprints should not be added to or enhanced in any way in order to appear more like, or to substitute for, the final versions of articles however authors can update their preprints on arXiv or RePEc with their Accepted Author Manuscript (see below).

If accepted for publication, we encourage authors to link from the preprint to their formal publication via its DOI. Millions of researchers have access to the formal publications on ScienceDirect, and so links will help users to find, access, cite and use the best available

version. Please note that Cell Press, The Lancet and some society-owned have different preprint policies. Information on these policies is available on the journal homepage.

Accepted Author Manuscripts: An accepted author manuscript is the manuscript of an article that has been accepted for publication and which typically includes author-incorporated changes suggested during submission, peer review and editor-author communications.

Authors can share their accepted author manuscript:

- immediately
  - via their non-commercial person homepage or blog
  - by updating a preprint in arXiv or RePEc with the accepted manuscript
  - via their research institute or institutional repository for internal institutional uses or as part of an invitation-only research collaboration work-group
  - directly by providing copies to their students or to research collaborators for their personal use
  - for private scholarly sharing as part of an invitation-only work group on commercial sites with which Elsevier has an agreement
- After the embargo period
  - via non-commercial hosting platforms such as their institutional repository
  - via commercial sites with which Elsevier has an agreement

In all cases accepted manuscripts should:

- link to the formal publication via its DOI
- bear a CC-BY-NC-ND license - this is easy to do
- if aggregated with other manuscripts, for example in a repository or other site, be shared in alignment with our hosting policy not be added to or enhanced in any way to appear more like, or to substitute for, the published journal article.

Published journal article (JPA): A published journal article (PJA) is the definitive final record of published research that appears or will appear in the journal and embodies all value-adding publishing activities including peer review co-ordination, copy-editing, formatting, (if relevant) pagination and online enrichment.

Policies for sharing publishing journal articles differ for subscription and gold open access articles:

Subscription Articles: If you are an author, please share a link to your article rather than the full-text. Millions of researchers have access to the formal publications on

ScienceDirect, and so links will help your users to find, access, cite, and use the best available version.

Theses and dissertations which contain embedded PJAs as part of the formal submission can be posted publicly by the awarding institution with DOI links back to the formal publications on ScienceDirect.

If you are affiliated with a library that subscribes to ScienceDirect you have additional private sharing rights for others' research accessed under that agreement. This includes use for classroom teaching and internal training at the institution (including use in course packs and courseware programs), and inclusion of the article for grant funding purposes.

Gold Open Access Articles: May be shared according to the author-selected end-user license and should contain a CrossMark logo, the end user license, and a DOI link to the formal publication on ScienceDirect.

Please refer to Elsevier's posting policy for further information.

18. **For book authors** the following clauses are applicable in addition to the above: Authors are permitted to place a brief summary of their work online only. You are not allowed to download and post the published electronic version of your chapter, nor may you scan the printed edition to create an electronic version. **Posting to a repository:** Authors are permitted to post a summary of their chapter only in their institution's repository.

19. **Thesis/Dissertation**: If your license is for use in a thesis/dissertation your thesis may be submitted to your institution in either print or electronic form. Should your thesis be published commercially, please reapply for permission. These requirements include permission for the Library and Archives of Canada to supply single copies, on demand, of the complete thesis and include permission for Proquest/UMI to supply single copies, on demand, of the complete thesis. Should your thesis be published commercially, please reapply for permission. Theses and dissertations which contain embedded PJAs as part of the formal submission can be posted publicly by the awarding institution with DOI links back to the formal publications on ScienceDirect.

Elsevier Open Access Terms and Conditions

You can publish open access with Elsevier in hundreds of open access journals or in nearly 2000 established subscription journals that support open access publishing. Permitted third party re-use of these open access articles is defined by the author's choice

of Creative Commons user license. See our open access license policy for more information.

Terms & Conditions applicable to all Open Access articles published with Elsevier:

Any reuse of the article must not represent the author as endorsing the adaptation of the article nor should the article be modified in such a way as to damage the author's honour or reputation. If any changes have been made, such changes must be clearly indicated.

The author(s) must be appropriately credited and we ask that you include the end user license and a DOI link to the formal publication on ScienceDirect.

If any part of the material to be used (for example, figures) has appeared in our publication with credit or acknowledgement to another source it is the responsibility of the user to ensure their reuse complies with the terms and conditions determined by the rights holder.

Additional Terms & Conditions applicable to each Creative Commons user license:

CC BY: The CC-BY license allows users to copy, to create extracts, abstracts and new works from the Article, to alter and revise the Article and to make commercial use of the Article (including reuse and/or resale of the Article by commercial entities), provided the user gives appropriate credit (with a link to the formal publication through the relevant DOI), provides a link to the license, indicates if changes were made and the licensor is not represented as endorsing the use made of the work. The full details of the license are available at http://creativecommons.org/licenses/by/4.0.

CC BY NC SA: The CC BY-NC-SA license allows users to copy, to create extracts, abstracts and new works from the Article, to alter and revise the Article, provided this is not done for commercial purposes, and that the user gives appropriate credit (with a link to the formal publication through the relevant DOI), provides a link to the license, indicates if changes were made and the licensor is not represented as endorsing the use made of the work. Further, any new works must be made available on the same conditions. The full details of the license are available at http://creativecommons.org/licenses/by-nc-sa/4.0.

CC BY NC ND: The CC BY-NC-ND license allows users to copy and distribute the Article, provided this is not done for commercial purposes and further does not permit distribution of the Article if it is changed or edited in any way, and provided the user gives appropriate credit (with a link to the formal publication through the relevant DOI), provides a link to the license, and that the licensor is not represented as endorsing the use made of the work. The full details of the license are available at

ELSEVIER LICENSE
TERMS AND CONDITIONS

May 12, 2024

This Agreement between Mr. MD ABDULLAH ASAD ("You") and Elsevier ("Elsevier") consists of your license details and the terms and conditions provided by Elsevier and Copyright Clearance Center.

License Number	5786651167839
License date	May 12, 2024
Licensed Content Publisher	Elsevier
Licensed Content Publication	Journal of Contaminant Hydrology
Licensed Content Title	Porewater chemistry in compacted re-saturated MX-80 bentonite
Licensed Content Author	Michael H Bradbury,Bart Baeyens
Licensed Content Date	Mar 1, 2003
Licensed Content Volume	61

Licensed Content Issue	1-4
Licensed Content Pages	10
Start Page	329
End Page	338
Type of Use	reuse in a thesis/dissertation
Portion	figures/tables/illustrations
Number of figures/tables/illustrations	1
Format	both print and electronic
Are you the author of this Elsevier article?	No
Will you be translating?	No
Title of new work	MODELLING LONG TERM CONDITIONS IN CANADIAN DEEP GEOLOGICAL REPOSITORY
Institution name	York University

Expected presentation date	Aug 2024
Portions	Figure 1
Requestor Location	Mr. MD ABDULLAH ASAD 360 ASSINIBOINE RD TORONTO, ON M3J1L3 Canada Attn: Mr. MD ABDULLAH ASAD
Publisher Tax ID	GB 494 6272 12
Total	0.00 CAD

Terms and Conditions

INTRODUCTION

1. The publisher for this copyrighted material is Elsevier. By clicking "accept" in connection with completing this licensing transaction, you agree that the following terms and conditions apply to this transaction (along with the Billing and Payment terms and conditions established by Copyright Clearance Center, Inc. ("CCC"), at the time that you opened your RightsLink account and that are available at any time at https://myaccount.copyright.com).

GENERAL TERMS

2. Elsevier hereby grants you permission to reproduce the aforementioned material subject to the terms and conditions indicated.

3. Acknowledgement: If any part of the material to be used (for example, figures) has appeared in our publication with credit or acknowledgement to another source, permission

must also be sought from that source. If such permission is not obtained then that material may not be included in your publication/copies. Suitable acknowledgement to the source must be made, either as a footnote or in a reference list at the end of your publication, as follows:

"Reprinted from Publication title, Vol /edition number, Author(s), Title of article / title of chapter, Pages No., Copyright (Year), with permission from Elsevier [OR APPLICABLE SOCIETY COPYRIGHT OWNER]." Also Lancet special credit - "Reprinted from The Lancet, Vol. number, Author(s), Title of article, Pages No., Copyright (Year), with permission from Elsevier."

4. Reproduction of this material is confined to the purpose and/or media for which permission is hereby given. The material may not be reproduced or used in any other way, including use in combination with an artificial intelligence tool (including to train an algorithm, test, process, analyse, generate output and/or develop any form of artificial intelligence tool), or to create any derivative work and/or service (including resulting from the use of artificial intelligence tools).

5. Altering/Modifying Material: Not Permitted. However figures and illustrations may be altered/adapted minimally to serve your work. Any other abbreviations, additions, deletions and/or any other alterations shall be made only with prior written authorization of Elsevier Ltd. (Please contact Elsevier's permissions helpdesk here). No modifications can be made to any Lancet figures/tables and they must be reproduced in full.

6. If the permission fee for the requested use of our material is waived in this instance, please be advised that your future requests for Elsevier materials may attract a fee.

7. Reservation of Rights: Publisher reserves all rights not specifically granted in the combination of (i) the license details provided by you and accepted in the course of this licensing transaction, (ii) these terms and conditions and (iii) CCC's Billing and Payment terms and conditions.

8. License Contingent Upon Payment: While you may exercise the rights licensed immediately upon issuance of the license at the end of the licensing process for the transaction, provided that you have disclosed complete and accurate details of your proposed use, no license is finally effective unless and until full payment is received from you (either by publisher or by CCC) as provided in CCC's Billing and Payment terms and conditions. If full payment is not received on a timely basis, then any license preliminarily granted shall be deemed automatically revoked and shall be void as if never granted. Further, in the event that you breach any of these terms and conditions or any of CCC's Billing and Payment terms and conditions, the license is automatically revoked and

shall be void as if never granted. Use of materials as described in a revoked license, as well as any use of the materials beyond the scope of an unrevoked license, may constitute copyright infringement and publisher reserves the right to take any and all action to protect its copyright in the materials.

9. Warranties: Publisher makes no representations or warranties with respect to the licensed material.

10. Indemnity: You hereby indemnify and agree to hold harmless publisher and CCC, and their respective officers, directors, employees and agents, from and against any and all claims arising out of your use of the licensed material other than as specifically authorized pursuant to this license.

11. No Transfer of License: This license is personal to you and may not be sublicensed, assigned, or transferred by you to any other person without publisher's written permission.

12. No Amendment Except in Writing: This license may not be amended except in a writing signed by both parties (or, in the case of publisher, by CCC on publisher's behalf).

13. Objection to Contrary Terms: Publisher hereby objects to any terms contained in any purchase order, acknowledgment, check endorsement or other writing prepared by you, which terms are inconsistent with these terms and conditions or CCC's Billing and Payment terms and conditions. These terms and conditions, together with CCC's Billing and Payment terms and conditions (which are incorporated herein), comprise the entire agreement between you and publisher (and CCC) concerning this licensing transaction. In the event of any conflict between your obligations established by these terms and conditions and those established by CCC's Billing and Payment terms and conditions, these terms and conditions shall control.

14. Revocation: Elsevier or Copyright Clearance Center may deny the permissions described in this License at their sole discretion, for any reason or no reason, with a full refund payable to you. Notice of such denial will be made using the contact information provided by you. Failure to receive such notice will not alter or invalidate the denial. In no event will Elsevier or Copyright Clearance Center be responsible or liable for any costs, expenses or damage incurred by you as a result of a denial of your permission request, other than a refund of the amount(s) paid by you to Elsevier and/or Copyright Clearance Center for denied permissions.

LIMITED LICENSE

The following terms and conditions apply only to specific license types:

15. **Translation**: This permission is granted for non-exclusive world **English** rights only unless your license was granted for translation rights. If you licensed translation rights you may only translate this content into the languages you requested. A professional translator must perform all translations and reproduce the content word for word preserving the integrity of the article.

16. **Posting licensed content on any Website**: The following terms and conditions apply as follows: Licensing material from an Elsevier journal: All content posted to the web site must maintain the copyright information line on the bottom of each image; A hyper-text must be included to the Homepage of the journal from which you are licensing at http://www.sciencedirect.com/science/journal/xxxxx or the Elsevier homepage for books at http://www.elsevier.com; Central Storage: This license does not include permission for a scanned version of the material to be stored in a central repository such as that provided by Heron/XanEdu.

Licensing material from an Elsevier book: A hyper-text link must be included to the Elsevier homepage at http://www.elsevier.com . All content posted to the web site must maintain the copyright information line on the bottom of each image.

Posting licensed content on Electronic reserve: In addition to the above the following clauses are applicable: The web site must be password-protected and made available only to bona fide students registered on a relevant course. This permission is granted for 1 year only. You may obtain a new license for future website posting.

17. **For journal authors:** the following clauses are applicable in addition to the above:

Preprints:

A preprint is an author's own write-up of research results and analysis, it has not been peer-reviewed, nor has it had any other value added to it by a publisher (such as formatting, copyright, technical enhancement etc.).

Authors can share their preprints anywhere at any time. Preprints should not be added to or enhanced in any way in order to appear more like, or to substitute for, the final versions of articles however authors can update their preprints on arXiv or RePEc with their Accepted Author Manuscript (see below).

If accepted for publication, we encourage authors to link from the preprint to their formal publication via its DOI. Millions of researchers have access to the formal publications on ScienceDirect, and so links will help users to find, access, cite and use the best available

version. Please note that Cell Press, The Lancet and some society-owned have different preprint policies. Information on these policies is available on the journal homepage.

Accepted Author Manuscripts: An accepted author manuscript is the manuscript of an article that has been accepted for publication and which typically includes author-incorporated changes suggested during submission, peer review and editor-author communications.

Authors can share their accepted author manuscript:

- immediately
  - via their non-commercial person homepage or blog
  - by updating a preprint in arXiv or RePEc with the accepted manuscript
  - via their research institute or institutional repository for internal institutional uses or as part of an invitation-only research collaboration work-group
  - directly by providing copies to their students or to research collaborators for their personal use
  - for private scholarly sharing as part of an invitation-only work group on commercial sites with which Elsevier has an agreement
- After the embargo period
  - via non-commercial hosting platforms such as their institutional repository
  - via commercial sites with which Elsevier has an agreement

In all cases accepted manuscripts should:

- link to the formal publication via its DOI
- bear a CC-BY-NC-ND license - this is easy to do
- if aggregated with other manuscripts, for example in a repository or other site, be shared in alignment with our hosting policy not be added to or enhanced in any way to appear more like, or to substitute for, the published journal article.

Published journal article (JPA): A published journal article (PJA) is the definitive final record of published research that appears or will appear in the journal and embodies all value-adding publishing activities including peer review co-ordination, copy-editing, formatting, (if relevant) pagination and online enrichment.

Policies for sharing publishing journal articles differ for subscription and gold open access articles:

Subscription Articles: If you are an author, please share a link to your article rather than the full-text. Millions of researchers have access to the formal publications on

ScienceDirect, and so links will help your users to find, access, cite, and use the best available version.

Theses and dissertations which contain embedded PJAs as part of the formal submission can be posted publicly by the awarding institution with DOI links back to the formal publications on ScienceDirect.

If you are affiliated with a library that subscribes to ScienceDirect you have additional private sharing rights for others' research accessed under that agreement. This includes use for classroom teaching and internal training at the institution (including use in course packs and courseware programs), and inclusion of the article for grant funding purposes.

Gold Open Access Articles: May be shared according to the author-selected end-user license and should contain a CrossMark logo, the end user license, and a DOI link to the formal publication on ScienceDirect.

Please refer to Elsevier's posting policy for further information.

18. **For book authors** the following clauses are applicable in addition to the above: Authors are permitted to place a brief summary of their work online only. You are not allowed to download and post the published electronic version of your chapter, nor may you scan the printed edition to create an electronic version. **Posting to a repository:** Authors are permitted to post a summary of their chapter only in their institution's repository.

19. **Thesis/Dissertation**: If your license is for use in a thesis/dissertation your thesis may be submitted to your institution in either print or electronic form. Should your thesis be published commercially, please reapply for permission. These requirements include permission for the Library and Archives of Canada to supply single copies, on demand, of the complete thesis and include permission for Proquest/UMI to supply single copies, on demand, of the complete thesis. Should your thesis be published commercially, please reapply for permission. Theses and dissertations which contain embedded PJAs as part of the formal submission can be posted publicly by the awarding institution with DOI links back to the formal publications on ScienceDirect.

Elsevier Open Access Terms and Conditions

You can publish open access with Elsevier in hundreds of open access journals or in nearly 2000 established subscription journals that support open access publishing. Permitted third party re-use of these open access articles is defined by the author's choice

of Creative Commons user license. See our open access license policy for more information.

Terms & Conditions applicable to all Open Access articles published with Elsevier:

Any reuse of the article must not represent the author as endorsing the adaptation of the article nor should the article be modified in such a way as to damage the author's honour or reputation. If any changes have been made, such changes must be clearly indicated.

The author(s) must be appropriately credited and we ask that you include the end user license and a DOI link to the formal publication on ScienceDirect.

If any part of the material to be used (for example, figures) has appeared in our publication with credit or acknowledgement to another source it is the responsibility of the user to ensure their reuse complies with the terms and conditions determined by the rights holder.

Additional Terms & Conditions applicable to each Creative Commons user license:

CC BY: The CC-BY license allows users to copy, to create extracts, abstracts and new works from the Article, to alter and revise the Article and to make commercial use of the Article (including reuse and/or resale of the Article by commercial entities), provided the user gives appropriate credit (with a link to the formal publication through the relevant DOI), provides a link to the license, indicates if changes were made and the licensor is not represented as endorsing the use made of the work. The full details of the license are available at http://creativecommons.org/licenses/by/4.0.

CC BY NC SA: The CC BY-NC-SA license allows users to copy, to create extracts, abstracts and new works from the Article, to alter and revise the Article, provided this is not done for commercial purposes, and that the user gives appropriate credit (with a link to the formal publication through the relevant DOI), provides a link to the license, indicates if changes were made and the licensor is not represented as endorsing the use made of the work. Further, any new works must be made available on the same conditions. The full details of the license are available at http://creativecommons.org/licenses/by-nc-sa/4.0.

CC BY NC ND: The CC BY-NC-ND license allows users to copy and distribute the Article, provided this is not done for commercial purposes and further does not permit distribution of the Article if it is changed or edited in any way, and provided the user gives appropriate credit (with a link to the formal publication through the relevant DOI), provides a link to the license, and that the licensor is not represented as endorsing the use made of the work. The full details of the license are available at